The Dissertation Committee for Shin Hum Cho Certifies that this is the approved version of the following Dissertation:

Infrared Plasmonic Doped Metal Oxide Nanocubes

Committee:

Delia J. Milliron, Supervisor

Brian A. Korgel

Thomas M. Truskett

Xiaoqin Elaine Li

Infrared Plasmonic Doped Metal Oxide Nanocubes

by

Shin Hum Cho

Dissertation

Presented to the Faculty of the Graduate School of

The University of Texas at Austin

in Partial Fulfillment

of the Requirements

for the Degree of

Doctor of Philosophy

The University of Texas at Austin

May 2020

Abstract

Infrared Plasmonic Doped Metal Oxide Nanocubes

Shin Hum Cho, Ph.D.

The University of Texas at Austin, 2020

Supervisor: Delia J. Milliron

Localized surface plasmon resonance (LSPR) in semiconductor nanocrystals (NCs) that results in resonant absorption, scattering, and near field enhancement around the NC can be tuned across a wide optical spectral range from visible to far-infrared by synthetically varying doping level. Cube-shaped NCs of conventional metals like gold and silver generally exhibit LSPR in the visible region with spectral modes determined by their faceted shapes. However, faceted NCs exhibiting LSPR response in the infrared (IR) region are relatively rare. We describe the colloidal synthesis of nanoscale fluorine-doped indium oxide (F:In_2O_3) cubes with LSPR response in the IR region, wherein fluorine was found to both direct the cubic morphology and act as an aliovalent dopant. The presence of fluorine was found to impart higher stabilization to the (100) facets, suggesting that the cubic morphology results from surface binding of F-atoms. In addition, fluorine acts as an anionic aliovalent dopant in the cubic bixbyite lattice of In_2O_3, introducing a high concentration of free electrons leading to LSPR. The cubes exhibit narrow, shape-dependent multimodal LSPR extinction peaks due to corner- and edge-centered modes. The spatial origin of these different contributions to the spectral response are directly visualized by electron energy loss spectroscopy (EELS) in a

scanning transmission electron microscope (STEM). A synthetic challenge in faceted metal oxide NCs is realizing tunable LSPR near-field response in the IR. We expand to colloidal synthesis of fluorine, tin co-doped indium oxide (F,Sn:In_2O_3) NC cubes with tunable IR range LSPR. Free carrier concentration is tuned through controlled Sn dopant incorporation, where Sn is an aliovalent n-type dopant in the In_2O_3 lattice. Monolayer NC arrays are fabricated through liquid-air interface assembly, NC film nanocavities with heightened near-field enhancement (NFE). The tunable F,Sn:In_2O_3 NC near-field is coupled with PbS quantum dots, via the Purcell effect. The detuning frequency between the nanocavity and exciton is varied, resulting in IR near-field dependent enhanced exciton lifetime decay.

Table of Contents

List of Tables

List of Figures

Chapter 1: Colloidal Synthesis of Plasmonic Doped Metal Oxide Nanocrystals

Doped metal oxide colloidal synthesis has emerged recently as route for expanding localized surface plasmon resonance (LSPR) to the infrared (IR) range[1]. Chemical synthesis of nanoparticles with carrier densities of 10^{21} cm^{-3} allows realization of plasmon physical properties. Recent advanced synthetic strategies in metal oxide and chalcogenide nanoparticles allow carrier density modulation, dopant spatial distribution, and shape control. Synthetic consideration to control plasmonic semiconductor nanocrystals can be classified in following sections: 1) growth method, 2) doping strategy, 3) shape control. Each methodology will be provided with a general framework followed by specific nanocrystal specimen example and in-depth characterization techniques focused in composition/structural properties.

NUCLEATION AND GROWTH KINETICS

Three major components comprise a typical synthetic system to prepare colloidal NCs: metal precursors, organic surfactants, and solvents, although surfactants can also serve as solvents in many schemes. The generation of reactive chemical species, in atomic or molecular form referred to as monomers hereafter, through various chemical reactions of the precursors is usually the first step in the synthesis. Identifying suitable precursors then carries a lot of importance in the synthesis design, which generally are organometallic compounds or inorganic salts (which are complexed with the surfactants *in situ*). A more detailed description of the underlying chemistry of the monomer generation is included in a subsequent subsection required for a typical colloidal

synthesis is shown in (Figure 1.1). The subsequent growth of NCs from these monomers is significantly influenced by the surfactant molecules present in the reaction mixture. Overall, NC formation through the colloidal route can be divided into two major steps: (a) nucleation (of seeds), and (b) growth (of seeds into NCs). The nucleation step is facilitated by the preceding monomer generation step that involves the reaction of the precursors at moderately high temperatures (typically, 200-350 °C), mandating the need for solvents exhibiting relatively high range of boiling points. At a critical concentration of the monomers when supersaturation is achieved, a "burst nucleation" of seeds occurs marking the nucleation event. The subsequent growth stage comprises of the assimilation of additional monomers, still present in the reaction mixture, by the growing seeds.

Nucleation and growth of NCs

A general understanding of the NC growth mechanism can be attained from the classic work of LaMer and Dinegar in the 1950s, on the formation of sulfur hydrosols from the acid decomposition of thiosulfate ions. [2] The concept of burst nucleation was described in this seminal paper where the formation of many nuclei in a single step and their subsequent growth without the occurrence of additional nucleation events was demonstrated. The principles described therein form the basis of understanding the growth progression of most modern colloidal NC syntheses. The LaMer-Dinegar growth curve, of temporal evolution of monomer concentration, is depicted in (Figure 1.1) with the three growth regimes. The initial monomer generation step comprises regime I, wherein the steady rise of the curve signifies the formation of monomers in the reaction mixture and a consequent rise in the concentration. The rate of monomer formation depends on the underlying reaction and also on the temperature of the reaction medium, with a higher rate of generation at higher temperature. However, the monomers do not

spontaneously “condense” into nuclei even at the saturation concentration, Cs, due to the considerably high energy barrier for the induction of the nucleation event. Above a critical concentration of the monomers, C_{min}^{nu}, i.e., the point of supersaturation, burst nucleation commences marking the onset of regime II. The monomers get rapidly consumed at this stage leading to an accelerated growth of the nuclei, partially relieving the supersaturation, and leading to a sudden drop in the monomer concentration (signified by the curve maximum). Additional nucleation events do not occur as the monomer concentration drops below the critical concentration. This marks the onset of regime III, where the nuclei grow by assimilation of monomers, occurring somewhat above the saturation concentration or solubility.

This is a general framework of nucleation and growth processes that pertains to colloidal NCs and the description is not an exhaustive review of the many principles that have been described by various authors over the years. More complete treatment of the subject can be found in the works of several other authors.[3–5]

Thermodynamic and kinetic control

Several thermodynamic and kinetic considerations come into play which determine the shape and size of the NCs produced from colloidal synthesis. A number of demonstrations have been made by researchers on thermodynamic and kinetic “control” in colloidal NC syntheses, mostly referring to the factors determining the shape of NCs but also having relevance for size distributions. It is important to be able to discern the differences between these two growth regimes, in order to design a successful synthetic strategy.[6,7] In broad terms, it is generally the relative magnitudes of the rates of monomer deposition on the nuclei and the surface monomer diffusion that dictate the final morphology of the NCs, and also the extent of thermodynamic or kinetic control. Under

thermodynamic control, the initially deposited monomers on the NC surface diffuse to lower energy sites. The diffusion of monomers occurs at a higher rate than their deposition – generally the case as the monomer concentration is well below the critical concentration needed for nucleation and is approaching the solubility, represented by most of regime III on the LaMer-Dinegar curve in Figure 1.1. Kinetically controlled growth conversely entails a higher rate of monomer deposition than diffusion. This can lead to thermodynamically disfavored shapes, and usually corresponds to monomer concentrations more significantly above the solubility in the LaMer-Dinegar description.

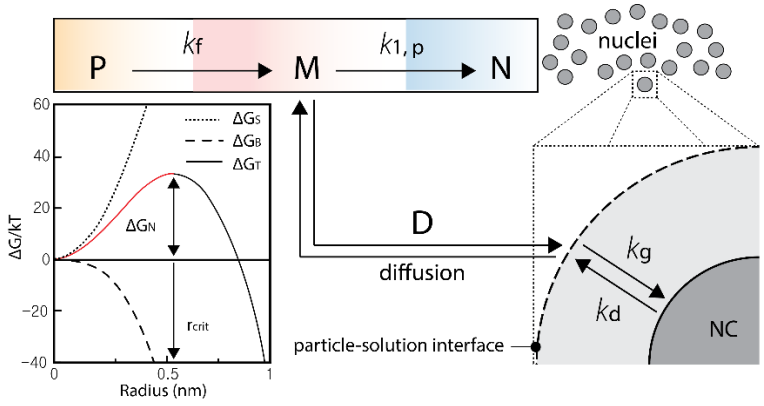

Figure 1.1: Nucleation kinetics schematic

Surface energy contribution (ΔG_S), bulk energy (ΔG_B) contribute to total energy contribution (ΔG_T). Critical radii for nucleation at critical nucleation energy barrier (ΔG_N). Precursor (P), monomer (M), nanocrystal (N) with kinetic rate between reaction steps (k_f, $k_{1,p}$). Diffusion limited growth occurs when nanocrystal growth rate k_g is higher than monomer diffusion rate k_d at particle-solution interface.

La Mer classical nucleation and growth theory[2] provides basic kinetic mechanistic framework in how chemical monomers eventually lead to monodisperse nanocrystals. Nucleation process provides the critical step for formation of nuclei seed that become the template core of individual particle.[3] Under the assumption of homogeneous nuclei formation, the total free energy of a nanoparticle is defined by sum of surface free energy and bulk free energy. A particle of radius r, surface energy of γ (surface Gibbs free energy:ΔG_S), and volumetric free energy of bulk crystal ΔG_B can be parameter for defining free energy on a nanocrystal nuclei (Figure 1.1 inset).

$$\Delta G = 4\pi r^2\gamma + 4/3\pi r^3 \Delta G_B$$

The minimized free energy with respect to particle radius ($\frac{d\Delta G}{dr} = 0$) is the nucleation energy barrier (ΔG_N), and a critical radius (r_{crit}) can be derived where nuclei can exist in a supersaturated solution without being redissolved back to the solution. Upon nucleation, diffusion limited growth occur on nuclei particle-solution interface where monomers further deposit onto surface. During diffusion limited condition, extrinsic dopants can deposit simultaneously with bulk nanocrystal monomer precursors and be embedded into the lattice during growth. Understanding diffusion limited growth kinetics provide synthetic platform for expanding synthetic doping strategies for plasmonic nanocrystals which will be elaborated in further sections.

The NC is said to have attained its equilibrium shape when it gets sufficient amount of time to let its atoms arrive at their final positions, leading to a local minimization of the Gibbs free energy, though in a global sense the system may still lower its energy by coalescence of NCs into larger crystals. This thermodynamically controlled product can be achieved by raising the temperature or by running the reaction

for a longer time. Now, the total Gibbs free energy of a NC is the sum of free energy contributions from the bulk and the surface: $\Delta G = A_i\gamma_i + 4/3\pi r^3 \Delta G_B$

Here, γ_i signifies the surface free energy per unit area while A_i denotes the surface area for a specific facet. Hence, a minimized total surface free energy (at a fixed volume) will lead to a minimum Gibbs free energy. The surface free energy (γ_i) varies for different crystallographic planes as a result of differences in atomic arrangement and interactions with bound surfactants and manipulating it has been central to conceptualizing shape-controlled growth of NCs. Ionic and molecular capping agents (such as organic surfactants) that exhibit selective binding to specific crystal facets play an important role by modifying the relative surface energies of these crystal facets. This leads to altered NC shape due to the maximized expression of the stabilized crystal facets. The chemisorption of surfactants as capping agents also results in hindered monomer deposition on those same crystal facets.[6,8,9] Kinetically, this means that the capping agent also modifies the relative growth rates of different crystal facets and a slow growth rate of a facet results in greater share of the surface area. Obviously, this implies that thermodynamic considerations can also productively guide the development of shape controlled NC synthesis taking place in the kinetically controlled regime. From yet another perspective, surface passivation can increase the energy barrier to surface diffusion and hence the final NC shape is determined by the interplay of these various processes.[6,8,9] It is important to note in this regard, that the equilibrium shape of a NC can never be completely spherical as a number of high-index facets with relatively high surface free energies will be needed to form a sphere, although NCs are often approximated as spherical for the sake of analysis of optical and electronic properties.

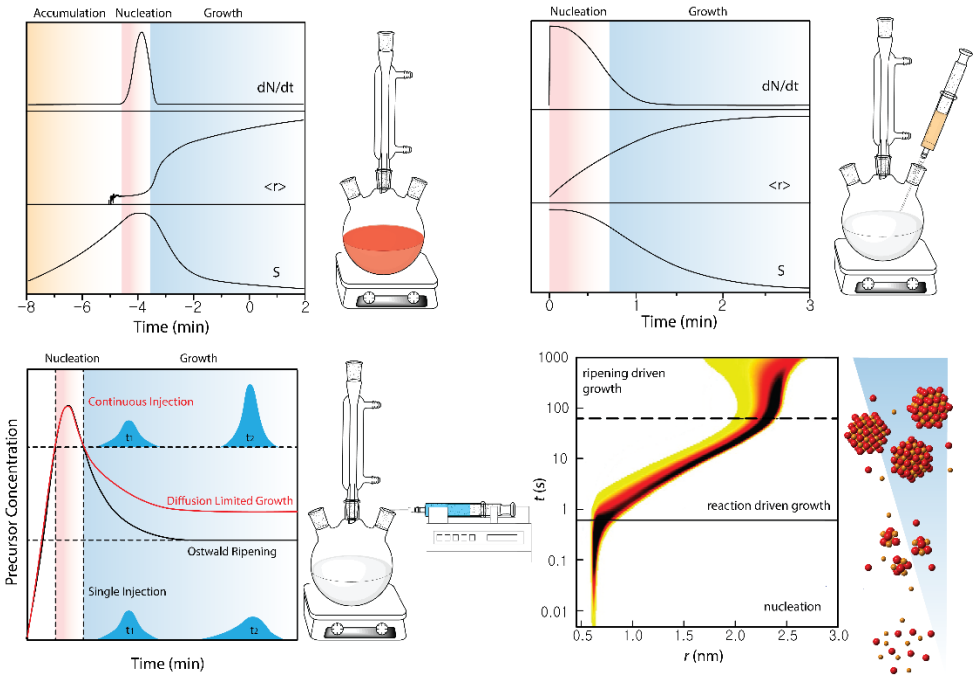

Figure 1.2: Colloidal nanocrystal synthesis schematic

a) Heat-up method setup schematic with nucleation rate (dN/dt), mean NC radius (<r>) and supersaturation (S) plot. b) Hot-injection method setup schematic with respective plot. c) Continuous slow injection setup schematic with precursor concentration plot (red line) and expected plot with single injection (black line). NC size distribution with continuous injection (top) and single injection (bottom). d) Size distribution simulation after nucleation, reaction driven growth, and ripening.

Hot-injection and heat-up approaches

The colloidal synthesis technique can be further divided into two major approaches, that of (a) hot-injection, and (b) heat-up methods. The primary difference in the growth progression of these two methods lies in the temporal separation of the events of nucleation and growth. In the hot-injection approach, an instantaneous burst nucleation

is achieved upon injection as a high degree of supersaturation is induced in a very short period of time. The synthesis setup generally comprises of that shown schematically in Figure 1.2, where two reactant solutions are brought together at a high temperature, one being in the flask and the other in the syringe, or both contained in the syringe with only solvent and surfactant in the flask. For instance, in case of metal chalcogenide NC synthesis, a typical hot-injection method encompasses heating the metal precursor in the flask while the chalcogen solution is injected into this flask at a suitable temperature. The aim is to produce a single nucleation event following the injection, and a subsequent growth stage which does not overlap with any secondary nucleation. Naturally, a more uniform NC morphology and narrow size distribution can be achieved when this approach succeeds in producing a single nucleation event. That said, achieving this result can be highly contingent on rapid mixing, to avoid inhomogeneities in monomer concentration, immediately following injection. As a result, reproducibility and scalability are notoriously challenging.

The heat-up approach, on the other hand, entails mixing all the components of the synthesis (precursors, surfactants and solvents) in a single flask and heating it up to initiate nucleation and subsequent growth. Due to the continuing monomer generation as a result of sustained heat supply, the nucleation event lasts longer in this case and it can substantially overlap with the growth stage. This means that fresh nucleation events may occur while the existing nuclei are at the growth stage. This can result in a broad size distribution and achieving a high degree of size and shape control is not always possible.

Each of these approaches have their advantages and disadvantages, and the choice of a suitable approach is largely dependent on the desired end result. For instance, the hot-injection approach is more suited for studies/applications which need an ensemble of NCs with a tight control over their physical properties which, in turn, are directly related

to the NC size and shape distribution. This is particularly more important for light emission from quantum dots as the size quantization effects come into play here. However, this approach is not easily scalable for large scale production due to various factors like: (a) heavy reliance on homogeneous reactant mixing at high temperatures in a short period of time in order to achieve a controlled nucleation – it becomes less controlled when the volume of the batch increases; (b) cooling rates differ at different volumes – immediately after the injection, the reaction temperature needs to drop in order to separate the nucleation and growth events; (c) injecting larger volumes become impractical, etc. The heat-up approach, on the other hand, can be an efficient synthetic scheme in this regard as it is more easily scalable and a far higher degree of reproducibility can be exercised due to the absence of the drawbacks mentioned above. Applications requiring larger batches of NCs are then inherently more disposed towards employing heat-up methods. Hence, great attention and progress has been made to improving the control over nucleation and growth in heat-up reactions, leading to scalable chemistries for some prototypical NC materials.[10,11] However, the chemical basis of the synthesis has to be designed in such a way that the nucleation and growth stages are essentially decoupled in order to lower polydispersity. This means that the interplay of the precursors and surfactants need greater attention in this case at that generally defines the reaction rate and thereby the period for which the nucleation stage lasts. This is particularly more important for NC cores comprising of more than one element (binary, ternary, quaternary compounds, and impurity doped materials) as then a good match amongst the reactivities of the different components becomes a top priority. The principles of hard and soft acid-base theory lend a qualitative assistance in determining the relative reactivities, as will be discussed in a later section. In connection to the above

discussion, the next section will demonstrate the role played by the underlying chemistry of monomer formation on the eventual NC composition.

After nucleation, reaction drives NC growth where monomers deposit onto the seed nuclei surface. Diffusion limited growth condition prevent dissolution of deposited monomers on nanocrystal surface due to supersaturated concentration of monomers. In plasmonic nanocrystals, it is critical to engineer synthetic doping strategies within this diffusion limited growth regime and experimental setup provide kinetic framework prior to chemical control. Three basic experimental setup in colloidal nanocrystal synthesis for exploiting kinetics is heat-up, hot-injection, and continuous slow injection.

Heat-up method is heavily utilized in metal oxide classes of plasmonic nanocrystals, confining all needed chemical precursor in three-neck reaction flask prior to nucleation. The heat-up colloidal synthesis method developed by Hyeon is illustrated in a three stage process: monomer accumulation, nucleation, and growth (Figure 1.2 a).[12] First step involve chemical precursors transitioning to monomers (P→M) with rate k_f through metal-oleate coordination (Figure 1.1 yellow). The nucleation energy barrier ΔG_N suppresses monomer decomposition at early heat-up stage and accumulation of supersaturated monomers (S) occur. In the second stage, nucleation burst occurs when significantly ramped temperature allow monomers to overcome nucleation energy barrier (M→N) with rate $k_{1,p}$ and rapid nanocrystal seed formation (dN/dt) occur (Figure 1.1 red). At the third stage, nanocrystal growth occur when nuclei undergo diffusion limited growth as mean NC radius <r> increase. Supersaturated monomer condition allow size focusing and narrow distribution of nanocrystal size. Excessive growth time leads to Ostwald ripening where agglomeration of nanoparticles lead to poor monodisperse products (Figure 1.2 d).[13] NC size distribution broadening occurs and all doping synthetic

strategies must be implemented in growth time period before Ostwald ripening to fine-tune plasmonic NC properties.

Hot-injection colloidal synthesis method, pioneered by Bawendi, provides general experimental method for synthesizing chalcogenide classes of colloidal plasmonic nanocrystals. Hot-injection method allow immediate nucleation without prior accumulation of monomers by swiftly injecting separate chalcogenide stock solution into degassed liquid phase metal precursor solution in three-neck flask (Figure 1.2 b). The two step process without monomer accumulation stage allow a versatile free range of anion-cation precursor ratio control, providing a kinetic foundation for stoichiometric controlled vacancy induced plasmonic chalcogenide nanocrystals. The first step involve extreme monomer supersaturation (S) after immediate injection of stock solution, providing kinetic driving force for rapid nucleation burst (dN/dt). Second step follow after nucleation, where size focused nanocrystal growth (<r>) occurs through diffusion limited growth until sufficient monomers are consumed, then polydisperse Ostwald ripening proceed. [12]

To compromise short or uncontrollable extent of nanocrystal growth regime, continuous slow injection synthesis setup (Figure 1.2 c) can be used to maximize extent of growth period and further fine-tune LSPR inducing dopant incorporation into the nanocrystal lattice.[14] A continuous source of precursors injected into the reaction solution enable sustained period of diffusion limited growth compared to a single injection.[15] The diffusion limited growth enables suppression of Ostwald ripening and allow monodisperse NC to be synthesized despite extension of growth reaction time. Ito et al demonstrated syringe pump dropwise addition of metal oleate precursor into hot oleyl alcohol solution induced rapid esterification and allowed continuous In_2O_3, Fe_2O_3, and CoO NC growth. This method also successfully demonstrated effective tin dopant

incorporation in ITO nanocrystal synthesis when extrinsic metal dopant precursor was controllably added to the stock injection solution.[16]

MONOMER CHEMICAL MECHANISM

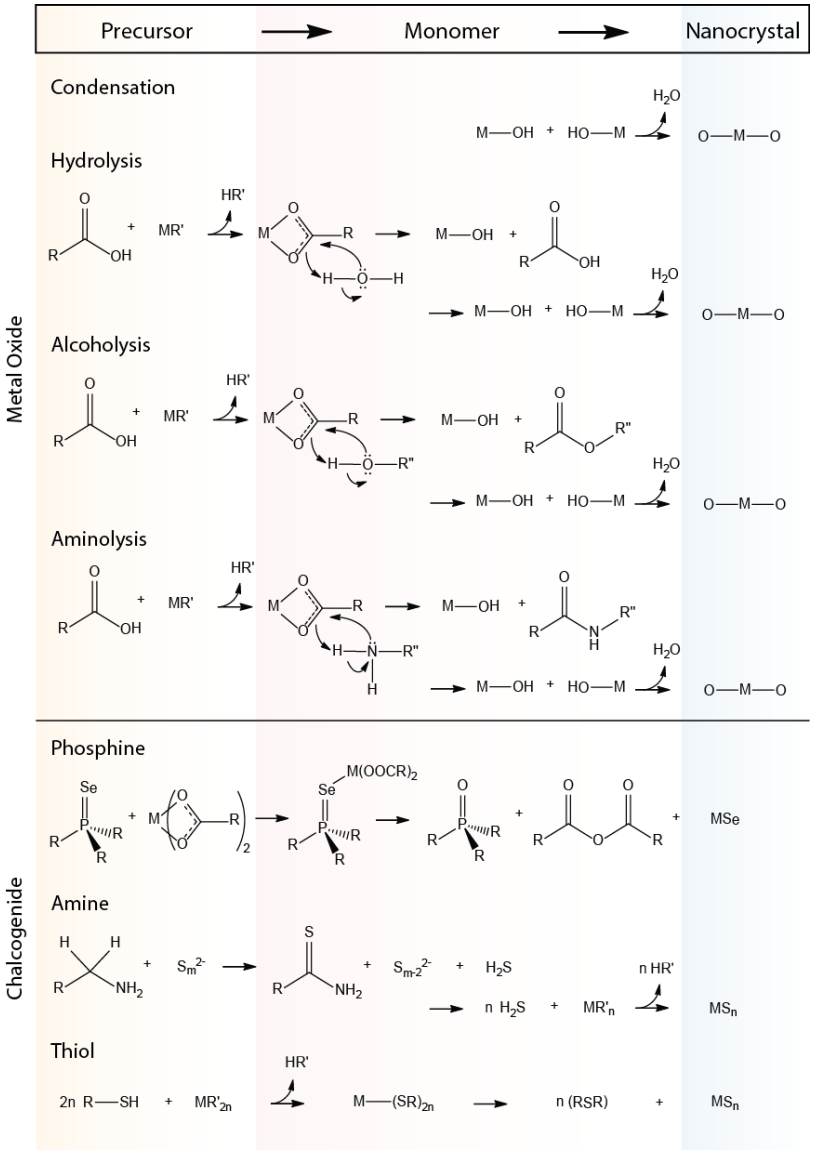

Figure 1.3: Chemical Decomposition Pathway

Chemical decomposition pathway consists of precursor, monomer accumulation and nanocrystal formation. 1) metal oxide: oxolation condensation, hydrolysis, alcoholysis, and aminolysis pathway; 2) chalcogenide: phosphine coordination, amine, and thiol decomposition.

Extending the prior discussion on nanoparticle growth kinetics, we discuss the basic bi-atomic component chemical perspective in colloidal nanocrystal synthesis. Myriad chemical precursors are available in the NC synthesis literature[17] yet the chemical toolbox library can be adapted to developing metal oxide and chalcogenide plasmonic nanoparticles. Sol-gel[18] and hydrothermal synthesis[19] methods have been employed in the earliest stage of nanomaterial research before the dawn of non-hydrolytic colloidal synthesis. Teflon capped autoclave vessel allows water medium and metal precursor mixture to reach high pressure reaction conditions. Sharp increase in OH^- and H_3O^+ ionic product of water occurs under high pressure allowing favorable hydrolytic reaction equilibrium toward metal hydroxide formation.[20] Under hydrothermal synthetic conditions, decomposition pathway can occur through oxolation condensation or hydrolysis reaction of solution dissolved metal hydroxide into metal oxides (Figure 1.3). Hydrothermal synthesis of plasmonic nanoparticles have been demonstrated in degenerately doped metal oxides by Nütz et al through antimony-doped tin dioxide ($Sb:SnO_2$) [21] and in oxygen vacant molybdenum oxide (MoO_{3-x}) by Hwang et al. [22]

Although the control offered by colloidal synthesis is undeniable, other solution synthesis methods like sol-gel and solvo(hydro)thermal techniques have also made significant contributions in nanomaterial research.[18,19,23,24] Solvo(hydro)thermal syntheses are typically conducted in Teflon lined stainless steel autoclaves where the precursors are sealed in with a suitable solvent and heated at elevated temperatures, generally in an oven. The term hydrothermal signifies reaction in water as a solvent while solvothermal denotes using a solvent other than water, usually a non-polar one exhibiting a higher boiling point. The advantages of this synthesis technique include accessibility of high pressure, which amplifies precursor reactivity and solubility with minimal peripheral

instrumental setup. For instance, in hydrothermal syntheses of metal oxide NCs, sharp increase in OH^- and H_3O^+ ionic product of water occurs under high pressure allowing favorable hydrolytic reaction equilibrium toward metal hydroxide formation.[20] The capability of these autoclaves to withstand high temperature and pressure environments over prolonged periods of time makes them attractive vehicles for achieving enhanced reaction rates (due to increased precursor solubility and reactivity) that are not normally accessible at standard atmospheric pressure. Solvents can also be taken above their atmospheric pressure boiling points, extending the range of accessible synthetic conditions, which can be especially helpful for materials that are difficult to crystallize at lower temperatures.

A number of examples of hydrothermal synthesis of LSPR active inorganic NCs have been demonstrated such as those of degenerately doped metal oxides like antimony-doped tin dioxide ($Sb:SnO_2$) by Nütz et al,[21] and oxygen deficient molybdenum oxide (MoO_{3-x}) by Hwang et al.[22] Early hydrothermal syntheses of irregularly shaped LSPR active NCs have been greatly improved by subsequently developed non-hydrolytic colloidal syntheses, providing enhanced uniformity and advancing material diversity. Although the autoclave-based solvo(hydro)thermal synthesis scheme is attractive for reasons introduced above, it does exhibit a few drawbacks. Primary among these is the extreme difficulty in collecting aliquots mid-synthesis for following up the progress of a reaction and also the "black-box" nature of the system makes it difficult to discern any visual changes that are generally afforded by the glassware setup of the colloidal technique. These considerations serve as a hindrance towards standardizing syntheses across laboratories or unravelling the mechanisms of NC formation and hence tailoring reactions towards targeted end result, such as realizing a specific optoelectronic property (e.g., LSPR or excitonic frequencies or linewidths), is generally difficult. Nevertheless,

autoclave-based syntheses have often been the first to access new materials because of the broad range of reaction conditions.

Early irregularly shaped hydrothermal synthesis of plasmonic NC has been greatly improved by non-hydrolytic colloidal synthesis, providing enhanced monodispersity and advancement in material diversity. The basic two-component (metal oxide, chalcogenide) under heat-up colloidal synthesis, alcoholysis or aminolysis of a wide range of metal carboxylate precursor have been an effective chemical decomposition pathway to provide monomers in metal oxide classes of plasmonic nanocrystals.[25,10,26,27] The abrupt nature of decomposition of monomers allow rapid nucleation and fast growth, enabling narrow size distribution quality in colloidally synthesized NCs. Typical chemical precursors include coordinated metals (metal acetate, metal acetylacetonates, and metal halides), organic surfactant (oleic acid, oleylamine, primary alcohol), and extrinsic metal dopant precursors. Coordinated metal precursors (P) re-coordinate with oleic acid surfactant which simultaneously act as a hard-base carboxylate group. The metal precursor chemical species slowly accumulate into metal carboxylate monomers (M) under moderate heat condition (P→M). Sufficiently high aging temperature rapidly initiate alcohols or amine group surfactants to nucleophilically attack the monomer carboxylate group and form metal hydroxides (Figure 1.3). The followed metal hydroxides rapidly undergo condensation (M→N) and results into solid phase crystalline metal oxides (N) that nucleate and subsequently deposit onto NC surface.[12]

Choice of precursors and monomer generation

As mentioned above, the composition of the final NC core is heavily dependent on the choice of the precursor and the monomer generation chemistry. For instance, pyrolysis of organometallic precursors is the traditional choice for producing NCs of

compound semiconductors while hydrolysis of metal salts and subsequent condensation is commonly employed for metal oxide NCs. Then again, a simple reduction of metal ions is used for generating metal NCs. This underlying chemistry of monomer generation plays a crucial role in sustaining the various steps of NC formation and the ligand shell formation, as schematically depicted in Figure 1.2.

Although generalizing and classifying the different chemical reactions available for producing NCs of varying core compositions is beyond the scope of this review, we discuss here the salient features of two model binary systems: metal oxide and metal chalcogenide NCs. The choice is based upon the fact that these two categories claim a major share of LSPR active inorganic NCs reported in the literature, and also serve as good examples for demonstrating vastly different chemical pathways employed in colloidal NC growth. Furthermore, these very principles can be extended to doped or ternary NCs (both oxides and chalcogenides) when additional factors like reactivity balance of different precursors are taken into account. Myriad chemical precursors are available in the NC synthesis literature which are generally inorganic salts or organometallic precursors. However, nonaqueous synthetic techniques commonly involve converting the metal salts into organometallic complexes *in situ* through their reaction with the surfactants, which then act as the reactive chemical species. This is necessary also to impart solubility to these NCs as the surface atoms of the resulting NCs remain coordinated to these surfactant molecules eventually. An example of such a coordination is the conversion of metal salts into metal carboxylates through their reaction with long chain carboxylic acid surfactants.

A favored route of formation of metal oxide NCs is through the “lysis” of metal carboxylates (Figure 1.3), which are usually prepared from the reaction of metal salts with long chain carboxylic acids like oleic acid, stearic acid etc.[10,26] The lysis can be

induced by a suitable nucelophile e.g. protic moieties like a long chain amine or alcohol or even water for that matter, which generates the metal hydroxide that eventually condenses into the oxide at high temperature accompanied by loss of water. Depending on the lysing agent used, the process is termed aminolysis (for amines),[28,29] alcoholysis (for alcohols),[14,25,27,30] or hydrolysis (for water).[30,31] Employing a long chain amine or alcohol is more appealing as these compounds do not become volatile at the high reaction temperatures and the yields for such reactions are generally higher due to the irreversible nature of the reaction.[30] This is so because esters or amides (Figure 1.3) that are formed as a result of the lysis are stable and do not exhibit a propensity to react back with the resulting metal hydroxides or oxides. Hydrolysis, on the other hand, can be reversible since it releases the more reactive carboxylic acids. Typical metal precursors include metal salts like metal acetate, metal acetylacetonates, and metal halides, which also serve as precursors for extrinsic metal dopants.[12]

Metal chalcogenides differ from metal oxides in that a separate chalcogenide source is needed to drive crystalline lattice growth[32], whereas carboxylate decomposition in metal oxide NC provide self-sufficient oxygen source in a degassed oxygen gas free precursor solution. Copper metal precursor undergo coordination with base (oleylamine, oleic acid) surfactants under moderate temperature condition in a reaction pot. A separate stock solution of chalcogenide source (S, Se, Te) can be prepared with coordinating surfactants (trioctylphosphine oxide (TOPO)[33], trioctylphosphine (TOP)[34]). Swift injection of chalcogenide stock solution into metal precursor solution allow cation-anion bonded monomers and formation of crystalline lattices during particle growth (Figure 1.2 b). For metal sulfide NC, wider sulfur source has been utilized beyond the typical phosphine coordination, including oleylamine[35–39] coordinated sulfur or thiol decomposition[40] (Figure 1.3). The decoupled metal cationic and chalcogenide anion

source provides greater degree of freedom in stoichiometric ratio induced metal vacancy or phase transformation induced LSPR control.

Unlike metal oxide NCs, where the component metal and oxygen atoms are often both contributed by the same precursor (metal carboxylates provide both the metal and the oxygen moieties, metal chalcogenide NC synthesis generally proceeds through a different pathway. As shown in the schematics in Figure 1.3, the metal and the chalcogen precursors are prepared separately and then brought into a mutual reaction.[32] The surfactants are chosen carefully in order to use this chemical pathway for incorporating them as surface capping agents. This is the general chemical scheme for the most commonplace cadmium and lead chalcogenide NCs, but the principle remains the same for the chalcogenide compositions more relevant to LSPR activity (notably, copper chalcogenide NCs), save for the mode of metal coordination with the surfactant. Since copper ions are softer than cadmium or lead, they are more effectively coordinately by softer bases like alkylamines, instead of alkylcarboxylates. For instance, in the synthesis of copper chalcogenide NCs, copper precursors coordinate with oleylamine molecules under moderate heating in a reaction flask. A separate stock solution of the chalcogenide source (S, Se, Te) is prepared by coordinating with trioctylphosphine (TOP) or oleylamine or even through dissolution in the non-coordinating octadecene in some instances.[34,41] Swift injection of the chalcogenide stock solution into the metal precursor solution then triggers the formation of metal-chalcogen bonded monomers (that may be poorly characterized) that eventually lead to NC growth (Figure 1.2 b). For metal sulfide NCs, a wide number of sulfur sources have been utilized extending beyond the typical phosphine or oleylamine coordination, which includes thiol decomposition as well. [35–40] The decoupled metal and chalcogenide sources provide a means for synthetic control over stoichiometric ratio to control metal vacancy concentrations and crystal phase, both

of which impact LSPR properties as highlighted throughout the metal chalcogenide NC literature.

Naturally, the synthetic considerations in these two widely different chemical approaches will vary and need deliberate design. With proper balance in the chemistry, both these reactions can be suitably tailored to fit a hot injection or a heat-up approach. In general, these factors become more important when attempting to synthesize multi-component (ternary, quaternary, or more complex) NC core compositions as the number of parameters that influence the synthesis increases. As a natural extension, these factors also pertain to doped compositions, which represent many LSPR active NCs.

Most of the design considerations for NC synthesis can be connected to the relative reactivities of the metal precursors and their strength of binding with the surfactants present in the reaction mixture. As can be envisaged from the above discussion, NC growth occurs in a rather complex mixture of salts and surfactants and therefore it is not always possible to delineate and predict the effect of modifying a reaction parameter (reactant composition, temperature, heating rate etc). However, qualitative tool is available to determine a suitable starting point of investigation. Pearson's hard and soft acid-base (HSAB) theory is one such tool that has been increasingly cited by researchers in rationalizing the outcomes of their synthetic endeavors and also narrowing down the precursor choices.[42–45] The principles of HSAB theory dictate that a hard (soft) cation will have preferential affinity towards a hard (soft) anion and hence will exhibit stronger binding than hard-soft pairs. The definition of the hardness of an ion is roughly related to its charge-to-size ratio and hence harder ions are those that are highly charged species with relatively small size and an ion is termed soft when a relatively small charge is accommodated in a large ionic size. It is easy to see that this definition directly correlates to the polarizability of the ion (with soft ions being more

polarizable). From this definition, it immediately follows that the harder Cd^{2+} ion shows higher affinity to the harder oxygen center of the carboxylate ion while a relatively soft Cu^{+} ion has the propensity to bind to the softer nitrogen-center of the amine ligand, leading to the differences in the surfactant chemistries employed in Cd and Cu chalcogenide NC syntheses. From the point-of-view of NC synthesis, HSAB theory assists in carefully balancing the metal-ligand interaction as it needs to be weak enough to facilitate rapid nucleation by increasing the availability of monomers while strong enough to coordinate with the eventual NC surface during growth by forming a stabilizing layer that hinders uncontrolled growth but permits monomers to precipitate at the NC surface.

Dopant-host reactivity balance

Doped semiconductor NCs claim a large share of the literature on LSPR active inorganic NCs since, as already discussed in Section 2, essentially any semiconductor NC can sustain LSPR, provided it exhibits appreciable charge carrier concentration.[46] It is, therefore, imperative to take a closer look at the various synthetic strategies that are employed to introduce dopant atoms in a semiconductor NC lattice. Over the past ten years or so, various research groups have developed synthetic strategies that can help establish tight control over the dopant incorporation in semiconductor NCs. The availability of such synthetic methods has fueled the advancement of understanding in this field of research as structure-property correlations allow researchers to elucidate fundamental physical principles across a diverse range of NC core compositions.

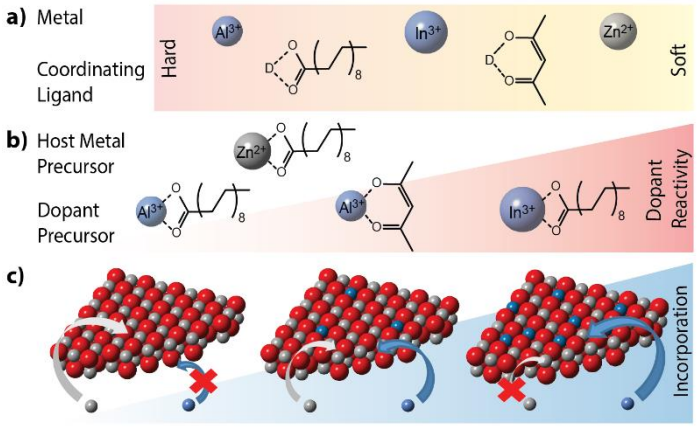

Figure 1.4: Extrinsic dopant incorporation schematic

a) Representative examples depicting the relative hard and softness of metal ions (Al^{3+}, In^{3+}, and Zn^{2+}) and coordinating ligands (stearate, acetylacetonate). b) Dopant (aluminum (III) stearate, aluminum (III) acetylacetonate, and indium (III) stearate) reactivity relative to host metal precursor (zinc (II) stearate). c) Dopant incorporation outcome scenarios: dopant incorporation failure due to low dopant precursor reactivity relative to host metal precursor (left); effective incorporation by balanced reactivity with host metal and dopant precursor (center); and phase segregation by excessive dopant reactivity (right).

Incorporating high concentrations of extrinsic aliovalent dopants can induce degeneracy in the dopant energy levels and spatial overlap between carriers associated with individual dopants so that the dopant states form bands. This degenerate doping implies high charge carrier concentrations in LSPR active NCs. Effective dopant incorporation requires that the dopants are able to substitute host atoms within the NC core rather than being adsorbed onto the NC surface. Dopant precursor reactivity can determine the success or failure in a NC synthetic methodology as a third atomic dopant component must be added into the single-phase binary compound semiconductor NC host

material, such as those of metal oxides or chalcogenides. To achieve extrinsic aliovalent substitutional doping, it is critical to carefully balance dopant reaction kinetics with the host NC growth rate by judicious dopant precursor selection.[47,48] Earlier studies deemed NCs as being undopable, citing a self-purification process due to the defect formation energy being higher compared to the bulk materials. Under thermodynamic equilibrium, NCs may be prone to annealing out dopants to minimize the total free energy.[49,50] However, effective NC doping has been realized throughout the literature in solution phase colloidal NC growth at relatively low temperatures (below 400 °C), owing partly to the dominant role of kinetics rather than thermodynamics governing the outcome of NC growth. [47] Kinetic factors can limit and control dopant incorporation, which can be controlled through careful precursor reactivity balance.

As described above, HSAB theory can be employed in comparing metal-ligand bond strength to fine-tune the reactivity balance in tertiary or doped compound semiconductor NCs. Dopant precursors include metal ions coordinated with a wide range of hard or soft bases such as halides (F^-, Cl^-, Br^-) or organic moieties (acetates, acetylacetonates, 2-ethylhexanoate, stearates). Metal and organic ligand components can be categorized as being hard, borderline, or soft depending on the ionic radius, oxidation state, polarizability, and electronegativity.[44,51] Metal ions (Lewis acids) with higher oxidation state and smaller ionic radius have a higher charge-to-radius ratio, leading to increased hardness.[42,52] Metal ions with lower oxidation state and larger radius, hence lower charge-to-radius ratio, are classified as soft acids and make bonds that are more covalent in nature (Figure 1.4 a). If the dopant cation is harder than the host cation, the dopant precursor is expected to be less reactive than the host when both cations are coordinated with the same hard ligands. For coordinating ligands (Lewis bases), head groups with larger atomic radius (P, S, Se, Te) or with electron delocalization (as in

acetylacetonate) tend to be soft compared to head groups with strongly localized charge (-COO^-, -OH, -NH_2).[44] Hard acids bind more strongly to hard bases due to the ionic nature of both components and the limitations on orbital overlap to form covalent bonds with hard acids.[45] The same affinity occurs for soft acids and soft bases due to their more covalent nature and high mutual polarizability. A mismatched hard-soft metal-ligand interaction leads to weaker binding, resulting in higher reactivity and high rate of metal-ligand dissociation (Figure 1.4 b).

Careful dopant reactivity balance must be achieved to synthetically incorporate extrinsic dopants into the NC host lattice, similar to the synthetic strategy employed in tertiary NCs to achieve homogeneous compounds or alloys.[53] Host precursors with a weak metal-ligand coordination bond provide favorable reaction environment for large accumulation of free monomers for facilitating rapid nucleation. Yet, the metal-ligand bonds must be sufficiently strong for both host and dopant precursors during growth phase to both avoid independent homogeneous nucleation and prevent uncontrolled growth by stabilizing monomer decomposition and promoting monolayer NC growth.[17] These trends were demonstrated in doped zinc oxide NC synthesis, where zinc (II) stearate ($Zn(St)_2$) was used as the host precursor for ZnO NCs along with controlled selection of metal-ligand dopant precursors. Buonsanti et al were able to synthesize colloidal NCs of aluminum-doped zinc oxide (AZO) by using aluminum (III) acetylacetonate ($Al(acac)_3$) as the dopant precursor to achieve well balanced reaction with $Zn(St)_2$.[54] The dopant precursor decomposition rate must be nearly equal to those of host precursor to incorporate dopant atoms uniformly in the NC lattice during growth (Figure 1.4 c, center).

This synthetic example in dopant precursor selection demonstrates the importance of balancing dopant-host precursor reactivity. Excessively stable dopant precursors

prevent coordinating ligands from dissociating and results in low or inhomogeneous incorporation of dopants into the NCs. If the dopant precursor dissociation is too slow, dopant ions cannot be liberated and fail to be incorporated into the host NC during growth (Figure 1.4 c, left). For example, no dopant incorporation was observed by Buonsanti et al when aluminum (III) stearate ($Al(St)_3$) replaced $Al(acac)_3$ as the dopant precursor.[54] Al^{3+} is a hard acid and hence binds more strongly with the harder stearate ligand than the comparatively softer and more electron delocalized acetylacetonate ligand. This leads to lower reactivity of $Al(St)_3$ compared to $Zn(St)_2$ host precursor, resulting in a failure to incorporate dopants in the ZnO NCs. On the other hand, if dopant precursor reactivity is too high, uncontrolled NC products with segregated dopant phases may occur as well (Figure 1.4 c, right). Studies by Liang et al have demonstrated that indium (III) stearate ($In(St)_3$) as a dopant precursor was far more reactive than the host zinc (II) stearate ($Zn(St)_2$) precursor and did not lead to a single phase indium-doped zinc oxide (IZO).[55] To improve reactivity balance, replacing the dopant precursor with indium (III) 2-ethylhexanoate ($In(EH)_3$) allowed steric hindrance to slow down the alcoholysis and hence reduced the reactivity to closely match that of $Zn(St)_2$.[56] Hence, a careful selection of metal-ligand coordinated dopant and host material precursors, guided by the HSAB theory, can determine the success or failure of synthetic designs aimed at producing extrinsically doped LSPR active semiconductor NCs.

DOPING SCHEMES FOR LSPR ACTIVE SEMICONDUCTOR NCS

Elemental metals and binary compound semiconductors were the focus of synthetic developments in the early stages of colloidal synthesis research, possibly due to the lower level of complexity inherent to the chemistry of these syntheses. However, the

advent of the more elaborate synthesis of multi-element NCs has paved the way for much deeper exploration of various physical properties and LSPR active inorganic NCs, esp. those of dopant incorporated semiconductors, have benefitted immensely with these developments. The preceding section comprised of a general discussion of the principles of colloidal synthesis as it served to provide the tools necessary for discussing the more involved chemistries required for the synthesis of LSPR active inorganic NCs. In continuation, this section is devoted to more in-depth assessment of the synthetic considerations for the different core compositions of LSPR active NCs with particular emphasis on introducing dopant atoms in these NC lattices. A general introduction to the various doping strategies will be given to the reader followed by specific examples for the different protocols.

A wide selection of doping strategies is available for compound semiconductors like metal oxides and metal chalcogenides, in order to introduce free charge carriers in their NCs for inducing the LSPR optical response. The organometallic chemistry toolbox available for colloidal NC formation already allows the synthesis of a multitude of these nanomaterials. One of the most potent synthetic methods for producing colloidal metal oxide NCs is through the previously mentioned lysis of metal coordinated monomers undergoing accumulation, and condensation thereafter into NC lattices. Whereas, metal chalcogenide NC synthesis greatly benefits from the strategy of bringing the reactive complexes of metal and chalcogen components together at high temperature. Additional doping strategies provide an extra dimension in the synthetic developments of LSPR active semiconductor NCs, on top of the previously established synthetic strategies. A rich variety of LSPR active semiconductor NCs have been reported in the literature, encompassing the doping methods introduced in this section and further discussed in-depth in respective sections.

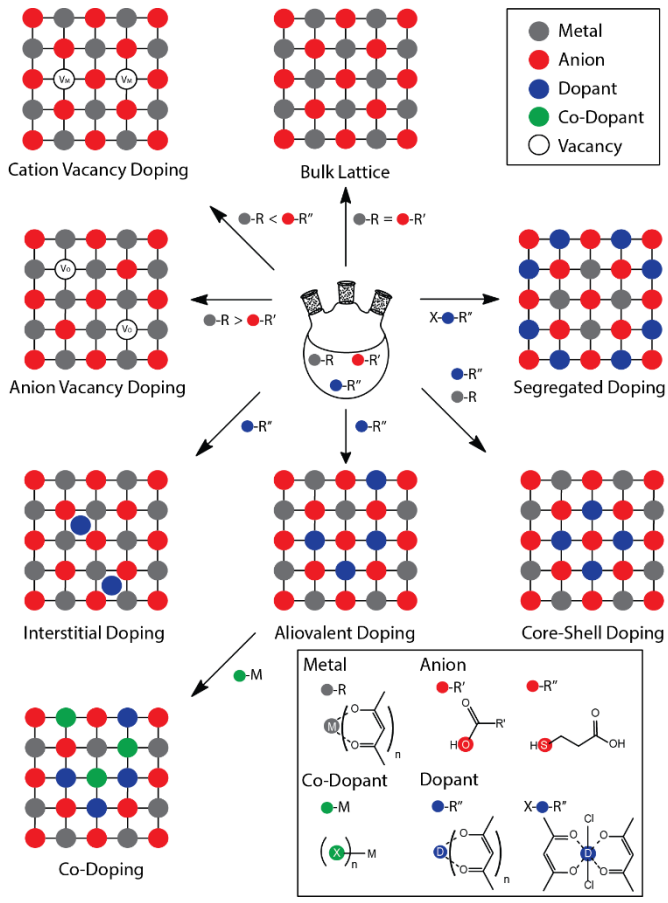

Figure 1.5: Doping strategies in synthesis of LSPR active metal oxide NCs

The various modes of doping a NC lattice include cation vacancy doping, anion vacancy doping, interstitial doping, extrinsic aliovalent doping, co-doping, core-shell doping, and segregated doping.

Certain metal oxides (ReO_3, VO_2, discussed below) and chalcogenides (CuS) are intrinsically metallic and hence exhibit LSPR response without requiring extrinsic dopant atoms or intrinsic vacancy doping in order to introduce free charge carriers. For those not having an appreciable concentration of free charge carriers, pristine lattices can be perturbed to induce electron or hole compensating defects through intrinsic or extrinsic

doping. LSPR active metal oxide NCs have been almost exclusively doped n-type while those of copper chalcogenides have been mostly p-doped. The various doping strategies can be classified through the schematic flowchart shown in Figure 1.5. In an overall sense, doping strategies can be hierarchically grouped into the following: intrinsic doping, interstitial doping, and substitutional doping.[57]

Intrinsic doping or self-doping can be realized without the need for dopants of a composition different from the atoms found in the stoichiometric material. When either a cation or anion is deficient with respect to the stoichiometric compound, the charge can be completely or partially compensated by free carriers, so the vacancies effectively dope the material. Anion vacancy doping is realized in substoichiometric oxygen vacancy-containing metal oxide NCs (e.g., WO_{3-x}[58], MO_{3-x}[22]). Oxygen vacancies are doubly charged, allowing up to two free electrons to be donated to the conduction band, leading to LSPR in some anion vacancy doped NCs. In a similar manner, the p-doping in copper chalcogenides especially the substoichiometric $Cu_{2-x}E$ (E = S, Se, Te) NCs is also a result of extensive self-doping through the creation of copper vacancies which leads to the generation of high density of holes in the valence band that can sustain an LSPR response in the near-infrared (NIR) region.[46,59,60]

On the other hand, interstitial doping is possible in metal oxides with interstitial crystal lattice sites large enough to accommodate an extrinsic dopant without inducing a structural phase change. As exemplified by tungsten bronze materials such as Cs_xWO_3, alkali cations are commonly doped in interstitial lattice sites.[61] Similar attempts of "doping" in copper chalcogenides generally leads to the formation of multinary chalcogenide phases accompanied with a change in the electronic band structure and a tunable LSPR response is not always the outcome,[62,63] unlike metal oxides. Part of the reason lies in the relatively smaller interstitial sites due to the similarity in the copper and

chalcogen atomic sizes which means inclusion of a foreign ion leads to complete overhaul of the atomic arrangements.

A wider spectrum of synthetic developments in LSPR active semiconductor NCs, especially for metal oxides, has been realized with the third type of doping: substitutional doping, by fully employing a wide selection of extrinsic dopant atoms, precursor reactivity balance, and growth kinetics. Aliovalent metal ions can substitutionally occupy host cation sites to induce n- doping. In n-doped metal oxide NCs, the higher oxidation state of cationic dopants relative to the host metal cation can be compensated by a free electron when the dopant creates a shallow donor level so that the electron is readily thermalized to the conduction band, leading to LSPR properties in the degenerate limit. LSPR spectral tuning can synthetically be achieved by varying the amount of dopant precursor to change the incorporated doping concentration in NCs.

Within the scope of extrinsic substitutional doping, advanced doping methods allow expansion of LSPR properties in metal oxide NCs while using already available chemical precursors. Co-doping with a secondary dopant atom species precursor allows further LSPR tuning to higher energies in metal oxide NCs (e.g., FICO[64], and FITO[65], in which anion doping by F^- accompanies aliovalent cation doping) and opens the possibility of multifunctional LSPR active magnetic NCs[66]. Control over the spatial distribution of substitutional dopants in NCs can be achieved by utilizing the dopant precursor reactivity difference between the host precursors. A segregated dopant distribution where dopants are distributed near the NC surface minimizes LSPR damping in ITO.[67] Using a slow-injection method and introducing dopant precursors at a specified stage during the growth of the NCs, core-shell doped ITO NCs with controllable radial distribution can be synthesized.[14] In the following sections, each doping strategy will be discussed in-depth with synthetic procedures and characterization techniques that have

been employed to respectively expand and understand plasmonic semiconductor NC development. In connection to the discussion encompassing the above text, p-type doping in metal oxide NCs is relatively rare although some recent works have been reported in this regard.[68]

Intrinsically metallic NCs

Few binary semiconductor NCs reported in the literature have metallic properties, yet these examples are interesting as they allow NCs to exhibit LSPR properties without requiring addition of extrinsic dopants. This allows LSPR active NCs to be synthesized based simply on binary compounds, bypassing the considerations of tertiary dopant reactivity balance in the growth reaction. For instance, rhenium oxide (ReO_3) has remarkable metallic properties for a metal oxide, with high electronic conductivity comparable to copper.[69,70] ReO_3 NCs exhibit LSPR in the visible range similar to that of metallic copper or gold nanoparticles due to free electrons within the conduction band.[69] ReO_3 has one more d electron per Re atom (and so, per formula unit) compared to tungsten (W) atoms in stoichiometric WO_3, which is a semiconductor with an empty conduction band. The extra electron in Re is donated into the conduction band, leading to a partially-filled conduction band and metallic properties.[1,71] Biswas et al performed ReO_3 NC synthesis, realizing LSPR between 490 nm to 540 nm wavelength using a solvothermal autoclave synthesis by decomposition of pre-synthesized Re_2O_7-dioxane complex in toluene at 200 °C.[69] Further, core@shell heterostructures with Ag, SiO_2, and TiO_2 were achieved by Ghosh et al. [72] ReO_3@Ag was prepared by shell growth upon reduction of Ag^+ ions, ReO_3@SiO_2 through the Stöber method, and ReO_3@TiO_2 by hydrolyzing titanium precursors. An atmospheric pressure colloidal synthesis has yet to be developed that produces ReO_3 NCs with a higher degree of monodispersity or

morphology control, which could reinvigorate investigations into LSPR properties of this material. Another intrinsically LSPR active NC material is lanthanum hexaborate (LaB_6), which has a fairly high energy LSPR with absorbance around a peak wavelength of 1000 nm, in the NIR region. LSPR-inducing free carriers in LaB_6 NCs are attributed to the finite density of state at the Fermi level with free carrier density corresponding to one free electron per formula unit,[73,74] similar to ReO_3. Mattox et al synthesized colloidal LaB_6 NCs at modest temperature (360 °C) compared to previously reported methods for synthesizing this refractory material by stirring sodium borohydride ($NaBH_4$) and lanthanum chloride ($LaCl_3$) in a three-neck flask.[73] Prior reports on LaB_6 NC synthesis involved autoclave routes at 400 °C and solid-state reactions under vacuum at 1200 °C.[75,76]

Some insulating metal oxides can undergo phase transitions into intrinsically metallic phases, providing inspiration for the idea of phase modulated LSPR active nanomaterials. Metal-insulator transitions occur in vanadium dioxide (VO_2) via a thermally induced phase transition without requiring aliovalent dopants or vacancies to introduce free charge carriers, thus opening opportunities for temperature dependent LSPR control.[77,78] Increasing temperature triggers a structural phase transition from an insulating monoclinic phase to metallic rutile. However, direct colloidal synthesis of VO_2 NCs has proved challenging. Instead, a colloidal synthesis of metastable bixbyite phase V_2O_3 NCs was established by Bergerud et al using a heat-up approach. Vanadyl acetylacetonate ($VO(acac)_2$) was used as the precursor in squalene, oleic acid, and oleylamine solution with growth temperatures between 310 and 370 °C. The presence of oleylamine to drive aminolysis was likely also responsible for vanadium reduction from 4+ oxidation state as in VO_2 to the 3+ state, resulting in V_2O_3 NCs.[79] Although direct colloidal synthesis of VO_2 has not been reported to this date, a film of metastable V_2O_3

NCs was shown to undergo conversion to VO_2 under controlled oxidative annealing at 375 °C.[80,81] Temperature-dependent NIR transmission modulation by annealed VO_2 phase films was observed to reveal the characteristic metal-insulator transition temperature near 70°C. The high temperature rutile phase of VO_2 is expected to have metallic properties arising from a half-filled 3d-derived outer shell, while in the low temperature monoclinic phase, dimerization of V results in band splitting that opens a bandgap and transforms the material into an insulator.[82,83] EXAFS analysis of post-synthetically annealed VO_2 revealed and verified the temperature dependent vanadium local bonding environment. Ordered octahedral symmetry characteristic of the metallic rutile phase was observed at high temperature (100 °C) while local distortion was observed in the lower temperature phase (room temperature) indicative of insulating monoclinic phase due to strained V dimerization.[79]

Covellite (CuS), a stoichiometric member of the rich and diverse phase space of the Cu-S system,[84] is yet another example of a compound semiconductor that exhibits an inherent metallic p-type character arising from a significant density of free holes in its valence band.[85–89] The bonding and oxidation states in covellite have been a matter of intense debate, but the general consensus is that it has a layered structure with alternating layers of planar CuS_3 triangles and CuS_4 tetrahedra accompanied by dimerized S-S moieties holding these layers together.[87,90,91] Consequently, the electronic structure of covellite has been modelled differently by different authors although the p-type conductivity is generally explained by the presence of delocalized holes in the valence band which is mainly constituted by the S-3p orbitals.[86,88,90,92] This material is then capable of sustaining an LSPR response in its nanostructured form, in line with its p-doped nature. The literature is rife with various reports of general synthetic strategies for producing covellite nanostructures,[93–96] but the optical characteristics were relatively

unexplored until the seminal paper by Burda et al. in 2009,[59] which prompted the more in-depth synthetic and optical studies by Xie et al. in 2013.[97] The synthetic strategy adopted by Xie et al. was the classical hot-injection method where the S-source was injected into a Cu-precursor solution at 180 ˚C. A subsequent heat-up approach was also demonstrated by Xie et al. in another report that was published around the same time where the authors demonstrated tunability of the Cu content in the NCs accompanied with a change in the optical response.[35] The Cu content of the NCs was varied by their reaction with a Cu(I) complex ($[Cu(CH_3CN)_4]PF_6$) and the optical response was tuned from a strong LSPR of the covellite NCs to the no LSPR of Cu_2S. They demonstrated that the valency of Cu remains close to 1+, but the average 1- valency of S of covellite gradually goes to 2-, i.e., sulphur gets progressively reduced which was due to the cleavage of the S-S dimers.

Cation vacancy doped NCs

Cation vacancy doping is the primary mode of self-doping in copper (I) chalcogenide NCs that routinely creates an appreciable density of free holes in the valence band of these nanomaterials, letting them exhibit an LSPR response.[33,34,39,46,59,60] The optical properties of non-stoichiometric $Cu_{2-x}E$ (E = S, Se, Te) NCs can be tuned with considerable level of control by gradually changing the copper content in these NCs. The Cu-vacancies that are formed in these NCs are compensated by the creation of holes in the valence bands and the concentration of these holes directly correlates with the copper content. Hence, increasing the Cu-deficiency increases the hole density which is characterized by the LSPR shifting to higher frequencies. This has been demonstrated by a number of researchers, starting with Burda et al. in 2009 with their synthesis of $Cu_{2-x}S$ NCs through sonoelectrochemical, hydrothermal and solventless thermolysis routes.[59]

The Cu:S molar ratio was varied in these NCs from covellite (CuS) to djurleite ($Cu_{1.97}S$) by adopting strategies particular to a synthetic method: reduction potential adjustment in the sonoelectrochemical method, pH adjustment for hydrothermal method, and different precursor pretreatments in the solventless thermolysis technique. Later in 2011, Luther et al. used a hot-injection technique to synthesize Cu_2S NCs of diameters in the range 2.5-6 nm and generated Cu-vacancies in these NCs through exposure to air, leading to the emergence of the LSPR peak which intensified and blue-shifted, due to increase in the number of free holes, to an eventual energy of 0.7 eV.[46] Increase in the hole concentration and consequent LSPR frequency tuning upon air exposure was also demonstrated on $Cu_{2-x}S$ and $Cu_{2-x}Se$ NCs by Kriegel et al.[34] These reports point towards the primary difficulty of working with copper chalcogenide NCs which are inherently unstable in ambient conditions due to the propensity of Cu ions to leach out of the NC lattice upon the slightest exposure to air. Recent work on stabilizing the LSPR response through forming a shell on the LSPR active NC core like that by Xie et al. demonstrated a chemical strategy to pin the LSPR position through the formation of an alloyed $CuPd_xS$ shell.[98]

Several other authors have shown this LSPR tunability in copper chalcogenide NCs through post-synthetic treatments in mostly air-free conditions in order to exercise a reasonable level of control on the carrier concentration.[34,60,99–101] Common oxidants like iodine,[99] and ceric ammonium nitrate were shown to generate free holes in the copper chalcogenide NC lattices whereby Cu+ ions were leached out of the lattice by way of oxidation.[60] A host of reducing agents were used to demonstrate the restoration of the Cu:Se stoichiometry which include thiols, sodium biphenyl,[99] diisobutylaluminium hydride,[34] lithium triethyl borohydride,[102] methyl viologen radicals,[100] cobaltocene,[101] etc. For instance, Dorfs et al. demonstrated a reversible tunability of the LSPR response of

$Cu_{2-x}Se$ NCs by creating holes in the NC lattice by Ce^{4+}-based oxidation, which decreased the Cu: Se molar ratio from the ideal 2: 1 to the lower limit of 1.6: 1[60], and restored the stoichiometry by reduction with Cu^{+} back to the as-synthesized stoichiometry.[41] Similar reversible tunability through redox pathways has been also demonstrated by other authors.[34,99]

Anion vacancy doped NCs

Anionic vacancy doped colloidal metal oxide NCs can be realized by stoichiometric deficiency of oxygen relative to metal atoms. Intrinsic doping in metal oxide NCs is achieved when certain metal oxides (WO_3, MO_3) exhibit strong LSPR response through lattice vacancies.[103,104] This self-doping mechanism does not require extrinsic dopants since oxygen vacancies provide charge balance to free electrons in the conduction band. Oxygen deficient synthetic conditions can favor the formation of oxygen vacancy point defects in NC lattices, especially when the metals are soft with large atomic radii and diverse oxidation states. Under low partial oxygen pressure synthetic conditions, where precursors are degassed prior to nucleation, metal oxide lattice vacancy equilibrium will be strongly biased towards forming oxygen vacancies and vacancy concentrations can be further adjusted through post-synthetic partial oxygen pressure exposure.[57,105] Oxygen vacancy can compensate two electrons per defect site according to the Kröger–Vink notation $O_O^{\times} \rightarrow V_O^{\bullet\bullet} + 2e' + \frac{1}{2}O_2$. The oxygen vacancy creates a shallow donor level that easily thermally ionizes to donate two electrons to the conduction band, leaving a dianion point defect $V_O^{\bullet\bullet}$ with a net two electron positive charge. Thus, the donated free electrons enable LSPR response to occur in stoichiometrically oxygen deficient WO_{3-x}[58] and MoO_{3-x}[22] NCs.

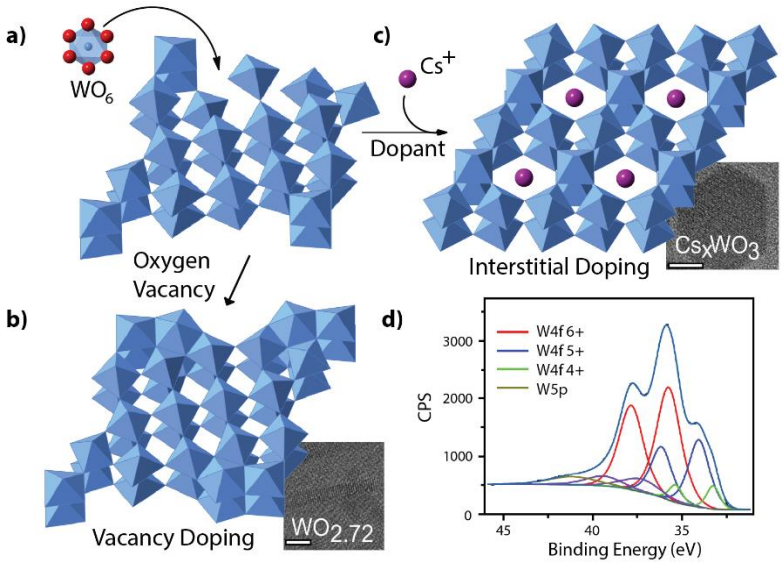

Figure 1.6: Vacancy doping and interstitial doping

a) WO_6 octahedron unit forming hexagonal tunnel perovskite structure. b) Crystal structures of the polyhedral model of oxygen substoichiometric $WO_{2.72}$ and high-resolution TEM image. (inset bar 5 nm) c) Interstitially doped Cs_xWO_3 and high-resolution TEM image. (inset bar 5 nm) Reprinted with permission from Reference [61]. Copyright © 2014, American Chemical Society. d) XPS spectrum exhibiting tungsten 6+, 5+, and 4+ oxidation state in $WO_{2.72}$. Reprinted with permission from Reference [106]. Copyright © 2017, American Chemical Society.

WO_3 can be described as a modified perovskite type ABO_3 lattice with tungsten occupied B site and unoccupied A site.[103] In an oxygen substoichiometric WO_{3-x}, WO_6 octahedron units form a distorted hexagonal tunnel due to oxygen vacant WO_{3-x} reduced forms (Figure 1.6 a). X-ray diffraction (XRD) pattern of undoped distorted substoichiometric WO_{3-x} phase NCs reveal consistency with monoclinic $WO_{2.72}$ bulk reference pattern.[61] X-ray photoelectron spectroscopy (XPS) in $WO_{2.72}$ tungsten metals exhibit 6+ and also reduced 5+, 4+ oxidation states induced by oxygen vacancies (Figure

1.6 d). [106,107] Various tungsten precursors have been employed in colloidal WO_{3-x} NC synthesis. Lee et al used tungsten hexacarbonyl ($W(CO)_6$) with oleylamine and trimethylamine N-oxide slurry to synthesize tungsten oxide nanorods.[108] Manthiram et al demonstrated colloidal $WO_{2.83}$ NC nanorod synthesis with strong LSPR at 900 nm wavelength by hot injection of tungsten (V) ethoxide in oleic acid and trioctylamine. [58] Mattox et al further demonstrated heat-up colloidal synthesis of $WO_{2.72}$ NC nanorods by decomposition of WCl_4 in oleylamine and oleic acid solution (Figure 1.6 b).[61] Using tungsten hexacarbonyl ($W(CO)_6$) as a precursor, further synthetic aspect ratio tuning from 30.2 nm long to 84.4 nm long $WO_{2.72}$ NC nanorods was demonstrated by increasing the ratio of trimethylamine N-oxide to the tungsten precursor in oleylamine.[106,108]

MoO_{3-x} is another oxygen vacant colloidal LSPR active NC material reported in the literature within the class of anion vacancy doped NCs. MoO_{3-x} are interesting 2D plasmonic materials due to their nanosheet morphology and XPS studies have been conducted to provide insight into metal oxidation state and valence changes induced by oxygen vacancies. Colloidal MoO_{3-x} NCs take a thermodynamically preferred nanosheet morphology based on the orthorhombic α-MoO_3 crystal structure consisting of MoO_6 octahedra sharing four corners to form a plane and two octahedral edges conjoining two planes into a single layered structure.[109] Colloidal oxygen vacancy doped MoO_{3-x} nanosheets were synthesized hydrothermally by Hwang et al with ammonium molybdate as the precursor dissolved in an emulsion of deionized water and hydrochloric acid with oleylamine and cyclohexane in an autoclave at 180 °C.[22] The resulting product was oleylamine surface passivated nanosheets with LSPR absorption peaking at 750 nm wavelength. XPS analysis verified the existence of oxygen vacancy-induced multivalent metals, where Mo(V) valence d^1 and Mo(VI) valence d^0 signals were observed at the XPS $3d_{3/2}$ and $3d_{5/2}$ doublet peak.[110] Post-synthetically after 24 h oxidization under air, the blue

MoO_{3-x} nanosheet solution oxidized to non-plasmonic white nanotubes. XPS analysis demonstrated oxygen vacancy induced Mo(V) valence 3d peak disappeared and exclusively Mo(VI) valent 3d peak was observed after oxygen exposure.[10] Post-synthetic LSPR peak tuning in MoO_{3-x} was further demonstrated by Li et al by manipulating the NCs with reducing agent.[111] Substoichiometric MoO_{3-x} nanodots were synthesized from pristine MoO_3 derived from chemical oxidation of bulk MoS_2. Exposing pristine MoO_3 to the reductant sodium borohydride ($NaBH_4$) lead to substoichiometric MoO_{3-x} and XPS analysis revealed substantial increase of the presence of the Mo(V) valent state. Aqueous MoO_3 exposed to controlled concentrations of the weaker reducing agent ascorbic acid at 60−70 °C resulted in MoO_{3-x} nanodots with tunable LSPR between 700−1000 nm wavelength. Controlled redshifting of the LSPR was attributed to the organic reducing agent lowering the free electron concentration.[111]

Interstitially doped NCs

Interstitial doping with extrinsic ions allows introduction of shallow donor states to the band structure of a metal oxide when interstitial lattice sites are sufficiently large to accommodate the dopants. Interstitial dopants can contribute electrons to the metal oxide conduction band, leading to LSPR response of free carriers at sufficient concentrations. For instance, theoretical studies of the tungsten bronze $NaWO_3$ suggest that the interstitial sodium alkali atoms donate their 3s electrons to the conduction band.[71]

LSPR has been realized in colloidal tungsten bronze (M_xWO_3) NCs by interstitially doping alkali metal cations in open channels within the WO_3 structure (Figure 1.6 c). Interstitial doping in tungsten bronze NCs was demonstrated by Mattox et al where alkali metal chlorides proved to be effective dopant precursors for driving interstitial doping in LSPR active tungsten bronze NCs. [61] Alkali metal cesium chloride or

rubidium chloride precursors were introduced in a heat-up colloidal synthesis. Cs^+ and Ru^+ dopants have large ionic radii of 1.2 Å and 1.7 Å respectively, which are compatible with the tunnel-like interstitial pathways in hexagonal WO_3. In Cs_xWO_3, the occupation of interstitial sites stabilizes the hexagonal crystal structure (which is unstable in undoped WO_3) and this structure was observed by XRD of the synthesized NCs, with the presence of Cs^+ ions verified by XPS using the Cs 3d peak. Post-synthetic redox chemistry was used to modulate the LSPR peak by near-surface oxidation or reduction of hexagonal Cs_xWO_3 platelets. Post-synthetic air exposure of 24 hours diminished the free electron population resulting in red-shifted LSPR. To reverse the oxidation, hydrazine was added incrementally to act as a reducing agent, which recovered the original LSPR peak energy of the Cs_xWO_3 NCs.[112]

Extrinsic aliovalent substitutional doped NCs

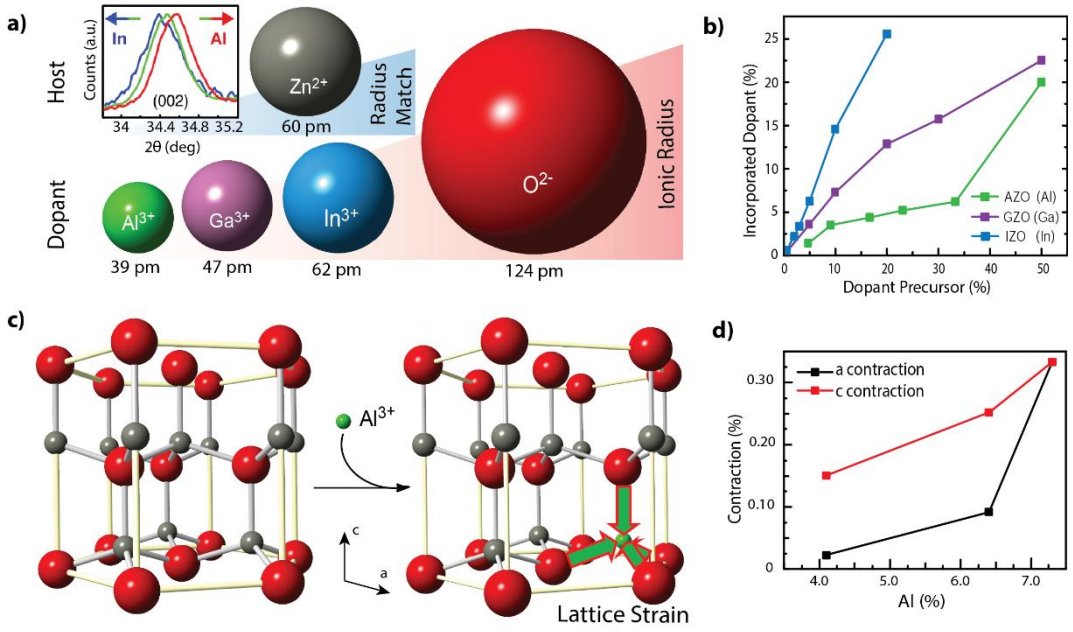

Figure 1.7: Extrinsic aliovalent substitutional doping

a) Dopant ionic radius comparison. Difference in host metal (Zn^{2+}) and dopant (In^{3+} and Al^{3+}) ionic radius leads to ZnO NC lattice expansion/contraction observed in (002) peak XRD analysis (inset).[113] b) AZO, GZO, and IZO, dopant incorporation characterized by ICP-AES, dependent on dopant radius induced lattice mismatch.[54,114,55] c) Schematic for aluminum dopant induced ZnO lattice straining. d) Aluminum doping induced a and c axis lattice contraction in ZnO NC.[54]

Extrinsic aliovalent substitutional doping requires synthetically replacing host atoms in a NC lattice structure with external atoms. During particle growth, substitutional dopants are added to either metal or oxide lattice sites, or both, simultaneously with metal oxide precursor decomposition and deposition leading to the growth of as-synthesized

doped NCs. Oxidation valence charge imbalance between host cation or anion and a dopant ion leads to electron or hole compensation per dopant atom.[115] (However, the energetic instability of holes in the deep valence band of most metal oxides has meant that metal oxides are almost exclusively electron doped, i.e. n-type.) A wide range of metal cation precursors can be selected to dope metal oxide NCs. Metal ion dopants with varying valence states are coordinated by various organic or inorganic moieties (e.g., acetate, acetylacetonate, chloride, or 2-ethylhexanoate) to form soluble precursors and to control dopant precursor reactivity during NC growth.

Building on previously established syntheses for metal oxide NCs that can serve as host materials, a wide selection of dopants enables the widest diversity and tunability of LSPR properties by design. In wurtzite phase ZnO NCs, substitutionally doped compositions with aliovalent dopants so far reported are aluminum- (Al:ZnO)[54], gallium- (Ga:ZnO)[116], indium- (In:ZnO)[55,114], and germanium-doped zinc oxide (Ge;ZnO)[117]. In rocksalt phase CdO NCs, indium- (In:CdO)[118], gallium- (Ga:CdO), aluminum- (Al:CdO), and tin-doped cadmium oxide (Sn:CdO) have been reported[119]. Tin- (Sn:In_2O_3)[120,121], cerium- (Ce:In_2O_3)[122], and titanium-doped indium oxide (Ti:In_2O_3)[123] have been reported based on bixbyite phase In_2O_3 NCs. Titanium oxide NCs have been substitutionally doped with aliovalent niobium (Nb:TiO_2)[124]. Anionic dopant in metal oxides such as fluorine has been demonstrated in indium- fluorine- codoped cadmium oxide (F,In:CdO).[64] The subsequent discussion will focus substantially on single elemental aliovalent substitutional doped ZnO NCs since crystallographic structural studies have been thoroughly conducted compared to most other examples.

Extrinsic aliovalent substitutional doped NCs retain their original crystallographic phase at modest doping concentration. Characteristic XRD peaks are retained in ZnO NCs without appearance of additional phases regardless of dopant choice.[114] Yet, the

incorporation of dopants induces strain in the NC lattice where contraction or expansion can be observed by XRD peak shifts. In wurtzite phase ZnO NCs, substitutional tetrahedral coordination of Al^{3+} ion in Zn^{2+} lattice[125] sites causes lattice contraction due to the smaller ionic radius of the dopant (Figure 1.7 c).[126] XRD of doped ZnO NCs reveals that (002) lattice expansion occurs when doping with larger radius In^{3+} (62 pm) while contraction occurs when doping with smaller radius Al^{3+} (39 pm) due to lattice strain (Figure 1.7 d).[113] Careful XRD peak refinement through Rietveld analysis revealed Al-doped ZnO NCs undergo progressive lattice contraction in both the a and c crystallographic directions at increasing Al^{3+} dopant ion (39 pm) concentration (Figure 1.7 d).[54] The consistency of the observed changes in lattice parameter with the relative size of the dopant and host material ionic radii is evidence supporting that dopants are incorporated substitutionally, rather than occupying interstitial or surface sites, or being present in a phase separated portion of the sample.

Progressive increases in the doping level, achieved by the addition of more dopant precursor to the reaction, allow the LSPR peak to be blue-shifted systematically due to increasing free charge carrier concentration. Dopant precursor concentration during synthesis and aliovalent substitutional dopant incorporation in the NC lattice exhibit a linear correlation until the lattice fails to accommodate more dopants or a phase change or other major change in the synthetic product occurs (Figure 1.7 b). Inductively coupled plasma atomic emission spectroscopy (ICP-AES) can be utilized along with energy-dispersive X-ray (EDX), X-ray photoelectron spectroscopy (XPS), and Rutherford backscattering spectrometry (RBS)[116] analysis to support dopant quantification. ICP is especially versatile for characterizing low concentration metal dopants by quantifying dopant and host metal spectral signatures in acid digested NC samples. Based on such studies, it is apparent that the efficiency in incorporation of extrinsic dopant differs with

composition of the dopant and the coordinating ligands in the dopant precursor. These trends can be influenced by ionic radius differences between dopants and the host material. Gaspera et al demonstrated using metal (III) acetylacetonate dopant precursors that doping efficiency is greater when the ionic radius of the trivalent dopant metal ion (here, In^{3+}, Ga^{3+}, and Al^{3+} (62 pm, 47 pm, and 39 pm respectively) were considered) closely matches that of tetrahedral coordinated Zn^{2+} (60 pm) in ZnO NCs (Figure 1.7 a).[114] In^{3+} was shown to have the most favorable dopant incorporation efficiency due to the similar radius size that minimizes lattice strain and the associated free energy cost to forming a substitutional defect on a Zn^{2+} site.

The crystallographic lattice position of dopant atoms in extrinsic aliovalent substitutional doped NCs is a factor to consider for dopant element selection. At high doping levels the LSPR frequency may no longer increae and, in some cases, may eventually red-shift due to the formation of defect clusters that create deep, mid-band gap states. This has been well studied in ITO, where $O_i''2Sn_{In}^{\bullet}$ cluster formation at high dopant concentration decreases the free electron concentration.[115] Kelchtermanns et al investigated the crystallographic position of dopants in Al-doped ZnO NCs with XRD crystallographic structure analysis, ICP elemental analysis, and solid state NMR.[125] In wurtzite phase ZnO crystal, substitutional tetrahedral coordination of Al^{3+} ion in Zn^{2+} lattice site enables free electron donation to the conduction band, while other site occupancy (e.g. interstitial) is not expected to yield this result.[126] Differing coordination preference such as interstitial octahedral or tetrahedral coordination would lead to Al^{3+} ion acting as an acceptor, quenching free electron carriers. Solid state ^{27}Al-NMR was used in solvothermally synthesized Al-doped ZnO NCs to differentiate tetrahedral and octahedral Al^{3+} coordinated with oxygen revealing the majority of the dopant ions were

located in octahedral sites ineffective, or even counterproductive, for charge carrier generation.[125]

P-type doped NCs

Hole doping in metal oxides is challenging to realize owing to typically deep valence bands and the moderate formation energy for oxygen vacancies, which can easily compensate any net negative charge on the crystal lattice. One example of p-type metal oxide NCs has been reported, which is spinel type gallium iron oxide (Ga_2FeO_4), investigated by Urso et al.[68] Off-stoichiometric precursor ratio control between Ga and Fe allowed either n- or p-type doping to be realized with both an LSPR peak at ~1000 nm in the NIR spectral range. The synthesis followed a typical heat-up procedure with gallium (III) acetoacetonate ($Ga(acac)_3$) and ferrous acetoacetonate ($Fe(acac)_2$) precursors in oleic acid, oleylamine, and octadecene solution resulting in Ga_2FeO_4 NCs. The gallium and iron precursor molar ratio was varied between Ga/Fe = 0.7 and 3.3 to induce off-stoichiometric Ga_2FeO_4 in which the NC compositions (determined by ICP) correlate with the compositional ratio of the precursors during the synthesis reactions. Shi et al experimental work validating first principle calculations have shown formation energy of antisite defect in spinel oxides is lower than vacancy and intersitital defects, minimizing associated defect compensation and enabling the realization of p-type doping in spinel oxides.[127] DFT band structure calculations in Urso et al implied Fe-rich synthetic conditions led to p-type LSPR active NCs through substitution of Ga^{3+} ion by Fe^{2+} ions (Fe^{2+}_{Ga3+}) resulting in free hole generation with a shallow acceptor level near the valence band maximum. Ga-rich conditions led to n-type doping by conversely replacing Fe^{2+} with Ga^{3+} ions (Ga^{3+}_{Fe2+}), producing free electrons and a donor level close to the conduction band minimum.[68] Fe^{2+}, not Fe^{3+} must substitute Ga^{3+} cations to allow

effective generation of hole carriers and thus XPS analysis was conducted to experimentally elucidate both ion oxidation state. In off-stoichiometric Fe-rich Ga_2FeO_4 NC samples, Ga $2p_{3/2}$ peak was consistent with 3+ oxidation state while Fe 2p peaks were 2+ oxidation states down to stoichiometric ratio of Ga/Fe =1.6. This implied Fe-rich NCs have Fe^{2+} that substitute Ga^{3+} cations, allowing p-type injection of free holes. To experimentally elucidate the p-type character of carriers in NC, transient photovoltage (PV) measurement and electrochemical impedance spectroscopy (EIS) was conducted with Fe-rich Ga_2FeO_4 NC film. PV measurement observed potential drop respect to Ag/AgCl reference electrode with exposure to light. The result was attributed to photogenerated hole carriers causing a downward band bending as a consequence of Fermi energy pinning, supported with EIS measurement. The band bending behavior was opposite direction of what is expected in n-type doped semiconductors, providing further evidence for p-type doped NCs.

Dopant spatial distribution control

Doping synthetic strategy is not limited to incrementing the level of incorporated dopants in extrinsic aliovalent substitutionally doped NCs, but also involves controlling the spatial distribution of the dopants within each NC. One approach to control spatial distribution of dopants is to manipulate the kinetics of dopant incorporation and crystal growth by revisiting the balance of reactivity between precursors for the dopant and host material, e.g. using combinations of organic and halide coordinating ligands. In doped NC growth, the kinetics rather than thermodynamics govern dopant incorporation since diffusion rates are low, so the dopants remain distributed as they are when initially incorporated.[47] Lounis et al reported that the spatial distribution of substitutional dopants can strongly impact the LSPR response in metal oxide NCs. Specifically, the authors

found that frequency-dependent plasmon damping due to impurity scattering is largely suppressed by distributing substitutional dopants near the surface of ITO NCs.[67] Previously developed ITO heat-up colloidal synthetic methods were found to result in either uniform or surface segregated tin-doped NCs. Uniformly doped ITO NCs were produced using the method of Kanehara et al. that uses indium (III) acetate and tin (II) 2-ethylhexanoate precursors.[121] Surface segregated ITO were prepared by the approach of Choi et al that uses indium (III) acetylacetonate ($In(acac)_3$) and tin (IV) bis(acetylacetonate) dichloride ($Sn\text{-}(acac)_2Cl_2$) precursors.[120] In $Sn\text{-}(acac)_2Cl_2$, the halide ligands coordinated with tin are expected to be harder and to bond strongly with Sn^{4+}, diminishing the reactivity of this precursor compared to tin (II) 2-ethylhexanoate. The production of surface doped ITO may be due to the reduced reactivity of $Sn(acac)_2Cl_2$ relative to the indium precursor ($In(acac)_3$), though other parameters such as surfactant composition also differed between the two protocols and their potential to influence dopant distribution cannot be ignored. Nonetheless, in general having a dopant precursor with a slower decomposition rate may delay doping until later in the reaction, leading to a spatial gradient of dopants favoring placement near the NC surface rather than being uniformly distributed within the NCs.[67] Further systematic investigation and realization of segregated doping in other compositions of doped NCs would be required to generalize this kinetically controlled strategy for controlling radial distribution of substitutional dopants. Virtual depth profiling by variable energy XPS is an effective tool to assess spatial distribution of dopants that was used in this case to observe the distribution of Sn in ITO NCs. The escape depth of photoelectrons increases with X-ray energy, so the ratio of signal detected from dopant and host metal ions varies with X-ray energy in case the dopants are not uniformly distributed. Thus, XPS analysis provides general information on dopant distribution without confronting the challenges of TEM-EDS spatial resolution

and elemental abundance limits. An expected linear relation (dashed line) in surface tin content compared to overall tin content measured by ICP is observed while using the synthesis method by Kanehara et al, indicating uniformly distributed tin (Figure 1.8 a, left). Meanwhile, the synthesis method by Choi et al showed higher surface tin content than the overall average doping level (dashed line), indicating surface segregated doping (Figure 1.8 a, right). [67]

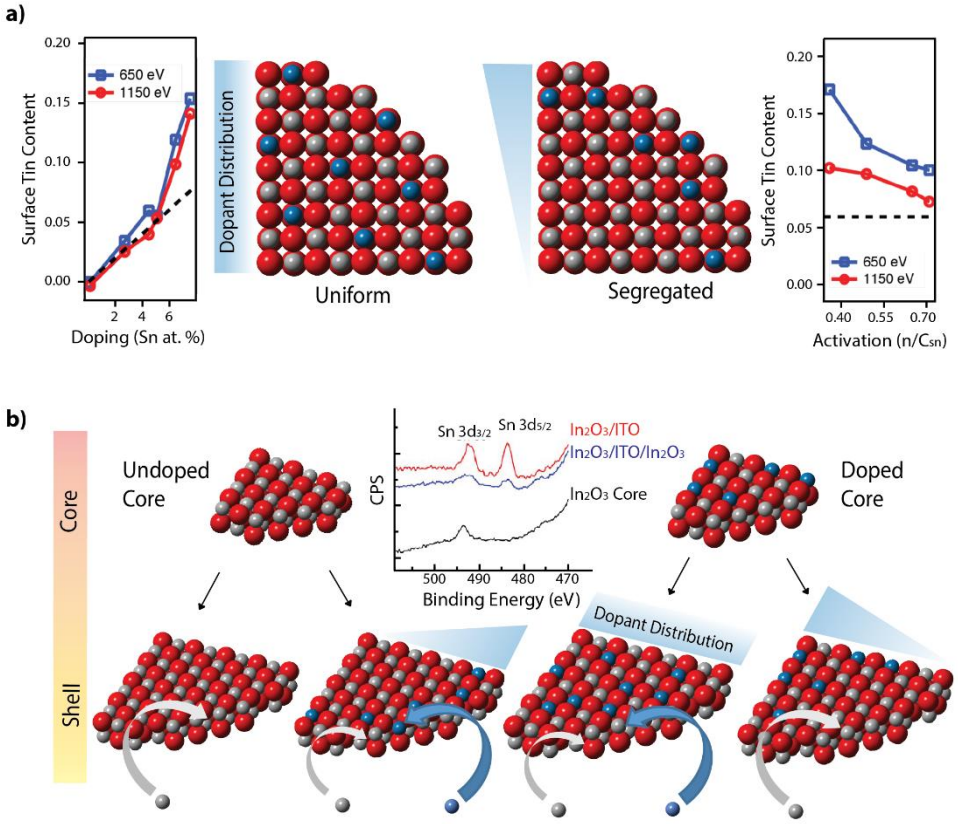

Figure 1.8: Dopant spatial distribution schematic

a) Uniformly doped ITO schematic with XPS depth profile (left); Surface segregated ITO with XPS profile (right).[67] b) Growth controlled dopant spatial distribution outcome: undoped In_2O_3 (far left); Core/shell In_2O_3/ITO (center left) doped ITO (center right); Core/shell ITO/In_2O_3 (far right); Decrease in XPS Sn 3d peak after undoped shelling in core/shell/shell In_2O_3/ITO/In_2O_3 (inset).[14]

Another strategy to control radial dopant distribution is to time the addition of dopant precursors during the NC growth process. To overcome differences in precursor reaction rates, it is helpful to slow the overall reaction, limiting growth by adding reagents continuously and dropwise to facilitate efficient incorporation of dopant atoms

without coalescence or ripening.[128] The dopant precursor can then be added at any specified stage of growth, allowing layer-by-layer growth and spatially precise control of layer composition. Ito et al. synthesized In_2O_3 NC by slow dropwise injection colloidal synthesis (Figure 1.8 b, far left) and demonstrated that doped metal oxide NCs, specifically ITO, can be synthesized by simultaneously adding host and dopant precursors dropwise into the solution. The indium (III) acetate and tin (IV) acetate precursors mixed in oleic acid contribute to NC growth without unwanted secondary nucleation when injected dropwise into oleyl alcohol at 230 °C (Figure 1.8 b, center right).[16] Jansons et al. further extended this method to achieve control over radial core-shell dopant profiles by timely injection of extrinsic dopant precursor solution during and continuous layer-by-layer growth during slow injection colloidal synthesis, allowing precise control over dopant distribution.[14] Continuous injection of a precursor solution containing tin (IV) acetate, indium (III) acetate, and oleic acid into oleyl alcohol heated to 290 °C, led to doped ITO NC core nucleation and growth. ITO/In_2O_3 core/shell NCs were synthesized by subsequently injecting a separate undoped indium oleate solution to epitaxially grow In_2O_3 shells around the ITO cores (Figure 1.8 b, far right). Conversely, Crickett et al demonstrated In_2O_3/ITO core/shell synthesis by reversing the order of injection of the Sn-doped and undoped solutions (Figure 1.8 b, center left).[129] In_2O_3/ITO/In_2O_3 core/shell/shell NCs were synthesized by subsequently growing outer In_2O_3 shells through injection of additional indium oleate solution to a reaction mixture containing the In_2O_3/ITO core/shell NCs.[14] XPS characterization revealed the complex internal dopant distribution structure in core/shell NCs synthesized by the continuous slow injection method. In_2O_3/ITO core/shell aliquot XPS spectra show appearance of Sn 3d peaks characteristic of tin dopants near the NC surface after doped shell growth on undoped cores. Decrease in Sn 3d peak amplitude was observed after subsequent growth

of the undoped In_2O_3 shell due to inelastic scattering caused by the outermost shell, supporting the formation of a In_2O_3/ITO/In_2O_3 core/shell/shell structure (Figure 1.8 b, inset).

Codoping in extrinsic substitutionally doped NCs

Further enhancement of charge carrier concentration to push the LSPR towards higher energy can be realized by simultaneously incorporating anion and cation codopants. Ye et al demonstrated that using indium (III) fluoride as a dopant precursor provided a simultaneous source for anionic fluorine and cationic indium cation doping in cadmium oxide NCs (Figure 1.9 a).[64] Cationic and anionic codoping enhances carrier concentration above the limits achievable by single element doping. F- and In-codoped CdO (FICO) and F- and Sn-codoped In_2O_3 NCs have extended the energy range of achievable LSPR wavelengths in metal oxide NCs down to 1500 nm or more.[64] The ionic radius of F^- anions as a dopant (1.33 Å) is slightly smaller than O^{2-} anions in the host (1.40 Å) in the CdO NC lattice.[64,130] Fluorine atoms can act as electron donors when substituting oxygen atom in the crystal lattice since the F^- anion has one more valence electron than the host O^{2-} anions. The independence of these defects from cationic substitutions allows for simultaneous doping on anionic and metal cation sites with aliovalent substitutional dopants. Indium (III) fluoride as a codopant precursor was used in a heat-up synthesized CdO NCs with cadmium (II) acetylacetonate, oleic acid, and 1-octadecene reaction mixture. Decoupling of the concentrations of the two dopants is also possible through the combination of an anionic dopant precursor (e.g., LiF, NaF) and a cationic dopant precursor (e.g., indium (III) acetate). Instead of using indium (III) fluoride as a codopant precursor, increasing the amount of LiF or NaF as an anionic dopant precursor allowed additional blue-shifting of the LSPR peak in doped CdO.

Fluorine- and tin-codoped indium oxide (FITO) was also demonstrated through a similar strategy by incorporation of extrinsic F anion and Sn cation dopants.[65] In a heat-up colloidal synthesis approach, tin (IV) fluoride was used as a codopant precursor with indium (III) acetylacetonate in a solution of oleic acid, trioctylamine, and octylamine. Fluorine anions similarly occupy the oxygen lattice site, forming $F_O^{\bullet}$ substitutional defects and contributing free electrons to the In_2O_3 conduction band.

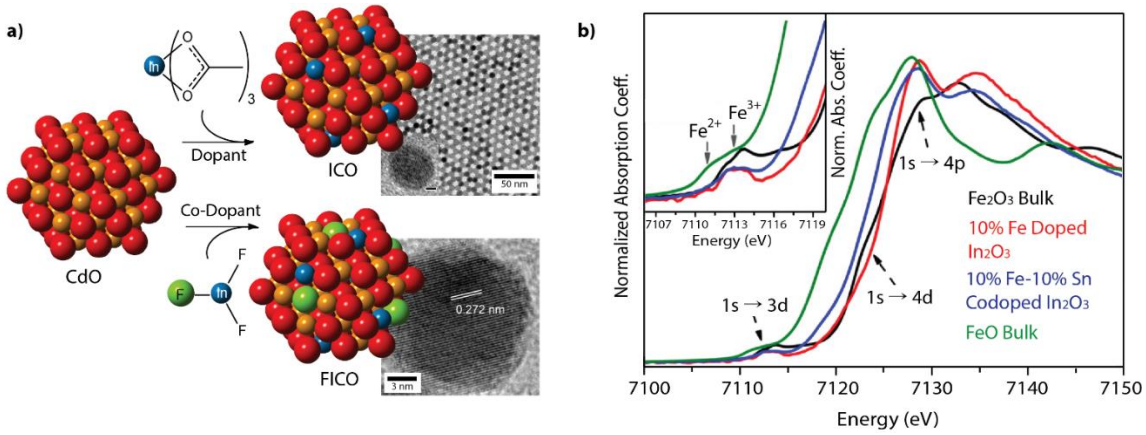

Figure 1.9: Codoping schematic

a) Indium-doped cadmium oxide (ICO) synthesis by indium (III) acetate dopant precursor schematic and TEM image (above).[118] Fluorine and indium-codoped cadmium oxide (FICO) by indium (III) fluoride dopant precursor schematic and TEM image (below). [131] b) Sn-Fe codoped In_2O_3 NC X-ray absorption near edge structure (XANES) spectrum of Fe dopant. Inset show 1s→3d signal peak for Fe^{2+} and Fe^{3+}. [66]

Simultaneous codoping with two different cationic dopants has also been demonstrated in metal oxide NCs, enabling LSPR spectral tunability and further multi-functionality. Ghosh et al reported Sn and Cd codoping in ZnO NCs by using host metal

precursor zinc stearate ($Zn(STA)_2$), and cadmium stearate ($Cd(STA)_2$) and tin myristate ($Sn(MTA)_4$) dopant precursors.[132] Increasing Cd alloying further expanded LSPR band spectral tunability from NIR towards the visible spectral range between 890 nm to 2600 nm wavelength. Tandon et al reported codoping In_2O_3 NCs with Fe and Sn leading to multifunctional magnetic and plasmonic propeties.[133] A heat-up colloidal synthesis was used with indium (III) acetylacetonate as the metal precursor in oleylamine solution, while tin (IV) bis(acetylacetonate) dichloride and iron (III) acetylacetonate was used as the codopant precursor. Substituting In^{3+} with Sn^{4+} as an aliovalent dopant provides one free electron to the conduction band, while Fe^{3+} ions function as a magnetic dopant with 5 unpaired d-electrons. Substituting In^{3+} with isovalent Fe^{3+} ideally should not affect free electron concentrations, yet a red shift and decrease in LSPR peak intensity was observed upon doping Fe into Sn-doped NCs. Shanker et al elucidated the origin of the red-shifted LSPR by identifying the dopant oxidation state in Fe- and Sn-codoped In_2O_3 NCs.[66] X-ray absorption near edge structure (XANES) and extended X-ray absorption fine structure (EXAFS) analysis of 10% Fe- 10% Sn-codoped In_2O_3 was conducted in this study. The study attributed lower LSPR energy and intensity damping to Fe^{3+} isovalent iron dopants reducing to Fe^{2+}. XANES spectral results indicated oxygen vacancies, which along with Sn can act as electron donors leading to Fe^{3+} reduction. Due to electron localization at Fe sites, the carrier concentration was diminished and the LSPR red-shifted when doping with Fe^{3+}. Sn K-edge XANES spectra showed no change in Sn^{4+} oxidation state regardless of the presence of Fe^{3+} codopants in the NCs. However, differences were observed through Fe K-edge XANES spectra supporting the reduction of Fe^{3+} into Fe^{2+}. In the Fe K-edge XANES (Figure In8b) a pre-edge peak at 7113 eV (1s→3d), a shoulder (1s→4s), and an edge crest (1s→4p) show difference from reference α-Fe_2O_3 (Fe^{3+} oxidation state) in Fe-Sn codoped In_2O_3. The Fe K XANES edge for 1s→3d (Figure 1.9 b,

inset) is broadened towards low energy with similar profile to reference FeO (Fe^{2+} oxidation state) bulk samples, suggesting small fraction of Fe^{3+} reduces to Fe^{2+}. EXAFS can be used to assess the local structure around dopants and verify their substitutional position in the crystal lattices. Here, EXAFS revealed a symmetric octahedral coordination environment around the iron center and similar distances to the second nearest neighbors surrounding each type of metal site (Fe, In, and Sn). This structural data supports both Fe^{3+} and Sn^{4+} codopants effectively substitute at the In^{3+} host lattice sites within the NC, rather than occupying surface or interstitial sites.

Chapter 2: Free Carriers in Doped Metal Oxide Nanocrystals

Charge carrier mobility in transparent conducting oxide (TCO) films is mainly limited by impurity scattering, grain boundary scattering, and a hopping transport mechanism. We enhanced the mobility in nanocrystal (NC)-based TCO films, exceeding even typical values found in sputtered thin films, by addressing each of these scattering factors. Impurity scattering is diminished by incorporating cerium as a dopant in indium oxide NCs instead of the more typical dopant, tin. Grain boundary scattering is reduced by using large NCs with a size of 21 nm, which nonetheless were sufficiently small to avoid haze due to light scattering. In-filling of precursor solution followed by annealing results in a NC-based composite film which conducts electrons through metal-like transport at room temperature, readily distinguished by the positive temperature coefficient of resistance. Cerium doped indium oxide ($Ce:In_2O_3$) NC-based composite films achieve an high mobility of 60.4 $cm^2/V{\cdot}s$, and a low resistivity of 1.25×10^{-3} $\Omega{\cdot}cm$. The films are transparent to a broad range of visible and near-infrared (NIR) light from 400 nm to at least 2500 nm wavelength. Based on the high conductivity and high transparency of the $Ce:In_2O_3$ NC-based composite films, the films are successfully applied as transparent electrodes within an electrochromic device.

INTRODUCTION

Transparent conducting oxides (TCO) play important roles in modern electronic devices, used for displays, touch panels, solar cells, and smart windows.[1-4] Main group d^{10} metal oxides (*e.g.*, In_2O_3, Ga_2O_3, ZnO, CdO, and SnO_2) are good candidates for TCO materials because of their high mobility due to overlap of the atomic orbitals comprising the conduction band.[5] Conductivity, $\sigma = ne\mu$, where n is the carrier concentration, e is the

charge of an electron, and μ is the mobility, is enhanced by doping the host metal oxides with aliovalent metal ions to generate charge carriers, such as tin-doped indium oxide ($Sn:In_2O_3$) and aluminum-doped zinc oxide (Al:ZnO). The mobility, μ, is described by Matthiessen's rule:[6]

$$\frac{1}{\mu} = \sum_i \frac{1}{\mu_i} = \frac{1}{\mu_{impurity}} + \frac{1}{\mu_{gb}} + \frac{1}{\mu_{hopping}} + \frac{1}{\mu_{phonon}} + \cdots \quad (1)$$

where $\mu_{impurity}$, μ_{gb}, $\mu_{hopping}$, and μ_{phonon} are factors that influence mobility from impurity scattering, grain boundary scattering, retardation by hopping transport, and phonon scattering, respectively. Ionized impurity scattering, the primary scattering source in dense conducting films, can be dominated by aliovalent doping.[5,7,8] As a result, increasing the dopant concentration often decreases the mobility.[3] Matthiessen's rule indicates that inverse relationship between dopant concentration and mobility fundamentally limits conductivity in TCO films.

A recent study of the optical properties of cerium-doped indium oxide ($Ce:In_2O_3$) nanocrystals (NCs) gives a clue in overcoming the intrinsic limitation of TCO films.[9] $Ce:In_2O_3$ NCs showed localized surface plasmon resonance (LSPR) with an exceptionally narrow peak due to the weak low frequency damping, indicating a low degree of impurity scattering. This is supported by density functional theory (DFT) calculations, which demonstrated that the conduction band minimum of the indium oxide host does not hybridize with relevant states of the cerium dopants. Based on this study, we expected that ionized impurity scattering from dopants can be minimized by using $Ce:In_2O_3$ NCs as a component material of TCO films.

NC-based TCO films have advantages of low processing costs compared to TCOs from conventional sputtering methods that are energy-intensive, requiring high vacuum

conditions or sol-gel films that require multiple depositions and annealing steps to achieve high performance.[2,10] Various TCO NCs, including Sn:In_2O_3, Al:ZnO, and In:CdO have been synthesized and assembled to demonstrate TCO films.[11-18] However, mobilities of these films were too low to be used as practical conductors because electrons in NC films are localized within individual NCs or groups of NCs with insulating barriers between these that originate from spatial gaps between NCs and from electronic surface traps.[19] Recently, the Sun group reported that conductivity of NC-based Sn:In_2O_3 films was improved a factor of two by decreasing the distance between NCs by means of exchanging long chain ligands with volatile short chain molecules, but their ligand exchange strategy still left gaps and smaller insulating barriers.[18] Efforts have been made to achieve electron delocalization in semiconductor NC films by adoption of all-inorganic nanocomposites fabricated by in-filling the inter-NC gaps with atomic layer deposition (ALD) or by ligand exchange with chalcogenometallate (ChaM) ligands, both of which strategies led to improved mobilities.[20-31] Unlike semiconductor quantum dots, ChaM ligands are not applicable for TCO NCs because misalignment of the Fermi level between oxide NCs and a chalcogenide matrix is expected to create a Schottky barrier, inhibiting transport.[32] Although in-filling the inter-NC gaps by ALD can improve the conductivity of NC-based films,[30,31] the process can be costly due to slow deposition rates and the required vacuum conditions. Herein, a solution is provided to overcome these challenges facing NC-based TCO films by in-filling an indium oxide precursor solution into porous array of Ce:In_2O_3 NCs, achieving high mobility.

FREE CARRIERS IN DOPED METAL OXIDE NC

Ce:In_2O_3 NCs were synthesized by modification of the slow growth technique introduced by the Hutchison group for Sn:In_2O_3.[9,33] Scanning electron microscopy (SEM) images show that addition of 2 mL and 5 mL of 0.5 M precursor solution (indium acetate and 5% cerium acetylacetonate in oleic acid) led to NCs of 7.61 nm ± 0.63 nm and 12.2 nm ± 1.2 nm, respectively (Figure 2.2). Further addition of oleyl alcohol and precursor solution allowed growth of larger Ce:In_2O_3 NCs with a size of 21.4 nm ± 2.2 nm in transmission electron microscopy (TEM) (Figure 2.2a and Figure 2.2). Scherrer analysis of the X-ray diffraction (XRD) pattern of these NCs yields a 21.4 nm ± 1.1 nm grain size (Figure 2.2e), consistent with the SEM analysis. The XRD pattern also confirms that the Ce:In_2O_3 NCs have cubic indium oxide bixbyite crystal structure (Figure 2.3). Doping level of the 21 nm-sized NCs was measured as 3.7% Ce using inductively coupled plasma – atomic emission spectroscopy (ICP-AES). The optical spectrum of the NC dispersion exhibited a narrow LSPR peak, indicating a low level of impurity scattering (Figure 2.4).[34]

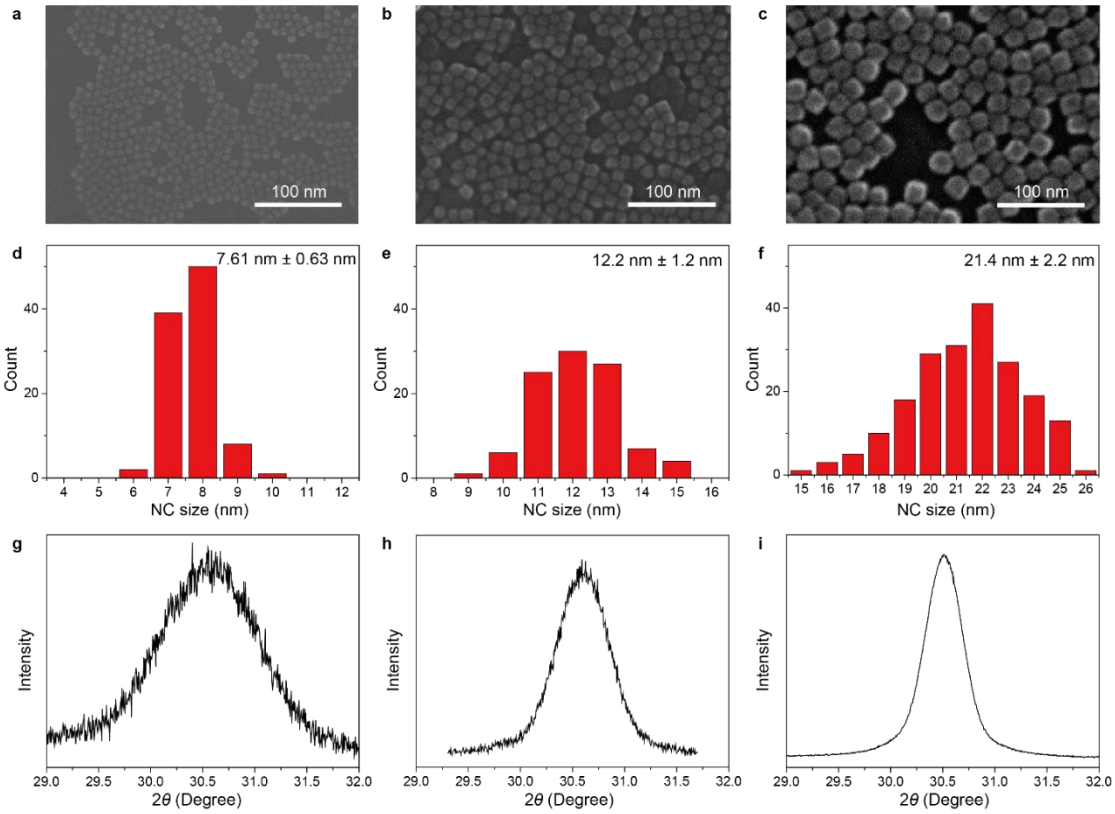

Figure 2.1: SEM image of Ce:In_2O_3 NCs

(a-c) Scanning electron microscopy (SEM) images, (d-f) histograms of size distributions counted from the SEM images, and (g-i) (222) peak of X-ray diffraction (XRD) patterns of (a,d,g) 7.61 nm ± 0.63 nm, (b,e,h) 12.2 nm ± 1.2 nm, and (c,f,i) 21.4 nm ± 2.2 nm Ce:In_2O_3 nanocrystals (NCs). Grain sizes of NCs were calculated to be (g) 7.42 nm ± 0.37 nm, (h) 12.3 nm ± 0.6 nm, and (i) 21.4 nm ± 1.1 nm by Scherrer analysis of the (222) peak of the XRD patterns.

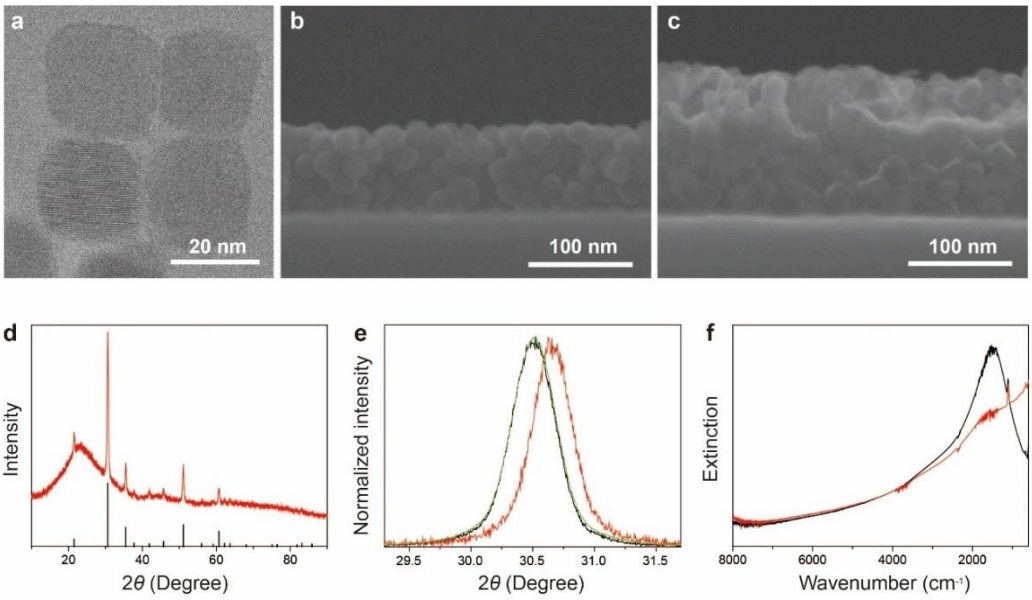

Figure 2.2: Ce:In_2O_3 NC-based thin film SEM and spectrum

Material properties of Ce:In_2O_3 NCs and Ce:In_2O_3 NC-based TCO thin films. (a) Bright field TEM image of 21 nm-sized Ce:In_2O_3 NCs (21.4 nm ± 2.2 nm) and (b) SEM cross-sectional image of a NC array of 21 nm-sized Ce:In_2O_3 NCs with a thickness of ~100 nm. (c) An SEM image of a composite film after in-filling of 1 M indium oxide combustion solution in an array of 21 nm-sized Ce:In_2O_3 NCs. (d) XRD pattern of a composite film after in-filling of 1 M combustion solution in an array of 21 nm-sized Ce:In_2O_3 NCs, where the black bars indicate the reference pattern for bixbyite In_2O_3 (JCPDF 01-071-2194). (e) Magnification of (222) peak of XRD patterns of (green) pristine 21 nm-sized Ce:In_2O_3 NCs before annealing, (black) an annealed Ce:In_2O_3 NC-only film, and (red) a composite film, (f) Fourier transformed infrared (FTIR) spectra of (black) an annealed 21 nm-sized Ce:In_2O_3 NC-only film and (red) a composite film after in-filling of 1 M combustion solution in an array of 21 nm-sized Ce:In_2O_3 NCs.

NC films with a thickness of about 100 nm were prepared by spin coating 21 nm-sized Ce:In_2O_3 NCs dispersed in octane onto glass substrates. Long chain organic surfactants on the NC surfaces were decomposed by thermal annealing at 500 ^oC for 1 h in air. Grain size of the annealed film calculated by Scherrer analysis of XRD was 21.2 nm ± 1.1 nm, comparable to that of pristine NCs (21.4 nm ± 1.1 nm), indicating that grain size change was negligible upon thermal annealing (Figure 2.2 e). An SEM image of the annealed NC film revealed that shape and size of individual NCs was retained, while pores between the NCs were generated as the surfactant molecules were removed (Figure 2.2 b and Figure 2.4). Electronic properties of a NC-only film were characterized after annealing at 500 ^oC in 1% H_2 / 99% N_2 to generate charge carriers. The annealed NC-only film showed very high resistivity of 12.6 Ω·cm, which we ascribe to poor NC-NC contact and the presence of trap states related to surface dangling bonds (Table 2.1).[35]

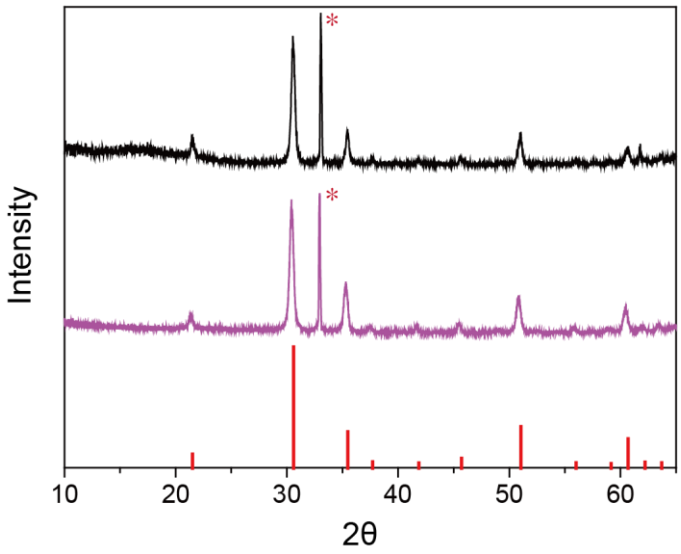

Figure 2.3: XRD patterns Ce:In_2O_3 NC

XRD patterns of (purple) the 21 nm-sized Ce:In_2O_3 NCs and (black) the NC-only film from the 21 nm-sized NCs. The red vertical lines represent peak position and relative intensity of indium oxide with bixbyite structure (PDF #: 01-071-2194). (*: Silicon substrates)

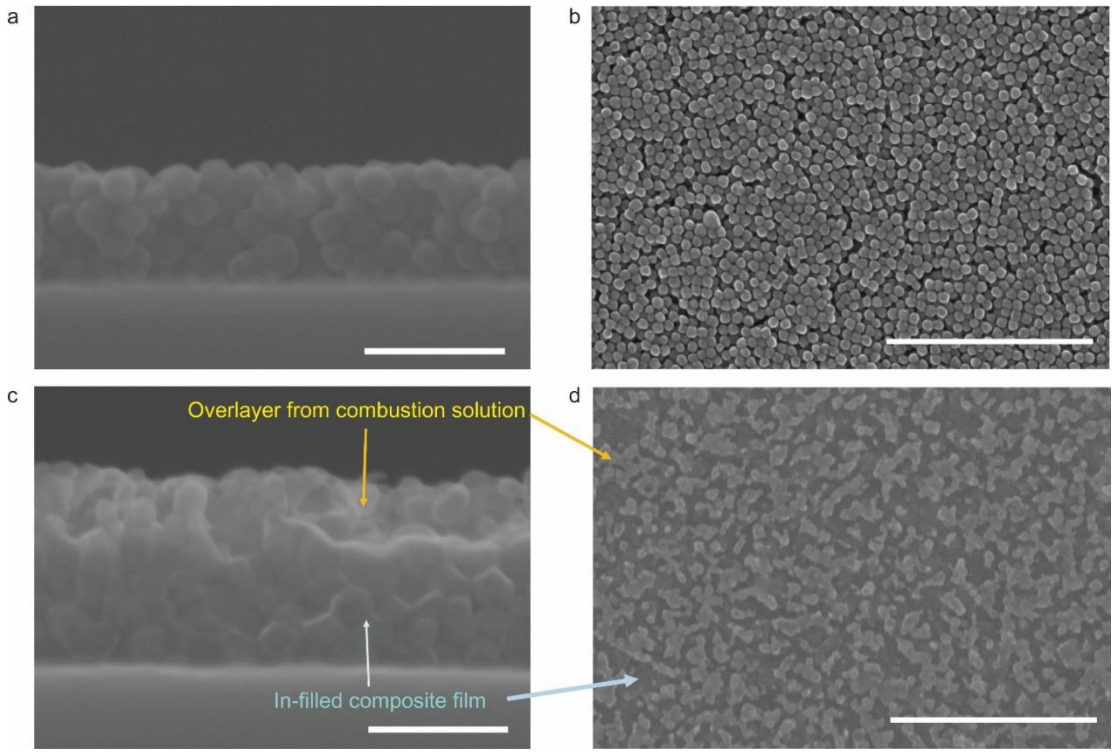

Figure 2.4: Ce:In_2O_3 NC film SEM

(a) An SEM cross-sectional image and (b) a surface topography of SEM image of a NC-only film composed of 21 nm-sized Ce:In_2O_3 NCs and (c) An SEM cross-sectional image and (d) a surface topography of SEM image of a Ce:In_2O_3 NC-based composite film after in-filling of 1 M indium oxide combustion solution in an array of 21 nm-sized NCs. The top-view and cross-sectional SEM images clearly show that the Ce:In_2O_3 NC-based composite film consists of a dense in-filled composite layer and an island-like overlayer generated from the combustion solution. Scale bars are (a,c) 100 nm and (b,d) 500 nm.

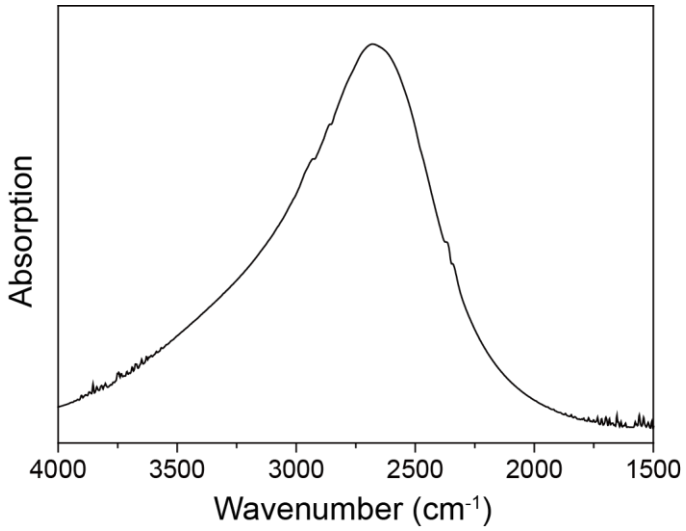

Figure 2.5: FTIR of Ce:In_2O_3 NC

Fourier transformed infrared (FT-IR) spectra of the 21 nm-sized Ce:In_2O_3 NCs.

Ce:In_2O NC-based composite TCO films were prepared by in-filling the porous and resistive NC array with an In_2O_3 precursor solution based on the 'combustion method'.[36-40] The solution includes urea, that undergoes combustion in the presence of nitrate ions. This solution is highly preferable to a conventional sol-gel solution for in-filling of small pores because of the small size of solute molecules and high capillary pressure between the combustion solution and a NC array with small pores (Text A2.1 in Supporting Information and Figure 2.6). In contrast, conventional sol-gel precursors react slowly over time at room temperature (aging) to form small particles that increase viscosity and can inhibit effective infiltration of small pores.[41] We deposited 1 M indium combustion solution on top of the NC array, waited for 5 s to in-fill the solution, and then spin-coated at 5,000 rpm. The film was annealed at 500 ^oC in air then in 1% H_2 / 99% N_2 to produce a composite film of NCs in an indium oxide matrix as seen by cross-sectional SEM (Figure 2.2 c). The SEM image shows that the in-filled composite film has

improved connectivity between grains with increased grain size. Based on the Scherrer analysis of the (222) peak of XRD patterns, grain size increased from 21.4 nm ± 1.1 nm to 24.6 nm ± 1.2 nm after infiltration and annealing (Figure 2.2 d,e). A slightly different (222) peak position of XRD pattern between the NC array and the NC-based composite films is ascribed to the lattice expansion of NCs associated with surface defect dipoles from dangling bonds.[42]

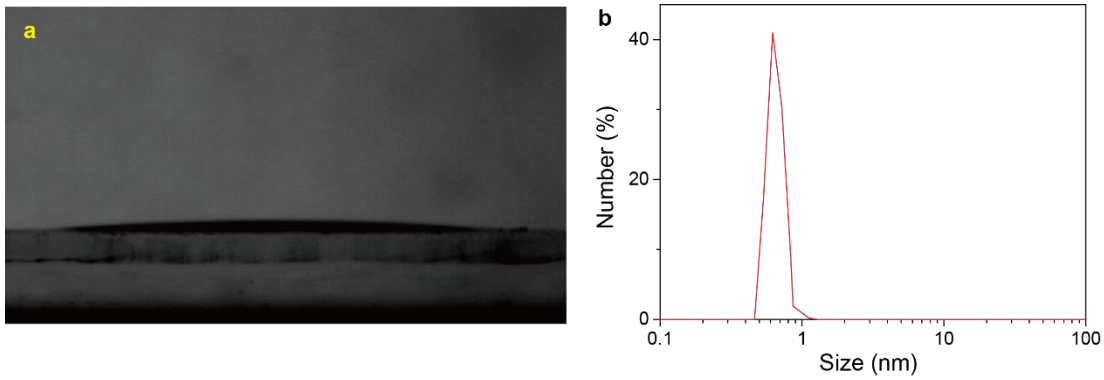

Figure 2.6: Ce:In_2O_3 NC film surface property

(a) A low contact angle (6.4^o) between indium combustion solution (indium nitrate-urea complex in 2-methoxyethanol) and flat Sn:In_2O_3 substrate took with goniometer. (b) Number-averaged dynamic light scattering (DLS) data of indium oxide combustion solution. The hydrodynamic diameter is calculated as 0.7 nm using the Stokes-Einstein relationship.

In-filling solution concentration was varied to maximize conductivity, mobility, and carrier concentration of the Ce:In_2O_3 NC-based composite films found by Hall effect measurements (Figure 2.2 a,b, Text A2.2, and Figure 2.7). As the in-fill solution concentration increased from 0 M to 1 M, the resistivity dramatically decreased to 1.25 x 10^{-3} Ω·cm before saturating at higher concentrations. These results suggest that the gaps

between NCs were effectively filled with 1 M solution so higher concentration offered no distinct improvement, despite the addition of a thicker overlayer of indium oxide (as shown below). While the mobility of the annealed Ce:In_2O_3 NC-only film was 0.197 $cm^2/V{\cdot}s$, mobilities of the Ce:In_2O_3 NC-based composite films after in-filling with 0.5, 1, and 1.5 M of combustion solution were 14.7, 60.4, and 40.9 $cm^2/V{\cdot}s$, respectively (Figure 2.2 b). The mobility of Ce:In_2O_3 composite films after in-filling with 1 M solution, 60.4 $cm^2/V{\cdot}s$, is a record-high value for NC-based TCO films and is higher than that of many commercial TCO films made by sputtering.[1-3] The carrier concentration increased ~3 times after in-filling, which may be ascribed to the removal of trapped electrons in NC surface states.[30]

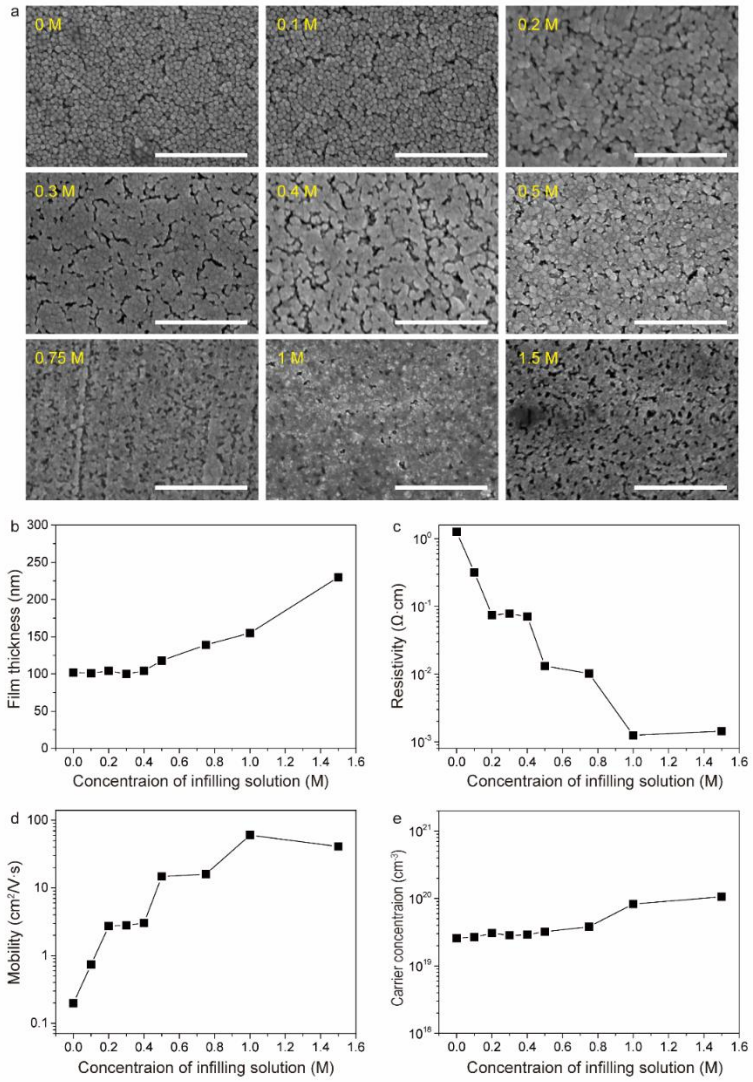

Figure 2.7: SEM images of composite films after in-filling

(a) SEM images of composite films after in-filling of 0, 0.1, 0.2, 0.3, 0.4, 0.5, 0.75, 1, and 1.5 M of indium combustion precursor solutions (indium nitrate and urea in 2-metholyethanol) in arrays of 21 nm-sized Ce:In_2O_3 NCs. Scale bars are 500 nm. (b) Thickness, (c) resistivity, (d) mobility, and (e) carrier concentration of the composite films corresponding to panel (a).

The influence of the improved connection between NCs on electronic properties can be identified in the optical spectra of the films.[43] As the distance between NCs decrease, coupling and electronic overlap can occur, leading to red-shifting of the LSPR peak.[43,44] Dense metallic thin films show a plasma edge beyond which lower energy photons are either absorbed or reflected, rather than a distinct peak.[45] Ce:In_2O_3 NC-only films showed an LSPR peak centered at 1800 cm^{-1} (Figure 2.2 f). While the high temperature annealing process induced coupling between NCs and a consequent red-shift of the LSPR peak (2600 cm^{-1}), the persistence of a peak indicated that electron localization persisted. In contrast, the in-filled nanocomposite film did not show a prominent LSPR peak, but exhibited continuous increasing of extinction towards the low-energy detection limit of the spectrometer (Figure 2.2 f).[45] The optical results imply that the collective oscillation of electrons propagates across the film, and electrons are not localized in individual NC grains.

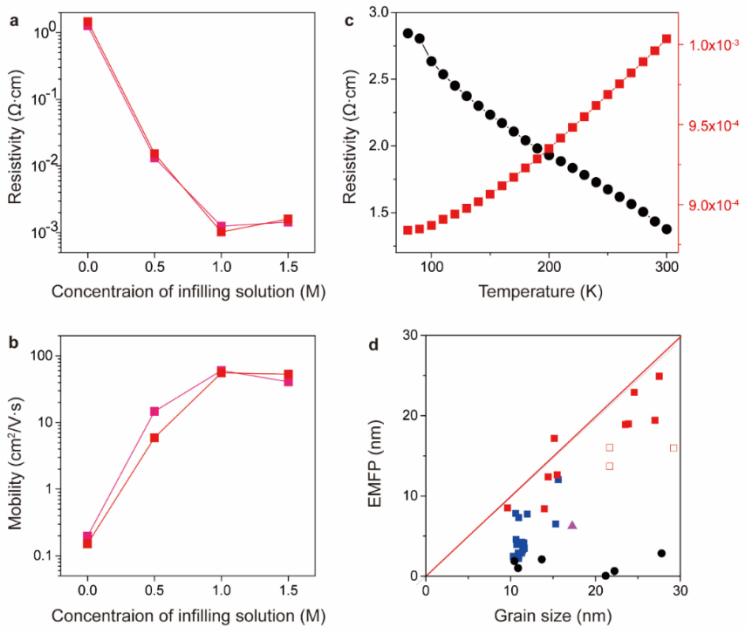

Figure 2.8: Electrical properties of NC-based TCO films

Electrical properties of Ce:In_2O_3 NC-based TCO films showing high mobility and metal-like transport. (a) Resistivity and (b) mobility of a NC-only film and composite films prepared by in-filling 0.5, 1 and 1.5 M of indium combustion solution (indium nitrate and urea in 2-metholyethanol) onto the NC arrays with a crystal size of 21 nm. Two set of data were obtained using a single batch of NCs to confirm reproducibility. (c) Temperature dependent resistivity data of (black) a Ce:In_2O_3 NC array and (red) a Ce:In_2O_3 NC-based composite film after in-filling with indium oxide. (d) Correlation between EMFP and grain size of (black) Ce:In_2O_3 NC arrays, (solid red) in-filled Ce:In_2O_3 NC-based composite films, (open red) partially in-filled Ce:In_2O_3 NC-based composite films, (blue) Sn:In_2O_3 NC-based composite films, and (violet) indium oxide thin films from combustion solution. The red line is an auxiliary line that indicates when the grain size and the EMFP are the same.

The delocalization of electrons in the composite film, apparent in the optical changes, led to metal-like transport of electrons in NC-based films. Temperature-dependent resistivity measurements were carried out to uncover the charge transport mechanisms of the thin films. The resistivity of the nanocomposite film increased linearly with temperature increase above 130 K (Figure 2.8 c). The positive linear relationship is a characteristic feature of metallic transport that originates from increased phonon scattering at elevated temperatures.[46] A temperature coefficient can be calculated by fitting with the linear equation, $\rho = \rho_0(1+\alpha\Delta T)$, where ρ is the resistivity, α is temperature coefficient of resistivity, and T is the temperature. The temperature coefficient α is calculated to be 6.7 $\times 10^{-4}$ K^{-1}, comparable to commercial Sn:In_2O_3 glass (~7.3 $\times 10^{-4}$ K^{-1}; Figure A2.7). Although we have not demonstrated that the Ce:In_2O_3 NC-based composite film has a zero bandgap, Figure 2.8 c clearly shows metal-like transport in the composite film at room temperature. In contrast to the in-filled nanocomposite films, the NC-only film showed opposite trend of resistivity with temperature (Figure 2.8 c). The negative correlation indicates localized electrons move to adjacent NCs or NC clusters by a hopping mechanism.[46] Apparently, the improved electronic connectivity in the in-filled composite films allows electrons move freely through a delocalized conduction band without inter-NC potential barriers dominating the mobility.

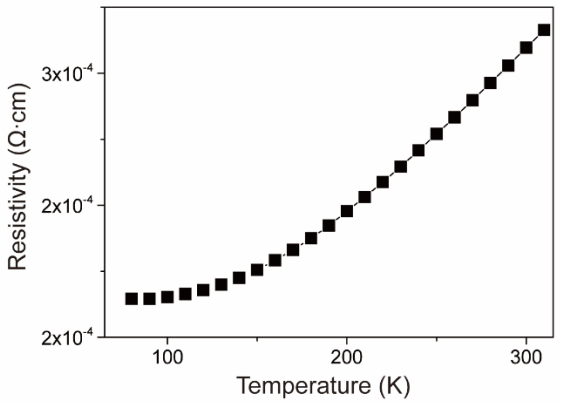

Figure 2.9: Temperature dependent resistivity

Temperature dependent resistivity data of a commercial $Sn:In_2O_3$ film. The temperature coefficient of the film is calculated to be 7.3×10^{-4} K^{-1}.

TCO films	Sheet resistance (Ω/sq)	Resistivity (10^{-3} Ω cm)	Mobility (cm^2/V s)	Carrier concentration (10^{19} cm^{-3})	Grain size (nm)	EMFP (nm)
NC-only film[a] (21.4 nm $Ce:In_2O_3$)	124000	12600	0.197	2.58	21.2 ± 1.1 nm	0.051
Composite[a] (21.4 nm $Ce:In_2O_3$)	80.6	1.25	60.4	8.28	24.6 ± 1.2 nm	22.9
Composite[a] (12.2 nm $Ce:In_2O_3$)	93.4	1.29	39.4	12.3	15.1 ± 0.8 nm	17.2
Composite[a] (9.5 nm $Sn:In_2O_3$)	220	2.42	12.6	20.5	15.3 ± 0.8 nm	6.49
Indium oxide combustion film[a,b]	1526	14.0	28.7	1.55	17.3 ± 0.9 nm	6.25

[a]All films were annealed in air at 500 °C for 1 h, and annealed in 1% H_2/99% N_2 at 500 °C for 1 h.

[b]Indium oxide combustion film was prepared by spin-coating of the 1 M combustion solution onto the Eagle XG glass substrate followed by annealing steps (annealed in air at 500 ^{o}C for 1 h, and annealed in 1% H_2/99% N_2 at 500 ^{o}C for 1 h).

Table 2.1: Electronic properties of NC-based TCO films.

Electronic properties of a NC-only film and composite films prepared by in-filling of combustion solution.

Mobility is proportional to an average time between scattering (τ), $\mu = e\tau/m^*$, and τ is related to the electron mean free path (EMFP), $L = v_{ave}\tau$, where e is the electron charge and m^* is the effective mass, and v_{ave} is average velocity.[47] The EMFP of thin films can be calculated by the following equation, $L = (3\pi^2)^{1/3}he^{-1}\mu n^{1/3}$, where h is Planck's constant.[43] It is known that EMFPs of degenerate TCO films, such as Sn:In_2O_3, are usually smaller than their grain size as a result of strong impurity scattering from dopants.[8] The calculated value of EMFP of the Ce:In_2O_3 NC-based composite film that has high mobility of 60.4 $cm^2/V{\cdot}s$ is 22.9 nm (Table 2.1). Interestingly, the EMFP value is comparable to the grain size, 24.6 nm ± 1.2 nm, obtained from Scherrer analysis. The correlation between grain size and maximal EMFP was shown reproducibly in across grain sizes of Ce:In_2O_3 NC-based composite films (Figure 2.8 d). For example, a Ce:In_2O_3 NC-based composite film with a grain size of 15.1 nm ± 0.8 nm prepared by in-filling onto a 12.2 nm ± 1.2 nm size NC array shows EMFP of 17.2 nm (Table 2.1). The correlation indicates that mobility in the NC-based Ce:In_2O_3 films was limited by grain boundary scattering instead of other scattering mechanisms in Matthiessen's rule, such as impurity scattering and hopping retardation (Equation 1). By contrast, conductivity of NC-based Sn:In_2O_3 films tends to be also limited by impurity scattering. The low

impurity scattering of the Ce:In_2O_3-based films is consistent with the experimental and theoretical results of Runnerstrom *et al*.[9] Based on their DFT calculations, the conduction band minimum of In_2O_3 is weakly hybridized with relevant orbitals of cerium dopants, thus electrons in Ce:In_2O_3 NCs can flow through the conduction band without significant scattering from dopants. In addition, ionic radius of Ce^{4+} (101 pm) is more similar to In^{3+} (94 pm) than Sn^{4+} (83 pm), reducing lattice strain upon doping.[9] Furthermore, the cerium dopants reduce the oxygen vacancy concentration, which cause strong ionized impurity scattering four times greater than cerium or tin dopants owing to the vacancies' double charge.[9] Therefore, the high mobility of the Ce:In_2O_3 NC-based film is attributed to the low impurity scattering of cerium dopants and oxygen vacancies, and minimized grain boundary scattering due to the large grain size. High mobility associated with minimal defect scattering has also been proposed in CdO thin films doped with yttrium, dysprosium, scandium, and indium, prepared by vapor phase deposition.[48-50] However, the high toxicity of cadmium hinders the practical application of CdO-based TCO films. Limited reports have been made that Ce:In_2O_3 thin films can be obtained by sputtering, but the resulting films do not have an optimum grain size to be used as transparent conductors.[51,52] We also found that it is difficult to obtain high quality Ce:In_2O_3 films directly from the combustion method. The Ce:In_2O_3 films prepared by the combustion method without the use of NCs have high resistances, exceeding 100,000 Ω·cm, so that pre-synthesized Ce:In_2O_3 NCs were necessary to achieve the favorable results reported here.

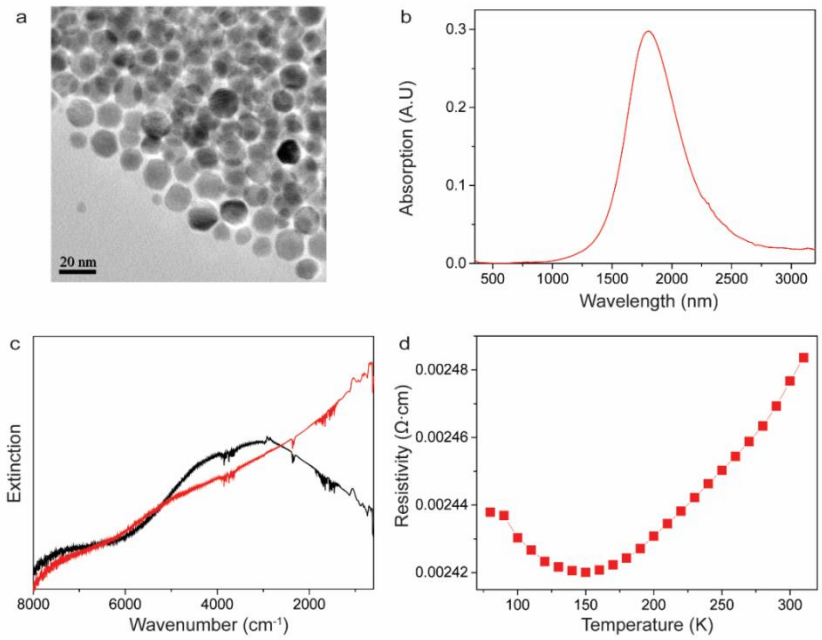

Figure 2.10: Properties of Sn:In_2O_3 NC film

Morphologies and properties of Sn:In_2O_3 NCs and Sn:In_2O_3 NC-based films. (a) a TEM image and (b) plasmon spectrum of Sn:In_2O_3 NCs. (c) optical spectra of (black) a Sn:In_2O_3 NC-only film and (red) a Sn:In_2O_3 NC-based composite film after in-filling of combustion solution in an array of NCs. (d) Temperature dependent resistivity data of the Sn:In_2O_3 NC-based composite film.

The in-filling process was also applied to more traditional TCO NCs, specifically Sn:In_2O_3 NCs (Figure A2.8).[53] Sn:In_2O_3 NC-based composite films were prepared by in-filling of the same indium oxide combustion precursors in Sn:In_2O_3 NC arrays. Continuity of the film and delocalization of electrons were again supported by the change in the optical spectrum from a distinct LSPR to a plasma edge. Sn:In_2O_3 NC-based composite films also exhibited a metal-like transport behavior at room temperature, based on the positive temperature coefficient of resistance. Despite the delocalization of

electrons, the mobility of the Sn:In_2O_3 NC-based film is only 12.6 $cm^2/V{\cdot}s$. EMFP of the Sn:In_2O_3 NC-based composite film is 6.49 nm, which is much smaller than grain size of the film, 15.3 nm ± 0.8 nm. The short EMFP indicates that impurity scattering becomes a significant factor in Sn:In_2O_3 films, in contrast to those based on Ce:In_2O_3 NCs.[8]

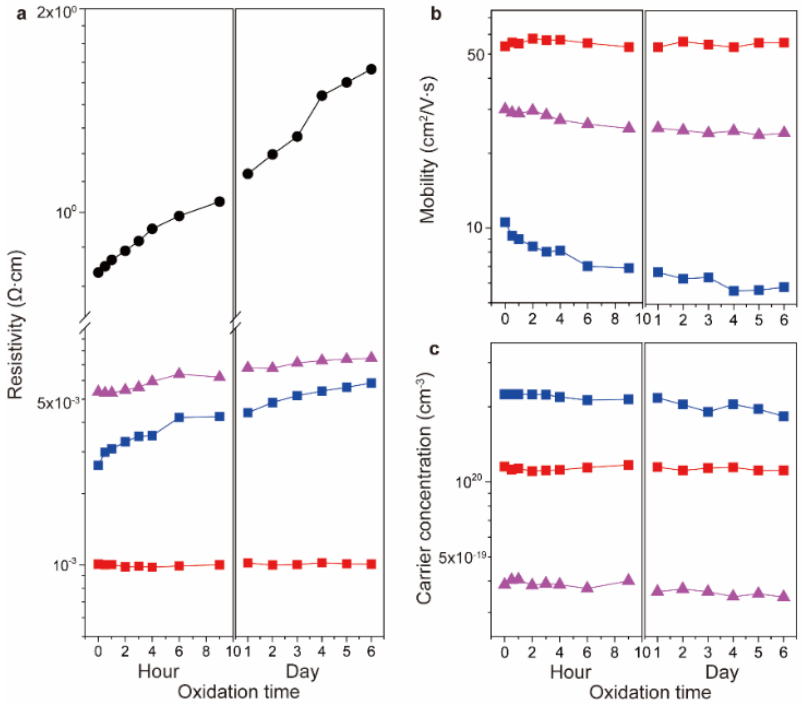

Figure 2.11: Carrier properties of NC-based TCO films

Temporal (a) resistivity, (b) mobility, and (c) carrier concentration change of (black) a Ce:In_2O_3 NC-only film, (red) a Ce:In_2O_3 NC-based in-filled composite film, (blue) an Sn:In_2O_3 NC-based composite film, and (violet) an indium oxide thin film from combustion solution upon air exposure.

Air stability is one inhibiting issue facing TCOs because heavily doped metal oxide materials can be prone to oxidation.[7] Oxidation is known to deteriorate TCO films

due to i) filling oxygen vacancies, ii) formation of oxygen interstitials, and iii) increasing defect states associated with surface groups. Oxygen vacancies, which contribute two free electrons per each vacant site, are subjected to removal under oxidation.[7] In addition, oxygen interstitial incorporation can lead to formation of neutral metal-oxygen defect complexes that trap electrons, such as $(Sn_{In}^{\bullet}\text{-}O_i'')^x$ in $Sn:In_2O_3$, resulting in decreases of both carrier concentration and mobility.[7] Air stability of the $Ce:In_2O_3$ NC-based composite film and the $Sn:In_2O_3$ NC-based composite films were examined by measuring time-dependent resistivity and Hall parameters upon air exposure, along with the $Ce:In_2O_3$ NC-only film and an undoped indium oxide film made by the combustion method (Figure 2.11). Among the four films, only the $Ce:In_2O_3$ NC-based composite film showed high air stability. The mobility and carrier concentration did not change significantly over six days, while the other films lost 11.3-19.6% of their carrier concentration and 17.3-45.2% of their mobility in the same time (Figure 2.11 b,c). As we discussed earlier, cerium dopants reduce the oxygen vacancy concentration,[9] so the degradation mechanism associated with oxygen-vacancy elimination may not be operative in $Ce:In_2O_3$. The undoped indium oxide thin film, however, does likely degrade by the vacancy-filling mechanism. The $Sn:In_2O_3$ thin film is additionally susceptible to the formation of $(Sn_{In}^{\bullet}\text{-}O_i'')^x$ complexes, which does not affect $Ce:In_2O_3$. In addition, the dense morphology of the $Ce:In_2O_3$ NC-based nanocomposite film minimizes the presence of internal surfaces and thereby the potential for surface dangling bonds, which can be present in high concentrations in NC-only films.[46] None of these degradation processes operate in the dense $Ce:In_2O_3$ NC-based composite films, resulting in air stable electronic properties.

OPTICAL PROPERTIES OF THE NC FILMS

The Ce:In_2O_3 NC-based nanocomposite films are highly transparent over a broad spectral range (Figure 2.12). The UV-vis-NIR spectra of the film shows that the transmittance is higher than 81.7% in the visible range (Figure 2.12 b). After subtraction of the extinction of the glass substrates, the nanocomposite film has a transparency of 89.7%. The nanocomposite film has a good figure of merit, T/R_s, where T is visible transmittance and R_s is sheet resistance (80.6 Ω/sq), 1.01 Ω^{-1}, that indicates high quality of the film as a transparent conductor.[54] The films are also transparent in a broad NIR spectral range from 700 to 2500 nm, above which substrate absorption become dominant. Unlike the commercial Sn:In_2O_3 films that usually have a strong absorption or reflection at wavelengths above 1500 nm (Figure 2.12 b), Ce:In_2O_3 NC-based composite films have relatively low carrier concentrations that result in high transparency in the NIR range.[5] The composite films have a wide transparent window that can be highly useful for smart windows or thin film photovoltaics that utilize NIR light.[4]

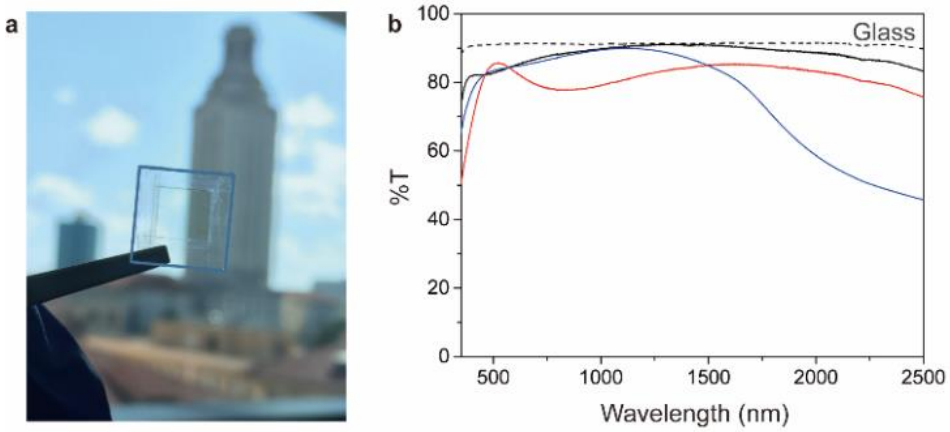

Figure 2.12: Optical properties of NC-based TCO films

Optical properties of NC-based TCO films. (a) A picture of a Ce:In_2O_3 NC-based composite film with a sheet resistance of 60.7 Ω/sq that represents high transparency. (b) Transmission spectra of (black) a Ce:In_2O_3 NC-only film, (red) a Ce:In_2O_3 NC-based in-filled composite film, (blue) a Sn:In_2O_3 NC-based composite film, and (black dot) a glass substrate.

As a model system, we tested our Ce:In_2O_3 NC-based composite films as transparent electrodes for an electrochromic smart window material. An electrochromic electrode is typically composed of a thin layer of electrochromic material deposited on a TCO film. The electrochromic layer modulates light transmittance as it undergoes charging and discharging of electrons and ions (*e.g.*, Li^+ ions).[55-58] The electrochromic application is not only a potential candidate for application of a new TCO material, but is also useful platform to evaluate TCO stability because an electrochromic cell requires enduring repetitive cycling under electrochemical bias and a homogeneous supply of charge and voltage.

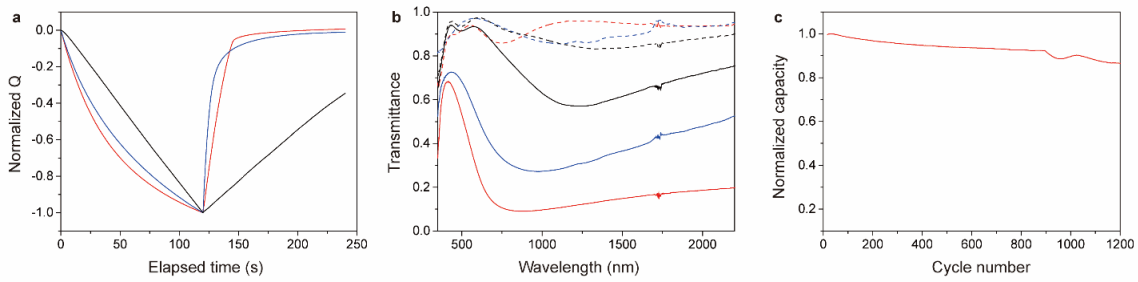

Figure 2.13: Electrochromic properties of NC-based TCO films.

(a) Normalized charging (1.5 V) and discharging (4 V) profiles of WO_{3-x} films on top of different TCOs [vs Li/Li^+ in 1 M bis(trifluoromethane)sulfonamide lithium salt (Li-TFSI) in tetraglyme]: (black) Ce:In_2O_3 NC-only film, (red) Ce:In_2O_3 NC-based composite film, and (blue) commercial Sn:In_2O_3 film with a sheet resistance of 200 Ω/sq. (b) Transmittance spectra of a 230 nm-thick WO_{3-x} NC film on the (black) Ce:In_2O_3 NC-only film, (red) Ce:In_2O_3 NC-based composite film, and (blue) commercial Sn:In_2O_3 film at different switching potentials: (dashed line) 4 V for bright state and (solid line) 1.5 V for dark state. (c) Normalized charge capacity profile over 1000 cycles of the same electrochromic film on a Ce:In_2O_3 NC-based composite film.

We deposited tungsten oxide (WO_{3-x}) NCs as an electrochromic material on top of the above-presented Ce:In_2O_3 composite film. This half-cell device was operated by electrochemical charging and discharging [vs Li/Li^+ in 1 M bis(trifluoromethane)sulfonamide lithium salt (Li-TFSI) in tetraglyme as the electrolye] while measuring the dynamic electro-optical response. Upon charging and discharging, the WO_{3-x} layer exhibited reversible optical modulation with a rapid switching speed, indicating fast and homogeneous electron transport through the TCO layer to the electrochromic layer (Figure 2.13 a,b). The measured optical density range and switching

time were much better than control samples prepared on NC-only films and comparable to the samples prepared on commercial Sn:In_2O_3 electrodes. Moreover, the film had high cycling stability as only 10% of the charge capacity fades over 1000 cycles (Figure 2.13 c), which is consistent with the typical degradation of the electrochromic layer.[57] A detailed description of the electrochromism of the same WO_{3-x} NCs on commercial Sn:In_2O_3 electrodes can be found in the literature,[58] for comparison.

Conclusion

In summary, the in-filling chemistry allowed the NC-based films to exhibit high conductivity based on delocalization of electrons, leading to a positive temperature coefficient of resistivity. When we in-filled 1 M indium combustion solution in films of 21 nm-sized Ce:In_2O_3 NCs, NC-based composite TCO films with an ultra-high mobility 60.4 $cm^2/V{\cdot}s$ were obtained. Their EMFP was comparable to their grain size, implying scattering contributions other than grain boundary scattering were unimportant in constraining the performance. The size correlation suggests that the mobility can be further improved if larger 'Texas-sized' NCs are synthetically developed, though eventually the larger grain size may lead to optical scattering. First order calculations show if a grain size of a NC film is 47 nm, its mobility would be 100 $cm^2/V{\cdot}s$, and if grain size is 60 nm, mobility would be 200 $cm^2/V{\cdot}s$, but it remains a challenge to synthesize and assemble NCs with such large dimensions. Our results demonstrate the example of NC-based TCO films with the thermal signature of metal-like transport at room temperature and we have clearly established the parameters that can be tuned and exploited to optimize TCO film performance for different applications in the future.

Experimental Methods

Materials.

Indium acetate ($In(Ac)_3$, 99.99%), cerium(III) acetylacetonate hydrate ($Ce(C_5H_7O_2)_3•(H_2O)_x$), tin(II) 2-ethylhexanoate (92.5-100%), oleyl alcohol (technical grade, 85%), oleic acid (90%), 2-ethylhexanoic acid (99%), dioctyl ether (99%), indium nitrate hydrate ($In(NO_3)_3•(H_2O)_x$), urea, 2-methoxyethanol (anhydrous, 99.8%), and octane (anhydrous, 99%) were purchased from Aldrich. Oleylamine (C18-content 80-90%) was purchased from Acros. The hydrate number of indium nitrate was assigned by inductive coupled plasma – atomic emission spectroscopy (ICP-AES) after digesting with nitric acid. Non-alkaline Corning Eagle XG glass was purchased from MTI Corp. Commercial Sn:In_2O_3 substrate with sheet resistance of 200 Ω/sq was purchased from Diamond Coatings.

Synthesis of Ce:In_2O_3 NCs.

Ce:In_2O_3 NCs were synthesized by modification of the literature on indium oxide NCs.[33] A precursor solution was prepared by mixing 2.080 g (7.125 mmol) of $In(Ac)_3$, 0.164 g (0.375 mmol) of $Ce(C_5H_7O_2)_3•(H_2O)_x$, and 15 mL of oleic acid in a glass vial and stirring under nitrogen at 150 ^oC for 1 h.

For the synthesis of 21 nm Ce:In_2O_3 NCs, 13 mL of oleyl alcohol was placed in a 3-neck round bottom flask and heated to 290 ^oC. Then, 10 mL of the precursor solution was added dropwise to the hot oleyl alcohol using a syringe pump at a rate of 0.2 mL/min under nitrogen flow. After the injection of the precursor solution, 10 mL of oleyl alcohol was injected dropwise at a rate of 0.2 mL/min. After the injection of oleyl alcohol, 5 mL of precursor solution was injected dropwise again at a rate of 0.2 mL/min. After the injection was complete, solution was cooled down to room temperature. The NCs were

purified by adding excess amount of ethanol, followed by centrifugation at 9000 rpm. Precipitated NCs were redispersed in toluene and the purification step was repeated four times. The final product was dispersed in octane.

The size of NCs was controlled by varying the amount of the precursor solution. For the synthesis of 12 nm-sized Ce:In_2O_3 NCs, 5 mL of the precursor solution was injected dropwise to 13 mL hot oleyl alcohol (290 ^oC) at a flow rate of 0.35 mL/min under nitrogen flow. After the injection was complete, the reaction was quenched by cooling the product to room temperature. The purification step for the 12 nm-sized NCs is the same as that for 21 nm-sized NCs. The 7 nm-sized Ce:In_2O_3 NCs were synthesized in the same protocol as the 12 nm-sized Ce:In_2O_3 NCs, except that the amount of the precursor solution was 2 mL.

Synthesis of Sn:In_2O_3 NCs.

Sn:In_2O_3 NCs were synthesized by modifications of previously reported methods.[53] 645 mg (2.2 mmol) of $In(Ac)_3$, 77.8 mg (0.192 mmol) of tin(II) 2-ethylhexanoate, 1.04 g of 2-ethylhexanoic acid, and 5.35 g of oleylamine was mixed with 20 mL of dioctyl ether in a 3-neck round bottom flask and degassed at 80 ^oC under vacuum for 1 h. The mixture was heated to 150 ^oC under nitrogen and held at that temperature for 1 h. The mixture was then heated to 280 ^oC, and aged for 2 h. After cooling down, the NCs were purified by the same protocols used for Ce:In_2O_3 NCs.

Characterization of NCs.

Transmission electron microscopy (TEM) characterization was performed on a JEOL 2010F with an accelerating voltage of 200 kV. Absorption spectra of NCs were collected on an Agilent-Cary-3000 spectrophotometer with NCs dispersed in

tetrachloroethylene. The concentration and doping level of NCs were characterized by ICP-AES on a Varian 720-ES ICP Optical Emission Spectrometer after digesting the NCs with hydrochloric acid. The doping levels of 21 nm, 14 nm, and 7 nm NCs were 3.82%, 1.46%, and 1.36%, respectively.

Preparation of NC-only films.

Non-alkaline Corning Eagle XG glass and undoped silicon substrates were cleaned by sonication with 2 vol.% Hellmanex aqueous solution, deionized water, acetone, and hexane for 30 min each. 0.6 M (based on the molar concentration of cation, [In] + [Ce]) NC dispersion was filtered through a 0.2 μm syringe filter and spin-coated onto the Eagle XG glass or the silicon substrates at 1500 rpm for 90 s, and then at 4000 rpm for 30 s. The coated films were dried at 120 ^{o}C for 15 min and then annealed in 500 ^{o}C in air for 1 h to remove long chain surfactants. The films were then annealed in 1% H_2 / 99% N_2 at 500 ^{o}C for 1 h with a flow rate of 20 sccm to generate free carriers.

Preparation of NC-based Composite Films by In-filling of a Combustion Solution.

The composite films were produced by in-filling a combustion solution onto the annealed NC films. A 1 M combustion solution was prepared by dissolving 1 mmol of $In(NO_3)_3•(H_2O)_x$ and 1 mmol of urea in 1 mL of 2-methoxyethanol. The hydrate number of $In(NO_3)_3•(H_2O)_x$ was assigned by inductive coupled plasma – atomic emission spectroscopy (ICP-AES) after digesting with nitric acid. The solution was deposited onto annealed NC films, left for 5 s to ensure complete in-filling, and spin-coated at 5000 rpm for 90 s. The in-filled films were dried on a hot plate at 120 ^{o}C for 15 min followed by annealing in air at 500 ^{o}C for 1 h in a tube furnace to remove organic residues. The films were annealed again in 1% H_2 / 99% N_2 at 500 ^{o}C for 1 h with a flow rate of 20 sccm.

Morphology Characterization of the TCO Films.

Top view and cross-sectional scanning electron microscopy (SEM) images were obtained using Hitachi S5500 SEM/STEM using a beam energy of 20 kV. Film thicknesses were determined using a KLA Tencor D-500 profilometer. X-ray diffraction (XRD) patterns of NC films were acquired on a Rigaku Miniflex 600 diffractometer with Cu Kα radiation. Grain sizes were calculated using the Debye-Scherrer equation, $t = K\lambda/\beta\cos\theta$, where λ is the x-ray wavelength (0.15418 nm), β is the line broadening, and θ is a Bragg angle of the peak used for calculation. The line broadening and the Bragg angle were obtained with a (222) peak of indium oxide XRD pattern through pseudo-Voigt fitting after linear background subtraction. The line broadening was corrected for instrumental broadening using $\beta = (w_{exp}^2 - w_{ins}^2)^{1/2}$, where w_{exp} is measured full width at half maxima (FWHM) and w_{ins} is the FWHM measured from LaB_6 powder standard (0.131^o). We set the Scherrer constant K to 0.9 ± 0.045 with reference to the data collected by Langford and Wilson.[59]

Electrical Characterization of the TCO films.

Sheet resistance, mobility, and carrier concentration of thin films were obtained by Ecopia HMS5000 Hall effect measurement system equipped with a 0.558 T magnet.

Optical Characterization of the TCO films.

Transmittance and absorbance spectra were collected with an Agilent Cary-5000 UV-Vis-NIR spectrophotometer. FTIR spectra of the thin films deposited on double-side polished undoped silicon substrates were obtained using a Bruker VERTEX 70.

Smart-Window Applications.

We prepared Ce:In_2O_3 NC-based composite TCO films by in-filling of 1 M of indium combustion solution onto 100 nm thick NC arrays with a crystal size of 21 nm. For the control experiment, we also prepared 100 nm-thick Ce:In_2O_3 NC-only films annealed under same condition as those of the composite films. To prepare the ink for electrochromic films, 5 nm-sized cubic-shaped WO_{3-x} NCs synthesized according to a previous paper,[58] were dispersed in a 1:1 octane/hexane mixed solvent at a concentration of 50 mg/mL. To make a porous NC network, 25 μL oleic acid was additionally added to the ink. Electrochromic devices were prepared by spin-coating the dispersion at 1000 rpm on either the Ce:In_2O_3 NC-based composite film, Ce:In_2O_3 NC-only film, or commercial Sn:In_2O_3 glass.

Transmission spectra of the WO_{3-x}/TCO films were acquired at applied electrochemical voltages of 1.5 V and 4 V. The films were used as working electrodes in a home-built spectroelectrochemical cell connected to a spectrometer and a light source with fiber-optic cables. A single Li foil was used as the counter and reference electrodes and 1 M bis(trifluoromethane)sulfonamide lithium salt (Li-TFSI; Sigma-Aldrich) in tetraglyme (Aldrich) was used as the electrolyte. The stability was measured by cyclic voltammetry cycling between 1.5 V and 4 V.

Chapter 3: Faceting in Plasmonic Doped Metal Oxide Nanocrystals

NC SHAPE CONTROL

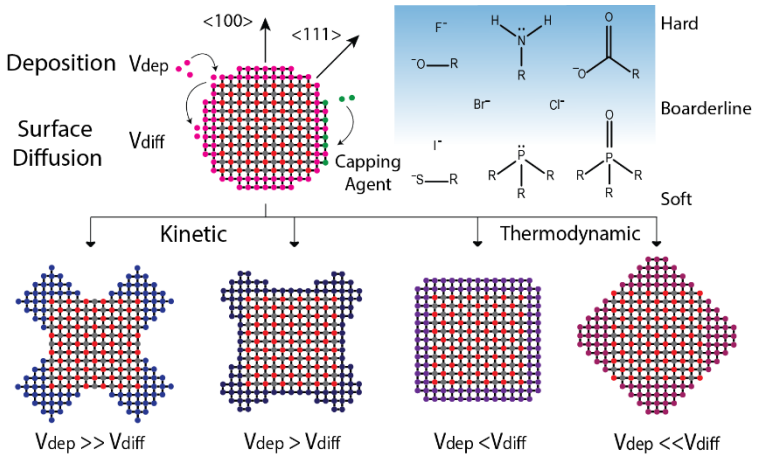

Figure 3.1: Shape control in NC synthesis

Kinetic/thermodynamic shape control by degree of deposition (V_{dep}) vs diffusion rate (V_{diff}) and hard-soft acid-base (HSAB) capping agent. [8]

Shape control of NCs has extensively matured in the noble metal nanoparticle literature[8,9,134], but is still in the early stages of development for LSPR active semiconductor NCs. Shape control is an attractive synthetic strategy for achieving high electric field enhancement around corners of sharply faceted LSPR active NCs and enabling oriented assemblies in which hot spots arise between NC faces. Three interwoven strategies can be applied to influence shape during NC synthesis: exerting control over relative growth kinetics and thermodynamic stability of different facets, capping agent selection, and cation dopant-induced faceting. Kinetic and thermodynamic control influence selective deposition on and surface diffusion along specific NC facets, leading to the preference to eliminate certain facets in favor of others as crystal growth

progresses.[96] The selection of capping agents can be used to modify the relative kinetic and thermodynamic stability of different crystal facets based on the strength and lability of surfactant bonding with NC surfaces and extrinsic metal dopants also influencing NC shape.[135]

Temperature dependent thermodynamic shape control

In thermodynamically controlled NC growth, the shape is ultimately dictated by the Wulff construction, which minimizes the overall surface energy by exposing a combination of stable facets. The surface energy (γ) varies by crystal facet based, in part, on the extent to which orbitals available for bonding are satisfied by bonding to the crystal lattices. A NC achieves a global minimum in Gibbs free energy (ΔG) by minimizing $\Delta G = \Sigma \gamma_i A_i$, which is the sum of contributions from each facet, considering their specific surface energy (γ_i) and area (A_i) while holding volume fixed.[136–138] The presence of high surface energy facets is energetically unfavourable, leading to preferential formation of low energy facets in NCs. Although the relative energetics of different facets depends on their chemical termination (see below), in the absence of specific binding it is generally agreed that the relative surface energies for low-index facets in a face centered cubic (FCC) crystals is in the order $\gamma_{(111)} < \gamma_{(100)} < \gamma_{(110)} < \gamma_{(\text{higher index})}$.[134,139] Taking a simple broken bond approximation, where the presence or absence (due to crystal truncation at the surface) of bonding interactions with nearest neighbors is considered, the surface free energy of a crystallographic plane can be represented as $\gamma_i = 1/2 N_B \varepsilon \rho_a$, where N_B is number of broken atomic bonds per surface unit cell, ε bond strength, and ρ_a is number of surface atoms per unit area.[140,141] In FCC structure with a_0 as the lattice constant, the number of broken bonds per surface unit cell N_B is 3, 4, 5 for each respective (111), (100), and (110) planes, leading to

$\gamma_{(111)} = 3.46(\frac{\varepsilon}{a_0^2})$, $\gamma_{(100)} = 4(\frac{\varepsilon}{a_0^2})$, and $\gamma_{(110)} = 4.24(\frac{\varepsilon}{a_0^2})$ when ρ_a is considered for each facet.[6] The broken bond approximation provides a simple and reasonable way to predict the relative energetics of different crystallographic facets, although computational models based on density functional theory (DFT) can provide more accurate values in which the surface can be allowed to structurally relax before assessing the energetic cost of truncating the crystal.[139,142–144]

NCs, however, are not generally equilibrium products and kinetic effects can either amplify or oppose the thermodynamic tendencies to dominate the resultant NC shape, as demonstrated in metal, metal oxide, and chalcogenide NCs.[145–148] The conceptual framework for this approach to NC shape control is that competing growth pathways occur at each exposed facet during NC growth, where growth involves two physicochemical processes, the first being deposition (V_{dep}) on a high surface energy crystallographic facet, and second being surface diffusion (V_{diff}) to minimize the total surface energy of the NC by exposing the lowest energy crystallographic planes (Figure 3.1).[6,8,9] At slow growth rates, thermodynamic considerations can be expected to reasonably explain NC shape surface diffusion rates can be significantly faster than the deposition rate of additional monomer ($V_{dep} \ll V_{diff}$) (Figure 3.1, far right).[9] Xia et al demonstrated in Pd nanocubes that a slow adatom deposition led to effective surface diffusion of adatoms to (100) facets despite those facets being passivated by Br^-, so the thermodynamically favored shape resulted, favoring (111) facets based on minimization of surface energy. Diverging from Wulff theory, kinetically determined NC products deviate from thermodynamically advantageous surface energy minimized shapes. Overall, the kinetically determined shapes may have a higher total energy compared to those predicted based strictly on thermodynamic considerations, even including the presentation of high index facets, which typically have high specific surface energy.

However, under kinetically driven conditions where the deposition rate is greater than the surface diffusion rate ($V_{dep} \gg V_{diff}$), adatoms site-selectively deposit on high energy facets and are retained there, leading to continuous overgrowth and propagation of these high energy surfaces (Figure 3.1, far left).[9] For instance, in FCC structure metals deposition leading to energetically disadvantageous <111> directional growth leads to growth of energetic protrusions and formation of unconventional high index facets.

Reaction temperature offers one option for control in regulating the importance of thermodynamic versus kinetic effects since deposition and diffusion, having different activation energies, will generally respond with differential sensitivity to changes in temperature. For example, at a higher reaction temperature, Diroll et al observed LSPR active ITO NCs with spherical shape and octahedral facets by changing the reaction temperature.[119] A heat-up colloidal synthesis with indium (III) acetate and tin (IV) acetate precursor in oleic acid and 1-octadecene solution under prolonged elevated temperature either at 320 °C and 300 °C allowed thermally induced decomposition of accumulated metal carboxylates. At the lower 300 °C temperature, larger sized thermodynamically predictable octahedral NCs were observed due to the generation of fewer nuclei, indicative of slower reaction rate. The slower production of monomers from precursors may also have allowed thermodynamically controlled conditions to occur where the rate of V_{diff} exceeds the deposition rate, (V_{dep}). Monomers may have diffused to the (100) crystallographic planes in the cubic bixbyite structure In_2O_3[142], with growth in the corresponding direction ultimately leading to the neat elimination of those planes and resulting in an octahedral shape with the most stable low surface energy (111) facets exposed. The resulting octahedrally shaped ITO NCs are consistent with the DFT-derived Wulff construction, where the calculated relaxed surface energy $\gamma_{(111)} = 0.891\, J/m^2$ is energetically preferred over oxygen terminated $\gamma_{(100)} = 1.759\, J/m^2$. At a higher

reaction temperature of 320 °C, spherical shaped ITO NCs were synthesized with faceting suggestive of a more kinetically controlled product due to a higher deposition rate and a diffusion rate that did not increase as substantially, presumably due to lower activation energy for diffusion. The high precursor decomposition rates possible at such high reaction temperatures may have accelerated deposition on all facets to the extent that monomer deposition leading to growth is not facet-selective and spherical NC shapes result. Similar observation were made in indium-doped cadmium oxide nanocrystals (In:CdO). Octahedral shaped In:CdO NCs were synthesized by Gordon et al[118] by extending a previous shape-controlled cadmium oxide synthesis procedure that had produced octahedral NCs.[149] Extrinsic aliovalent doping with indium in CdO allowed LSPR response centered around 3900 nm with a shape-dependent broadened peak shape. Heat-up colloidal synthesis at higher and lower reaction temperatures with cadmium (II) acetylacetonate as the host precursor and indium (III) acetate as the dopant source in oleic acid and 1-octadecene solution allowed thermodynamically expected shape control in In:CdO NCs. Synthesis at a reaction temperature of 300 °C also led to octahedral NCs, the thermodynamically expected product (Figure 3.2 a, top) and growth at 320 °C led to spherical In:CdO NCs (Figure 3.2 a, bottom).[118] Despite prominent synthetic examples in metal and metal oxide NC developments, there remains a significant opportunity in LSPR active semiconducting NCs to controllably synthesize complex shapes and to demonstrate how kinetic and thermodynamic shape control can be leveraged to create high index facets and especially high curvature regions that can be produced maximal near field enhancement under resonant excitation by far field radiation.

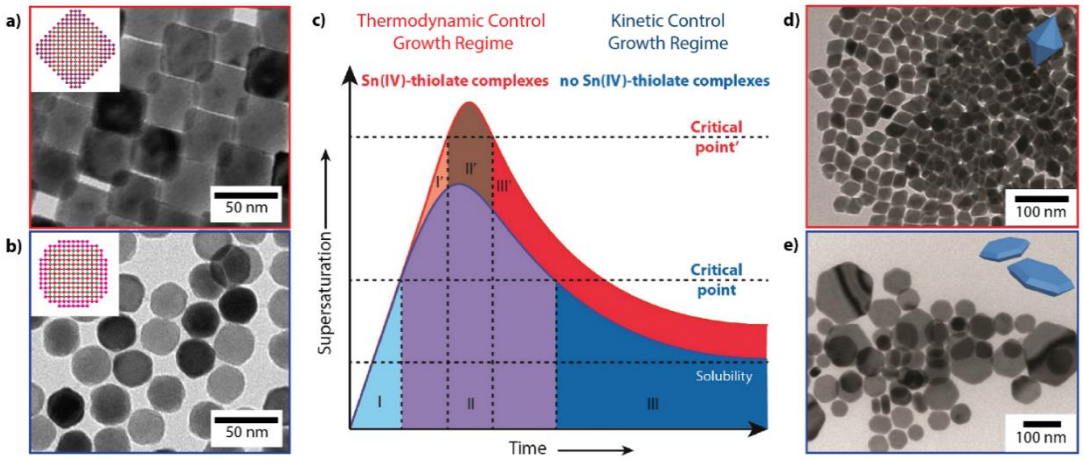

Figure 3.2: Thermodynamic/kinetic shape control in NC synthesis

a) TEM image of octahedral shaped NC synthesized at lower 300 °C reaction temperature and b) spherical shaped In:CdO NC synthesized at 320 °C.[118] c) Critical supersaturation point of $Cu_{2-x}S$ NC influenced by presence of Sn(IV) thiolate complex. Sn(IV) complex inhibit nucleation and raise the critical point from kinetic growth towards thermodynamic growth. d) Bipyramid shaped $Cu_{2-x}S$ NC from thermodynamic growth synthesized under Cu:Sn ratio of 2:1, and e) nanoplatelet shaped $Cu_{2-x}S$ NC from kinetic growth without Sn.[148]

Complexing agent thermodynamic and kinetic shape control

Changing the nucleation rate through chemical intermediates can provide an additional mode of control in achieving thermodynamic or kinetically induced NC shapes. Thermodynamic and kinetic shape control by tuning the nucleation rate in copper chalcogenide NCs was realized by employing inorganic complexing agents. Chen et al demonstrated shape control in djulerite phase nanodisk shaped $Cu_{2-x}S$ NCs by adding tin (IV) chloride pentahydrate to the reaction, which led to elongated tetradecahedra shaped NCs.[150] The introduction of foreign metal cations influenced the morphology of the Cu_{2-}

$_{x}$S NCs, yet the mechanism was unclear. $Cu_{2-x}S$ NCs treated with Sn (IV) failed to contain Sn elements since only detection limit EDX signal was observed, hinting a mechanism other than adsorption of dopant cations on specific crystal planes.[150]

Further studies by van der Stam et al. suggested that Sn (IV) additives are complexing agents with thiols that can dramatically change NC products from kinetic to thermodynamic controlled shapes based on their sequestering of the thiols.[148] The inclusion of a Sn(IV) complexing agent can give rise to substantial changes in the $Cu_{2-x}S$ NCs supersaturation critical point, facilitating differing depletion of monomers available for NC growth after nucleation. $Cu_{2-x}S$ NCs synthesized through a heat-up colloidal method with CuCl precursor in 1-dodecanethiol (DDT) and oleylamine led to polydisperse nanoplatelet shaped NCs (Figure 3.2 e). The DDT thiolate coordinates with the Cu(I) leading to accumulation of copper (I) thiolate single-source precursors, then the thermally induced cleavage of C-S bond into [Cu-S] monomers becomes the rate limiting step in $Cu_{2-x}S$ NC nucleation and growth. Solution and solid state ^{119}Sn NMR spectroscopy elucidated that the addition of $SnBr_4$ in the thiol solution leads to bromide replacement with thiol molecules and formation of the Sn-thiolate complexes ($Sn(DDT)_xBr_y$). A mechanism was proposed where $Sn(DDT)_xBr_y$ imposes an additional nucleation barrier by interacting with [Cu-S] monomer, where Sn(IV)-Cu(I) thiolate complexes were observed through NMR.[151,152] The presence of Sn(IV) complexes significantly increase the activation energy for nucleation and allows a higher concentration of monomers to accumulate (Figure 3.2 c), so that a higher nucleation rate would ultimately be expected, leading to the observed monodisperse and smaller hexagonal bipyramid shaped NC product (Figure 3.2 d).

The morphology of the $Cu_{2-x}S$ NCs was further rationalized by the concepts of kinetic and thermodynamic control over NC growth. $Cu_{2-x}S$ NCs synthesized with

pristine Cu-DDT complexes resulted in NC shapes that were consistent with kinetic considerations, where the high surface energy facets, specifically (010) and (001) rapidly added material, leading to the hexagonal nanoplatelet morphology as typically observed in previous $Cu_{2-x}S$ NC syntheses.[153–155] The presence of $Sn(DDT)_xBr_y$ induces a high nucleation rate as mentioned before, leading to a high concentration of nuclei and a rapid depletion of monomers available for growth. The result is slower NC growth, allowing thermodynamic growth regime to occur where the monomers are deposited and diffuse across the dynamic surface of the growing NC so that the total NC surface energy resulting in a [100] directionally elongated hexagonal bipyramid equilibrium shape.[38,150]

CAPPING AGENT SHAPE CONTROL

Surface ligand groups can be employed in engineering shape control within the context of the above-described thermodynamic and kinetic concepts for controlling NC shapes leading, in some cases, to highly faceted shapes, even exhibiting high index facets.[156,157] As described above, the energetic ordering in an elemental metal with the fcc structure is $\gamma_{(111)} < \gamma_{(100)} < \gamma_{(110)}$ and the relative surface energies can be reasonably estimated using the broken bond approximation.[134,139] However, unlike noble metal LSPR active NCs, diatomic metal oxide NC facets have energetics that are influences substantially by their termination with either oxygen or metal or mixed atomic layers, leading to differing degrees of polarity. Highly polar surfaces tend to have high energy in vacuum, but these energetics can be drastically modified by passivation with organic surfactants.[158,159] As thoroughly investigated in the literature regarding CdSe NC synthesis, the surfactants used in synthesis (e.g. oleic acid, oleylamine, alkyl-thiols, and trialkyllphosphines, phosphonic acids etc) can induce inversions in the crystallographic

plane energies due to their binding affinity and specificity for different crystalline facets.[160] Surfactants thus play a central role in tailoring shape control in NCs, including the LSPR active semiconductor NCs. Specificity refers to the difference in binding strength between crystallographic planes due to the varying presence of dangling bonds at metal and oxygen sites that may be coordinated by the surfactant. To some extent, the importance of surface bonding in modifying surface energy and the ligand affinity for different facets can be rationalized by the HSAB principle, where strong binding affinity can suppress growth in a specific crystallographic direction, resulting in the prevalence of the corresponding facets in the realized NC shape. The surfactant head groups are generally Lewis bases across the spectrum from hard to soft, and metal atom sites on the terminated NC surface facets serve as Lewis acids with varying degree of hardness. Hard Lewis bases commonly employed in synthesis include alkyl carboxylates ($R\text{-}COO^-$), fluoride (F^-), and chloride (Cl^-), which energetically prefer electrostatic interactions with hard Lewis acid metals (e.g., In^{3+}, Al^{3+}, Ti^{4+}, Sn^{4+}). Soft Lewis bases include trialkylphosphines ($R_3\text{-}P$:), trioctylphosphine oxide ($R_3\text{-}P{=}O$), and thiolates ($R\text{-}S^-$) which bind more strongly to soft Lewis acid metals (Cu^+, Au^+, Ag^+, Hg^+, Cd^{2+}) (Figure 3.1, inset).[53,143,161] Alkylamines ($R\text{-}NH_2$), which are commonly used, have intermediate hardness and have frequently been reported to effect significant changes in NC shape as a result.

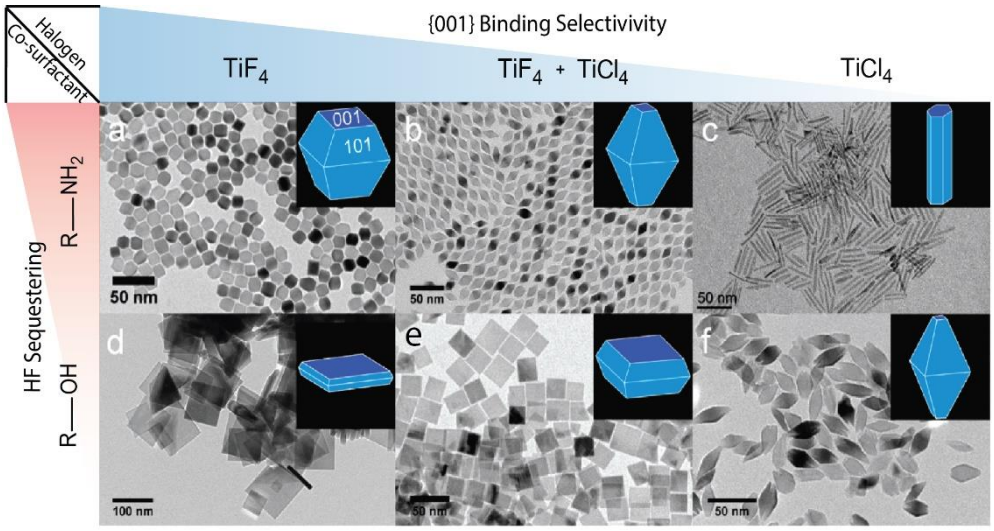

Figure 3.3: Halogen capping agent shape control

Increased fluorine enables selective {001} facet passivation in anatase phase TiO_2 NC (right to left). Amine head groups in surfactant cause HF sequestering effect (top) compared to that of alcohols (bottom), leading to less pronounced {001} surface passivation. [162]

Anionic halogen capping agents (F^-, Cl^-, Br^-, and I^-) can provide effective selective facet passivation in LSPR active semiconductor NCs due to their chemical stability, electronegativity, and wide range of hardness. Anionic capping agents allow control over NC morphology motivated by the goal to examine shape-dependent LSPR modes and their properties. In plasmonic metal oxide NCs, shape control induced by anionic halogen capping agents along with surfactants oleylamine or 1-octadecanol was demonstrated in anatase phase titanium dioxide (TiO_2) nanocrystals by Gordon et al.[162] In situ release of hydrofluoric acid (HF) in the reaction solution leads to favorable selective binding of F^- at {001} facets resulting in a platelet morphology.[163] First-principle calculations supported this observation where surface energy of the fluorine terminated {001} facet in anatase TiO_2 is lower than fluorine terminated {101} facets,[164] which have

been observed to be dominant in the absence of F^-. Synthetic control over the extent of fluorine capping was effected by varying the ratio of F^- to Cl^- by respectively changing the TiF_4 or $TiCl_4$ precursor ratio. Pronounced exposure of {001} facets was observed as more TiF_4 was used (Figure 3.3 a,d) while using more of the chloride precursor led to reduced exposure of {001} facets (Figure 3.3 c,f). Chemical interaction between HF and oleylamine, included in this case as a surfactant and nucleophile to drive the reaction, was described as playing a role in shape control. Amines may sequester in situ generated HF by forming alkyl ammonium fluoride salts ($RNH_3^+F^-$) and reducing the availability of F- to passivate {001} facets. The use of 1-octadecanol instead of oleylamine prevented HF sequestering and lead to enhanced {001} facet formation, resulting in platelet NCs (Figure 3.3 d). Use of oleylamine led to less pronounced {001} facets and resulted in truncated tetragonal bipyramidal shape NCs (Figure 3.3 a,b). Pure $TiCl_4$ precursor in oleylamine led to NCs exhibiting a rod-like morphology, in which {001} facets were minimally present (Figure 3.3 c).

Anionic capping agents have also been employed to realize shape control in LSPR active metal chalcogenide NCs, although softer halide anions (typically, I^-) show effective passivation due to the softer acid Cu+, contrasting with the harder halogen preference (F^-) in metal oxide NCs. Previous literature reported the synthesis of various $Cu_{2-x}S$ or $Cu_{2-x}Se$ NCs with hexagonal nanoplatelet morphologies with LSPR response in the NIR.[39,97,153,165,166] Hsu et al further investigated shape control in (001) faceted triangular prism morphology CuS NCs by comparing binding interactions between various halide anions (Cl^-, Br^-, and I^-).[37] To controllably induce shape growth of covellite phase CuS, a two-phase colloidal synthesis was conducted involving a top layer of octadecene and oleylamine with dissolved elemental S, and bottom layer of 1,5-pentanediol with $Cu(NO_3)_2$ and sodium halide (NaX) salt. CuS nucleation occurs at the two-phase interface

along with halide passivation and the NCs diffuse towards non-polar top solution, so they experience minimal halide exposure after growth. The low-index facets were stabilized similarly in anion shape directed growth of anisotropic Au nanoprisms.[167] Only in the presence of Cl^-, Br^-, or I^- halide capping agents were triangular prism morphologies of CuS NCs realized, while the absence of halogens lead to spherical NCs.[37,153] It was observed that I^- capping led to the most monodisperse triangular NC product with the order of $Cl^- < Br^- < I^-$, ascribed to stronger affinity to the CuS surface for the softer halides.[168] Both size and shape were well controlled in this study, demonstrating the potential for strongly surface interacting halide ions to direct NC growth.

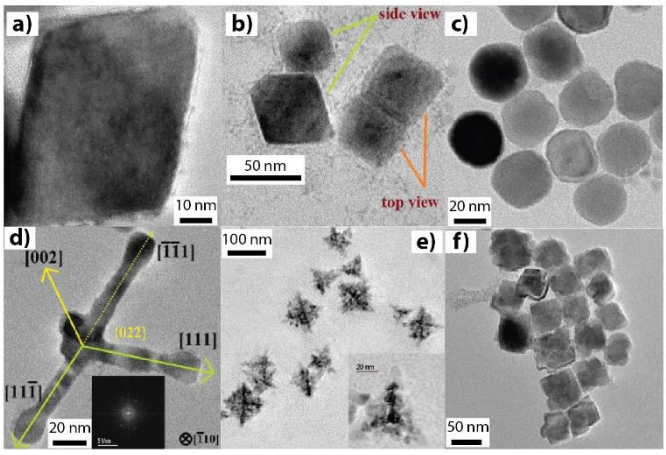

Figure 3.4: Organic ligand capping agent shape control

TEM image of tin-doped cadmium oxide (Sn;CdO) NC with morphology control through surfactant. (a) Octahedral NC with oleylamine surfactant. (b) Truncated octahedron NC with oleic acid/oleylamine. (c) Irregular sphere NC with oleic acid under high temperature. (d) Anisotropically branched NC with 1-octadecanol/oleylamine. (e) Dendritic NC with 1-octadecanol/TOP. (f) Rhombohedra shaped NC with oleylamine/TOPO. [169]

Organic ligand capping agents influence morphology of doped LSPR active NCs and provide an avenue for shape control and combining their selective binding with concepts of kinetic growth allows the realization of anisotropic NC morphologies with high aspect ratios. In interstitially doped metal oxide NCs, Mattox et al induced shape control in Cs_xWO_3 by varying the ratio between oleylamine and oleic acid capping agents, observing strongly faceted shapes when the oleic acid concentration was high.[61] Cs_xWO_3 nanocrystals with hexagonal prism shapes resulted when an oleic acid:oleylamine ratio of 12.5-31 was used, truncated cubes were seen at 5.2-12.5 ratio, and pseudospheres at 2.1-5.2 ratio. [61] Among LSPR active metal chalcogenide NCs, Kriegel et al. synthesized, anisotropic rod and tetrapod shaped $Cu_{2-x}Te$ NCs using surfactants to control the morphology of CdTe NCs[170,171] as a template then conducting cation exchange from Cd^{2+} to Cu^{+} ions.[33] Among aliovalent substitutional doped LSPR active NCs, Ghosh et al. explored surfactant induced shape control in tin doped cadmium oxide (Sn:CdO) NCs. Sn:CdO NC synthesis was conducted with oleylamine, oleic acid, 1-octadecene, trioctylphosphine (TOP), and trioctylphosphine oxide (TOPO) surfactants and resulted in a wide variety of anisotropic morphologies.[169] CdO was selected as a model material, since the relative growth rates of {111} and {100} facets in the cubic rock salt phase can be controlled by the choice and ratio of surfactant capping agents. Octahedral shaped Sn:CdO NCs were synthesized with cadmium (II) acetate ($Cd(acac)_2$) and tin (IV) myristate ($Sn(MTA)_4$) precursors using a heat-up colloidal synthesis in myristic acid and oleylamine solution at 240 °C (Figure 3.4 a). The polar {111} facets of the cubic rock-salt CdO structure consists of alternating stacks of Cd and O atomic layers. Capping this facet with polar $-NH_2$ head groups, the surface energy of the polar {111} planes can be diminished, and they can even be dominating the resulting NCs, leading to an octahedral shape. By introducing oleic acid surfactant as a capping agent into the reaction, the oleic

acid acted as a selective stabilizer for the neutral {001} facet, leading to a truncated octahedron NC morphology (Figure 3.4 b). It was observed that increasing the ratio of oleic acid to oleylamine led to higher {001} facet stabilization, resulting in progression of the NC morphology from octahedral, truncated octahedral, to cuboctahedraln NCs supporting the role of oleic acid as a selective facet capping agent in CdO. However, it must be recognized that organic ligands are typically weakly bound at high temperatures typical of NC growth, especially at non-polar facets. Indeed, dynamic, labile coordination is a preresuisite to facilitate NC growth at all. The implications of weakening coordination at higher temperature for NC shape control was revealed, for example, by the failure of oleic acid to selectively passivate the neutral {001} facet of CdO at the high temperature of 300 °C, leading to irregular spherical Sn:CdO NCs without any apparent faceting (Figure 3.4 c). [169]

A combination of kinetic shape control and capping agents allowed synthesis of highly anisotropic plasmonic Sn:CdO NCs with complex shapes.[169] Highly anisotropic branched Sn:CdO NCs were observed with arm lengths up to 55 nm long and 10 nm wide when synthesized using an oleylamine and 1-octadecanol surfactant mixture (Figure 3.4 d). During a relatively short growth time (15 min) ascribed to kinetic control, the [111] direction growth was more pronounced due to the highly polar {111} facets that alternate in Cd and O termination. This was attributed to the polar {111} facets being stabilized by oleylamine, while the neutral {200} facets were stabilized by the presence of 1-octadecanol. Employing TOP and TOPO surfactant resulted in Sn:CdO NCs with interesting complex shapes due to coalescence and aggregation of smaller particles. TOP capping agent in 1-octadecanol resulted in dendrite structure Sn:CdO NCs (Figure 3.4 e), and TOPO with oleylamine mixture resulted in distorted rhombohedra shaped NCs (Figure 3.4 f).[169] The use of such phosphine based ligands may have led to weaker NC

surface stabilization due to weakened Van der Waals interactions between sterically hindered chain molecules on NC surface.[172,173]

Cationic dopant shape control

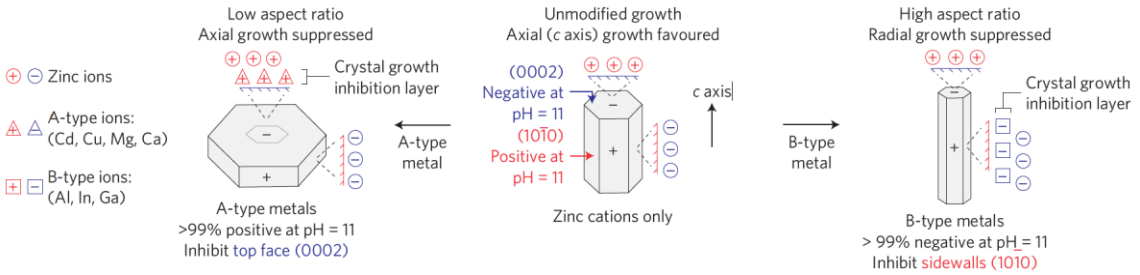

Figure 3.5. Cation dopant shape influence

Cation influence in ZnO NC. Bivalent cation influencing charged complex passivating (0002) facet growth (left) and trivalent cation passivating (10$\bar{1}$0) facet growth (right). [174]

Cationic substitutional dopants can also direct faceting during NC growth since ionic impurities can influence phase and shape in metal oxides or chalcogenides under high doping conditions, resulting in a shapes differing from those expected based solely on the host material.[135] Joo et al carried out aspect ratio control covering three orders of magnitude (height/diameter ratio: 0.1~100) in hydrothermal growth of ZnO nanowires from platelet to needle morphology through selective addition of bivalent or trivalent cations. Principle for a rational shape control was attributed to facet selective electrostatic interaction between charged crystal surface and metal ions during growth. Cationic ions form negatively or positively charged, but largely unreactive complexes that can localize

towards the oppositely charged crystal surface in hydrothermal synthesis. This would competitively limit the access of the reactive zinc intermediates and inhibit growth in a facet specific manner. Facet selective electrostatic interaction in wurtzite phase ZnO can influence either (0002) or $(10\bar{1}0)$ facet growth depending on the cationic specimen.[174] Trivalent cations such as Al^{3+}, In^{3+}, and Ga^{3+} can lead to negatively charged complex ions advantageous for passivating positively charged $(10\bar{1}0)$ sidewall facets, leading to a needle-like shape. Bivalent cations including Cd^{2+}, Cu^{2+}, Mg^{2+}, and Ca^{2+} can form positively charged complexes that block negatively charged (0002) top surface plane growth (Figure 3.5) and lead to a platelet morphology.

However, thorough studies of the influence of cationic dopants on NC are scarce in the LSPR active NC literature and this topic could benefit from further synthetic investigations in the future. The transition of observation made regarding dopant-induced shape control in hydrothermal synthesis to a systematic understanding such effects in colloidally synthesized LSPR active metal oxide NCs is uncertain. Understanding the influence of cationic dopants on NC shape involves decoupling thermodynamic and kinetic effects along with the roll of surfactants as capping agents, all of which impose significant challenges as the effects are convoluted and influenced by one another. Dopant influenced shape control is an interesting avenue for investigation that remains insufficiently distinguished from other synthetic parameters affecting shape. Indeed, cationic dopants influencing the shape and crystal phase have been noted throughout the LSPR active semiconductor NC literature. In colloidal niobium-doped titanium oxide (Nb:TiO_2) NCs, increasing Nb^{5+} doping induced a transition from TiO_2 tetragonal platelets to peanut-shaped nanorods when a Nb precursor concentration of 14% was reached. It was attributed to systematic elongation of the anatase structure along the longitudinal *c* axis, while the *ab* plane lattice parameter was reduced.[124,135] Among metal

oxide exhibiting phase transition, Gao et al observed cation dopants influencing phases in VO_2.[175] Hydrothermally synthesized VO_2 without dopants resulted in large micron-sized rods with tetragonal VO_2 (A) (I4/m) phase selected area electron diffraction (SAED) pattern. Whereas the addition of antimony (Sb^{3+}) dopant resulted in 8-30 nm sized monoclinic rutile-type, VO_2 (M) (P21/c) phase Sb:VO_2 NCs. It was attributed partially substituting the larger radius Sb^{3+} valent cation to the smaller V^{4+} lattice host ion would distort and induce lattices to a different phase.[176] The change in size from large rods into hexagonal NCs was due to positively charged Sb^{3+} dopant cations suppressing the adsorption of VO_2^+ aqua ions, and therefore inhibiting growth. In metal chalcogenide NCs, Al^{3+} ions were used to direct usually spherical Cu_xSe NCs into monodisperse cube shaped NCs. It was hypothesized that the Al^{3+} blocks the binding of hexadecylamine (HDA) to the {111} facet early in the synthesis. During ripening to evolve the NC shape, HDA capped {100} facets are stable towards Cu and Se dissolution and preserved, while {111} facets are subject to fast exchange of Cu and Se ions and disappear as the reaction proceeds.[102]

Shape influence from aliovalent substitutional dopants in LSPR active indium or aluminum doped ZnO (IZO, AZO) was investigated by Mehra et al using slow injection synthesis.[113,177] In this study, a continuous injection of precursor was used, as hot-injection would lead to spatially inhomogeneous doping of ZnO nanocrystal with Al^{3+} when diffusion length of 1 nm should be expected in a 4 h synthesis at 250 °C. Nanorods with branches and rough surface morphology were prevalent when In^{3+} or Al^{3+} dopants were introduced. This observation was ascribed to lattice straindue to the larger In^{3+} metal cation (94 pm) compared to Zn^{2+} (86 pm). Through Rietveld refinement of the nanorod XRD, lattice expansion was observed in In-doped nanorods and lattice contraction in Al-doped, due to its smaller ionic radius. The nanorod shapes were more regular when the

dopant precursors were introduced during the latter stages of growth when the shape was already well established by the growth of pure ZnO. Morphological irregularities due to lattice strain might be expected to be more severe when dopants are incorporated within the NC core.

Chapter 4: Fluorine-Induced Faceting in Syntheses of Colloidal Nanocubes

Cube-shaped nanocrystals (NCs) of conventional metals like gold and silver generally exhibit localized surface plasmon resonance (LSPR) in the visible region with spectral modes determined by their faceted shapes. However, faceted NCs exhibiting LSPR response in the infrared (IR) region are relatively rare. Here, we describe the colloidal synthesis of nanoscale fluorine-doped indium oxide ($F:In_2O_3$) cubes with LSPR response in the IR region, wherein fluorine was found to both direct the cubic morphology and act as an aliovalent dopant. Single crystalline 160 nm $F:In_2O_3$ cubes terminated by (100) facets and concave cubes were synthesized using a colloidal heat-up method. The presence of fluorine was found to impart higher stabilization to the (100) facets through density functional theory (DFT) calculations that evaluated the energetics of F-substitution at surface oxygen sites. These calculations suggest that the cubic morphology results from surface binding of F-atoms. In addition, fluorine acts as an anionic aliovalent dopant in the cubic bixbyite lattice of In_2O_3, introducing a high concentration of free electrons leading to LSPR. We confirmed the presence of lattice fluorine dopants in these cubes using solid-state ^{19}F and ^{115}In nuclear magnetic resonance (NMR) spectroscopy. The cubes exhibit narrow, shape-dependent multimodal LSPR extinction peaks due to corner- and edge-centered modes. The spatial origin of these different contributions to the spectral response are directly visualized by electron energy loss spectroscopy (EELS) in a scanning transmission electron microscope (STEM).

INTRODUCTION

Colloidal syntheses of doped metal oxide NCs have emerged recently as new means of extending localized surface plasmon resonance (LSPR) to the infrared (IR) range,[178] although shape control has yet to be broadly established.[179] A wide range of morphologies have been reported for colloidal gold and silver NCs,[6] including cubes[180,181] and octopods,[182] leading to the observation of shape-dependent LSPR and strongly enhanced electromagnetic near-fields around corners and edges. Yet, metal NCs intrinsically possess high free carrier concentrations exceeding 10^{23} cm^{-3}, so the optical response of isotropic NCs tends to be restricted to the visible region of the electromagnetic spectrum.[183,184] On the other hand, controlled doping of semiconductor NCs allows lower carrier concentrations around 10^{21} cm^{-3}, resulting in IR-range LSPR.[46,185] In this study, we demonstrate shape-controlled colloidal syntheses of highly faceted, fluorine-doped indium oxide (F:In_2O_3) cubes with an LSPR response in the IR range.

Typically, doping strategies in plasmonic metal oxide NCs (e.g., Sn:In_2O_3,[120] Al:ZnO,[54] and In:CdO[118] NCs) have focused on aliovalent cation substitution. Halogen anions, meanwhile, can act as surface capping agents[186] that have been used for shape control of metal,[9] metal oxide,[163] and metal chalcogenide[187,188] NCs. In some metal oxide NCs, fluorine has been incorporated as an anionic co-dopant (e.g., F,In:CdO,[64] F,Sn:In_2O_3[65]). Very little has been reported regarding fluorine doping alone to induce LSPR, as in fluorinated TiO_2 NCs.[162] Furthermore, while anionic doping in nanocrystalline F:SnO_2 has been demonstrated, the effects of fluorine on faceting or LSPR properties of metal oxide NCs have not been well explored.[189] A comprehensive materials characterization is yet needed to simultaneously unravel role of fluorine in

LSPR inducing internal doping and shape inducing surface faceting effect for metal oxide NCs.

Faceted NCs give rise to shape-dependent LSPR phenomena not observed for spherical NCs, including highly enhanced near field hot spots around corners and edges[190] that, in conventional metals, have been leveraged for plasmonic nanoantennae[191,192] and surface-enhanced Raman spectroscopy (SERS).[193,194] Shape effects and understanding of plasmonic behavior have advanced in other classes of non-noble metal plasmonic materials, such as copper chalcogenides[195,196] and being extended in refractory metal nitrides.[184,197,198] Disks and elongated NCs of copper chalcogenides have been reported in shape effects on their LSPR properties,[196] which are likely to be strongly influenced by crystalline anisotropy as well.[199] Yet, shape-dependent studies of LSPR specific to doped metal oxide NCs are few,[118,199] motivating the development of new strategies for synthetic shape control, as large cube NC sizes,[65] and well-defined corners[185] can lead to higher magnitude in near-field enhancement for doped metal oxide NCs. Focal to this work, access to large NC size with larger volume-to-surface ratio allow F:In_2O_3 NCs as a model material in decoupling internal role of fluorine dopant from surface fluorine, supported by extensive materials characterization and high spatial resolution for single particle analysis.

We succeed in modulating the shape of F:In_2O_3 NCs by varying the ratio of InF_3 to $In(acac)_3$ precursors and observe multimodal shape-dependent LSPR extinction features. The role of fluorine in defining NC facets and inducing LSPR spectral response is attributed to the presence of fluorine on the external surfaces and internally within the NCs, respectively. Through X-ray photoelectron spectroscopy (XPS) and solid-state ^{19}F magic-angle-spinning (MAS) nuclear magnetic resonance (NMR) spectroscopy correlated with density functional theory (DFT) calculations, fluorine is found to occupy

surface sites on dominantly exposed {100} facets. Fluorine dopant species internal to the NCs are probed by X-ray diffraction (XRD), energy dispersive X-ray spectroscopy (EDX), time of flight-secondary ion mass spectrometry (TOF-SIMS), and ^{19}F MAS-NMR spectroscopy. Aliovalent substitutional fluorine doping on oxygen lattice sites leads to free carrier compensation, inducing LSPR. The local metallic environments of the sub-surface fluorine and indium atoms in the NC lattices are established by analyses of ^{19}F spin-lattice T_1 relaxation times and wideline ^{115}In NMR spectra, which are shown to exhibit temperature- and frequency-dependencies that are characteristic of coupling to free (metallic) electron carriers. Arising from the free carriers and highly faceted NC shape, single NC LSPR spatial modes are directly visualized by monochromated electron energy loss spectroscopy (EELS) performed in a scanning transmission electron microscope (STEM) to assign the observed multimodal features to distinct spatial dipolar modes. The observed material characteristics lead to IR light near field localization, making F:In_2O_3 NCs a foundation material for near field enhancement applications in the IR.

NC SHAPE CONTROL

The shapes of the F:In_2O_3 NCs were controlled by varying the molar ratio of InF_3 to $In(acac)_3$ precursors during synthesis, which also determined the extent of fluorine incorporation in the resulting NCs. F:In_2O_3 NCs with well-defined morphology were produced for 1–3% InF_3 in the growth solution, as shown in Figure 4.1. SEM images showed that monodisperse NCs (edge length 162.1 ± 9.2 nm) with cubic morphology were obtained exclusively in the presence of InF_3 (3% in molar ratio to $In(acac)_3$) (Figure 4.1 a, rightmost panel). By comparison, in the absence of InF_3 during the synthesis,

NCs with pseudospherical morphology were observed (Figure 4.1 a, leftmost panel), with no cubic-shaped NCs observed. Intermediate amounts of InF_3 led to variations in the NC morphology, specifically forming concave cubes with edges protruding outwards for 2% InF_3 (Figure 4.1 a, second from right) and 1% InF_3 (Figure 4.1 a, second from left). The cube morphology persists for higher concentrations of InF_3 (4% and 5%) as well, until a threshold is reached at 6% InF_3, beyond which NCs exhibit roughened surfaces (Figure 4.2).

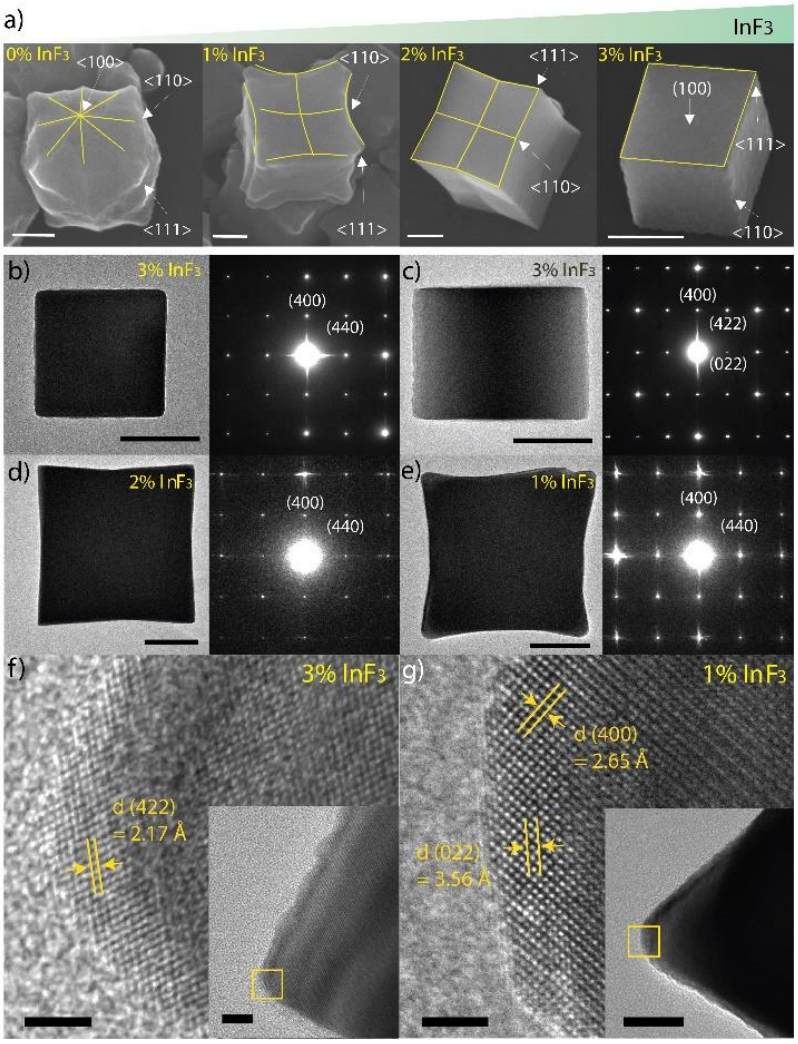

Figure 4.1: F:In_2O_3 NC morphology

(a) SEM images showing the progressive effect of F on In_2O_3 NC morphology. Outlines are shown as guides to visualize the indicated facets. TEM images (left panels) and the corresponding SAED patterns (right panels) of (b) cube, (c) edge-oriented cube, (d) sharp concave cube, and (e) concave cube F:In_2O_3 NCs. Scale bars are 100 nm for a-e. (f) HRTEM image of a single F:In_2O_3 cube corner with NC oriented on its edge (inset). (g) Extended corner of concave cube F:In_2O_3 NC (inset). Scale bars are 2 nm in f and g, and 20 nm in the insets.

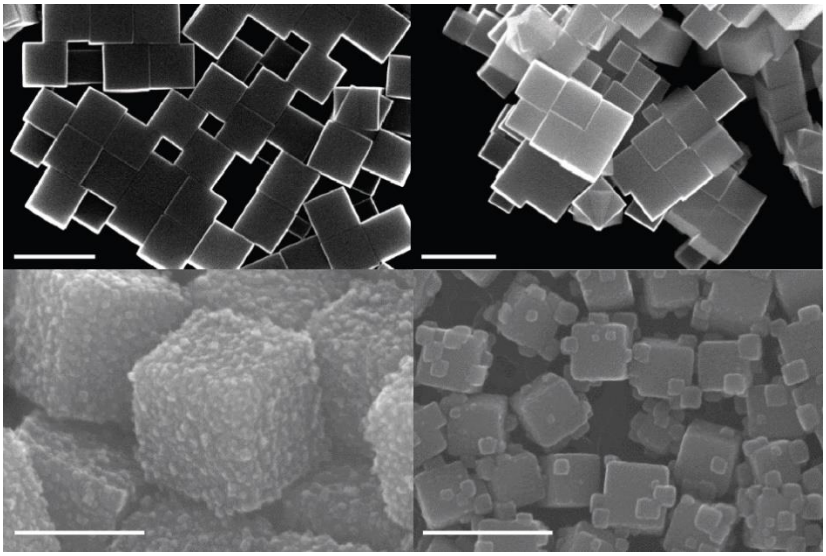

Figure 4.2: SEM Images of More Highly Doped F:In_2O_3 NCs

SEM images of F:In_2O_3 (4% InF_3) cube NCs (top left), F:In_2O_3 (5% InF_3) cube NCs (top right), F:In_2O_3 (6% InF_3) cube NCs (bottom left), and F:In_2O_3 (12% InF_3) NCs (bottom right). Defective surfaces are observed in F:In_2O_3 NCs using 6% and 12% InF_3. Scale bars are 500 nm, 500 nm, 200 nm, and 400 nm, respectively.

The TEM images in Figure 4.1 show that the as-synthesized F:In_2O_3 cubes exhibit well-defined crystalline facets. Selected-area electron diffraction (SAED) confirms that the F:In_2O_3 cubes are each single crystals and allows indexing of their surface facets. A TEM image of an F:In_2O_3 cube (3% InF_3) is shown in Figure 4.1 b, which exhibits a flat (100) face and a well-defined edge. The cube is terminated with (100) facets of the In_2O_3 cubic bixbyite structure, corroborated by the position of the (400) reflections in the SAED pattern (Figure 4.1 b, right). A cube on <110> zone axis orientation exhibits (422) reflections in the SAED pattern (Figure 4.1 c, right), corresponding to the (422) spacings

observed by HRTEM (Figure 4.1 f). Concave F:In_2O_3 cubes (1 and 2% InF_3) are also single crystalline as observed in SAED patterns collected down the <100> zone axis (Figure 4.1 d,e right). An HRTEM image of the elongated tip on a concave cube (1% InF_3) shows (022) lattice spacing (3.56 Å), along with (400) lattice spacing parallel to the facets (Figure 4.1 g). Together, these observations indicate that the as-synthesized F:In_2O_3 cubes have cubic bixbyite {100}-dominant surface facets.

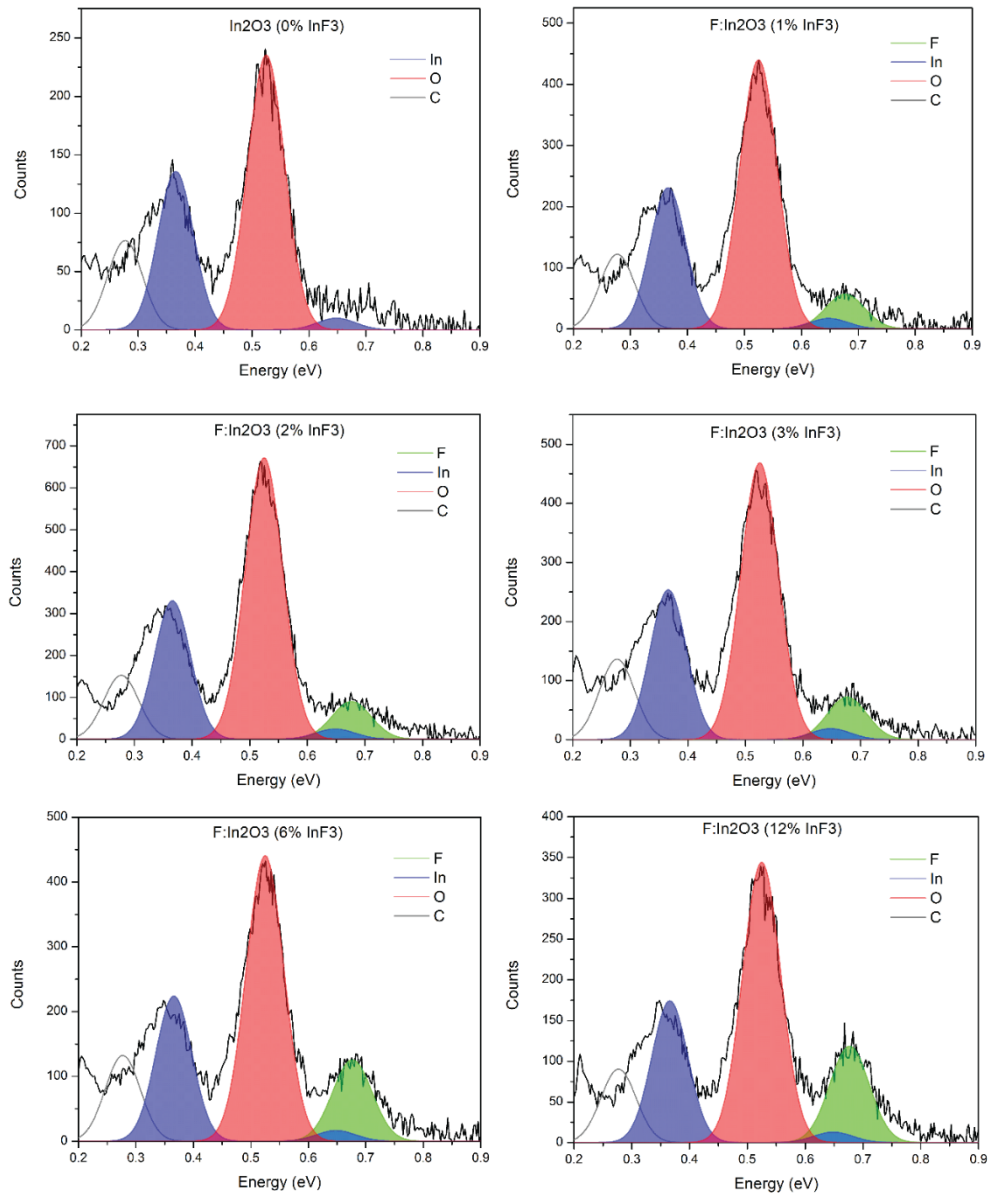

Figure 4.3: EDX Spectra

EDX spectra of F:In_2O_3 NCs. (a) In_2O_3 NCs (0% InF_3), (b) F:In_2O_3 NCs (1% InF_3), (c) F:In_2O_3 NCs (2% InF_3), (d) F:In_2O_3 NCs (3% InF_3), (e) F:In_2O_3 NCs (6% InF_3), and (f) F:In_2O_3 NCs (12% InF_3).

To quantify total fluorine incorporation in F:In_2O_3 NCs (Table 4.1), EDX spectroscopy (Figure 4.3) and TOF-SIMS analysis were conducted (Figure 4.4). Because the emitted X-rays are of high energy, EDX has an effective probe depth of about 200 nm, the entire volume of the NCs is probed and the results approximately reflect the overall F/In atomic (at.) composition ratio. However, owing to the low sensitivity of EDX to fluorine in the low dopant concentration NC samples, (e.g. 1% InF_3), TOF-SIMS was employed to quantify the F/In atomic ratio as a film of NCs was progressively etched. EDX with TOF-SIMS both support a trend of increasing F atomic composition in F:In_2O_3 NCs as a function of InF_3 concentration employed during synthesis. Lower F/In was observed in 12% InF_3 when compared to initial F/In, suggesting fluorine saturation within the NC lattice under excessive addition of dopant precursor. Syntheses with $InCl_3$ and $InBr_3$ precursors were observed to result in low halide (X = Cl, Br) incorporation instead.

Sample	Precursor $In(acac)_3$:InX_3 (mmol)	Initial at. X/In %	Measured X/In % (EDX)	Measured F/In % (TOF-SIMS)
1% InF_3	0.99:0.01	3.0	6.65±0.48	2.7
2% InF_3	0.98:0.02	6.0	8.56±1.59	9.2
3% InF_3	0.97:0.03	9.0	11.76±2.70	10.3
6% InF_3	0.94:0.06	18.0	26.40±0.36	22.7
12% InF_3	0.88:0.12	36.0	30.58±2.40	30.6
3% $InCl_3$	0.97:0.03	9.0	0.32±0.11	-
3% $InBr_3$	0.97:0.03	9.0	2.62±0.06	-

Table 4.1: Halide quantification for synthesized NCs

EDX quantification of fluorine in F:In_2O_3 NCs synthesized with 1-12% InF_3 precursor, and halide quantification for NCs synthesized with 3% $InCl_3$ and 3% $InBr_3$ precursors. The EDX fluorine quantification in F:In_2O_3 NCs are accompanied by TOF-SIMS results.

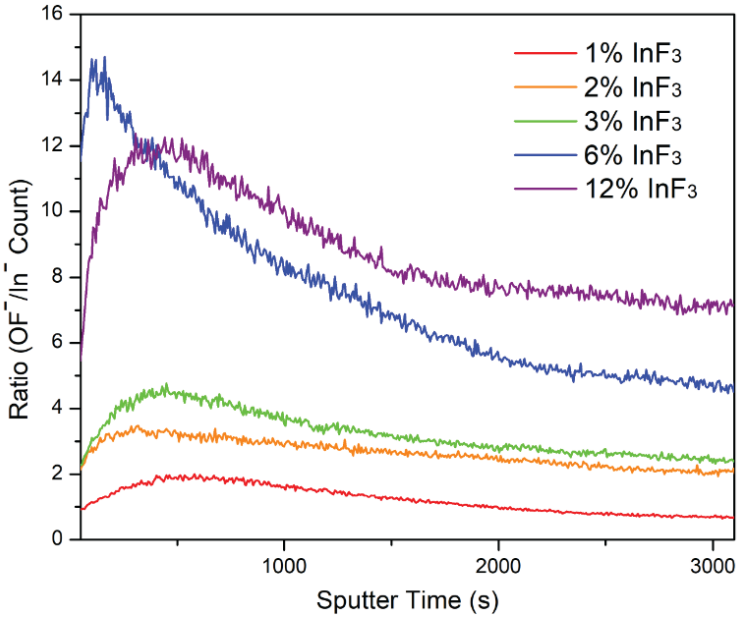

Figure 4.4: TOF-SIMS

TOF-SIMS data acquisition of secondary ions (OF^-, In^-) ratio count from dropcast F:In_2O_3 NC (1-12% InF_3) films, with sputtering time until non-corrugated averaged composition ratio is attained for relative comparison with EDX.

Aliquots taken during the synthesis of F:In_2O_3 cubes (3% InF_3) were analyzed by FTIR spectroscopy to assess the chemical decomposition mechanism. Typically, $In(acac)_3$ and oleic acid were heated at 120 °C to form an indium oleate (In-OA) precursor. For F:In_2O_3 NCs, a ramp rate of 15 °C/min to 320 °C was used to rapidly decompose the indium precursors. In-OA and octylamine (OcAm) lead to the formation of indium monomers and amide byproducts[27,30] (Figure 4.5). The FTIR fingerprint region shows that the precursor undergoes an aminolysis reaction with OcAm during synthesis. The metal carboxylate (1614 cm^{-1} and 1582 cm^{-1}) peak signals[26,200] are significantly reduced in intensity after heating to 260 °C and continue to fall as the reaction progresses from 0

to 5 min, past this point. Concurrently, amide byproduct C=O stretching (1688 cm^{-1}) and N-H bending (1651 cm^{-1}) signals[201,202] increase as In-OA is decomposed (Figure 4.5). These observations indicate that aminolysis is a primary mechanism of growth, which entails nucleophilic attack of the alkylamine on the metal-alkylcarboxylate complex, which is a common NC growth mechanism for metal oxides.[28,29] An aliquot taken during decomposition at 280 °C showed small irregularly shaped particles indicative of aggregative nucleation (Figure 4.5).[4] Irregular nuclei cohere together through oriented attachment as observed in HRTEM, resulting in large size NC seeds. Average NC product yield was 54.3% by weight for all F:In_2O_3 NC samples. Differing from typical doped In_2O_3 NC syntheses,[67] such large sized (100 nm scale) NCs are enabled by a combination of aminolysis-driven growth, aggregative nucleation, and a concentrated precursor solution (0.2 mmol/ml) at high reaction temperature (320 °C).

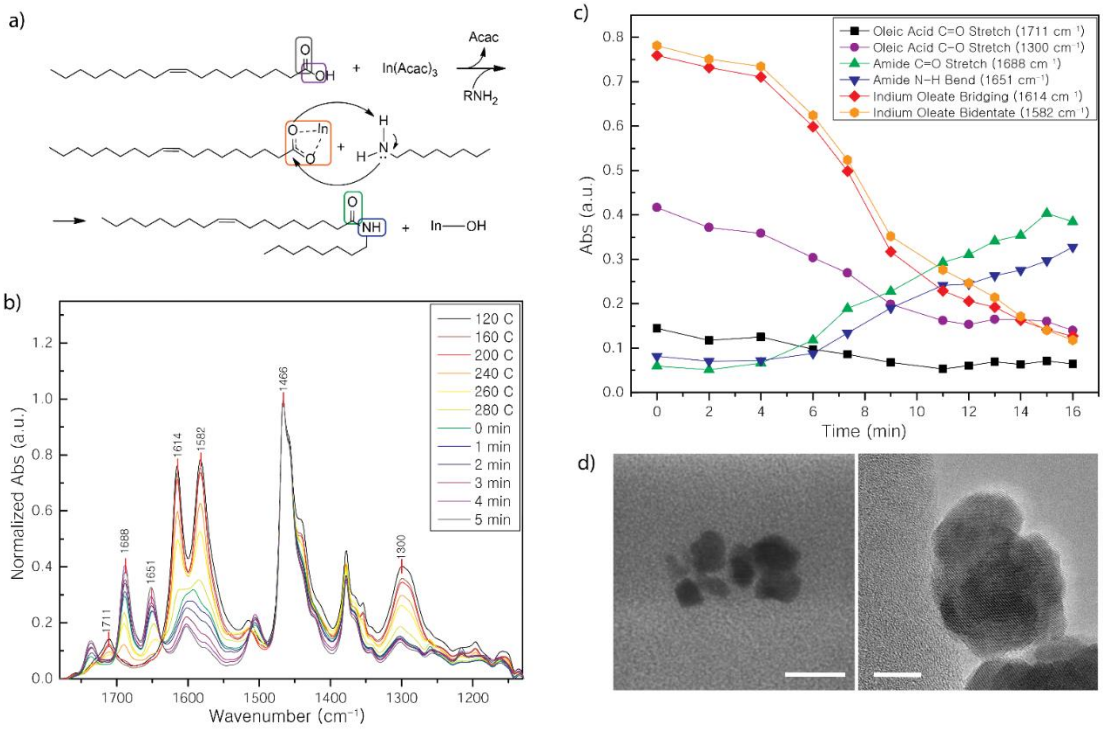

Figure 4.5: F:In_2O_3 Cube Aliquots

(a) Aminolysis scheme with indium oleate undergoing aminolysis with octylamine, leading to amide byproduct formation. (b) FTIR fingerprint region of F:In_2O_3 cube NC (3% InF_3) aliquots taken during reaction. (c) Bridging and bidentate peaks from indium oleate precursor are observed to rapidly decompose during heat-up synthesis. Increasing IR peak intensity from F:In_2O_3 cube aliquots are assigned to C=O stretching and N-H bending vibrations in the amide byproduct. (d) F:In_2O_3 (3% InF_3) irregular aggregate aliquot taken at 280 °C imaged with STEM (left). Lattice alignment is observed in HRTEM, indicative of nuclei oriented attachment (right). Scale bars are 200 nm, and 10 nm, respectively.

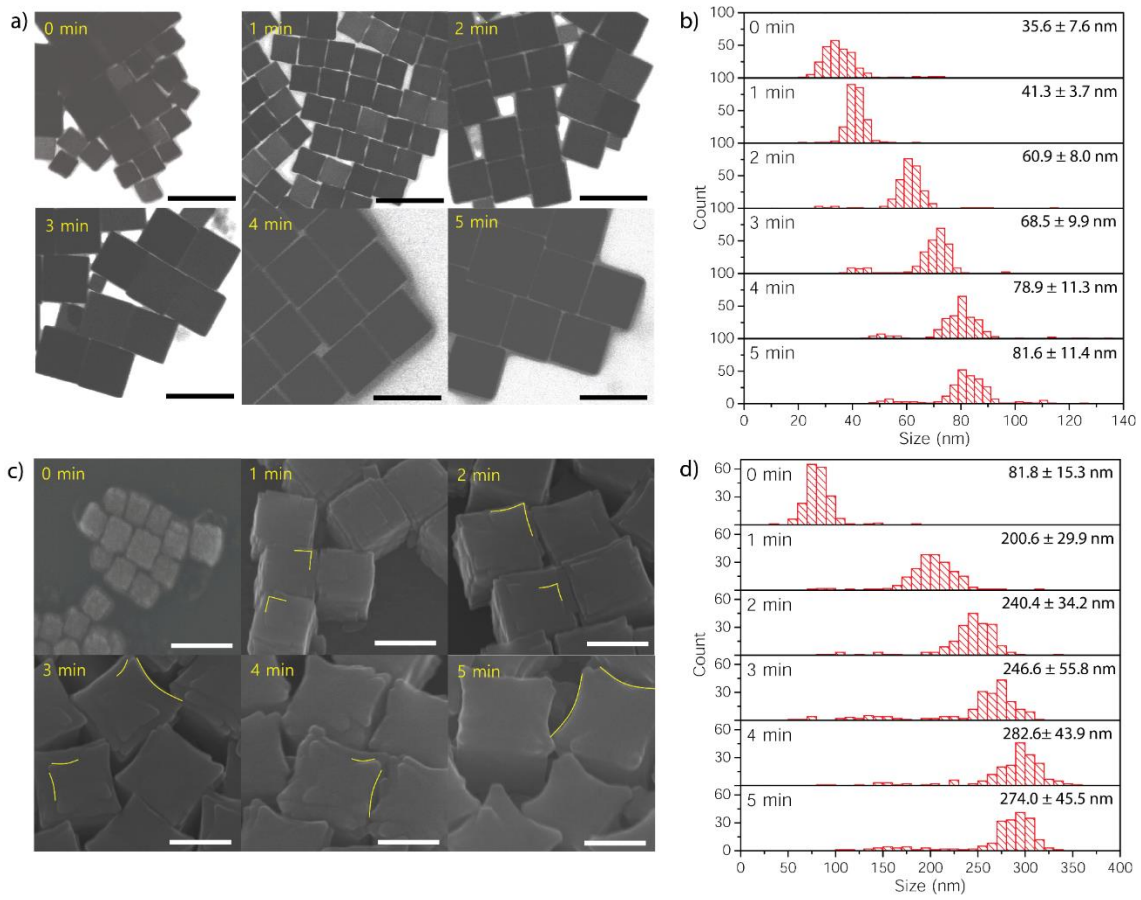

Figure 4.6: SEM images of aliquots taken at different stages of F:In_2O_3

(a) SEM images of aliquots taken at different stages of F:In_2O_3 (3% InF_3) cube synthesis (0 to 5 min). Scale bars are 100 nm. (b) Size distribution histograms for the corresponding F:In_2O_3 cube aliquots (panel a) taken during the growth progression (250 particle count). (c) SEM images of aliquots taken during the growth of F:In_2O_3 (1% InF_3) concave cubes (0 to 5 min). Yellow lines are drawn as a visual guide to follow the gradual ledge-converging to eventually form the elongated corners. Scale bars at 200 nm. (d) Size distribution histograms for the corresponding F:In_2O_3 concave cube aliquots (panel c).

To evaluate the progression of NC shape with reaction time, SEM analyses were performed on aliquots collected during the growth of F:In_2O_3 cubes. As reaction time progresses and the precursors progressively decompose, NC size is expected to increase, accompanied by either shape retention or changes. Aliquots taken during the growth of F:In_2O_3 cubes (3% InF_3) show that the cube morphology is retained throughout the 5 min growth period (Figure 4.6 a) as size increases from 35.6 ± 7.6 nm to 81.6 ± 11.4 nm (Figure 4.6 b). This indicates {100} surface stabilization throughout growth at sufficient InF_3 concentration, allowing synthesis of well-defined cube-shaped NCs. The cubic morphology was established after an initial nuclei aggregation phase as irregular aggregates became cubic during growth. Aliquots over longer reaction times (at 5 min, 30 min, 1 h, and 2.5 h) at 320 °C were also taken to observe the morphology evolution. At extended reaction times, corner rounding was observed. At longer reaction times of 2.5 h or more, the well-defined edge and corner morphology becomes a truncated cube with the appearance of {111} facets at the cube edges (Figure 4.7). At even longer growth times, pitting is apparent on the {100} facets, potentially due to corrosion by F^- ions or their reaction byproducts.[9,186]

For the concave F:In_2O_3 cubes (1% InF_3), SEM images of aliquots reveal progressive growth at the corners that results in morphological evolution (Figure 4.6 c). The initial aliquot, taken when turbidity was first observed in the reaction flask (0 min), shows cube-shaped NCs that are 81.3 ± 15.3 nm in size. SEM images show a second stage involving rapid NC size growth (Figure 4.6 d) and observation of ledges on the faces. In the final stage, ledges converge into elongated tip extensions that project in the <111> directions, from the corners. A smooth concave surface has replaced the flat {100} cube facets in the final 5 min aliquot to form 274.0 ± 45.5 nm sized F:In_2O_3 concave cubes with elongated corners. This suggests that the {100} facets may not be as stable for

this case, compared to the cubes synthesized with 3% InF_3 in the reaction mixture. At longer reaction times of 2.5 h or more, further rounding of the elongated corners occurs (Figure 4.7).

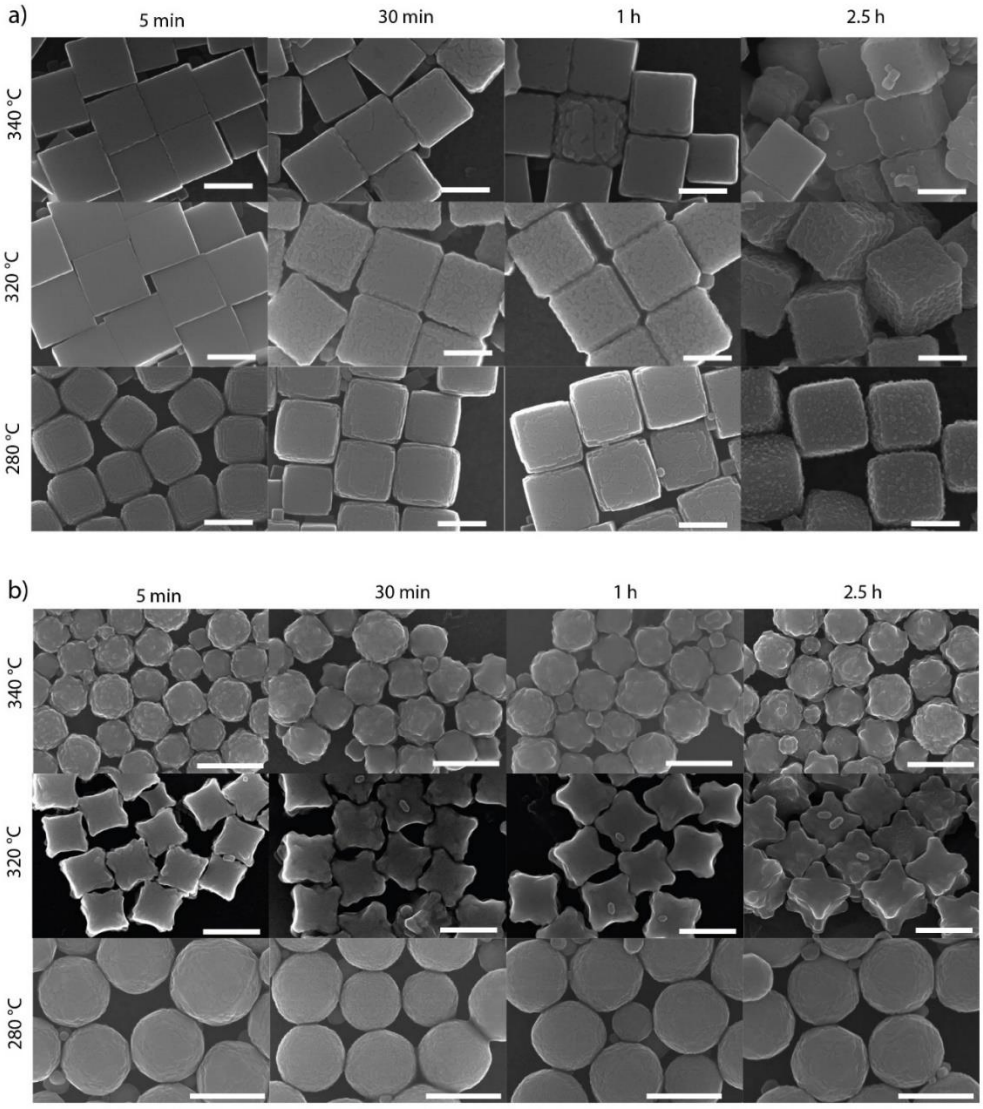

Figure 4.7: Temperature and Reaction Time NC Series

(a) Cube (3% InF_3) and (b) concave cube F:In_2O_3 NC (1% InF_3) growth aliquots at 5 min, 30 min, 1 h, and 2.5 h were taken to reveal growth time influence on NC shape. Reaction time aliquot series with varying reaction temperatures at 280 °C, 320 °C, and 340 °C. Scale bars are 250 nm in Figure a, and 500 nm in Figure b.

The synthesis of well-defined F:In_2O_3 cubes was also found to depend on the reaction temperature. For the 3% InF_3 synthesis, which produced optimally structured cubes at 320 °C, the morphological evolution was studied for reactions at temperatures between 280 and 340 °C. Strongly faceted cube shapes were produced at reaction temperatures of 340 and 320 °C (Figure 4.7). However, at a lower reaction temperature (280 °C), smaller rounded cubes were observed at 5 min reaction time, evolving after 30 min to more defined cubic shapes.

The concave cube morphology is more sensitive to reaction temperature. Synthesizing F:In_2O_3 NCs (1% InF_3) at an elevated reaction temperature (340 °C) resulted in irregular pseudospherical shapes with growth in randomly oriented directions (Figure 4.7). Apparently, the preference for growth in the <111> direction is weakened at higher growth temperatures, which is consistent with growth occurring without directional preference potentially due to enhanced monomer diffusion along the surface at high temperatures.[134] Synthesizing F:In_2O_3 NCs (1% InF_3) at a lower reaction temperature (280 °C) resulted in rounded NCs instead of a concave cube morphology, up to 2.5 h reaction time (Figure 4.7).

INFLUENCES OF FLUORINE ON NC SHAPE

SEM and HRTEM analyses indicate that fluorine has a facet-directing function in the growth of F:In_2O_3 NCs. The cube-shaped NCs were produced only in the presence of fluorine (Figure 4.1 a, right), while the cubic shape is not observed in its absence (Figure 4.1 a, left). To assess whether fluorine is unique compared to other halides as a morphology-directing agent under these synthesis conditions, $InCl_3$ and $InBr_3$ were used in place of InF_3. The bond dissociation energy is 439 kJ/mol for the In-Cl bond and 418

kJ/mol for the In-Br bond, which are lower than for In-F at 506 kJ/mol.[203] In-F bonds, being stronger than In-O bonds (at 360 kJ/mol), are hypothesized to be highly stable at In_2O_3 NC surfaces, while weaker In-Cl or In-Br bonds are less favorable due to lower electronegativity than fluorine and differing ionic radii (Cl^-: 1.81 Å and Br^-: 1.96 Å) causing strain when substituting surface oxygen (O^{2-}: 1.28 Å).[164,186] The NC products synthesized in the presence of $InCl_3$ or $InBr_3$ were large and rounded: 246.7 ± 16.6 nm for Cl:In_2O_3 NCs and 348.3 ± 58.1 nm for Br:In_2O_3 NCs with poorly defined facets (Figure 4.8), whereas F:In_2O_3 cubes synthesized with the same precursor ratio had well defined shape with edge lengths of 162.1 ± 9.2 nm (Figure 4.10).

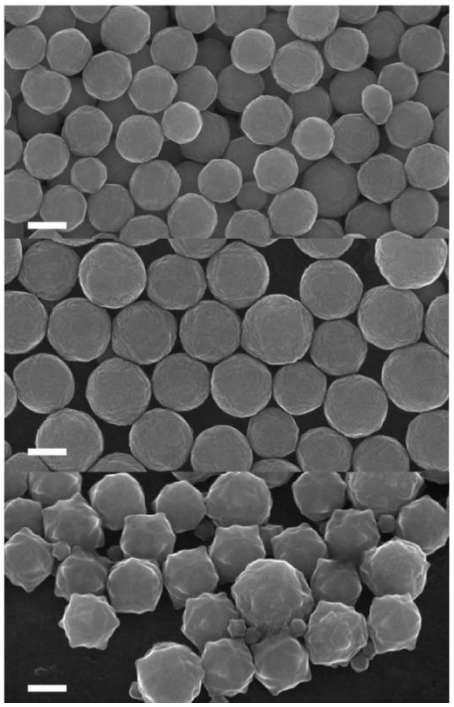

Figure 4.8: Cl, Br Doped NC SEM Image

SEM images of rounded Cl:In_2O_3 (3% $InCl_3$) (top), Br:In_2O_3 (3% $InBr_3$) (middle), and undoped In_2O_3 (0% InF_3) NCs (bottom). Scale bars are 200 nm.

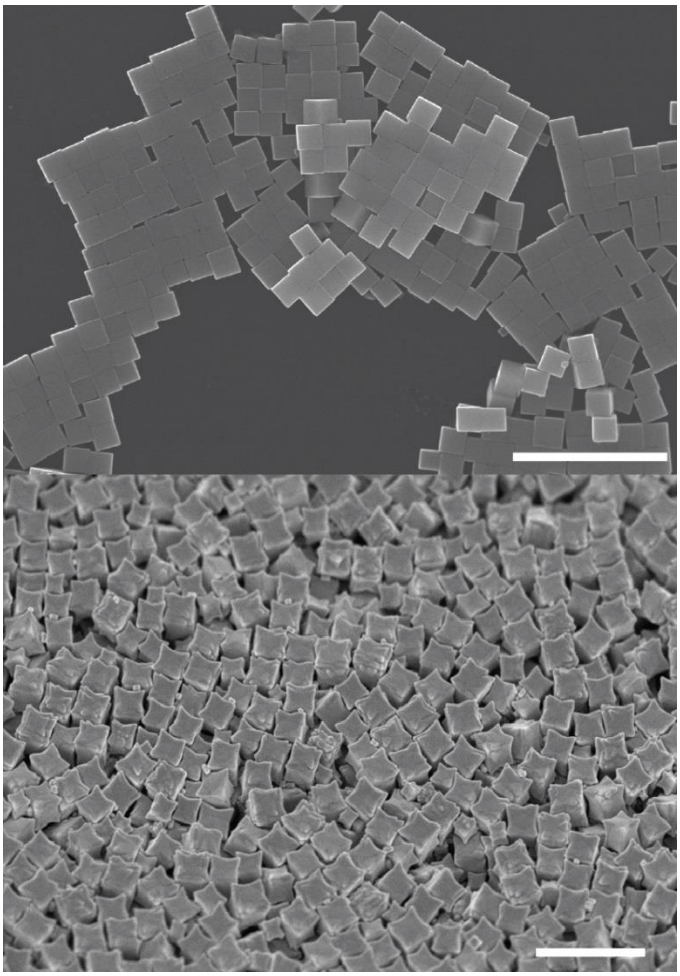

Figure 4.9: Cube and Concave Cube SEM Images

SEM image of F:In_2O_3 (3% InF_3) cube NCs (top) and F:In_2O_3 concave cube (1% InF_3) NCs (bottom left) dropcast on Si substrates. Scale bars are 1 μm.

Since fluorine plays an important role in the faceting of the In_2O_3 NCs, XPS was used to probe the presence of fluorine on their surfaces. XPS is sensitive to surface composition, since the escape depth of photoelectrons is only a few nanometers. The existence of fluorine on the F:In_2O_3 NC surfaces was revealed by XPS spectra acquired for the In 3d (Figure 4.3 a) and F 1s (Figure 4.3 b) regions. As shown in Figure 4.3 a, the

In $3d_{5/2}$ signal was deconvoluted into components that are assignable to lattice In-O (444.3 eV), In-OH (445.0 eV), and In-F (445.8 eV) species,[204] with the peak due to the In-F species becoming more dominant as the InF_3 precursor concentration is increased. Furthermore, the F 1s peak at 684.6 eV, flanked by the In 3p doublet peaks, also exhibits an increase in relative intensity as the InF_3 precursor concentration is increased (Figure 4.3 b). Deconvolution of the O 1s signal is shown in Figure 4.8, with components that are assignable to lattice oxygen (530.0 eV), oxygen adjacent to oxygen vacancies or other charged defects, such as $F_O^{\cdot}$ (531.0 eV), surface hydroxyl (531.8 eV), and carboxyl (533.1 eV) species, respectively.[204] Overall, the undoped In_2O_3 NCs are observed to have more surface-adsorbed hydroxyl and carboxyl species, as compared to F:In_2O_3 NCs which further signifies the incorporation of F species as surface-capping agents. XPS characterization thus suggests that fluorine adsorbs on the In_2O_3 NC surfaces, which may be linked to the stability and prevalence of {100} facets in cube-shaped NCs.

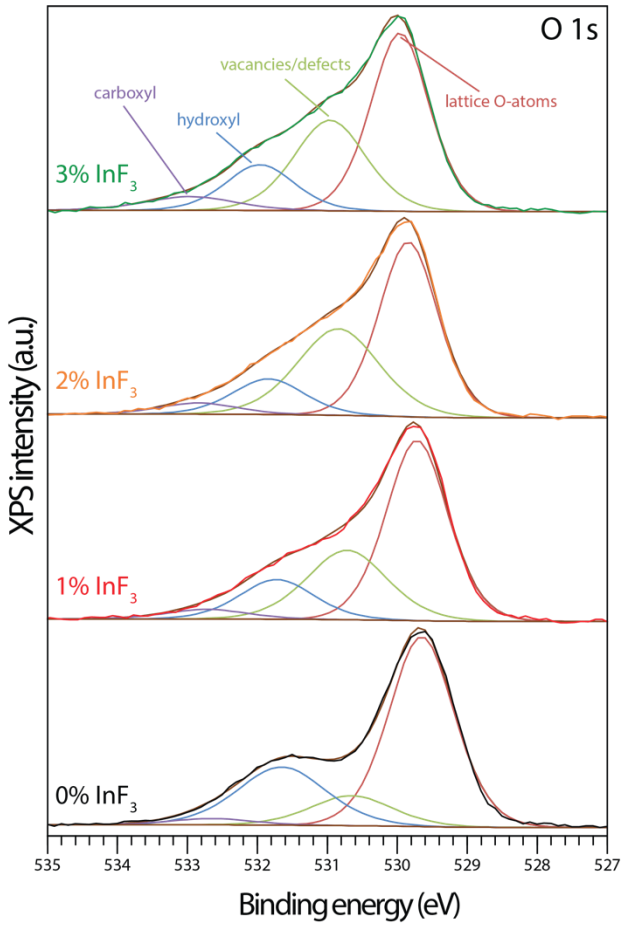

Figure 4.10: XPS Analysis

O 1s XPS spectra for undoped In_2O_3 NCs (black curve), concave cube (red curve), sharp concave cube (orange curve), cube (green curve) F:In_2O_3 NCs. The spectra were further deconvoluted into 530.0 eV, 531.0 eV, 531.8 eV, and 533.1 eV components assignable to lattice oxygen (red), oxygen adjacent to oxygen vacancies or other defects (green), and surface hydroxyl (blue), and carboxyl (purple) oxygen species, respectively.

Fluoride anions have been described as facet-directing agents in metal oxide NCs,[186] such as in the fluorinated synthesis of TiO_2 NCs[162,164] and may also have played

this role in the synthesis of F and Sn co-doped In_2O_3 NCs.[65] Metal fluoride precursors, such as InF_3, decompose into HF in the presence of oleic acid during the reaction, releasing fluoride anions and passivating the In-O surfaces with In-F bonds.[162] Walsh et al.[142] determined through density functional theory (DFT) calculations that for bixbyite In_2O_3, relaxed {111} facets are energetically preferred over oxygen terminated {100} facets ($\gamma_{(111)} < \gamma_{(100)}$). However, surface-passivation by F^- in metal oxide NCs can be expected to alter the energetic sequence of the facets: F^- passivation of the {100} facets results in surface energy inversion ($\gamma_{(111)} > \gamma_{(100)}$).[164] Correspondingly, F^- functions as a favorable {100} facet capping agent over {111} in the bixbyite In_2O_3 NCs, which we expect hinders growth at F^- terminate {100} surfaces due to fewer O sites available for In-OH monomer condensation to occur. We suggest that this directs the synthesis of well-defined F:In_2O_3 cube NCs (3% InF_3) wherein sufficient F^- passivation occurs at the {100} facets.

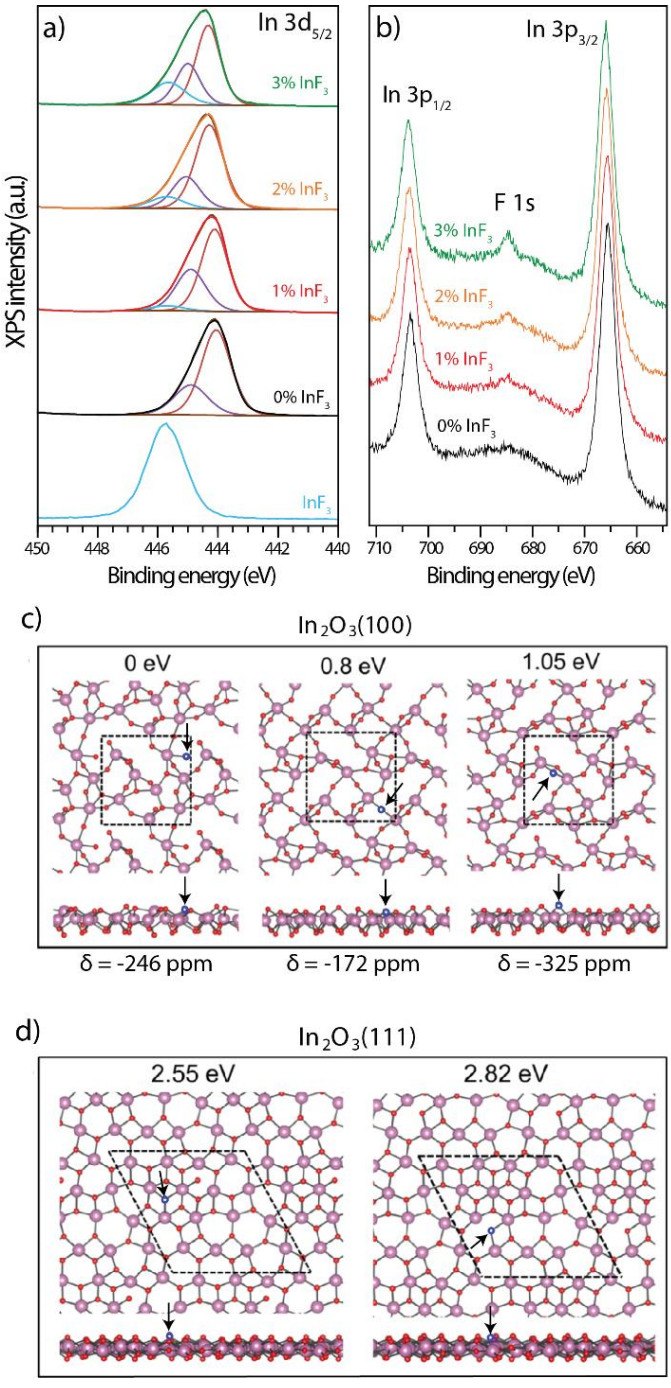
a)
In 3d5/2
3% InF3
2% InF3
1% InF3
0% InF3
InF3
XPS intensity (a.u.)
450 448 446 444 442 440
Binding energy (eV)
b)
In 3p3/2
In 3p1/2
F 1s
3% InF3
2% InF3
1% InF3
0% InF3
710 700 690 680 670 660
Binding energy (eV)
c)
In2O3(100)
0 eV
0.8 eV
1.05 eV
δ = -246 ppm
δ = -172 ppm
δ = -325 ppm
d)
In2O3(111)
2.55 eV
2.82 eV

Figure 4.11: F incorporation in the F:In_2O_3 NCs by XPS and DFT

(a) In $3d_{5/2}$ XPS showing the contributions of various components (red = In-O, purple = In-OH and blue = In-F), and (b) F 1s XPS (along with In 3p) for undoped In_2O_3 NCs (black curve), concave cubes (red curve), sharp concave cubes (orange curve), and cubes (green curve). Note that the In-F component (blue curve in panel a) increases in intensity as the InF_3 concentration used during synthesis is increased. In $3d_{5/2}$ spectrum for InF_3 is shown for reference (blue curve, bottom). DFT calculated top and side views of an F atom substituting O on (c) (100) surface, and (d) (111) surface. Red: O; Purple: In; Blue: F (marked with arrow). For clarity, only the top In layer and the coordinated O and F are shown. The number on top of each panel shows the corresponding formation energy of the F/O substitution (see SI) with respect to the most stable configuration (c, left). δ_{iso} is the calculated NMR isotropic chemical shift. Only low energy structures for each surface are shown.

To understand the surface effects of fluorine on the morphology of In_2O_3, DFT calculations were conducted (details in SI, Text A4.1) by calculating relative formation energies of F substituting at surface O atomic sites on (100) and (111) surfaces. The (111) surface was selected for comparison with (100) as it has been reported to have the lowest surface energy in In_2O_3 without F doping.[142] All possible F substitution sites were considered, and only the low formation energy surface configurations are shown in Figure 4.11 c and d. F substitution is more energetically favorable on the (100) surfaces than the (111) surfaces, with F substitution at (111) surfaces yielding formation energies (2.55 eV, 2.82 eV) that are higher than the (100) surface configurations. Since growth through monomer deposition requires addition of new In and O atoms on oxygen

terminated sites,[205] it can be expected that this process is more difficult at fluorine capped (100) surfaces than on (111) surfaces. This explains why the (100) facets grow more slowly and become the dominant NC surface. NMR chemical shifts of ^{19}F atoms in different configurations on the (100) surface are calculated, with the most stable structure (Figure 4.11 c, left) corresponding to a chemical shift of -246 ppm, to be compared below to experimental ^{19}F NMR spectra.

The complex concave cube shape of moderately passivated F:In_2O_3 NCs (1% InF_3) can be rationalized through the shape control model previously described for other halide-passivated NCs.[9,186] Colloidal syntheses of NCs involve both thermodynamic and kinetic effects that impact NC shape. The conceptual framework involves two monomer addition processes: deposition on facets with high surface energy (kinetic) and monomer surface diffusion to minimize total surface energy of NC facets (thermodynamic).[6] The high rate of In-OA precursor decomposition, driven by aminolysis, leads to a high rate of monomer deposition onto growth-favorable NC facets at a short reaction time (5 min). During fluorine-free synthesis, undoped In_2O_3 NCs exhibit growth in all <100>, <110>, and <111> directions into irregularly shaped NCs (Figure 4.1 a, leftmost panel). With intermediate InF_3 concentrations (1-2% InF_3), the {100} facets are partially capped by F^-, and In monomer deposition becomes unfavorable on {100} facets with more F^- capped sites. Instead, the reaction conditions are favorable for selective monomer deposition on the less F^- surface occupied {111} facets. Thus, F^- passivated {100} facets have slower growth and monomers preferentially deposit on {111} facets during NC growth.[145] Through this process, elongated <111> direction tips are seen in F:In_2O_3 concave cube NCs (1% InF_3), with concave {100} facets (Figure 4.1 a, second from left). Well-defined concave cube F:In_2O_3 NCs of 290.4 ± 17.9 nm size with sharp elongated <111> corners result when using a 2% InF_3 precursor content, showing distinct high-index quadrant

boundaries on the {100} facets (Figure 4.1 a, second from right). With higher InF_3 concentration (3% InF_3), the {100} facets become increasingly passivated by F^- capping, fluorine terminated {100} surface exposure is favored for minimizing total surface energy, and well-defined cube-shaped NCs result.

Since metal oxide NC growth through monomer deposition requires addition of new In and O atoms on oxygen terminated sites, the observed NC growth in higher InF_3 precursor ratio reaction is expected to be slower due to fluorine termination on the NC surfaces. This slower growth leads to the smaller NC size in 3% InF_3 compared to 1% InF_3 throughout the growth aliquot observed in Figure 4.6. Due to aggregative nucleation,[4] we rationalize that the aggregative nuclei is also less prone to cohesion due to fluorine passivation of oxygen terminated NC nuclei surface. A higher InF_3 precursor would lead to smaller size seeds and indicate larger number of nuclei. NC aliquot size in Figure 4.6 (0 min in Figure 4.6) is smaller in 3% InF_3 growth (35.6 nm) compared to a lower level of 1% InF_3 precursor (81.8 nm).

Although the XRD and electron diffraction patterns indicate substantial long- and short-range lattice order in the $F:In_2O_3$ NCs, the non-stoichiometric distributions of fluorine species introduce significant and important complexity to the NC structures that govern their growth and optical properties. The types, distributions, and electronic environments of fluorine atoms in $F:In_2O_3$ NCs are established by solid-state ^{19}F MAS NMR analyses. The solid-state 1D ^{19}F MAS NMR spectrum of $F:In_2O_3$ NCs (3% InF_3) in Figure 4.12 a reveals four resolved ^{19}F signals at 50, -50, -208, and -234 ppm, which are assigned on the basis of the 2D $^1H\{^{19}F\}$ NMR correlation spectrum and ^{19}F spin-lattice relaxation time analyses discussed below to ^{19}F nuclei in different types of chemical and electronic environments in the $F:In_2O_3$ NCs.

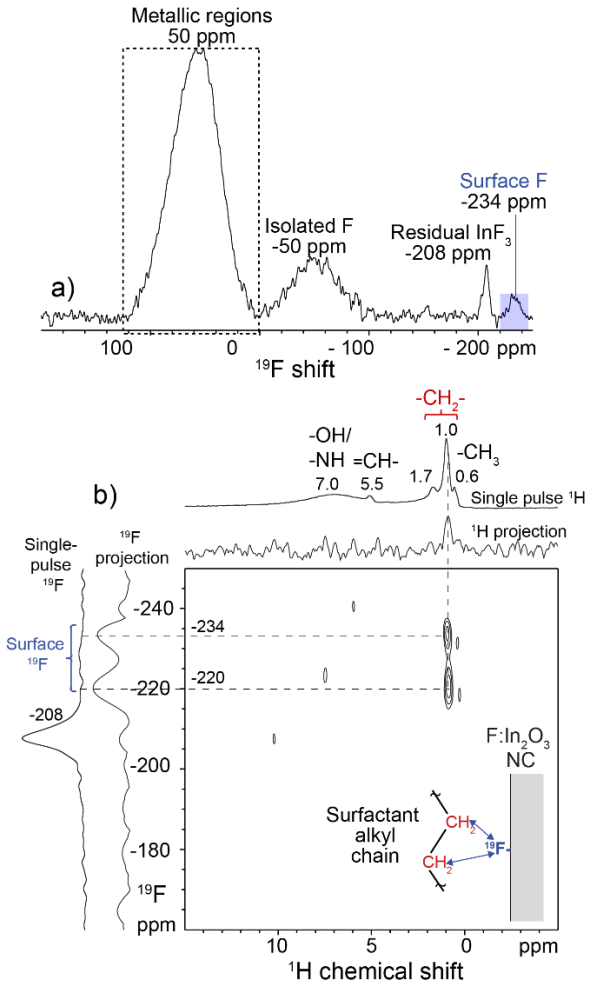

Figure 4.12. Solid state ^{19}F and 2D $^{1}H\{^{19}F\}$ correlation NMR spectra of $F:In_2O_3$ NCs

Solid state (a) 1D ^{19}F echo and (b) 2D $^{1}H\{^{19}F\}$ correlation MAS NMR spectra of $F:In_2O_3$ NCs (3% InF_3) diluted in 1:1 ratio by mass with KBr. Solid state 1D single-pulse ^{1}H and ^{19}F spectra acquired under the same conditions are shown along the horizontal and vertical axes of the 2D spectrum in (b) for comparison with the 1D projections. The inset shows a schematic diagram of a surface ^{19}F moiety interacting with the alkyl chain of a surface-bound organic ligand, as indicated by arrows. The spectra were acquired at 9.4 T, (a) 35 kHz MAS and 395 K or (b) 25 kHz MAS and 327 K.

Importantly, dilute surface fluorine moieties are detected and identified in the solid-state two-dimensional (2D) $^{1}H\{^{19}F\}$ correlation NMR spectrum in Figure 4.12 b. The spectrum is shown as a 2D contour plot, having ^{1}H and ^{19}F frequency axes (with units of ppm) on the abscissa and ordinate, respectively. Correlated signal intensities in the 2D spectrum arise only from ^{1}H species that are dipole-dipole-coupled with ^{19}F atoms over nanoscale distances (<0.5 nm for the short dipolar recoupling time, 0.96 ms, used here), thereby establishing the mutual proximities of the ^{1}H and ^{19}F species with associated signals. For comparison, a standard 1D ^{1}H MAS NMR spectrum is shown above the ^{1}H axis of the 2D spectrum, which exhibits signals at 0.6, 1.0, 1.7, 5.5, and 7.0 ppm that are all assigned to ^{1}H moieties on the octylamine, trioctylamine, or oleate organic surfactant molecules as indicated by the labels above the respective ^{1}H signals. The 2D $^{1}H\{^{19}F\}$ correlation spectrum resolves two ^{19}F signals at -234 and -220 ppm that are correlated to ^{1}H signals at 1.0 ppm from $-CH_2-$ moieties on the organic surfactant molecules, unambiguously establishing the interactions and proximities of the corresponding ^{1}H and ^{19}F species at the $F:In_2O_3$ particle surfaces. Notably, no correlated signal intensity is observed for the relatively narrow ^{19}F signal at -208 ppm (6 ppm full-width-half-maximum, FWHM), which is assigned to residual InF_3 precursor species.[206] Furthermore, while ^{1}H signal intensity is detected in 1D $^{1}H\{^{19}F\}$ NMR spectra acquired with ^{19}F excitation at -210 ppm, the same excitation frequency used to acquire the 2D spectrum in Figure 4.12 b, no ^{1}H signal intensity is detected for ^{19}F excitation at different frequencies (Figure 4.13). These results indicate that only the ^{19}F signals in the -220 to -234 ppm frequency range correspond to ^{19}F surface species, and that the other types of ^{19}F environments detected in the 1D ^{19}F MAS NMR spectra in Figure 4.12 a are located in sub-surface environments, within the detection limits of the NMR measurements.

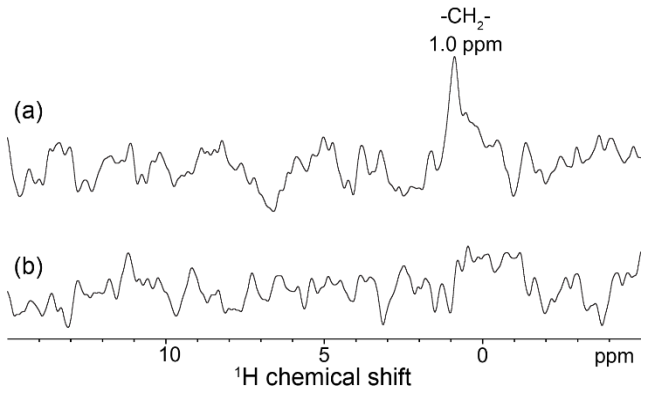

Figure 4.13: Solid-State ^{19}F and ^{115}In NMR

Solid-state 1D $^{1}H\{^{19}F\}$ MAS NMR spectra of F:In_2O_3 NCs (3% InF_3) diluted in 1:1 ratio by mass with KBr (the same sample as Figures 4.4 and 5.2), acquired at 9.4 T, 25 kHz MAS, at a sample temperature of 327 K, and with ^{19}F excitation at (a) -210 ppm, near the ^{19}F signals from InF_3 and surface In-F moieties, the same excitation frequency used to acquire the 2D $^{1}H\{^{19}F\}$ correlation spectrum in Figure 4.12 b, and (b) 20 ppm, near the ^{19}F signals from F^- anions incorporated into the In_2O_3 lattice. No ^{1}H signal intensity is detected in the spectrum in (b), indicating that the F^- species embedded in the In_2O_3 lattice are not within nanoscale proximity of ^{1}H moieties on the organic surfactant molecules, within the detection limits of the measurement.

From the quantitative single-pulse 1D ^{19}F MAS NMR spectrum (Figure 4.14), the ^{19}F signals in the frequency range from -220 to -234 ppm account for only 1-2% of all the ^{19}F signal intensity, indicating that <2% of all of the ^{19}F species in the F:In_2O_3 NCs are in surface environments. These surface-related ^{19}F signals in the range of -220 to -234 ppm are close to the shift values predicted by DFT calculations for the most energetically

stable ^{19}F structure on the (100) surface (-246 ppm, Figure 4.11 c, left). While the DFT models neglect other possible adsorbates for computational simplicity and represent an idealized subset of numerous possible surface configurations, this agreement suggests that the DFT calculations capture the main effects of fluorine on the (100) surface. The combined solid-state 1D ^{19}F and 2D $^{1}H\{^{19}F\}$ NMR analyses and DFT calculations, thus identify and quantify the small fraction of ^{19}F species at the surfaces of the F:In_2O_3 NCs that are hypothesized to direct the NC morphology by adsorbing on (100) facet surface sites.

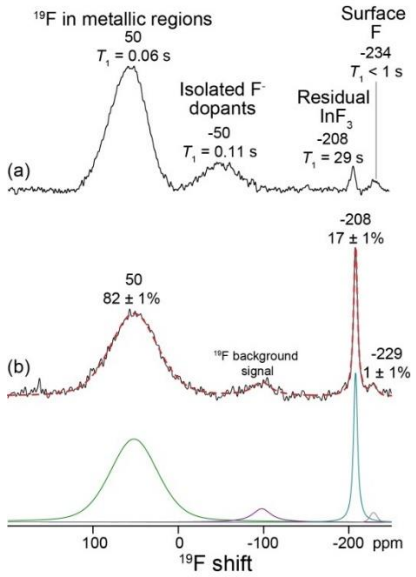

Figure 4.14: Quantitative ^{19}F MAS NMR Spectra

Solid state 1D (a) ^{19}F echo (same as Figure 4.12 a) and (b) quantitative single-pulse ^{19}F MAS NMR spectra of F:In_2O_3 (3% InF_3) diluted with KBr in a 1:1 ratio by mass (the same sample as Figures 4.4, 5.2 and A4.10). The spectra were acquired at 9.4 T, 35 kHz MAS, and sample temperatures of 395 K. The ^{19}F spin-lattice T_1 relaxation times, measured under the same conditions, are given under the respective signal labels in (a). The dotted red line in (b) is the simulated ^{19}F spectrum, with the deconvolution shown offset below. The relative integrated signal intensities are shown above the corresponding signals. The ^{19}F signal at -50 ppm from isolated F^- dopant species is not detected or resolved in the quantitative 1D single-pulse ^{19}F spectrum in (b), indicating that the corresponding ^{19}F species comprise <1% of the total amount of fluorine atoms in the material. The relatively weak ^{19}F signal at ca. -100 ppm in (b) is a ^{19}F background signal from Teflon in the MAS NMR probehead, and was not included in the quantification of the ^{19}F NMR signals from the F:In_2O_3 NCs.

Chapter 5: Infrared Plasmonic Response in Nanocubes

FLUORINE AS AN ANIONIC DOPANT.

The discussion regarding fluorine has so far been limited to the NC surface: F^- selectively passivate NC surfaces to influence shape. The possible impact on the crystal lattice when F^- is incorporated into the In_2O_3 NCs is investigated by analyzing XRD as a function of fluorine incorporation. Fluorine being more electronegative than oxygen, and the crystal ionic radius[130] of F^- (1.19 Å) being only slightly smaller than the O^{2-} site (1.28 Å) in bixbyite phase In_2O_3, would allow it to easily occupy oxygen sites.[64,207] XRD patterns (Figure S4.12) of F:In_2O_3 NCs (1-12% InF_3) confirm the cubic bixbyite In_2O_3 crystal structure is maintained[208] and reveal that the F^- doping induces lattice strain. Lattice contraction relative to undoped In_2O_3 NCs is observed based on the shift in the position of the (400) diffraction reflection at low doping level (1% InF_3), which is ascribed to the smaller ionic radius of F^- as a substitutional dopant occupying O lattice sites not only at the surface, but also internal to the NCs (Figure S4.12). Lattice contraction is also observed at low dopant concentrations in Sn:In_2O_3 [115] and F:SnO_2,[207] where it has been similarly ascribed to aliovalent dopants with smaller ionic radii substituting the larger ions in host lattices. Rietveld refinement[209] of the full XRD pattern was conducted to quantify this initial lattice contraction and revealed the subsequent displacements of the (400) and (222) reflections at higher concentrations of F^- doping that correspond to lattice expansion (Figure S4.12). Size-induced lattice expansion or contraction, though reported in sub-10 nm metal oxide NCs, can be excluded due to the large size (100 nm or larger) of the In_2O_3 NCs considered here.[210] Undoped In_2O_3 NCs have a lattice constant of a = 10.126 Å, close to the reported bulk In_2O_3 value of a = 10.119 Å.[211] In low-doped 1% InF_3 concentration NCs, a contracted lattice constant of a

= 10.083 Å was measured. However, lattice expansion occurs at higher dopant concentrations, similar to the structural changes reported in highly doped F:SnO_2 and Sn:In_2O_3 films.[115,212] The (400) reflection shifts with F^- incorporation to a = 10.190 in 12% InF_3 doped NCs, resulting in a maximum observed lattice expansion of 0.58 % that is attributed to dopant-screening effects from electrostatic repulsions.[115] Residual InF_3 is evident by XRD in the F:In_2O_3 NCs prepared with 3-12% InF_3 and can likely be attributed to emergent indium fluoride (InF_3) or indium oxyfluoride (InOF) residuals[213] (Figure 4.15).

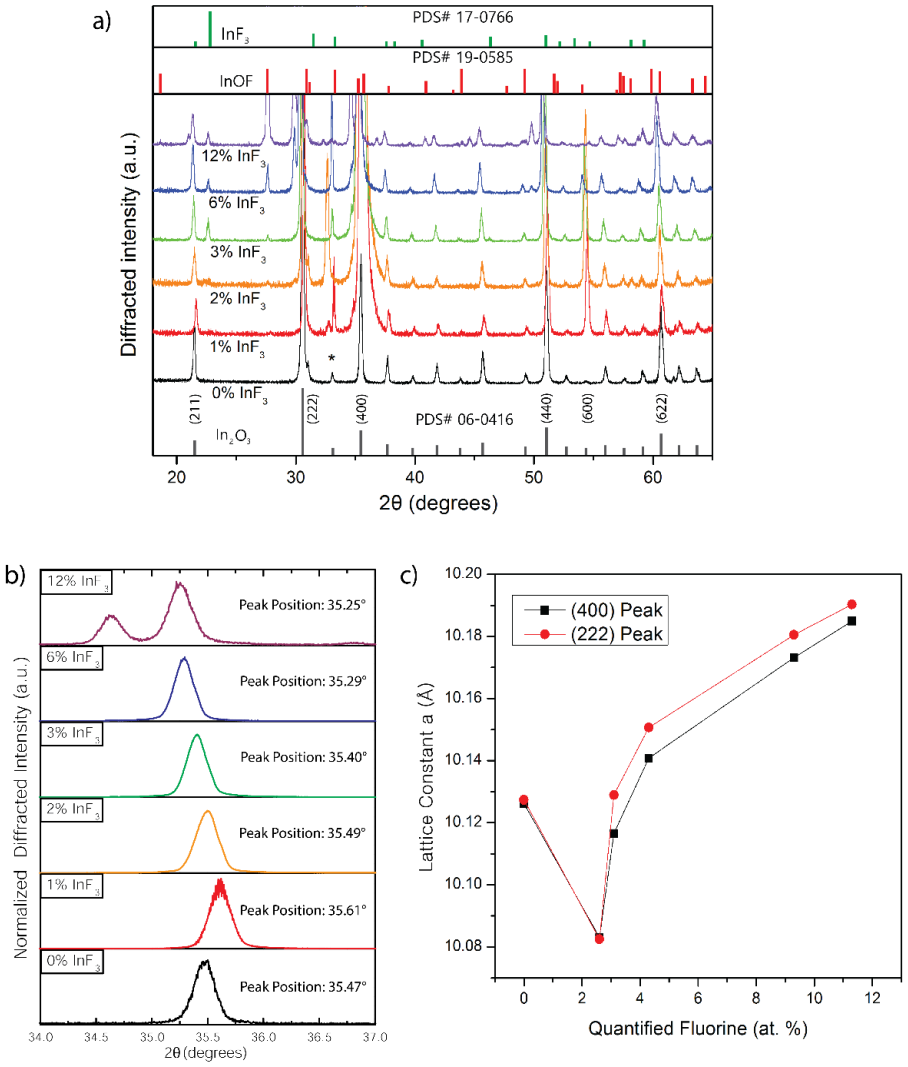

Figure 4.15: F:In_2O_3 XRD patterns

(a) XRD patterns from F:In_2O_3 NCs, with indium oxide (In_2O_3) PDS# 06-0416, indium fluoride (InF_3) PDS# 17-0766, and indium oxide fluoride (InOF) PDS# 19-0585 references. Asterisk denotes silicon substrate peak. (b) XRD patterns showing the shift of the (400) diffraction peak with InF_3 addition. (c) Rietveld refined[209] XRD lattice constant shift correlated with fluorine incorporation quantified by EDX.

To further understand the fluorine incorporation in the synthesized NC lattice, TGA was performed, as fluorine is known to diffuse out of NCs during high temperature annealing under inert conditions.[214] TGA analysis shows initial weight loss starting at 400 °C that is ascribed to the removal of organic ligands. Upon further heating to 1100 °C, F:In_2O_3 cubes exhibit 1.3% weight reduction by fluorine liberation (Figure 5.1), corresponding to F/In = 9.6 % atomic composition ratio. This TGA-based quantification agrees well with F/In = 10.3 % quantified by TOF-SIMS. Concave F:In_2O_3 cubes show a 0.5 % mass reduction corresponding to F/In = 3.7 %, whereas undoped In_2O_3 NCs shown little or no weight loss that could be associated with fluorine when heated to high temperatures. SEM images reveal the F:In_2O_3 cube NCs sinter into irregularly shaped massive particles during high temperature annealing (Figure S4.13).

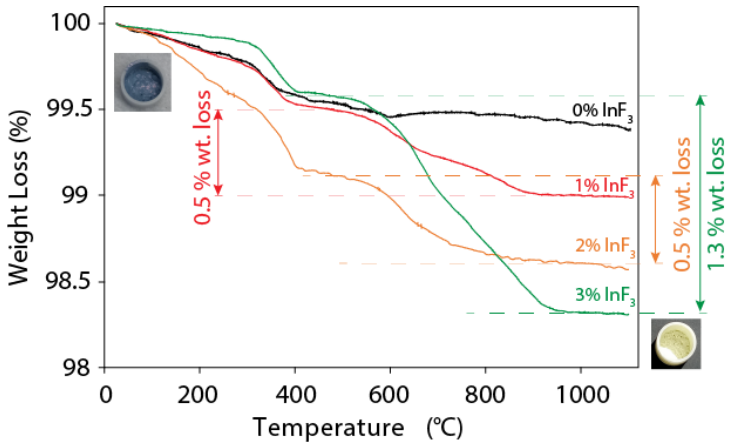

Figure 5.1. TGA curves of F:In_2O_3 NCs

TGA curves for undoped In_2O_3 NCs (black curve), concave F:In_2O_3 cubes (red curve), sharp concave F:In_2O_3 cubes (orange curve), and F:In_2O_3 cubes (green curve). Photographs of the F:In_2O_3 cube sample (in alumina crucible) before (left inset) and after TGA (right inset).

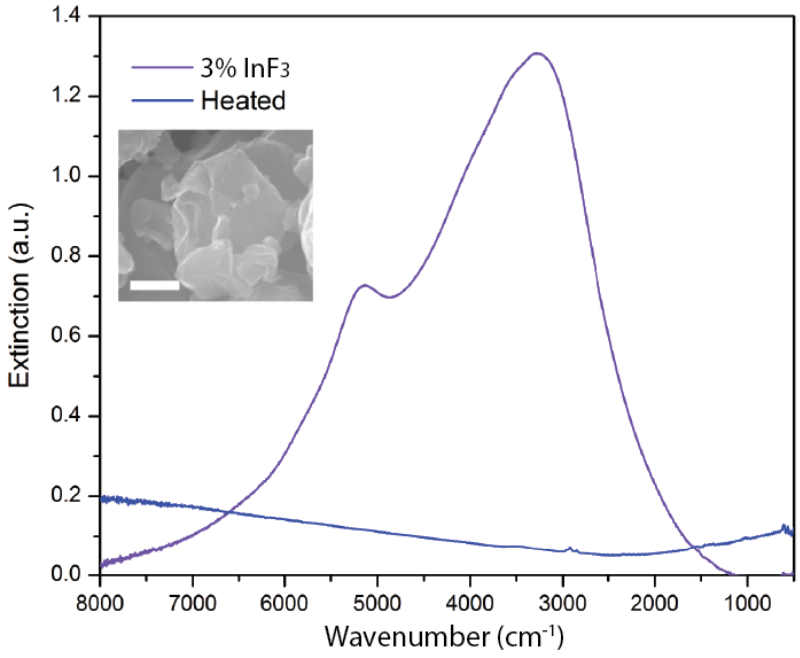

Figure 5.2: F:In_2O_3 Cube NC TGA

KBr pellet sample FTIR spectra. F:In_2O_3 cube NC (3% InF_3) (purple), compared to F:In_2O_3 cube TGA sample (inset) heat treated at 1100 °C to remove fluorine (blue). Inset scale bar is 200 nm. LSPR peak position is observed to red-shift in higher refractive index KBr as compared to tetrachloroethylene medium.

Substitutional fluorine dopants incorporated in the NCs can be charge-compensated by free electrons. Fluorine is well-established as an anionic n-type dopant that induces high free electron concentrations in fluorine-doped tin oxide (F:SnO_2) transparent conductive oxide films.[189,207] The Kröger-Vink equation[215] for oxygen vacancy formation demonstrates that such defects in the In_2O_3 lattice can be charge compensated by two electrons (eq. 1).[216] Oxygen substitution by F induces one free electron per fluorine ion (eq. 2).[217,218]

$$In_{In}^{\times} + O_O^{\times} \rightarrow In_{In}^{\times} + V_O^{\bullet\bullet} + 2e' + \frac{1}{2}O_{2\,(g)} \quad (1)$$

$$In_{In}^{\times} + 3O_O^{\times} \xrightarrow[InF_3]{} 2In_{In}^{\times} + 3F_O^{\bullet} + 3e' + \frac{3}{2}O_{2\,(g)} \quad (2)$$

Band structure derived from DFT calculations predicts an elevated Fermi level when fluorine substitutes oxygen in In_2O_3, as compared to undoped In_2O_3. Fermi level is calculated to be 1.1 eV above the conduction band minimum (Figure 5.4) with presence of F dopants in the In_2O_3 lattice unit cell (F:O = 1:47), due to free electron carriers contributed to the conduction band, which leads to LSPR optical properties in F:In_2O_3 NC cubes. Electron paramagnetic resonance (EPR) spectroscopy provides evidence for free electrons in F:In_2O_3 NCs. The induced extra electrons are delocalized in the conduction band,[219,220] leading to an observed EPR signal at $g \approx 2.20$ in doped F:In_2O_3 cubes. By comparison, undoped In_2O_3 NCs exhibit a weak EPR signal at $g \approx 2.00$ due to a low population of oxygen vacancy-induced free electrons or shallow donors (Figure 5.3).[221,222] EPR spectra of the F:In_2O_3 cubes at cryogenic temperatures (100 K) showed increased signal intensity, which decreased at room temperature due to rapid free electron relaxation.[124]

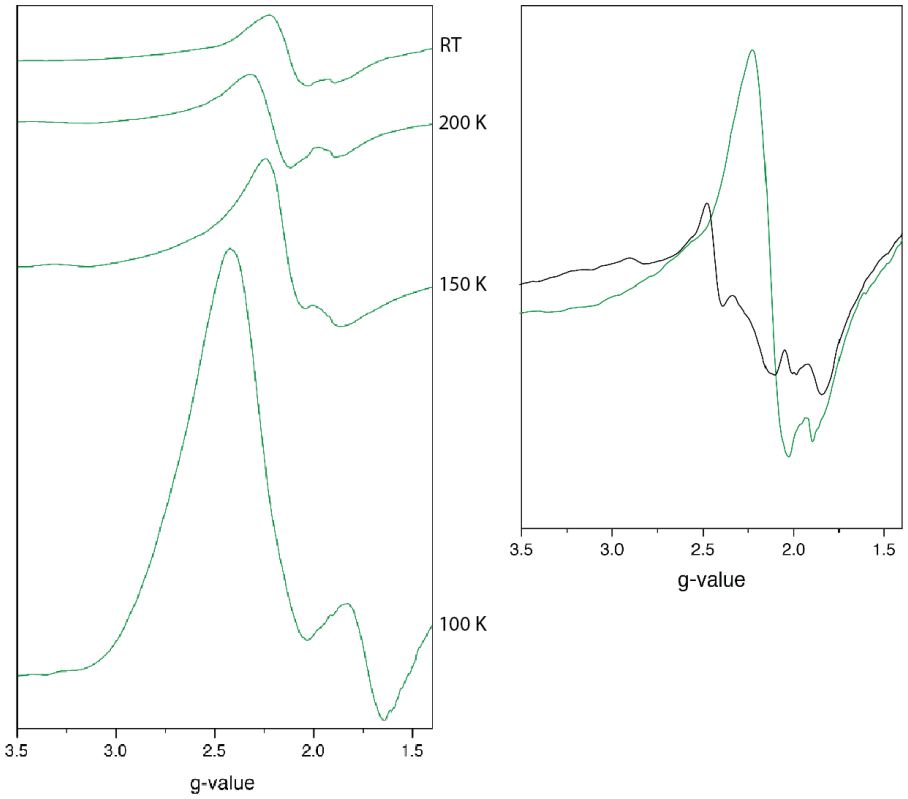

Figure 5.3: EPR Spectra

Temperature dependent X-band EPR spectra of (left) F:In_2O_3 cube NCs (3% InF_3), and (right) room temperature (RT) EPR spectrum F:In_2O_3 cube NC (3% InF_3) (green) and undoped In_2O_3 NCs (black).

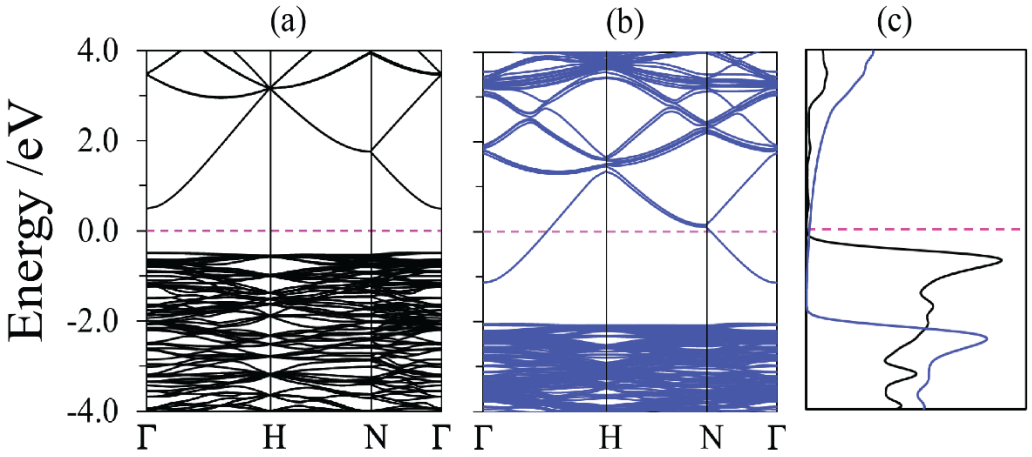

Figure 5.4: Undoped In_2O_3 and F-doped In_2O_3 Band Structure

Band structures of (a) undoped In_2O_3 and (b) F-doped In_2O_3 (at the concentration of F : O = 1 : 47 by number of atoms). (c) Electronic density of states in undoped In_2O_3 (black lines) and F-doped In_2O_3 (blue lines), where Fermi level is set to zero. In F-doped In_2O_3 (F : O = 1 : 47), the Fermi level is 1.1 eV above the conduction band minimum.

Kröger-Vink notation suggests halogen dopants with the same valency as F^-, should contribute to free-electron compensation. However, the large ionic radii of chloride (Cl^-) or bromide (Br^-) suggests that they are not suitable dopants to incorporate in In_2O_3 NCs. Doping of Cl or Br atoms into In_2O_3 NCs was attempted to check the viability of other halogen dopants. EDX quantification showed very low halide incorporation for these NCs, as compared to F:In_2O_3 NCs synthesized at the same dopant precursor concentration (3% InX_3, X= F, Cl, Br) (Table 5.1). Cl:In_2O_3 NCs show only Cl/In = 0.32 ± 0.11 % atomic composition ratio and Br:In_2O_3 NCs had Br/In = 2.62 ± 0.06 %, whereas F:In_2O_3 cubes show higher F/In = 11.76 ± 2.70 %. The low anionic dopant concentration observed can be attributed to Cl^- (1.81 Å) having a much larger

ionic radius than F^- (1.19 Å), which would yield a correspondingly large ionic radius mismatch (41.4 %) with O^{2-} (1.28 Å) and cause significant lattice strain in the host lattice.[130] Similarly, Br^- (1.96 Å) is not incorporated within the In_2O_3 NC lattice, consistent with similar straining (53.1 %).[130]

Based on quantitative 1D ^{19}F MAS NMR and ^{19}F spin-lattice relaxation time analyses, the majority of ^{19}F atoms in the F:In_2O_3 NCs are located in metallic sub-surface environments. The 1D ^{19}F MAS NMR spectrum in Figure 4.12 a shows two broad ^{19}F signals at 50 ppm and -50 ppm with FWHM signal linewidths of 66 ppm and 26 ppm, respectively. The ^{19}F signal at -50 ppm is similar to ^{19}F signals observed for some other metal oxyfluorides[223–225] and is assigned to isolated F^- anionic dopant species in the F:In_2O_3 NCs. By comparison, based on temperature-dependent analyses of ^{19}F spin-lattice (T_1) relaxation times, the ^{19}F signal at 50 ppm is confidently assigned to a distribution of ^{19}F species in metallic environments in the F:In_2O_3 NCs. In metallic materials, including degenerately doped semiconductors,[226] nuclear spins and conduction band electrons in *s*-like orbitals couple through Fermi contact interactions. These interactions give rise to two characteristic effects that are manifested in the ^{19}F NMR spectra of F:In_2O_3 NCs: a frequency displacement of the ^{19}F NMR signals called the Knight shift,[226–228] and a Korringa-type temperature-dependence of the rate of ^{19}F nuclear spin-lattice relaxation.[227,229,230] For the ideal case of isolated nuclear spins coupled to a degenerate gas of electron spins, the Korringa contribution to the relaxation rate, $T_{1,K}^{-1}$, is related to the Knight shift, K, by the well-known Knight-Korringa relation:[227,229]

$$T_{1,K}^{-1}(K,T) = \left(\frac{\gamma_n}{\gamma_e}\right)^2 \frac{4\pi k_B T}{\hbar} K^2 \qquad (3)$$

where γ_n and γ_e are the gyromagnetic ratios of the nuclear and electron spins, respectively, k_B and $\hbar$ are the Boltzmann and Planck constants, and T is the absolute temperature.

The Knight-Korringa relation shows that the $T_{1,K}^{-1}$ values for nuclear spins in metallic environments are proportional to both temperature, T, and the square of the Knight shift, K^2. Fluorine species in metallic environments may therefore be identified on the basis of analysis of the ^{19}F T_1^{-1} values as functions of both NMR frequency position and temperature.

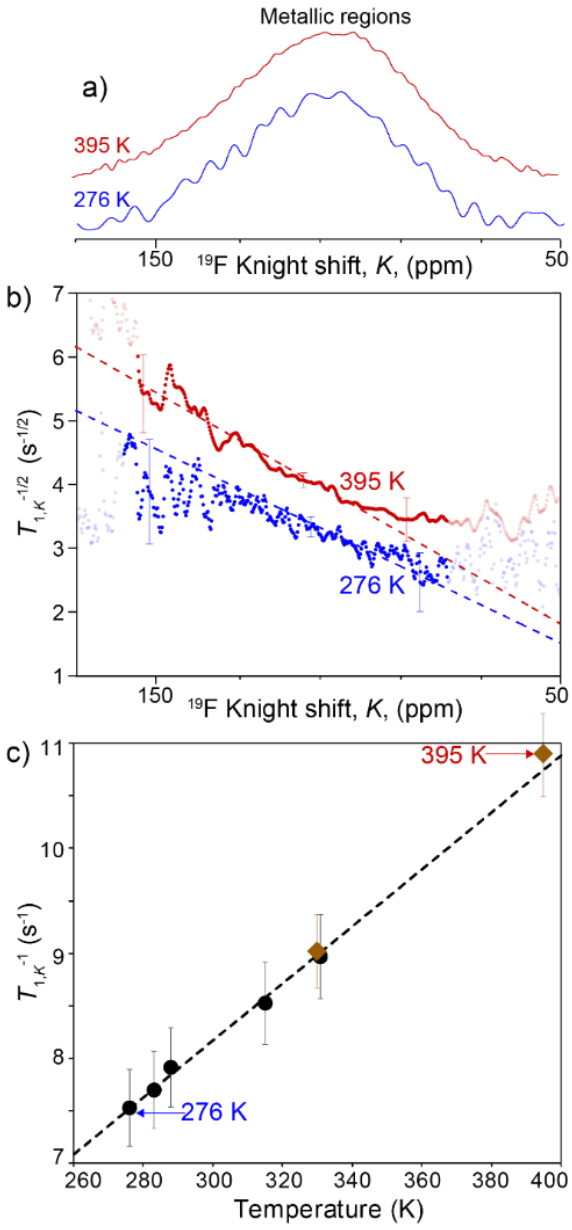
Metallic regions
a)
395 K
276 K
150
^{19}F Knight shift, K, (ppm)
50
b)
$T_{1,K}^{-1/2}$ ($s^{-1/2}$)
395 K
276 K
150
^{19}F Knight shift, K, (ppm)
50
c)
$T_{1,K}^{-1}$ (s^{-1})
395 K
276 K
Temperature (K)

Figure 5.5: Knight-shifted ^{19}F MAS NMR spectra of F:In_2O_3 NCs

(a) Enlargement of the Knight-shifted ^{19}F spectral region (boxed region in Fig. 4a) showing a comparison of the 1D solid-state ^{19}F echo MAS NMR spectra of F:In_2O_3 NCs (3% InF_3) diluted in 1:1 ratio by mass with KBr. The frequency axis is renormalized with the zero Knight shift peak at -50 ppm, corresponding to the signal from isolated F^- dopants in the F:In_2O_3 NCs. The spectra were acquired at 9.4 T, 35 kHz MAS and 395 K (red) and 25 kHz MAS and 276 K (blue). (b) Plot of the square root of the ^{19}F spin-lattice relaxation rate due to Korringa relaxation, $T_{1,K}^{-1/2}$, for different ^{19}F Knight shifts K in F:In_2O_3 NCs (3% InF_3), measured at 9.4 T, 35 or 25 kHz MAS, and at 395 K (red) or 276 K (blue). Partially transparent data points correspond to spectral regions with little or no ^{19}F signal intensity, resulting in large uncertainties that are not pertinent to the analyses. (c) Plot of the ^{19}F $T_{1,K}^{-1}$ at the peak maximum of the Knight shift distribution (K = 100 ppm) as a function of temperature. Black circles and brown diamonds indicate $T_{1,K}^{-1}$ values measured under MAS conditions of 25 kHz and 35 kHz, respectively. The dashed lines in (b) and (c) indicate theoretical values obtained from the Knight-Korringa equation (eq. 3).

Analyses of the 1D ^{19}F MAS NMR spectra and T_1^{-1} relaxation rates at temperatures of 276-395 K, shown in Figure 5.5, reveal that the broad ^{19}F signal at 50 ppm in Figure 4.1 a corresponds to ^{19}F dopant atoms in metallic environments within the F:In_2O_3 NCs that exhibit Korringa-type relaxation behavior. By comparison, the ^{19}F signal at -50 ppm, which also manifests a broad distribution of ^{19}F environments, exhibits no Korringa-type temperature-dependencies in its spin-lattice relaxation behavior, consistent with its assignment to a distribution of isolated ^{19}F dopants in the In_2O_3 lattice

that experience chemical and/or paramagnetic shifts, but not metallic Knight shifts. The ^{19}F frequency axis in Figure 4.12 a is renormalized in Figure 5.5 a such that the signal from isolated F^- dopant species (-50 ppm in Figure 4.12 a) is set to a Knight shift K of 0 ppm. As shown in Figure 5.5 a, the broad ^{19}F signal distribution at K = 100 ppm (50 ppm in Figure 4.12 a) from ^{19}F species in metallic environments does not change significantly in width or position over the temperature range 276-395 K, consistent with the expected temperature-invariance of Knight shifts for heavily-doped semiconductors with Fermi level above conduction band minimum (Figure 5.4).[227] The ^{19}F T_1^{-1} values were measured by ^{19}F saturation recovery experiments, and the $T_{1,K}$ values for each isochromat across the ^{19}F Knight-shifted signal distribution were extracted by subtraction of the temperature-independent contribution ($T_{1,0}^{-1}$) from the overall relaxation rate, T_1^{-1}:

$$T_{1,K}^{-1}(K,T) = T_1^{-1}(K,T) - T_{1,0}^{-1} \quad , \quad (4)$$

The temperature- and shift-independent term $T_{1,0}^{-1}$ depends on the MAS rate and was measured to be 6.9 ± 0.3 s^{-1} at 25 kHz MAS and 4.8 ± 0.5 s^{-1} at 35 kHz MAS. Due to the MAS dependence of $T_{1,0}^{-1}$, this term likely reflects the contribution to the ^{19}F T_1^{-1} relaxation rate of strong ^{19}F-^{19}F and/or ^{19}F-electron dipole-dipole couplings, which are partially averaged under MAS conditions. Additional details on the ^{19}F T_1 relaxation analyses and the extraction of the $T_{1,0}^{-1}$ and $T_{1,K}^{-1}$ terms are provided in the Supporting Information (Figure 5.6). The square root of the temperature-dependent relaxation term, $T_{1,K}^{-1/2}$, is plotted as a function of K for the K = 50 to 175 ppm region (boxed region in Figure 4.12 a) in Figure 5.5 b. At temperatures of 395 K (red) and 276 K (blue), the measured $T_{1,K}^{-1/2}$ values show excellent agreement across the entire ^{19}F Knight shift distribution with the theoretical values predicted by the Knight-Korringa expression at the different temperatures (dotted lines), which notably has no adjustable parameters and is derived from first principles.[226,227,229] Additionally, the Knight-Korringa relation holds

across the entire temperature range of 276-395 K. The Korringa-type plot in Figure 5.5 c shows a plot of the $T_{1,K}^{-1}$ values extracted at the maxima of the ^{19}F Knight shift distribution (K = 100 ppm), as a function of temperature, revealing excellent agreement with the Knight-Korringa relation over the entire temperature range. This corroborates the conclusion that the broad ^{19}F signal at 50 ppm in Figure 4.12 a arises from a distribution of Knight shifts that manifest a range of couplings of ^{19}F nuclei to conduction band electrons in regions of the F:In_2O_3 NCs with different extents of metallic character. The ^{19}F atoms, acting as anionic n-type dopants, therefore are sufficiently dense that their associated unpaired electrons form a conductive network within the heavily-doped In_2O_3 lattice.

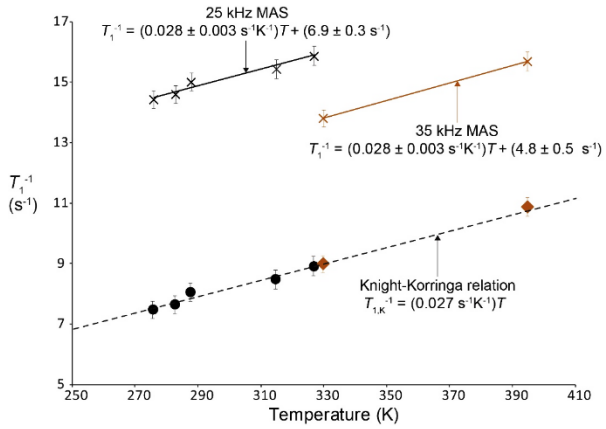

Figure 5.6: Knight-Korringa Relation

Plot of the experimental ^{19}F T_1^{-1} values (X symbols) measured at the peak maximum of the Knight shift distribution (K = 100 ppm) as a function of temperature. The black and brown data points were measured under MAS conditions of 25 and 35 kHz, respectively. The black and brown solid lines are linear fits to the data points, with the corresponding equations shown. The slopes of the linear fit equations are within experimental error of the slope predicted from the theoretical Knight-Korringa relation (black dashed line), and the intercept

values are the temperature-independent $T_{1,0}^{-1}$ values for the different MAS conditions. The black circles and brown diamonds are the experimental data points corrected for the temperature-independent $T_{1,0}^{-1}$ terms (same points as in Figure 5.5 c), which show excellent agreement with the Knight-Korringa relation, as discussed in the text. Error bars were calculated using standard error propagation methods and indicate uncertainties associated with the signal-to-noise ratios of the ^{19}F MAS NMR spectra and the quality of the fits to the ^{19}F saturation-recovery measurements.

Furthermore, based on the quantitative single-pulse ^{19}F NMR spectrum of the F:In_2O_3 NCs (3% InF_3) (Figure 4.14), approximately 82 ± 1% of all of the ^{19}F species are in sub-surface metallic environments in the In_2O_3 lattice, 17 ± 1 % in residual InF_3 which is assigned based on the XRD pattern and long ^{19}F relaxation time (23 s), and <1% at isolated dopant sites in the In_2O_3 lattice. The combined solid-state 2D ^{1}H{^{19}F} NMR correlation and ^{19}F T_1 relaxation analyses establish that only a small percentage (1-2%) of ^{19}F species are at the surfaces of the F:In_2O_3 NCs. The majority of ^{19}F species are incorporated into the F:In_2O_3 NCs in sub-surface metallic domains, consistent with F^- as an anionic dopant within the In_2O_3 lattice.

The metallic domains are also manifested by evidence of conduction band electron influences on local ^{115}In environments in the F:In_2O_3 crystal lattice. Specifically, analyses and comparison of the solid-state wideline ^{115}In NMR spectra in Figure 5.7 of undoped bulk In_2O_3 and F:In_2O_3 NCs show differences that are characteristic of the coupling of ^{115}In nuclei to free electrons. Acquisition of solid-state ^{115}In NMR spectra has been exceedingly challenging in the past due to the highly quadrupolar character of ^{115}In nuclei (I = 9/2), which often exhibit very broad (several MHz) and poorly resolved ^{115}In

NMR signals.[231] Very few solid-state ^{115}In NMR spectra of inorganic materials have been reported, with emphases primarily on materials with ^{115}In atoms in symmetric environments, such as cubic zincblende semiconductors like InP and InN,[232,233] which yield narrower and more tractable lineshapes. Nevertheless, recent wideline NMR techniques enable the detection and analysis of very broad NMR signals, even for quadrupolar nuclei in paramagnetic or conductive materials.[234–236]

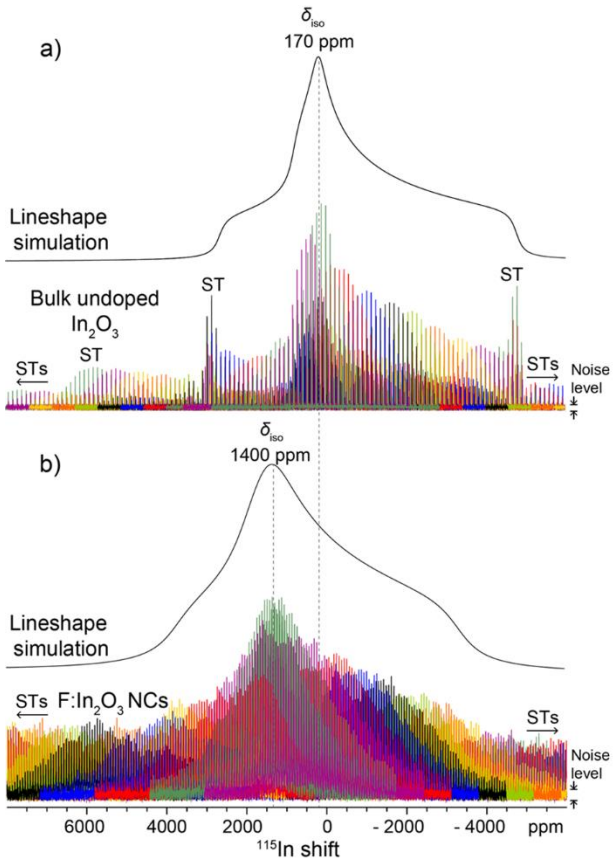

Figure 5.7: Solid-state ^{115}In NMR spectra

Solid-state 1D ^{115}In NMR spectra of (a) undoped microcrystalline In_2O_3 and (b) F:In_2O_3 NCs (3% InF) acquired at 295 K, under static conditions, and at magnetic field strengths of (a) 18.8 T and (b) 19.6 T. The spectra are an overlay of 22 different sub-spectra (shown as different colors) acquired at evenly-spaced frequency intervals. Simulated ^{115}In NMR lineshapes generated using the parameters in Table A4.1 are shown offset above the experimental ^{115}In NMR spectra. Signal intensities arising from ^{115}In satellite transitions are indicated by "ST."

Here, the frequency-stepped quadrupolar Carr-Purcell-Meiboom-Gill (QCPMG) technique[237] was used to measure the solid-state ^{115}In NMR spectra of bulk undoped polycrystalline In_2O_3 and F:In_2O_3 NCs (Figure 5.7). The QCPMG pulse sequence yields manifolds of very narrow, evenly spaced NMR signals (spikelets) that cannot cover the entire ^{115}In spectral range of these materials, but can be systematically acquired as a series that can be overlain to map the full ~2 MHz broad central transition (CT) region of the ^{115}In NMR spectrum. For example, the ^{115}In NMR spectrum in Figure 5.7 a of bulk undoped In_2O_3 is presented as a mosaic overlay of 22 individual QCPMG sub-spectra (plotted in different colors) that were acquired at evenly spaced frequency intervals. Though detailed analysis of the ^{115}In NMR lineshapes is complicated by overlap of the numerous ^{115}In satellite transitions (STs) of the quadrupolar ^{115}In nuclei, the sensitivity and resolution of the wideline ^{115}In QCPMG spectra is sufficient to simulate the ^{115}In CT regions and estimate the quadrupolar coupling constant (C_Q), asymmetry parameter (η), and isotropic shift (δ_{iso}) for the bulk In_2O_3 (Table A4.1). Such NMR parameters are highly sensitive to the chemical and electronic environments of ^{115}In species in In_2O_3 and to our knowledge have never previously been measured or reported.

Compared to bulk In_2O_3, the ^{115}In NMR spectrum of F:In_2O_3 NCs is displaced and broadened, consistent with the coupling of ^{115}In nuclei to unpaired conduction band electrons. Both undoped polycrystalline In_2O_3 (Figure 5.7 a) and F-doped In_2O_3 NCs (Figure 5.7 b) exhibit very broad spectral features in the -4000 to 4000 ppm range that arise from the CT of ^{115}In nuclei in the different materials. The ^{115}In CT regions for both materials are reproduced by a single simulated ^{115}In lineshape with $C_Q \approx 130$ MHz and $\eta = 1$, though with different isotropic shifts (Figure 5.7, black spectra, see also Table A4.1). The bulk undoped In_2O_3 (cubic bixbyite phase by XRD, Figure 5.8) exhibits an isotropic ^{115}In shift of 170 ppm, consistent with diamagnetic ^{115}In environments in the In_2O_3 lattice.

By comparison, the ^{115}In spectrum of F:In_2O_3 NCs (3% InF) exhibits an isotropic ^{115}In shift of 1400 ppm, displaced more than 1200 ppm from the position for diamagnetic In_2O_3. This displacement provides evidence that the majority of ^{115}In species in the F:In_2O_3 lattice experience substantial Knight shifts[226] arising from interactions with unpaired conduction band electrons associated with the F dopant species. The ^{115}In Knight shifts corroborate the ^{19}F NMR and T_1 spin-lattice relaxation time analyses discussed above. The ^{115}In NMR spectrum of the F:In_2O_3 NCs is also broadened compared to that of bulk undoped In_2O_3, indicating a larger distribution of chemical shifts, Knight shifts, and/or quadrupolar parameters (Table A4.1). The continuous distributions of signal intensity extending to higher and lower frequencies in both of the ^{115}In NMR spectra in Figure 5.7 arise from the very broad and overlapping ^{115}In satellite transitions, which are expected to span frequency regions of tens of MHz. To the best of our knowledge, the solid-state ^{115}In NMR spectra presented here are the first ^{115}In NMR analyses of In_2O_3, and evidence the sensitivity of ^{115}In NMR to different electronic environments in technologically important In_2O_3 materials.

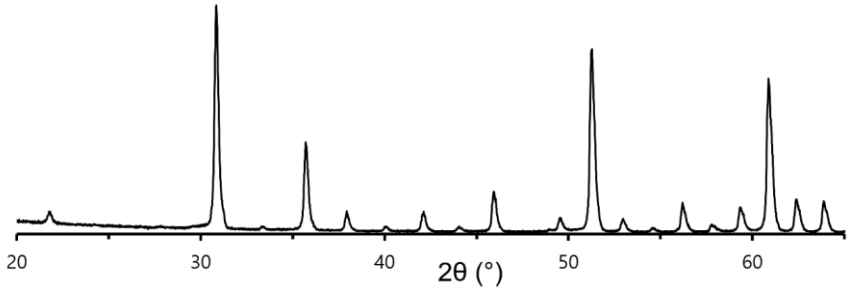

Figure 5.8: XRD Pattern of Undoped Bulk In_2O_3

XRD pattern of the bulk undoped In_2O_3 material measured by solid-state ^{115}In NMR (same sample as Figure 5.7). All reflections are indexable to cubic bixbyite In_2O_3.

In summary, the solid-state ^{19}F and ^{115}In NMR analyses together provide complementary and consistent evidence for metallic ^{19}F and ^{115}In environments in the heavily-doped F:In_2O_3 lattice. Free electrons at conduction band and spatially internal to F:In_2O_3 NCs interact with nuclear spin of extrinsic dopant (F), and host element (In) composing NC lattice. This gives rise to consistent effects manifested in degenerately doped semiconductors, including ^{19}F NMR signal Knight shift, supported with Korringa-type temperature dependent nuclear spin-lattice relaxation.

OPTICAL PROPERTIES

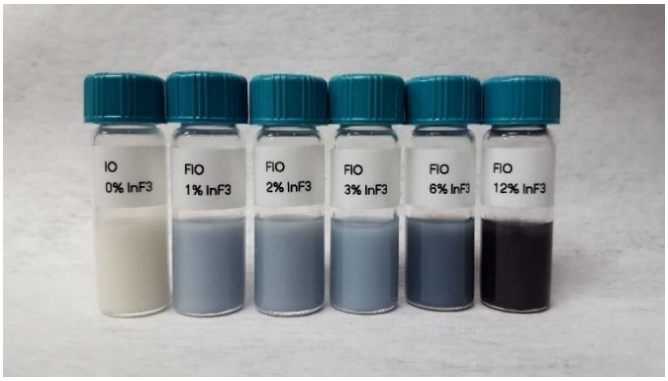

Figure 5.9: Photograph of NC Dispersions

In_2O_3 and F:In_2O_3 NCs dispersed in toluene (10 mg/ml, average product yield: 54.3%) colloidally synthesized with InF_3 dopant precursor ratio (0%, 1%, 2%, 3%, 6%, 12% InF_3) in increasing order, from left to right.

Considerations of charge compensation accompanying fluorine doping (eq. 2) as well as the NMR analyses of the ^{19}F and ^{115}In species show that the anionically doped F:In_2O_3 NCs contain substantial free electron populations leading to LSPR response. By eye, doped F:In_2O_3 NCs in solvent dispersions appear blue, in contrast to clear or white

undoped In_2O_3 NCs (Figure 5.9). Liquid-cell FTIR spectra confirm that the F:In_2O_3 NCs exhibit IR range LSPR, with an absorption tail towards the visible region that is responsible for their blue appearance. The role of fluorine as an anionic dopant is apparent even in rounded F:In_2O_3 NCs (1% InF_3) synthesized at 280 °C. These NCs have a mean diameter of 338.0 ± 51.0 nm with 4.4 ± 0.4 at.% F by EDX, and exhibit an LSPR extinction peak at 3497 cm^{-1} (Figure 5.10). For comparison, undoped pseudospherical In_2O_3 NCs show a low energy LSPR peak located at 1370 cm^{-1}, consistent with a low concentration of free electrons induced by the presence of oxygen vacancies (eq. 1)[238] (Figure 5.10). In both Cl:In_2O_3 and Br:In_2O_3 NCs however, the LSPR peak is at 1743 cm^{-1}, indicating low free electron concentrations compared to F:In_2O_3 NCs due to low dopant incorporation (Figure 5.10). These comparative observations demonstrate that fluorine is a uniquely effective anionic halide dopant for In_2O_3 NCs to induce LSPR in the IR region.

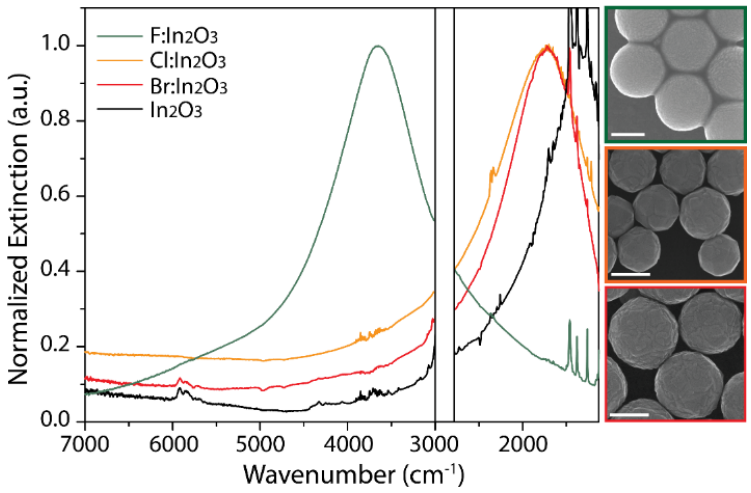

Figure 5.10: Liquid-cell FTIR spectra for halogen doped In_2O_3 NCs

Liquid-cell FTIR spectra for spherical F:In_2O_3 (green line), Cl:In_2O_3 (orange line), Br:In_2O_3 (red line), and In_2O_3 NCs (black line). Spectral bands saturated by ligand absorption are shown as blank regions. (Inset) SEM images showing F:In_2O_3 (green), Cl:In_2O_3 (orange), and Br:In_2O_3 (red) NCs. Scale bars are 200 nm.

In the F:In_2O_3 cubes, the highly defined corners and edges are expected to result in multimodal LSPR extinction peaks in the IR spectral range. F:In_2O_3 cubes (3% InF_3) have highly pronounced plasmon peaks at 3496 cm^{-1} (FWHM 1157 cm^{-1}) and 5469 cm^{-1} (Figure 5.12 a, green), respectively ascribed to corner- and edge-dominated LSPR modes, by comparison to analogous modes observed for silver cubes.[239] Through the Drude model, the free carrier density within the F:In_2O_3 cube (3% InF_3) is estimated to be 6.8 × 10^{20} cm^{-3} based on the LSPR extinction spectrum (Figure 5.11). Estimated from the NMR results, the concentration of F atoms in metallic environments in the F:In_2O_3 cubes is 2.5 × 10^{21} cm^{-3}, considering 80% of the F as being in a sub-surface environment and that the F/In atom ratio is 0.10. Combined, these estimates indicate only a fraction of sub-surface

F atoms (27 %) is activated and contributes electron carriers to the conduction band, while the remainder of the internal F dopants are otherwise compensated.

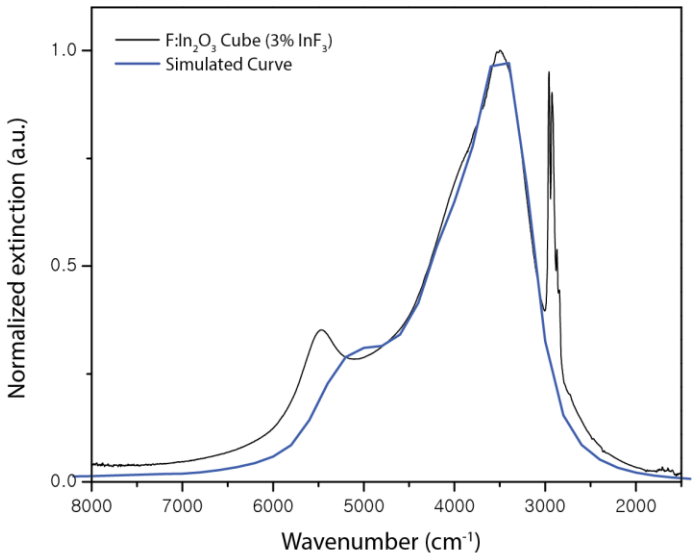

Figure 5.11: Drude Model Extinction Curve

FTIR spectrum of F:In_2O_3 cube NCs (3% InF_3) dispersed in tetrachloroethylene (black) and simulated extinction curve (blue). A Drude model was used to define the NC dielectric function $\epsilon_p = \epsilon_\infty - \frac{\omega_p^2}{\omega^2 - i\gamma\omega}$ (Plasma frequency ω_p = 12300 cm^{-1}, damping parameter γ = 600 cm^{-1}, ϵ_∞= 4). A cube shaped geometry model was input into the COMSOL design module based on experimental observations, using an edge-to-edge length of a = 160 nm and corner curvature of a/20, with surrounding medium refractive index of n = 1.5. The corresponding free electron concentration based on the derived plasma frequency was n_e = 6.8 × 10^{20} cm^{-3}.

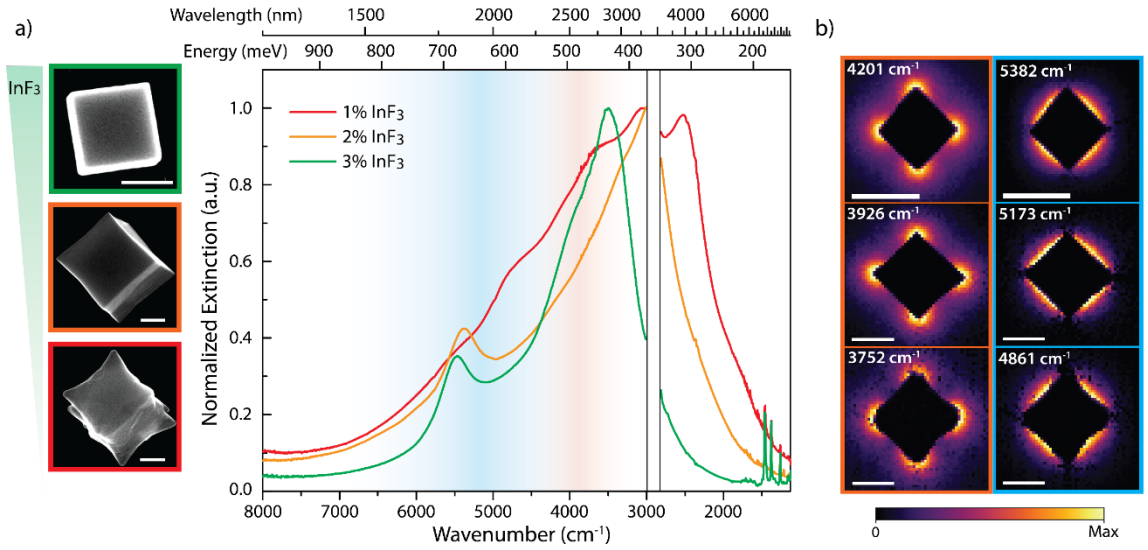

Figure 5.12: FTIR spectra and EELS map for F:In_2O_3 NCs

(a) Liquid cell FTIR spectra of F:In_2O_3 NCs with corresponding SEM images. F:In_2O_3 cube (green), F:In_2O_3 concave cube (orange), and F:In_2O_3 concave cube (red). Scale bars are 100 nm. Spectral bands saturated by ligand absorption are shown as blank regions. Sharp peaks observed at 1000 cm^{-1} region are assigned to surface bound organic ligands. (b) F:In_2O_3 (3% InF_3) cube (top), F:In_2O_3 (2% InF_3) concave cube (middle), and F:In_2O_3 (1% InF_3) concave cube (bottom) EELS maps for corner mode frequencies (around 3900 cm^{-1}, left, orange) and edge mode frequencies (around 5100 cm^{-1}, right, blue) LSPR mode. Scale bars are 200 nm.

Lower fluorine-doped F:In_2O_3 concave cube NCs exhibit changes in LSPR peak shape due to NC shape effects. Sharp concave cubes (2% InF_3) show well-defined modes with LSPR peaks at 2974 cm^{-1} and 5378 cm^{-1} (Figure 5.12 a, orange). Concave cubes (1% InF_3) with elongated <111> directional corners, exhibit a complex LSPR response centered at 3030 cm^{-1} (Figure 5.12, red). Previous literature on plasmonic octopod Ag NCs has described the breakdown of simple cubic LSPR modes due to elongated

corners.[240,241] By contrast, no multimode LSPR peaks are observed for rounded F:In_2O_3 NCs (1% InF_3) grown at 280 °C due to their mostly spherical shape (Figure 5.12, green).[185] During the growth of F:In_2O_3 NC cubes (3% InF_3), FTIR of aliquots demonstrate retention of both edge- and corner-mode LSPR peaks (Figure 5.213). The edge-mode LSPR at higher wavenumber range is observed at 5690 cm^{-1} and retained during 1-4 min reaction time. The corner-mode LSPR peak is also retained at 3340 cm^{-1} until the end of the growth reaction (2-4 min). It is observed that the F:In_2O_3 cube aliquot dopant composition is steady at F/In = 11.8 ± 0.4 % throughout the growth reaction. This suggests that incorporation of sub-surface fluorine species, as detected by ^{19}F NMR, is sustained during NC growth.

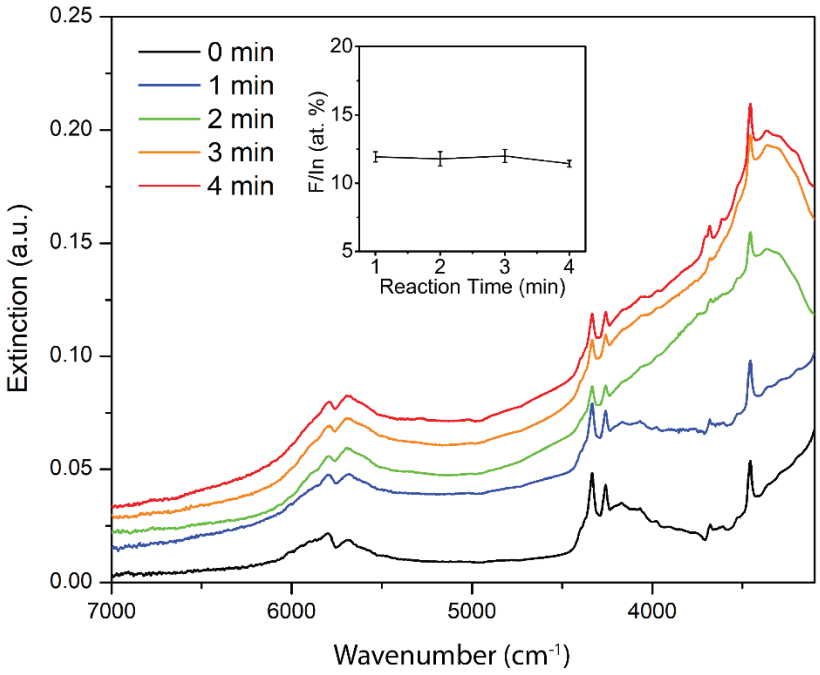

Figure 5.13: F:In_2O_3 Cube NC Aliquot FTIR

Liquid cell FTIR spectra of F:In_2O_3 cube NC (3% InF_3) aliquots taken from 0 min to 4 min growth reaction. The LSPR edge mode (higher wavenumber) and corner mode (lower wavenumber) LSPR peaks can be seen. (Inset) F:In_2O_3 cube NC F/In% atomic composition quantified by EDX retained as NC growth reaction time progress.

To definitively assign the contributions to the multimodal FTIR peaks observed in faceted F:In_2O_3 NCs, we perform STEM-EELS mapping of individual cubes. Optical LSPR excitation in the FTIR only allows ensemble far-field extinction measurements of cubes, where the incidence IR excitation wavelength (1250-10000 nm) is within the LSPR quasi-static limit range.[185] The sub-Ångstrom diameter probe available in the STEM can directly sample and map the near-field localization of LSPR modes, and thanks to recent advances in monochromation these mid-infrared frequencies are now

accessible using EELS.[242,243] The spatial maps are acquired through spectrum imaging (SI), where the beam is rastered across the region of interest and a spectrum is acquired at each probe position resulting in a three-dimensional dataset with two spatial-dimensions and one spectral dimension. From here, individual plasmon modes are deconvoluted through the non-negative matrix factorization (NMF) method to produce spatially resolved EELS maps of individual LSPR modes.[239] For each structure spatially- and spectrally-distinct corner and side modes can be observed and mapped through the deconvolved spectrum imaging, which are plotted in Figure 5.12 b. The corner modes of F:In_2O_3 cube (3% InF_3), sharp concave cube (2% InF_3), and concave cube (1% InF_3) NCs, are observed at 4201 cm^{-1}, 3926 cm^{-1}, and 3752 cm^{-1} respectively, with the side mode resonances centered at 5382 cm^{-1}, 5173 cm^{-1} and 4861 cm^{-1}. It is important to note that for the side modes, the NMF-deconvolution results in a spectral component with multiple peaks, likely corresponding to spatially overlapped edge and face modes. The reported peak center is the average of these face and edge modes. Details of the deconvolution and the EELS experiments are presented in greater detail in Supporting Information, Text A4.3.

While FTIR samples the ensemble behavior and EELS samples individual structures, the match is strong enough to determine the modal nature of the FTIR peaks from the EEL-SI. The STEM analysis support that the high energy FTIR peaks correspond to the edge and face modes, while the lower energy peaks correspond to the corner modes. As in FTIR, in EELS the edge mode is observed at higher energy for the cube (3% InF_3) than for the sharp concave cube (2% InF_3). The frequencies of the corner modes do differ significantly between FTIR and EELS, which can be understood as originating from differences in the dielectric function in the liquid-cell FTIR experiments and the SiN/ultra-high-vacuum environment in the STEM.[244] The observed blueshift in

the EELS mode relative to the FTIR spectrum is attributed to the lower refractive index (n=1) of surrounding vacuum in STEM, as compared to the TCE solution medium (n=1.5) in the liquid-cell optical measurement.[245,246]

CONCLUSION

Fluorine plays a dual role as a dopant, influencing preferential growth of certain crystal facets and directing morphology of colloidally synthesized In_2O_3 NCs, as well as inducing IR range LSPR by aliovalent doping within the In_2O_3 NC lattice. In this study, we have demonstrated that introducing fluorine precursors in a typical heat-up method colloidal synthesis yields highly faceted F:In_2O_3 cube NCs with shape-dependent LSPR response. Morphological control is demonstrated for the formation of concave cubes by adjusting the dopant concentration during F:In_2O_3 NC synthesis. Small percentages (1-2 at.%) of fluorine species are shown to be at the surfaces of the F:In_2O_3 NCs and hinder growth of {100} facets, as determined by combined XPS, solid-state 2D $^{1}H\{^{19}F\}$ NMR and DFT analyses. By comparison, the majority of fluorine species are incorporated into sub-surface metallic environments in the F:In_2O_3 lattice, consistent with F^- acting as an anionic dopant, as revealed by variable-temperature analyses of ^{19}F spin-lattice relaxation times and comparison to the Knight-Korringa relation. Complementary analyses of wideline ^{115}In NMR spectra show that the majority of ^{115}In species in the F:In_2O_3 species interact with unpaired conduction band electrons, providing corroboratory evidence that the F:In_2O_3 NC lattice is heavily doped beyond the metal-insulator transition. Arising from the combined effects of dopant-induced free-carriers and highly-faceted NC shapes, multimodal LSPR extinction features are observed in the IR. Single-NC LSPR near-field

modes spatially localized around sharp morphological features are directly observed by STEM-EELS.

With this understanding of the role played by fluorine both on the NC surface and in the lattice, F:In_2O_3 NCs provide a valuable platform material for exploring properties and applications of LSPR-active NCs. Analogous to Ag nanocubes that exhibit visible LSPR,[239] well-defined In_2O_3 nanocubes are able to be colloidally synthesized, with shape-dependent LSPR in the IR spectral range. Near-field localization of IR light will make these highly faceted F:In_2O_3 NCs a platform material to evaluate near-field enhancement effects and explore applications unique to the infrared, including coupling LSPR to molecular vibrational modes[65] and IR emissive excitons.[247] To meet these demands, control of NC sizes and LSPR spectral tunability need be advanced. Large cube NC sizes lead to greater magnitude in near-field enhancement,[65] and full NC size control ranging from small to large cubes may allow a range of near-field intensity to be achieved. Further synthetic advances, such as the systematic incorporation of co-dopants,[64] may lead to additional LSPR tuning by increasing free electron compensation in In_2O_3 NCs. However, synthetic questions remain to fully understanding cationic co-dopant incorporation in metal oxides in the presence of anionic dopants.[65,248] The understanding of the dual role of fluorine as an anionic dopant in F:In_2O_3 NCs is expected to provide a foundation for addressing these questions and challenges, and further improving the properties of these versatile materials.

Experimental Methods

Materials:

Indium (III) acetylacetonate ($In(acac)_3$, 99.99%), Indium (III) fluoride (InF_3, > 99.9%), Indium (III) chloride ($InCl_3$, 99.999%), Indium (III) bromide ($InBr_3$, 99.999%), Oleic acid (OA, 90%, technical grade), Octylamine (OcAm, 99%), Trioctylamine (TOA, 98%) and tetrachloroethylene (TCE, ≥ 99%) were purchased from Sigma-Aldrich. Toluene (99.5%) was purchased from Fisher Chemical. All chemicals were used as received without any further purification.

Fluorine-Doped Indium Oxide ($F:In_2O_3$) Cube (3% InF_3) Synthesis:

All synthesis procedures were carried out using standard Schlenk line techniques aided by a nitrogen-filled glovebox. For the growth of 3% doped $F:In_2O_3$ cubes, a mixture of $In(acac)_3$ (399.78 mg, 0.97 mmol), InF_3 (5.15 mg, 0.03 mmol), OA (1 ml), OcAm (0.5 ml) and TOA (3.5 ml) was loaded in a three-neck round-bottom flask in the glovebox. This precursor mixture was then stirred with a magnetic bar at 600 rpm and degassed under vacuum at 120 °C for 15 min. The mixture turned transparent during this operation signifying the formation of indium oleate. Thereafter, the flask was filled with nitrogen and further heated at a ramp rate of 15 °C/min to 320 °C. The reaction mixture turned cloudy and opaque which signified cube growth and was designated as the growth reaction start time. The growth reaction was allowed to run for 5 min at 320 °C or the desired set point temperature. Subsequently, growth was terminated by removing the heating mantle and the reaction mixture was cooled by blowing an air jet on the flask. The cubes were washed and dispersed in toluene and centrifuged at 4500 rpm for 5 min. This washing process was repeated three times. The resultant cubes were redispersed in toluene for further analysis.

Varying concentrations of F doping in these NCs were achieved by controlling the molar ratio of InF_3 to $In(acac)_3$, while keeping other reaction parameters identical.

Aliquots (0.1 ml), at various reaction times during growth, were extracted from the reaction mixture with a nitrogen purged syringe needle and quenched into TCE for further analysis.

Indium Oxide (In_2O_3) NC Synthesis:

Undoped indium oxide (In_2O_3) NCs were synthesized by adding $In(acac)_3$ (1 mmol) in the reaction flask without InF_3 while keeping other reaction parameters identical to the procedure described above for the F-doped NCs.

Chlorine/Bromine Doped Indium Oxide ($Cl:In_2O_3$, $Br:In_2O_3$) NC Synthesis:

$Cl:In_2O_3$ (3% $InCl_3$) NCs were synthesized by adding $In(acac)_3$ (0.97 mmol), substituting $InCl_3$ (0.03 mmol) precursor for InF_3 in the reaction flask, while keeping other reaction parameter identical. In a similar manner, $InBr_3$ (0.03 mmol) was used to synthesize $Br:In_2O_3$ (3% $InBr_3$) NCs keeping other reaction parameters identical.

Fourier Transform IR (FTIR) Spectra:

FTIR spectral measurements were conducted using a Bruker Vertex 70 FTIR at 4 cm^{-1} resolution. Aliquot solutions were diluted in TCE and loaded into a liquid cell with KBr windows for FTIR measurements. NCs dispersed in TCE were sonicated for 1 hour to prevent aggregation before loading into the liquid cell.

XRD Analysis:

Samples for XRD measurements were prepared by drop-casting a 10 mg/mL dispersion of $F:In_2O_3$ NCs on silicon substrates. The data were collected with a Rigaku

MiniFlex 600 X-ray diffractometer using Cu Kα radiation, 1.54 Å, and analyzed with GSAS-II software.[209]

Electron Microscopy:

Samples were prepared by drop-casting NC dispersions onto carbon-coated 400 mesh copper grids (Ted Pella) and the imaging was performed in a Hitachi S5500 scanning electron microscope (SEM) operating in the STEM mode at an accelerating voltage of 30 kV. NC size analysis was performing with ImageJ software with 250 NC count. High resolution transmission electron microscopy (HRTEM) images and selected-area electron diffraction (SAED) patterns were acquired with JEOL 2010F transmission electron microscope (TEM) equipped with a CCD camera and a Schottky field emission gun operating at 200 kV.

Elemental Analysis:

Elemental spectrum acquisition of F:In_2O_3 cubes drop-cast on silicon substrates was carried out using a Hitachi S5500 SEM with a Bruker XFlash EDX detector attachment at 5 kV. Elemental deconvolution was performed with the Bruker Quantax software reference library at zero-tilt angle P/B-ZAF correction. TOF-SIMS was conducted on TOF.SIMS 5, ION-TOF GmbH with Cs^+ sputtering at 2 kV.

Thermogravimetric Analysis (TGA):

Measurements were carried out using a Mettler Toledo TGA2 thermogravimetric analyzer. Dried NC powders were loaded into alumina crucibles of 100 μl volume and heated from 25 to 1100 °C at a heating rate of 5 °C/min under nitrogen flow (50 sccm).

XPS:

Samples were prepared by drop casting NC solutions on silicon substrates and the measurements were performed in a Kratos Axis Ultra DLD spectrometer with a monochromatic Al Kα source (1486.6 eV). Wide survey scans were acquired at analyzer pass energy of 80 eV and the high-resolution narrow region scans were performed at a pass energy of 20 eV with steps of 0.1 eV. Spectral acquisitions were performed with photoelectron take-off angle at 0° with respect to the surface normal and pressure in the analysis chamber was maintained at around 10^{-9} torr. Data analysis was performed in CasaXPS software using the Kratos relative sensitivity factor library. The binding energy (BE) scale was internally referenced to the C 1s peak (BE for C-C = 284.8 eV).

Electron paramagnetic resonance (EPR) spectroscopy:

Spectra were measured in a Bruker Biospin EMXplus 114 X-band spectrometer equipped with a liquid nitrogen variable temperature cryostat. Dried NC powders were loaded into quartz EPR tubes for the measurements.

DFT Calculations:

DFT calculations were performed using the Vienna Ab-initio Simulation Package (VASP)[249,250] with PAW pseudopotentials[251] in the package. The Perdew-Burke-Ernzerhosf (PBE) exchange-correlation functional[252] was used in all the DFT calculations. A 3×3×1 Monkhorst-Pack k point mesh for the Brillouin zone integration was used, with a vacuum layer of 15 Å to prevent interactions between periodic images of the slab. Further details are in the Supporting Information, Text A4.1.

Solid-State ^{19}F and ^{115}In NMR Spectroscopy:

Solid-state ^{1}H and ^{19}F MAS-NMR spectra were acquired on a Bruker ASCEND 400 MHz (9.4 T) solid-state DNP NMR spectrometer operating at Larmor frequencies of 400.202 and 376.532 MHz for ^{1}H and ^{19}F, respectively. For the solid-state MAS-NMR measurements, the F:In_2O_3 NCs were mixed with KBr powder in a 1:1 ratio by mass. The KBr served as an internal temperature probe for accurate determination of the sample temperature under the different measurement conditions.[253,254] The 1D ^{19}F Hahn echo spectrum was acquired at 35 kHz MAS, at 395 K, and using a 90°-τ-180°-τ pulse sequence with rotor-synchronized τ delay times of one rotor period and 100 kHz rf pulses. The 2D $^{1}H\{^{29}F\}$ NMR correlation spectrum was acquired by using a 2D dipolar-mediated *H*eteronuclear *M*ultiple *Q*uantum *C*orrelation (HMQC) pulse sequence, where the ^{1}H-^{19}F nuclear dipole-dipole couplings were reintroduced by using $SR26_4^{11}$ recoupling[255] with 50 kHz rf power for recoupling. The ^{19}F spin-lattice (T_1) relaxation analyses relaxation times at different temperatures were measured by using a saturation-recovery pulse sequence with Hahn echo detection.

The solid-state ^{115}In NMR spectrum of undoped bulk polycrystalline In_2O_3 (99.9% purity, Aldrich) was acquired on Bruker AVANCE-III Ultrashield Plus 800 MHz (18.8 T) narrow-bore spectrometer operating at a Larmor frequency of 174.354 MHz for ^{115}In and using a Bruker 3.2 mm broadband double-resonance H-X probehead. The solid-state ^{115}In NMR spectrum of the F:In_2O_3 NCs was acquired on a 19.6 T Bruker DRX NMR spectrometer (National High Magnetic Field Laboratory) operating at a Larmor frequency of 182.266 MHz for ^{115}In and using a custom-build 3.2 mm double resonance H-X probehead. The ^{115}In NMR spectra were acquired using a quadrupolar Carr-Purcell-Meiboom-Gill (QCPMG) pulse sequence,[237] which yields manifolds of very narrow, evenly-spaced NMR signals (spikelets), which can be systematically acquired as a series that can be overlaid to map the full central transition (CT) region of the ^{115}In NMR

spectra. Each ^{115}In NMR spectrum is presented as a mosaic overlay of 22 individual QCPMG sub-spectra (plotted in different colors) acquired at evenly spaced frequency intervals. The ^{115}In spectra were referenced to a 1 M $In(NO_3)_3$ solution at 0 ppm. Further details on the ^{19}F and ^{115}In NMR analyses are provided in the Supporting Information, Text A4.2.

STEM-EELS:

Plasmon mapping was performed in a Nion high-energy-resolution monochromated EELS STEM (HERMES) at Oak Ridge National Laboratory operated at 60 kV and a Nion prototype spectrometer.[256,257] Using a variable slit we choose an energy resolution of 186 cm^{-1} (23 meV) to optimize the resolution between the plasmon peaks and the signal in the monochromated beam. For the plasmon deconvolution we use the non-negative matrix factorization routine available in the Python HyperSpy library (http://hyperspy.org/). More details can be found in the Supporting Information (Text A4.3).

Chapter 6: Infrared Plasmon Spectral Tuning in Nanocubes

A synthetic challenge in faceted metal oxide nanocrystals (NCs) is realizing tunable localized surface plasmon resonance (LSPR) near-field response in the infrared (IR). Cube-shaped nanoparticles of noble metals exhibit LSPR spectral tunability limited to visible spectral range. Here, we describe the colloidal synthesis of fluorine, tin co-doped indium oxide (F,Sn:In_2O_3) NC cubes with tunable IR range LSPR for around 10 nm particle sizes. Free carrier concentration is tuned through controlled Sn dopant incorporation, where Sn is an aliovalent n-type dopant in the In_2O_3 lattice. F shapes the NC morphology into cubes by functioning as a surfactant on the {100} crystallographic facets. Cube shaped F,Sn:In_2O_3 NCs exhibit narrow, shape-dependent multimodal LSPR due to corner, edge, and face centered modes. Monolayer NC arrays are fabricated through liquid-air interface assembly, further demonstrating tunable LSPR response as NC film nanocavities that can heighten near-field enhancement (NFE). The tunable F,Sn:In_2O_3 NC near-field is coupled with PbS quantum dots, via the Purcell effect. The detuning frequency between the nanocavity and exciton is varied, resulting in IR near-field dependent enhanced exciton lifetime decay. LSPR near-field tunability is directly visualized through IR range scanning transmission electron microscopy - electron energy loss spectroscopy (STEM-EELS). STEM-EELS mapping of the spatially confined near-field in the F,Sn:In_2O_3 NC array interparticle gap demonstrates elevated NFE tunability in the arrays.

INTRODUCTION

Colloidal synthesis of doped metal oxide nanocrystals (NCs) has emerged recently as a route for expanding localized surface plasmon resonance (LSPR) to the

infrared (IR) range.[258] With a suitable metal oxide NC host material, free electron compensating point defects are engineered by introducing n-type dopants. Doping strategies in plasmonic metal oxide NCs involve aliovalent cation substitution (e.g., Sn:In_2O_3,[120] Al:ZnO,[54] and In:CdO[118] NCs), and anionic fluorine doping (e.g., F,In:CdO,[64] F,Sn:In_2O_3,[65] and F:In_2O_3 NCs[259]) in metal oxide NC host lattices. Spectral advantages are nascent in doped metal oxide NC systems. Metal nanoparticles intrinsically possess high free-carrier concentrations exceeding 10^{23} cm^{-3}, leading to LSPR optical response restricted to the visible region of the electromagnetic spectrum.[183,184] Spectral tunability relies on increasing particle size in such metal classes of NCs to red-shift LSPR modes,[260,261] adding dimensional constraints to nano-assembly architectures. Alternatively, doped metal oxide NCs relieve particle size constraints, expanding tunable IR range LSPR through variable dopant incorporation with free-carrier concentration control in the 10^{21} cm^{-3} range.[46,185] Intraband and interband transition effects optically observed in Au nanoparticles,[262] can be circumvented in doped metal oxide NCs. Due to low free-carrier concentration, the LSPR located in the IR range is well separated from the UV range optical band edge in wide-bandgap metal oxide materials.[258,263]

Shape-dependent optical properties need be further developed in doped metal oxide classes of NCs to achieve spectral dominance in the IR. Colloidal Au and Ag cube nanoparticles sculpted by faceting agents led to the observation of shape-dependent LSPR and enhanced electromagnetic near-fields at morphological discontinuities.[6,239] Halogen anions are capping agents that have been used for shape control of metal[9] and metal chalcogenide[187,188] classes of NCs, while shape control in LSPR active metal oxide[163] NCs is only recently being realized.[186] Morphologies reported for colloidal Au and Ag nanoparticles include cubes,[6,180,181] where faceted nanoparticles provide shape-dependent

LSPR properties not observed in spherical particles. This including strong near-field enhancement (NFE) hot spots around corners and edges[190,239] that, in well-established metal nanoparticles, have been leveraged for plasmonic nanoantenna[191] and surface-enhanced Raman spectroscopy (SERS).[193,194] [9] Despite well-defined studies in noble metal NCs, limitations in IR range tunability for noble metal NCs are inherent. This includes fixed high free carrier concentration, intraband or interband losses contributing to spectral linewidth, and spectral tunability dependent on particle size. Spectral tunability, while retaining high NFE still needs to be addressed and may be approached through alternative materials for IR spectral dominance.

We advance LSPR spectral tunability in the IR range while preserving highly-faceted cube morphology, via co-doped F,Sn:In_2O_3 NCs. In our previous work, shape control in this developing class of nanocrystalline materials was investigated using fluorine n-type dopant as a faceting agent in fluorine-doped indium oxide (F:In_2O_3) cube NCs, yet broad LSPR tuning was not realized.[259] Leveraging recent synthetic developments employing a continuous slow injection of indium and dopant precursors into a heated reaction solution, a high degree of NC shape and size control can be realized.[14,264] The resulting LSPR properties with Sn and F co-dopants along with faceting effects are investigated here. We show that the cationic Sn dopant is simultaneously incorporated into F surface passivated cube shaped In_2O_3 NCs to spectrally tune LSPR. The anionic F dopant suppresses divalent scattering centers, leading to enhanced quality factor and narrow LSPR spectral linewidth. Controlled Sn dopant introduction in NCs allows tunable carrier concentrations around 10^{21} cm^{-3}, resulting in synthetic access to IR range LSPR tunability control with high quality factor in NC solvent dispersions.

Attaining advantages in IR range LSPR tunability, F,Sn:In_2O_3 NCs are further self-assembled to fabricate dense plasmonic NC array films. Relieving spatial restrictions from size dependent LSPR tuning in prior studies of noble metal nanoparticles, LSPR tunable F,Sn:In_2O_3 NCs allow densely packed nanogap cavities in monolayer film assemblies while retaining small particle size. Spectrally tuned dense nanocavity arrays demonstrating NFE can be used to influence optical properties of other classes of NCs. Utilizing strides in synthetic chemistry, access to two classes of photophysical light-matter interactions has been achieved over the past decade through colloidal NC synthesis.[265] Excitonic light emission of quantum dot (QD) NCs is possible through quantum confinement effects, allowing photoluminescence in inorganic semiconductor materials (CdSe[266], InP[267], PbS[268], HgS[269]) through exciton electron-hole pair recombination. Meanwhile, confinement of electromagnetic field beyond the diffraction limit has been enabled through free-electron carrier confining in nanoparticles smaller than one fifth of the incident wavelength dimension, allowing LSPR-induced NFE to occur.[270] Such maturation in two classes of NCs allows hierarchical assembly of matter to be achieved. Here, architectures containing PbS QDs and F,Sn:In_2O_3 NCs were fabricated by stacking monolayer films together through a modified liquid-air interface self-assembly method.[271,272] Local and long-range NC ordering was respectively observed through scanning electron microscopy (SEM) and small angle X-ray scattering (SAXS), ensuring film uniformity. Self-assembled LSPR tunable F,Sn:In_2O_3 NCs allow a degree of control in nanocavity film NFE by detuning the frequency to enhance PbS QD lifetime decay rates at a photoluminescence (PL) wavelength located in the conventional-band (C-band) low-loss optical telecommunication window.[273,274] Excitonic and plasmonic light-matter interaction can optically be coupled when spatially in vicinity of each other, via the Purcell effect. Strong LSPR near-field antenna NFE enhances PL lifetime decay rate

in excitonic materials in the Purcell weak-coupling regime.[191,275] The IR range LSPR near-field of F,Sn:In_2O_3 NC film arrays is observed to influence exciton decay rate in excitonic PbS QDs through optical time resolved PL measurements.

Such IR range LSPR near-field, expected to be spatially localized around F,Sn:In_2O_3 NCs, is directly visualized through monochromated scanning transmission electron microscopy - electron energy loss spectroscopy (STEM-EELS).[276] With recent improvement in monochromator energy resolution,[256,257,277] STEM-EELS allows access to plasmonic near-field mapping at increasingly low-energy scales and at nanoscale spatial resolution. Intense IR near-field spatially confined between F,Sn:In_2O_3 NCs in interparticle gaps was directly visualized through EELS mapping. We observe that the F,Sn:In_2O_3 NC ordered array has emergent collective near-field ensemble behavior, unique from localized in-gap confined near-field modes. The collective NC film array ensemble was observed to have long range spatially delocalized near-field decay length extending from the edges of the NC array. This was further supported by a delocalized mode volume extracted from Purcell enhancement PL decay lifetime in PbS QDs coupled to the F,Sn:In_2O_3 NC film. The observed materials and optical characteristics lead to IR light near-field localization, making F,Sn:In_2O_3 NCs a gateway material in emergent IR near-field enhancement applications.

F,Sn:In_2O_3 NC Synthesis

The shapes of the F,Sn:In_2O_3 NCs were controlled by varying the molar ratio of SnF_4 to $Sn(ac)_4$ precursors added to the injection solution. This determines the extent of fluorine and tin dopant incorporation into the resulting NC products. F,Sn:In_2O_3 NCs with well-defined morphology were produced for 0–3% SnF_4 in the growth solution, as

exhibited in Figure 6.1 a. SEM images show that monodisperse NCs with cubic morphology were obtained exclusively in the presence of SnF_4 at this dopant range. For comparison, synthesis in the absence of SnF_4 and exclusively with $Sn(ac)_4$ dopant precursor was conducted. Spherical $Sn:In_2O_3$ NCs were observed (Figure 6.2), implying fluorine plays a faceting role in shaping cubic $Sn:In_2O_3$ NCs. It was observed that higher amounts of SnF_4 led to deterioration of cubic NC morphology by forming rough facets. In the absence of $Sn(ac)_4$ precursor, the cube morphology is retained at adequate concentrations of SnF_4 (3% and 5%). Yet, NCs with evident rough surfaces attributable to F^- ion induced corrosion pitting[9,186] are observed under excessive SnF_4 addition at 10% molar ratio (Figure 6.1). For the sake of retaining high-quality cube shapes in this study, 5% SnF_4 molar precursor ratio is nominally maintained while further addition of $Sn(ac)_4$ cationic co-doping agent is deliberately varied for LSPR tunability.

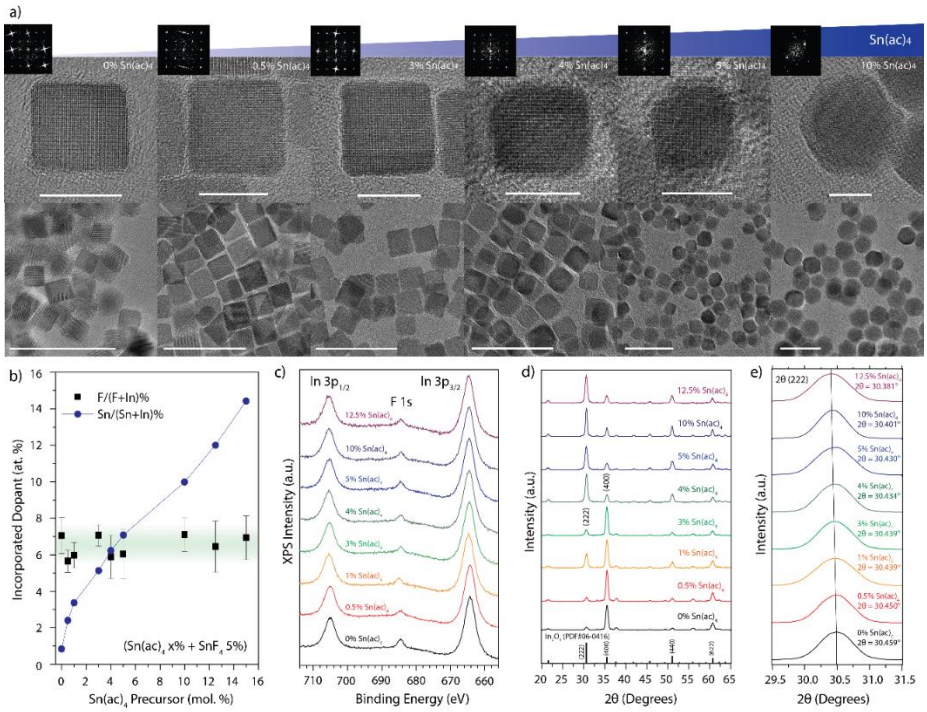

Figure 6.1: F,Sn:In_2O_3 NC materials properties

(a) HRTEM image of F,Sn:In_2O_3 NC with progressively increased 0-10% $Sn(ac)_4$ and maintained 5% SnF_4 dopant precursor molar ratio. FFT (inset) show {100} facet orientation of NC cubes, and single particle HRTEM show NC crystallinity (middle) with scale bar at 10 nm. Wide field view HRTEM image scale bar is at 50 nm (bottom). (b) Dopant incorporation in F,Sn:In_2O_3 NC for F and Sn. Fluorine dopant precursor was maintained at 5% SnF_4, with controlled Sn incorporation at 0-15% $Sn(ac)_4$ dopant precursor concentration range. (c) XPS spectra of F,Sn:In_2O_3 NC Sn dopant concentration series for F 1s and In 3p. (d) XRD diffraction pattern of F,Sn:In_2O_3 NCs, (222) and (400) peaks labeled with In_2O_3 powder reference pattern (PDF #00-006-0416) (e) XRD diffraction pattern for (222) reflection show peak shift towards lattice expansion as Sn dopant precursor ratio increases.

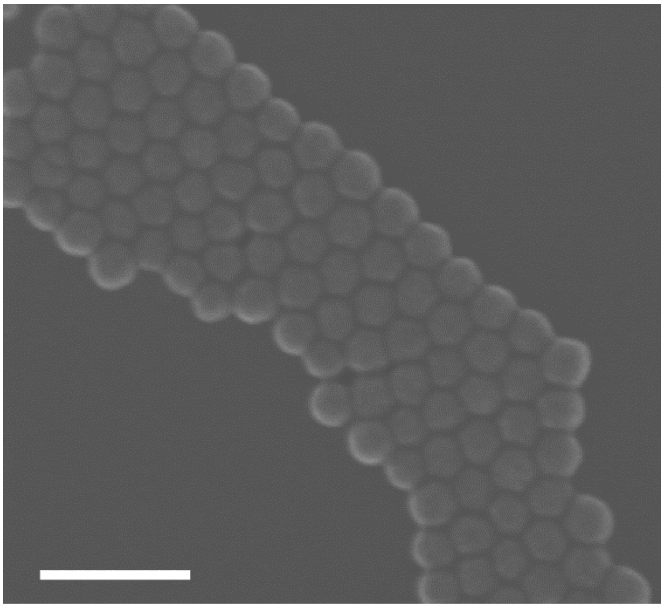

Figure 6.2: Round Sn:In_2O_3 NC SEM Image

SEM image of round Sn:In_2O_3 (3% $Sn(ac)_4$) NCs synthesized without the presence of fluorine precursor (SnF_4). Scale bar is 100 nm.

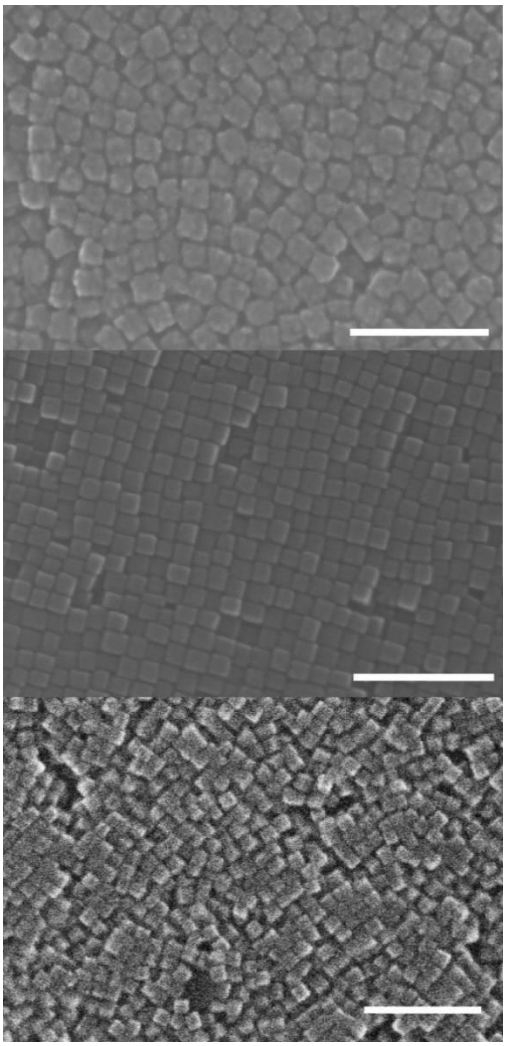

Figure 6.3: Rough Surface F,Sn:In_2O_3 NC SEM Images

SEM image of F,Sn:In_2O_3 (10% SnF_4) NCs (top), with defective surface and rough surface morphology synthesized with excessive fluorine precursor (SnF_4) concentration. F,Sn:In_2O_3 (5% SnF_4) cube NCs (middle) and F:In_2O_3 (3% InF_3) cube NCs (bottom) exhibit defined faceting under moderate fluorine precursor concentration. NCs were synthesized without the presence of $Sn(ac)_4$. Scale bars are 100 nm.

TEM images of F,Sn:In_2O_3 NC cubes from 0% to 3% $Sn(ac)_4$ exhibit well-defined facets, shown in Figure 6.1 a. Fast Fourier transform (FFT) of HRTEM images confirms that F:In_2O_3 NC cubes are single crystalline particles and allows indexing of dominant surface exposed facets (Figure 6.1 a, inset). Observations show the cubes are terminated with {100} facets of the In_2O_3 cubic bixbyite structure, consistent with previously reported fluorine passivated In_2O_3 NCs.[259] Crystallinity in NCs is well retained over the full $Sn(ac)_4$ dopant range as shown in FFT patterns collected down the <100> zone axis. Rounded cube morphology appears above a threshold of 4% $Sn(ac)_4$, until NCs become dominantly spherical in shape near 10% $Sn(ac)_4$. The size of the NCs remained consistent with edge length of 12.6 ± 0.6 nm (Figure 6.4), when synthesized with 10 mL of precursor solution injection while $Sn(ac)_4$ dopant precursor ratio was controllably incremented. Versatility in NC cube size control is demonstrated when precursor solution between 1 to 20 mL is controllably injected into hot oleyl alcohol solution. The cubic shape is retained as observed in F,Sn:In_2O_3 NC cube (3% $Sn(ac)_4$) SEM images, following an expected injection volume to NC size trend (Figure 6.5).

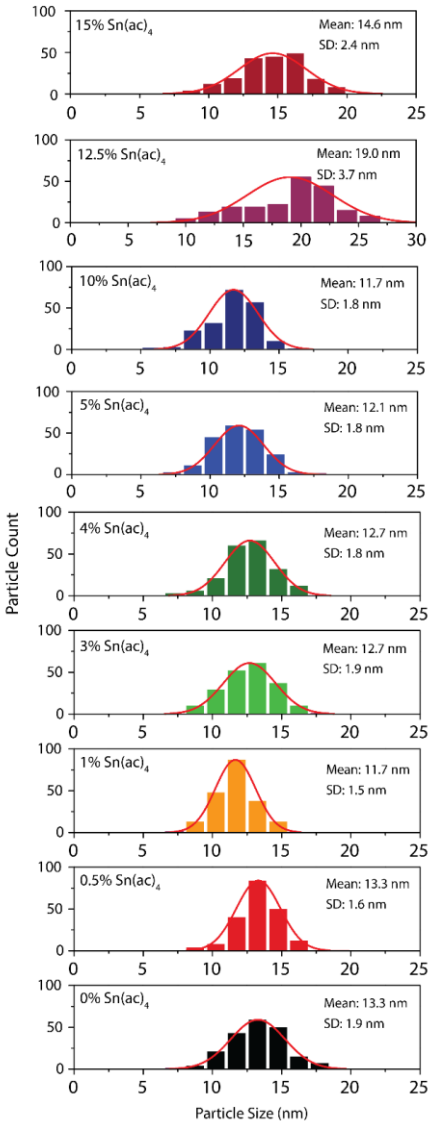

Figure 6.4: F,Sn:In_2O_3 NC Size Histograms

Size distribution histograms of F,Sn:In_2O_3 NC dopant series (0 – 15% $Sn(ac)_4$) STEM images, with mean average sizes and standard deviations.

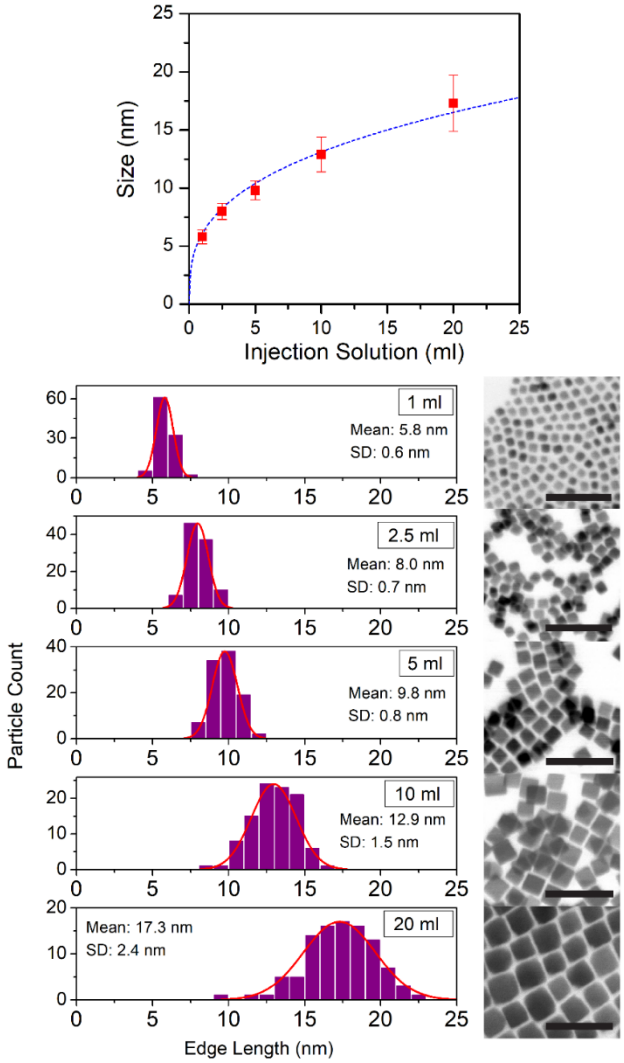

Figure 6.5: NC Size Control

NC size in F,Sn:In_2O_3 NCs (3% $Sn(ac)_4$) as a function of precursor solution injection volume (1 to 20 mL) (top). Size distribution histograms of F,Sn:In_2O_3 NC cubes from 1 to 20 mL injection solution, with mean average size and standard deviation, and representative STEM images at far right. Scale bars are 50 nm (bottom).

To quantify total F and Sn dopant incorporation in F,Sn:In_2O_3 NCs, inductively coupled plasma-atomic emission spectroscopy (ICP-AES) and energy dispersive X-ray (EDX) spectroscopy were conducted. Since the emitted X-rays have high energy after electron beam penetration, EDX has an effective probe depth of about 200 nm, so the results reflect the overall F composition of the NC ensemble in the drop-casted sample.[259,278] Atomic component quantification (Figure 6.1 b, Figure 6.6) show F atomic composition being sustained in F,Sn:In_2O_3 NCs around 6.5 at.% as SnF_4 fluorine precursor concentration employed during synthesis is maintained at 5% molar ratio. Sn peak signatures being in close vicinity to In peaks in EDX, ICP-AES trace metal elemental analysis was employed for Sn dopant quantification. Sn atomic composition in NCs is observed to systematically increase as a function of $Sn(ac)_4$ precursor addition (0 to 15%), demonstrating the efficacy of Sn cationic dopant incorporation into the NCs. The Sn dopant incorporation into NCs shows monotonic increase as $Sn(ac)_4$ is proportionally increased in the precursor injection solution. The substantial increase in Sn dopant incorporation observed between 0 and 1% $Sn(ac)_4$ levels can be attributed to effective liberation of Sn from $Sn(ac)_4$ due to soft binding acetate ligands as compared to harder binding halides when SnF_4 is the only dopant precursor.[42,178]

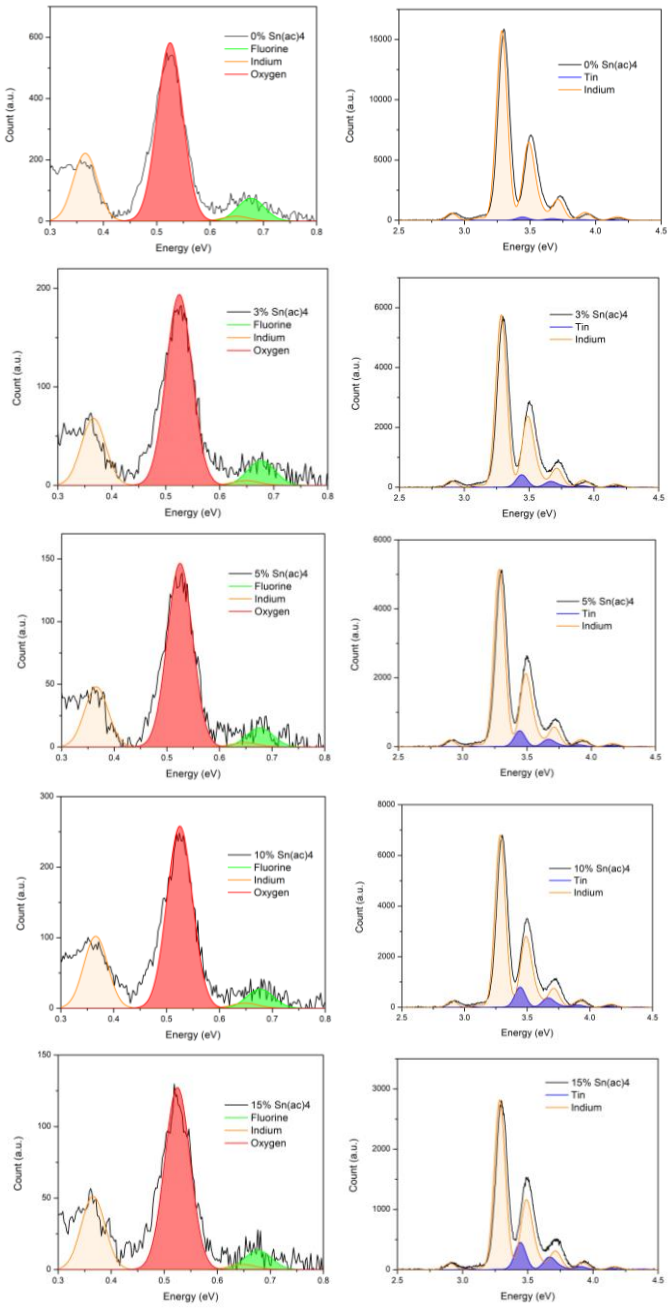

Figure 6.6: EDX Spectra

EDX spectra of F,Sn:In_2O_3 NCs with concentration range from 0 - 15% $Sn(ac)_4$. (left) F, O, and In peaks in the 0.3 to 0.8 eV range. (right) Sn and In peaks in the 2.5 to 4.5 eV range.

NC SURFACE CHARACTERIZATION.

Fluoride anions (F^-) have been described as facet-directing agents in metal oxide NCs,[186] exemplified in the fluorinated synthesis of TiO_2 NCs[162,164], F doped F:In_2O_3,[259] and Sn co-doped F,Sn:In_2O_3 NCs[65]. Metal fluoride precursors, such as SnF_4, decompose into HF in the presence of oleic acid during the reaction, releasing fluoride anions and passivating the In-O surfaces with In-F bonds.[162] Walsh et al. previously determined through density functional theory (DFT) calculations that for bixbyite In_2O_3, relaxed {111} facets are energetically preferred over oxygen terminated {100} facets ($\gamma_{(111)} < \gamma_{(100)}$).[142] However, surface-passivation by F^- in metal oxide NCs can be expected to alter the energetic sequence of the facets: F^- passivation of the {100} facets results in surface energy inversion ($\gamma_{(111)} > \gamma_{(100)}$).[164] Correspondingly, F^- functions as a favorable {100} facet capping agent over {111} surfaces in the bixbyite In_2O_3 NCs, hindering In atomic layer growth at F^- terminated {100} surfaces. This directs the synthesis of well-defined F:In_2O_3 cube NCs as previously elucidated when sufficient F^- passivation occurs at the {100} facets.[259]

Observation through electron microscopy strongly indicates that F functions as a facet-directing agent in the synthesis of F,Sn:In_2O_3 NCs, and XPS was used to further probe the presence of F on their surfaces (Figure 6.1 c, Figure 6.6). XPS is sensitive to surface composition, since the escape depth of photoelectrons is only a few nanometers.[214] The existence of F on the F,Sn:In_2O_3 NC surface is revealed by XPS spectra acquired in the In 3p and F 1s regions (Figure 6.1 c). The intensity of the F 1s peak at 684.6 eV, flanked by the In 3p doublet peaks, is consistent as fluorine precursor concentration is maintained at 5% SnF_4 in NC synthesis. As shown in Figure 6.7, In $3d_{5/2}$

signal components are assignable to lattice In-O (444.3 eV), In-OH (445.0 eV), and In-F (445.8 eV) species.[204,259] O 1s signal components are assignable to lattice oxygen (530.0 eV), oxygen adjacent to oxygen vacancies or other charged defects, such as $F_O^{\cdot}$ (531.0 eV), surface hydroxyl (531.8 eV), and carbonyl (533.1 eV) species, respectively.[204,259] The presence of Sn near the NC surface can also be observed through the Sn 3d XPS signal indicating co-existence of Sn and F near the NC surface (Figure 6.7). XPS characterization thus supports the adsorption of fluorine on the In_2O_3 NC surfaces, which is linked to the stability and prevalence of {100} facets in cube-shaped NCs.

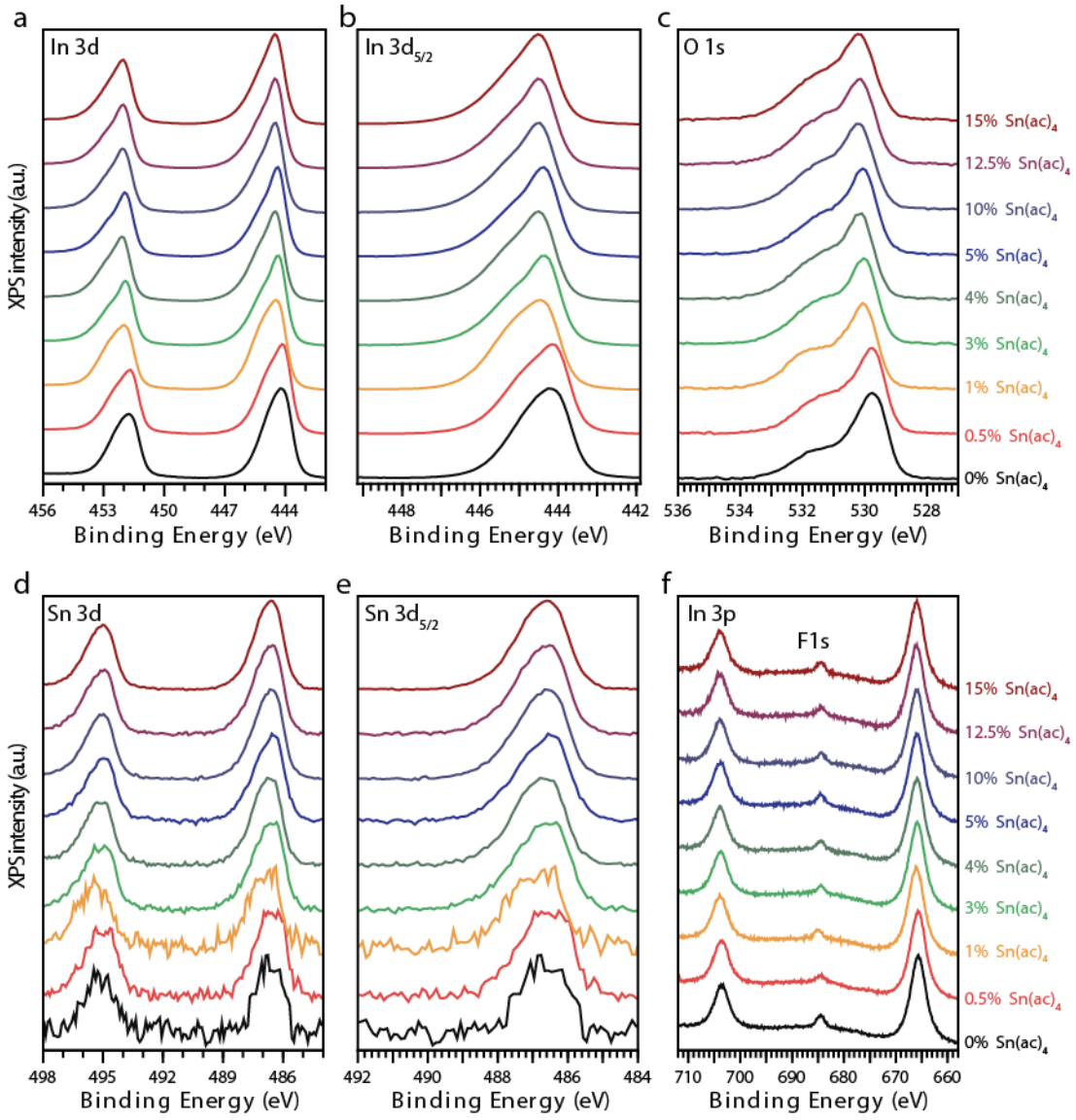

Figure 6.7: XPS Analysis

XPS spectra of F,Sn:In_2O_3 NC Sn dopant concentration series (0 - 15% $Sn(ac)_4$) centered at (a) In 3d doublet, (b) In $3d_{5/2}$, (c) O 1s, (d) Sn 3d doublet, (e) Sn $3d_{5/2}$, and (f) F 1s flanked by In 3p doublet signal peaks.

The cube shape of F,Sn:In_2O_3 NCs can thus be rationalized through the shape control model demonstrated for halide-passivated NCs.[9,186] The {100} group facets become strongly passivated by F^- capping on the F,Sn:In_2O_3 cube NC surfaces when adequate SnF_4 fluoride precursor is present during the NC growth reaction. Fluorine terminated {100} surface exposure becomes favorable, minimizing total surface energy and resulting in well-defined cube-shaped NCs. Under Sn co-doping, stable surface faceting is observed to continue to be prevalent in the range from 0 to 3% $Sn(ac)_4$ dopant precursor concentration as observed through XRD (Figure 6.1 d) through the prevalence of the (400) crystalline index indium oxide bixbyite peak for drop-casted NC samples. $Sn(ac)_4$ precursor concentration over 4% results in rounding of the cube shape until spherical morphology becomes dominantly observed in TEM and a weaker (400) diffraction peak is seen in XRD. This can be explicated by the difference in preferred surface energy in Sn-rich surfaces, as compared to pristine In_2O_3. Fluorine termination of SnO_2 surfaces is reported to cause preferential surface energy stabilization of {102} facets rather than stabilizing {100} surfaces.[279,280] Excessive Sn doping will make In_2O_3 surfaces prone to forming Sn-rich surfaces that more resemble the SnO_2 tetragonal rutile phase, as to cubic bixbyite In_2O_3,[115] leading to perturbed non-{100} facet fluorine terminated NC surface stabilization. Thus, the presence of Sn near the surface results in rounded cube NC morphologies at higher $Sn(ac)_4$ concentration (4 - 5%), and spherical NC shapes at excessive Sn dopant incorporation (10%) as observed in Figure 6.1 a.

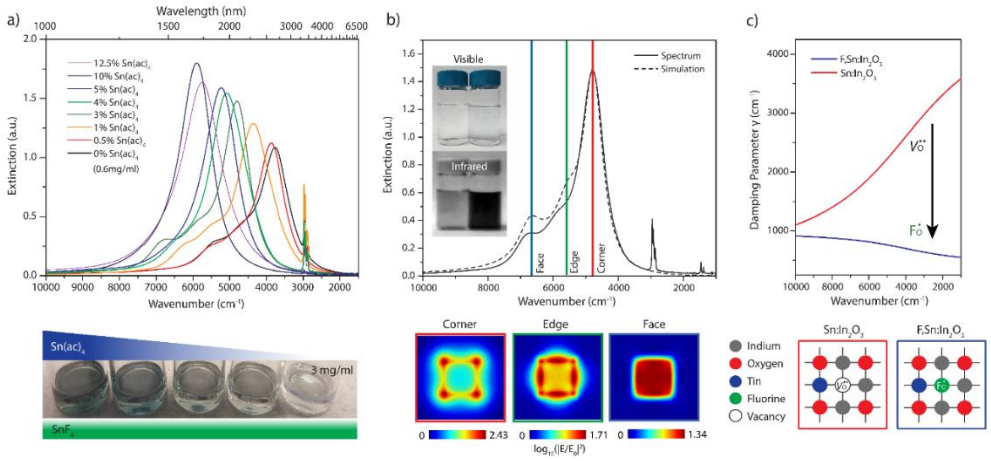

Figure 6.8: F,Sn:In_2O_3 NC optical properties

(a) F,Sn:In_2O_3 NC UV-Vis-NIR/FTIR extinction spectra. Tunable blue-shifted LSPR response is observed as $Sn(ac)_4$ dopant concentration is increased, until the blue shift saturates beyond 10% $Sn(ac)_4$. (bottom) Photograph of hexane dispersed F,Sn:In_2O_3 NCs (3 mg/ml) (0 - 5% $Sn(ac)_4$, left to right). (b) UV-Vis-NIR/FTIR measured extinction spectrum (solid line) for F,Sn:In_2O_3 (3% $Sn(ac)_4$) NC cubes, and simulated extinction spectrum (dotted line). (inset) IR camera photograph of hexane at left, and dispersed F,Sn:In_2O_3 NC 3% $Sn(ac)_4$ (0.1 mg/ml) in hexane at right demonstrating strong, spectrally selective extinction in the IR. (bottom) Near-field maps showing FEM simulated corner (left), edge (middle), and face (right) modes, with 4800 cm^{-1} corner, 5600 cm^{-1} edge, and 6600 cm^{-1} face centered eigenmodes respectively. (c) Extended Drude model damping parameter extracted from extinction spectra for F,Sn:In_2O_3 3% $Sn(ac)_4$ NC (blue) demonstrating low damping, benchmarked to damping parameters from Sn:In_2O_3 NC (red) at similar plasma frequency. (bottom) Schematic of F dopant monovalent ionized impurity occupying divalent oxygen vacancy center, reducing ionized impurity scattering in indium oxide.

NC DOPANT INCORPORATION.

Prevalent in n-type doped metal oxide NC systems,[1,178] substitutional Sn and F dopants incorporated in In_2O_3 NCs can be charge compensated by free electrons. Through additional co-doping of Sn and F in the In_2O_3 lattice, Kröger-Vink defect equilibrium equations demonstrate that deliberate co-doping may promote additional free carriers over a single dopant.[64] The added Sn cationic dopant allows additional free-carrier compensation beyond previously reported F-doped In_2O_3 NCs,[259] leading to LSPR tuning to higher frequency due to higher free carrier concentration within the NCs. Sn is a well-established cationic n-type dopant that induces high free electron concentration in tin doped indium oxide ($Sn:In_2O_3$) transparent conductive oxide films.[189,207] Substitutional F dopants incorporated in the NCs can also be charge compensated by free electrons. F is a similarly established anionic n-type dopant analogue to Sn, inducing a high free electron concentration in fluorine doped tin oxide ($F:SnO_2$) transparent conductive oxide films.[189,207] A Kröger-Vink defect notation equation[215] demonstrates that deliberate In site substitution by Sn cations (Eq. 1), and substitution on O sites by F anions (Eq. 2) induce one free electron per site.[217,281]

$$(2Sn_{In} \cdot O_i)^{\times} \rightarrow 2Sn_{In}^{\bullet} + \frac{1}{2}O_{2\,(g)} + 2e' \qquad \text{(Eq. 1)}$$

$$In_{In}^{x} + 3O_O^x \xrightarrow[InF_3]{} 2In_{In}^{x} + 3F_O^{\bullet} + \frac{3}{2}O_{2\,(g)} + 3e' \qquad \text{(Eq. 2)}$$

It is expected that the extent of dopant incorporation will affect strain of the crystalline lattice. The impact on crystal lattice straining when F^- and Sn^{4+} are incorporated into In_2O_3 NCs is observed by analyzing XRD as a function of Sn

incorporation. F,Sn:In_2O_3 NC (1 - 12.5% $Sn(ac)_4$) XRD patterns confirm the cubic bixbyite In_2O_3 crystal structure is well maintained throughout the Sn dopant range (Figure 6.1 d).[208] The fluorine crystal ionic radius of F^- (1.19 Å) being smaller than that of O^{2-} (1.28 Å) in bixbyite phase In_2O_3,[130] lattice contraction is expected when fluorine occupies oxygen sites.[64,207] Since the Sn^{4+} (0.83 Å) ionic radius is smaller than In^{3+} (0.94 Å), Sn^{4+} cations substituting In^{3+} are also expected to cause lattice contraction to occur.

However, lattice expansion was observed instead of the expected lattice contraction due to F^- and Sn^{4+} incorporation when XRD peak shifts were analyzed through Rietveld refinement. XRD patterns revealed the displacements of the (222) reflections that correspond to lattice expansion induced by Sn^{4+} doping (Figure 6.1 e). Through Vegard's Law fitting, the y-intercept for F,Sn:In_2O_3 NC is at 10.164 Å indicative of an expanded lattice constant when assuming F is present and Sn dopants are not present in the lattice for NCs with similar size, excluding size effects (Figure 6.9).[210] This is larger than the reported bulk In_2O_3 value of a = 10.119 Å,[211] with the expansion attributed to electrostatic repulsion of F ion dopants.[259] Lattice expansion is observed to occur in F,Sn:In_2O_3 NCs, similar to structural trends reported in F:SnO_2 and Sn:In_2O_3 films.[115,212] This expansion can be explained by electronic repulsion of doped impurity centers, as observed in bulk tin doped indium oxide by Köstlin et al.[115] The observed trend indicates at incremental doping levels, the high effective charge of the Sn ions cause a repulsion force which cannot be completely screened by the free electron gas.

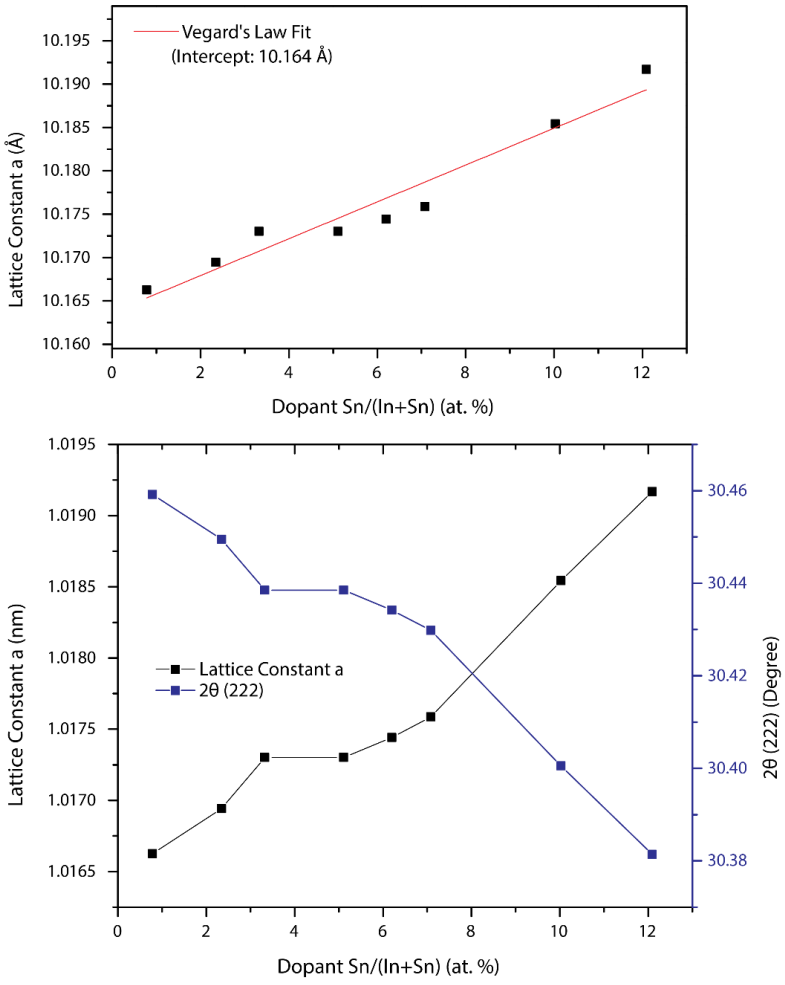

Figure 6.9: XRD Diffraction Peak Shift

XRD (222) peak shift analysis indicating lattice expansion as Sn dopant concentration is increased. (a) Vegard's Law fit of (222) diffraction peak shift, with 10.160 Å intercept. (b) XRD (222) diffraction peak shift as function of incorporated Sn at.% (blue), with expanding lattice parameter constant (black).

F,SN:IN_2O_3 NC LSPR OPTICAL PROPERTIES.

LSPR spectral tuning is achieved by dopant incorporation control, with incremental addition of Sn resulting in generation of free carriers (Eq 1.) leading to higher free charge carrier concentration within the NCs.[57] With the naked eye, NC solvent dispersions are observably bluer in color as Sn dopant is increased (Figure 6.8 a, bottom). UV-Vis-NIR spectra show blue-shifting of LSPR extinction as $Sn(ac)_4$ dopant precursor is increased (Figure 6.8 a). At a high Sn dopant concentration (4 - 15% $Sn(ac)_4$), the NC shape is progressively more spherical leading to observation of a single mode LSPR peak characteristic of sphere shaped plasmonic nanoparticle ensembles. At a lower 0 - 3% $Sn(ac)_4$ dopant concentration, a well-defined multimodal lineshape is observed arising from the cubic NC morphology.[259] The faceting effect of F dopant in this low Sn dopant concentration window allows cube NC morphology to be retained while Sn is incrementally doped.

$$\epsilon_p = \epsilon_\infty - \frac{\omega_p^2}{\omega^2 + i\gamma\omega} \qquad \text{(Eq. 3)}$$

$$\gamma = \gamma_L - \frac{\gamma_L - \gamma_H}{\pi}\left[\arctan\left(\frac{\omega - \gamma_X}{\gamma_W}\right) + \frac{\pi}{2}\right] \qquad \text{(Eq. 4)}$$

The optical properties in plasmonic metal oxides are determined by the dielectric function (Eq. 3), also known as permittivity. It is treated with the Drude model for a collective free electron gas oscillation under an externally applied electromagnetic field. This depends on the bulk plasma frequency ω_p, which is a function of the free electron concentration n_e within the NC, while perturbed by the high frequency dielectric background ϵ_∞. This model has been broadly applied for $Sn:In_2O_3$.[57,263,282] The relation between plasma frequency and free electron concentration $\omega_p = \sqrt{\frac{n_e e^2}{\varepsilon_0 m^*}}$, where n_e is the free electron concentration, e is the elementary electronic charge, ε_0 is the permittivity of free space, and m* is the effective mass, allows assessment of free carrier concentration within the NCs.[65,282] In the extended Drude model, an empirical frequency-

dependent damping function (Eq. 4) is used to model ionized impurity scattering of the free electrons.[283,284] Under external electromagnetic oscillation frequencies lower than the plasma frequency, oscillating free electrons are strongly influenced by screened ionized impurity scattering effectively akin to a direct current electrical field.[57] Ionized scattering centers include intrinsic divalent ionized oxygen vacancy donors[282] and substitutional monovalent dopant ions ($Sn_{In}^{\bullet}$ and $F_{O}^{\bullet}$) in the synthesized NC,[57,65] leading to changes in γ_L low frequency damping. Transiting into the high-frequency regime and above the crossover frequency γ_X, the free electrons no longer interact as strongly with local ionized impurity centers, and damping levels off to a constant high frequency damping value, γ_H, due to reduced scattering probability at higher oscillatory frequency.[57,285]

At higher Sn dopant concentrations, F,Sn:In_2O_3 NCs are near spherical, so their LSPR spectra were fit to a single peak using the extended Drude model. The experimentally collected spherical 10% $Sn(ac)_4$ NC spectrum was fitted using MATLAB, implementing the extended Drude model and reduced square method to extract free carrier concentration determined by the plasma frequency ω_p and impurity scattering-influenced frequency dependent damping parameters γ_H at high and γ_L at low frequencies.[67,122] Plasma frequency parameter extraction allowed determination of a free carrier concentration of n_e = 1.15 × 10^{21} cm^{-3} in the NCs. The plasma frequency of ω_p = 17155 cm^{-1} in this F,Sn:In_2O_3 NC sample is noticeable blue-shifted compared to previously reported highly doped Sn:In_2O_3 NCs at ω_p = 15841 cm^{-1},[67] which is associated with anionic fluorine co-doping effecting additional free carriers in F,Sn:In_2O_3 NCs.[65,259]

Shape induced LSPR modes become dominant in well-faceted cubic particles, with oscillatory near-field eigenmodes becoming apparent in corner-, edge-, and face-centered modes in each NC.[239] Spectral simulation was conducted with the finite element

method (FEM) in the COMSOL wave design module inputting MATLAB extracted dielectric function parameters, reproducing the main absorption spectral feature of the spherical NCs (Figure 6.10). For the multimodal extinction spectra in cubic shaped F,Sn:In_2O_3 NCs, simulations using the FEM based COMSOL wave design module were iteratively refined with the extended Drude model initial parameters from the MATLAB least square method.[65,122] A simulated spectrum showing the three distinct LSPR modes induced by shape, comparable to the experimental extinction spectrum (Figure 6.8 b) was obtained for a F,Sn:In_2O_3 (3% $Sn(ac)_4$) NC. The main peak observed at 4750 cm^{-1} is attributed to the corner mode (red), 5600 cm^{-1} the edge mode (green), and 6600 cm^{-1} the face mode (blue). In F,Sn:In_2O_3 NCs synthesized using variable Sn dopant precursor levels, the free carrier concentrations are observed to increase with Sn dopant concentration until the observed blue-shifting saturates at the maximum observed value of n_e = 1.32 × 10^{21} cm^{-3} for 10% $Sn(ac)_4$ and red-shifts again for higher Sn dopant precursor concentration (Table 6.1). This demonstrates the viability of LSPR tuning in faceted NCs through synthetic dopant incorporation control, while the cubic shape is retained within the range of fluorine induced faceting effects.

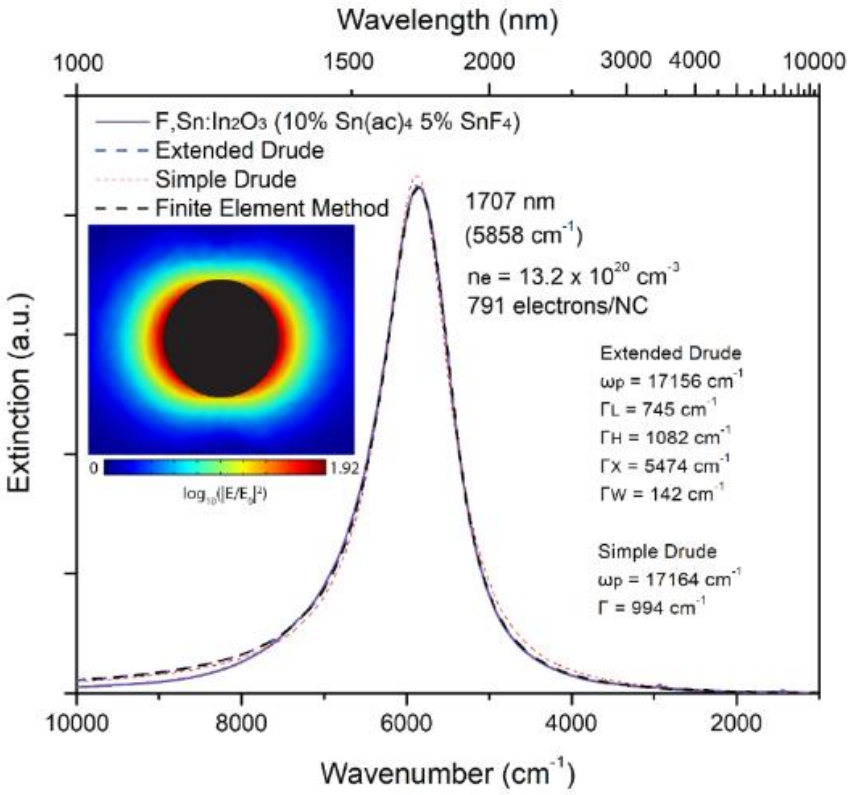

Figure 6.10: LSPR Spectral Fitting

MATLAB fitting and FEM simulated extinction spectrum with near-field enhancement map of a F,Sn:In_2O_3 (10% $Sn(ac)_4$) NC.

F,Sn:In_2O_3 NC	ω_{LSPR} (cm^{-1})	n_e (cm^{-3})	Q
0% $Sn(ac)_4$	3744	0.69×10^{21}	3.59
0.5% $Sn(ac)_4$	3845	0.74×10^{21}	4.04
1% $Sn(ac)_4$	4338	0.94×10^{21}	3.77
3% $Sn(ac)_4$	4789	1.15×10^{21}	5.22
4% $Sn(ac)_4$	5066	1.17×10^{21}	4.26
5% $Sn(ac)_4$	5216	1.25×10^{21}	2.65
10% $Sn(ac)_4$	5858	1.32×10^{21}	5.61
12.5% $Sn(ac)_4$	5737	1.26×10^{21}	4.33

Table 6.1: F,Sn:In_2O_3 NC free carrier concentration

F,Sn:In_2O_3 NC (0 - 12.5% $Sn(ac)_4$) dopant series LSPR spectral peak position (ω_{LSPR}), free carrier concentration (n_e), and NC quality factor (Q) value.

The low-frequency damping parameter is substantially reduced by F co-doping, leading to narrower LSPR modes as compared to only Sn doped In_2O_3 (Figure 6.8 c). The damping function (Eq. 4) incorporates the low frequency damping γ_L that reflects the strength of internal scattering of free electrons.[67,282] The scattering cross section in ionized impurity scattering is proportional to the square of the ionic charge (Z^2). Fluorine induced substitutional $F_O^{\bullet}$ defects, according to Eq. 2, reduce divalent oxygen vacancies $V_O^{\bullet\bullet}$ and allow suppressed ionized impurity scattering to occur within the co-doped F,Sn:In_2O_3 NCs (Figure 6.8 c, bottom).[57,65] As compared to fluorine-free uniformly doped Sn:In_2O_3 NCs previously reported in literature,[67] the damping parameter in fluorine-containing F,Sn:In_2O_3 (3% $Sn(ac)_4$) NCs is observed to be significantly lower with γ_L=

585 cm^{-1} (Figure 6.8 c). Similarly, F,Sn:In_2O_3 NCs at various Sn dopant precursor levels consistently demonstrate reduced impurity scattering near γ_L = 650 cm^{-1} between 0-10% $Sn(ac)_4$ (Table A6.1). In uniformly doped Sn:In_2O_3 NCs, oxygen vacancies and neutral defect clusters $(Sn_{In}^{\bullet} - O_i'')^{\times}$ cause noticeable ionized impurity scattering induced damping in the low frequency regime.[57,67] Previous work demonstrated that damping parameters in Sn:In_2O_3 NCs with surface segregated dopants approach that of oxygen vacancy ($V_O^{\bullet\bullet}$) doped In_2O_3 NCs, around 1000 cm^{-1},[115,286] which was lower than the reported damping in Sn:In_2O_3 NCs with uniformly distributed dopants. The damping parameter of fluorine incorporated F,Sn:In_2O_3 NCs are less than reported values in these surface segregated Sn:In_2O_3 NCs, due to suppression of $V_O^{\bullet\bullet}$ divalent oxygen vacancies with $F_O^{\bullet}$ monovalent ionized defect incorporation. This favorable reduction in ionized defect scattering enables high NC quality factor $Q = \omega_{LSPR}/\kappa$ (Table 6.1), where narrow spectral linewidth κ and high energy LSPR peak frequency ω_{LSPR} is achieved.[287]

Since F,Sn:In_2O_3 NCs exhibit narrow LSPR optical response, it is expected that they can create strong near-field enhancement (NFE) in the IR range. NFE is prominent in the near-field simulations, with intense electromagnetic hot-spots localized at the distinctive morphological features of the NC cube. NFE is observed in cubic F,Sn:In_2O_3 (3% $Sn(ac)_4$) NCs at the geometric corner, edge, and face-centered eigenmodes with NFE factor ($\log_{10}|E/E_o|^2$) values of 2.43, 1.71, and 1.34, respectively (Figure 6.8 b, bottom). At lower Sn dopant precursor levels, e.g. F,Sn:In_2O_3 (0% $Sn(ac)_4$) NCs, lower NFE factor values of 2.23, 1.57, and 1.21 are respectively obtained for corner, edge, and face modes (Figure 6.11). In spherical F,Sn:In_2O_3 (10% $Sn(ac)_4$) NCs with a single LSPR mode, a comparatively low NFE value of 1.92 was obtained due to the absence of high-curvature sharp morphological corner features. To experimentally probe IR near-field effects in

ensemble F,Sn:In_2O_3 NC structures, NCs were assembled to form nanocavity architecture arrays.

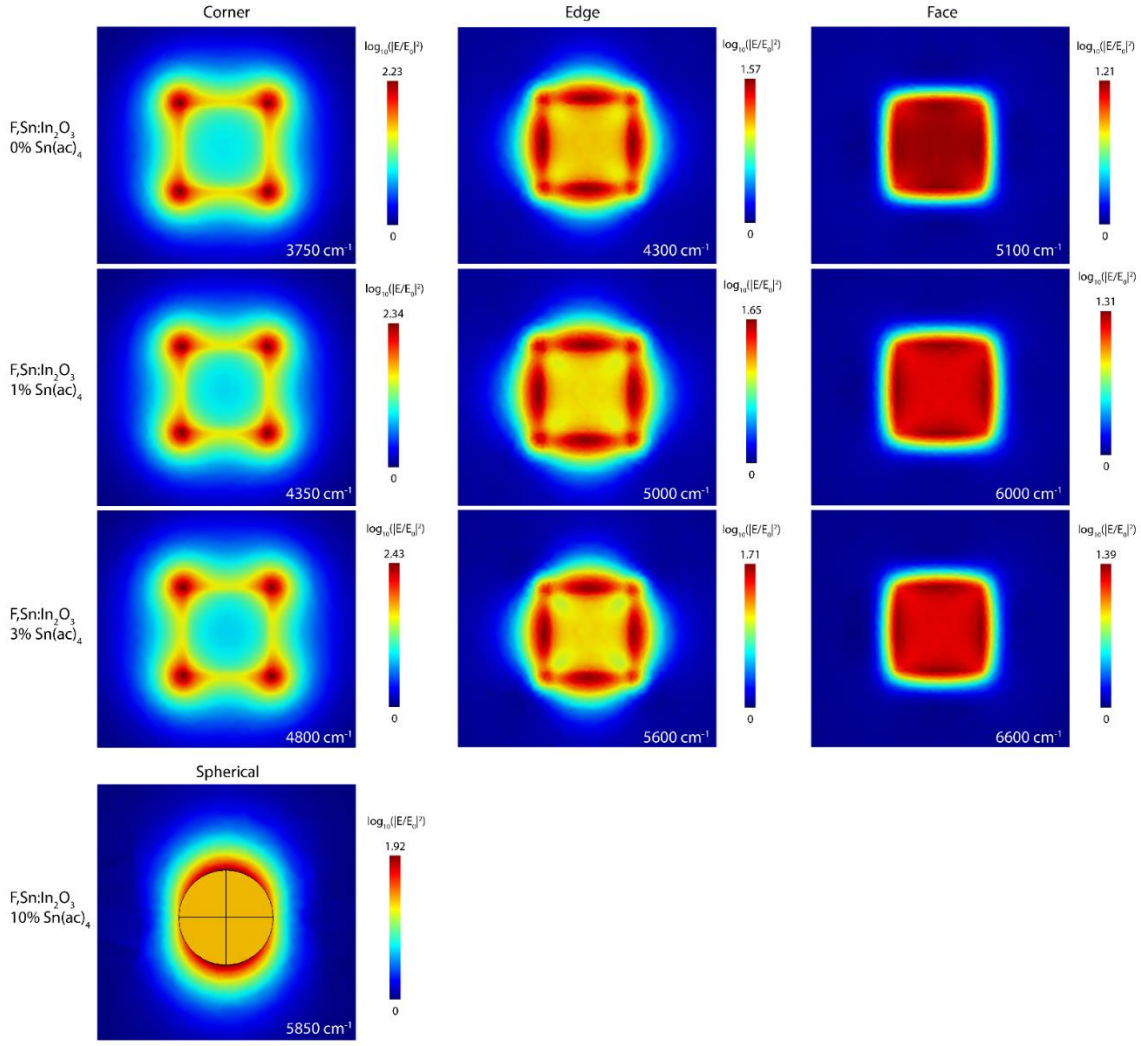

Figure 6.11: Simulated NFE Intensity Maps

FEM simulated near-field enhancement maps of F,Sn:In_2O_3 (0-3% $Sn(ac)_4$) NC cubes and F,Sn:In_2O_3 (10% $Sn(ac)_4$) NC sphere.

Chapter 7: Plasmon-Exciton Coupling in NC Nanocavity Arrays

MONOLAYER F,SN:In_2O_3 NC FILM ASSEMBLY.

Spectral tunability can be advantageously used in monolayer NC film array architectures, realizing tunable IR range near-field nanocavities between the NC arrays and substrate without being restricted to particle size dependent tuning.[261] Spectral LSPR tunability in solution dispersed NCs was achieved as discussed above through chemical Sn dopant incorporation control during colloidal synthesis. By assembling LSPR tuned F,Sn:In_2O_3 NC monolayer films on top of PbS QD monolayer films, self-assembled nanocavities can be fabricated, sandwiching PbS QD emitters between substrate and LSPR active cube NC monolayers. To assemble a nanocavity layer over excitonic PbS QDs, a F,Sn:In_2O_3 cube NC monolayer is fabricated using a modified two-phase assembly method,[271,288] NCs dispersed in an immiscible non-polar hexane phase (1 mg/ml, 100 µl) were floated on top of a polar ethylene glycol phase (Figure 7.1 a, Figure 6.12). Separately, PbS QD monolayer films were fabricated from a dilute hexane-octane dispersion (5 mg/ml) by spin-coating. The ethylene glycol subphase layer was drained through a connected ball valve near the bottom of the Teflon trough. This approach minimizes perturbation of the liquid-air interface assembled film that forms after the hexane layer is fully evaporated under a glass cover.

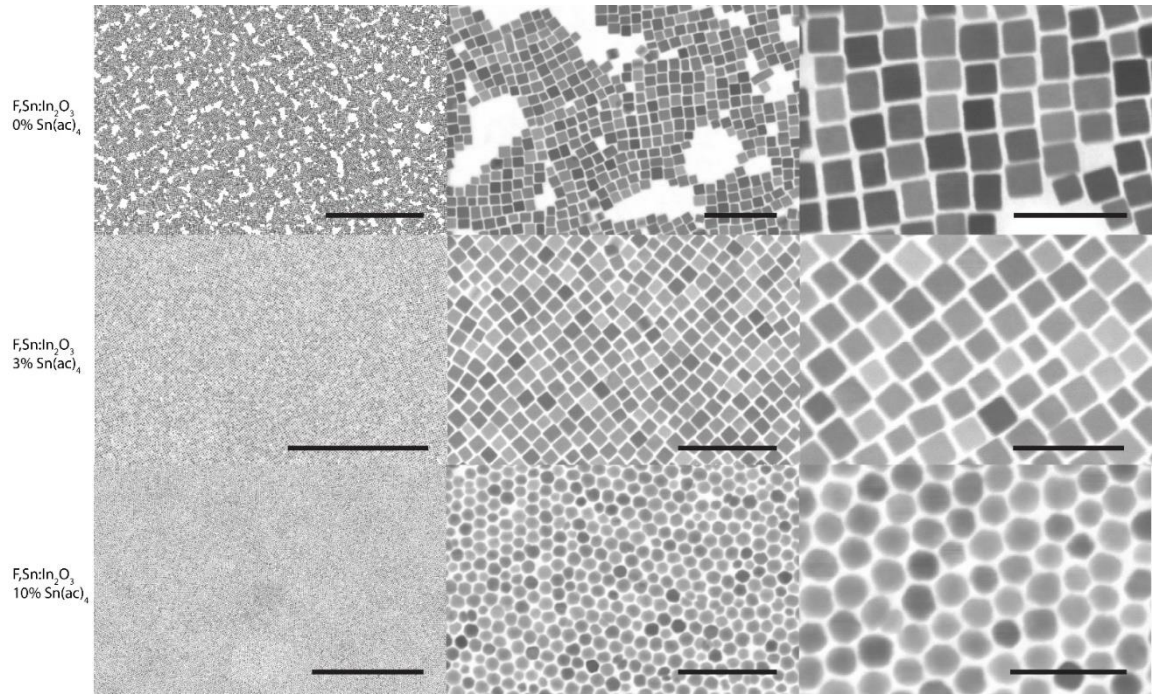

Figure 6.12: Monolayer NC Assemblies

Bright field STEM images of monolayer assemblies of F,Sn:In_2O_3 (0% $Sn(ac)_4$) NC cubes (top), F,Sn:In_2O_3 (3% $Sn(ac)_4$) NC cubes (middle), and F,Sn:In_2O_3 (10% $Sn(ac)_4$) NC spheres (bottom) on SiN TEM grid. Scale bars are 1 μm (left), 100 nm (center), and 50 nm (right).

In simulations, dopant controlled tunable LSPR nanocubes show NFE at well-defined morphological features. To experimentally probe enhanced electromagnetic field due to F,Sn:In_2O_3 NC arrays, emission of PbS QD films is used as a probe. The dependence of the quantum transition rate of the emitters on nanocavity electromagnetic field intensity and the relationship between detuning frequency of the LSPR cube array can be experimentally interrogated, via plasmon-exciton coupling effects. PbS QDs are a direct bandgap semiconductor material with tunable IR photoemission influenced by size-

dependent quantum confinement.[268,289] PbS QDs are synthesized to tune the 1s exciton peak position and correspondingly the PbS film photoluminescence peak frequency (Figure 7.1 b) towards longer wavelengths near the F,Sn:In_2O_3 cube NC cavity resonance.[268]

LSPR spectral tunability in self-assembled F,Sn:In_2O_3 NC monolayer films is characterized using UV-Vis-NIR spectroscopy (Figure 7.1 c). The F,Sn:In_2O_3 and PbS composite film LSPR extinction feature is only modestly perturbed compared to the F,Sn:In_2O_3 NC only films. The F,Sn:In_2O_3 cube (0% $Sn(ac)_4$) monolayer assembly shows a nanocavity mode LSPR peak at ω_{cav} = 3030 cm^{-1}, F,Sn:In_2O_3 cube (3% $Sn(ac)_4$) at ω_{cav} = 3740 cm^{-1}, and F,Sn:In_2O_3 NC (10% $Sn(ac)_4$) at ω_{cav} = 4527 cm^{-1}. Monolayer NC film arrays show LSPR red-shifting due to interparticle plasmon coupling with adjacent NCs when compared with non-interacting TCE solution dispersed NCs. Monolayer F,Sn:In_2O_3 cube (0% $Sn(ac)_4$) arrays show LSPR peak shift of $\Delta\omega_{LSPR}$ = 714 cm^{-1}, F,Sn:In_2O_3 cube (3% $Sn(ac)_4$) of $\Delta\omega_{LSPR}$ = 1049 cm^{-1}, and F,Sn:In_2O_3 NC (10% $Sn(ac)_4$) of $\Delta\omega_{LSPR}$ = 1331 cm^{-1}. This trend is consistent with stronger red-shift due to coupling for NCs with higher overall dopant concentration.[287] The interparticle plasmon coupling resulting in LSPR red-shifting indicates that the NC arrays form a collective ensemble as a nanocavity that can be probed through PbS emissive lifetime measurement correlation.

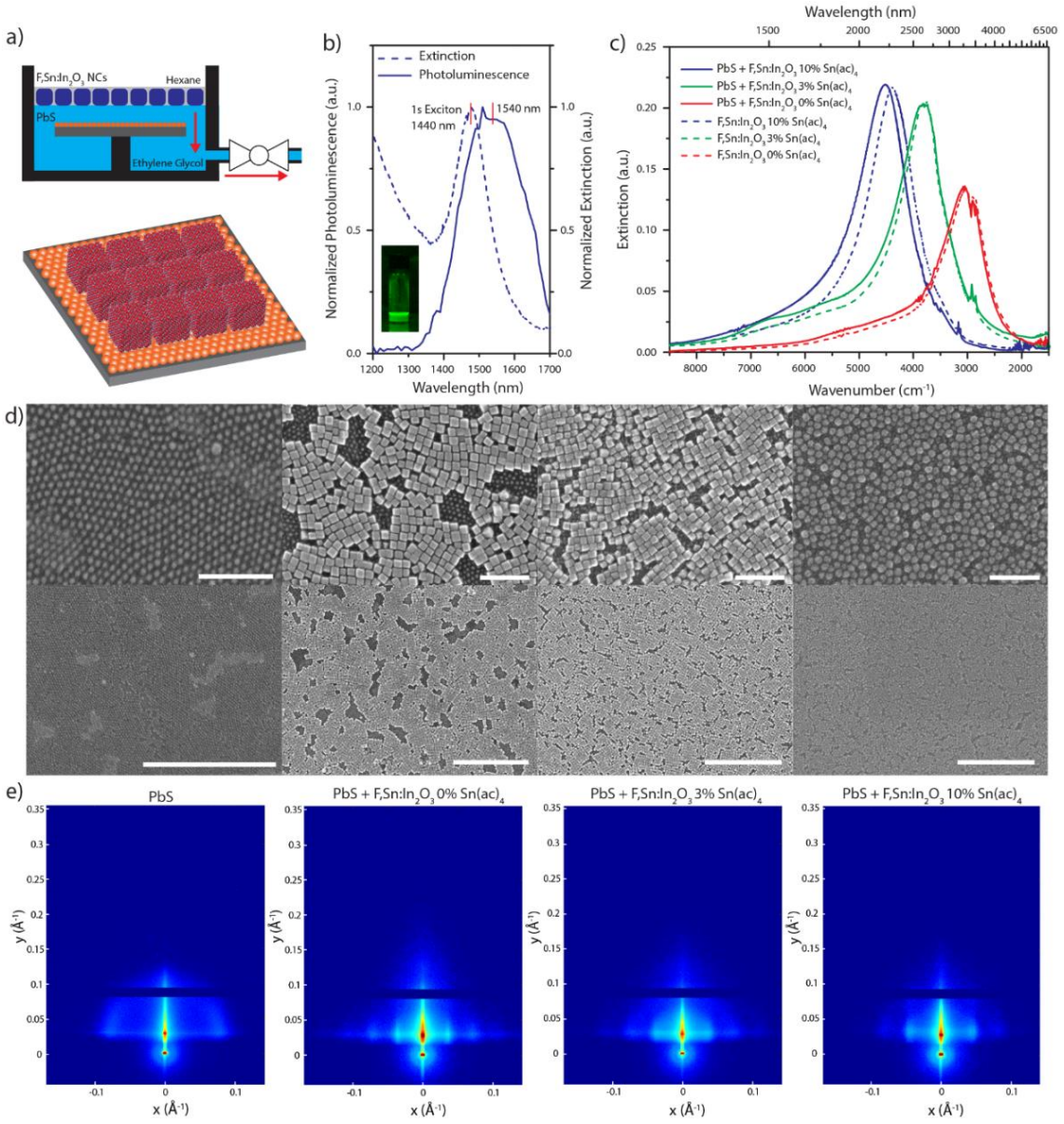
a)
F,Sn:In2O3 NCs
Hexane
PbS
Ethylene Glycol
b)
Extinction
Photoluminescence
1s Exciton
1440 nm
1540 nm
Normalized Photoluminescence (a.u.)
Normalized Extinction (a.u.)
Wavelength (nm)
c)
Wavelength (nm)
PbS + F,Sn:In2O3 10% Sn(ac)4
PbS + F,Sn:In2O3 3% Sn(ac)4
PbS + F,Sn:In2O3 0% Sn(ac)4
F,Sn:In2O3 10% Sn(ac)4
F,Sn:In2O3 3% Sn(ac)4
F,Sn:In2O3 0% Sn(ac)4
Extinction (a.u.)
Wavenumber (cm-1)
d)
e)
PbS
PbS + F,Sn:In2O3 0% Sn(ac)4
PbS + F,Sn:In2O3 3% Sn(ac)4
PbS + F,Sn:In2O3 10% Sn(ac)4
y (Å-1)
x (Å-1)

Figure 7.1: F,Sn:In_2O_3 NC film assembly properties

(a) Liquid-air monolayer NC assembly schematic of Teflon trough, hexane dispersed F,Sn:In_2O_3 NCs on ethylene glycol, and spin-coated PbS QD substrate (top). Ethylene glycol is drained to place a monolayer F,Sn:In_2O_3 NC assembly on top of PbS QD layer (bottom). (b) UV-Vis-NIR spectrum of 1s exciton absorption peak of PbS NCs (dotted) dispersed in tetrachloroethylene with 1540 nm PbS NC film photoluminescence (solid). IR photo (inset) shows photoemission of PbS sample dispersed in hexane. (c) FTIR extinction spectrum of F,Sn:In_2O_3 NC monolayer assembled film on a Si substrate (dotted), and F,Sn:In_2O_3 NC monolayer film overlayered on PbS QD film on a Si substrate (solid) exhibiting very similar extinction. (d) SEM images of PbS QD films, and F,Sn:In_2O_3 (0, 3, 10% $Sn(ac)_4$) NC monolayers over PbS NC films. Bars correspond to 100 nm (top). Wide field SEM images of same films showing monolayer uniformity of film architecture. Bars correspond to 500 nm (bottom). (e) GISAXS of NC monolayer film on Si substrates for (far left) PbS QDs, (middle left) F,Sn:In_2O_3 cubes (0% $Sn(ac)_4$), (middle right) F,Sn:In_2O_3 cubes (3% $Sn(ac)_4$), and (far right) F,Sn:In_2O_3 (10% $Sn(ac)_4$) layered over PbS QD films. Monolayer NC cube arrays show first, second, and third order scattering peaks corresponding to regular NC packing in a planar array.

SEM images of assembled films show the local ordering in F,Sn:In_2O_3 NC monolayers on PbS QDs, with micrometer range uniformity (Figures 7.1 d, A6.11). The F,Sn:In_2O_3 NC cube (0, 3% $Sn(ac)_4$) monolayers show planar cubic packing while the F,Sn:In_2O_3 NC spheres (10% $Sn(ac)_4$) show monolayer hexagonal packing over the PbS QD layers. The PbS QD monolayer is maintained after the F,Sn:In_2O_3 cube NC

monolayer film layer is deposited using the two-phase solution assembly method (Figure 7.2). To further characterize the uniformity of the films, GISAXS was used to observe the ordering of layered F,Sn:In_2O_3 cube and PbS QD films (Figure 7.1 e).[271,290] The scattering peaks for these composite F,Sn:In_2O_3 cube and PbS QD films are consistent to regular particle spacing of the F,Sn:In_2O_3 NC cubes, with periodicity representing the interparticle NC center-to-center distance. For F,Sn:In_2O_3 cubes (0% $Sn(ac)_4$), the periodicity is measured as a = 17.2 ± 0.3 nm with scattering peaks consistent with first, second, and third order in-plane peaks. Higher Sn doped F,Sn:In_2O_3 cubes (3% $Sn(ac)_4$) are observed to have a = 16.7 ± 0.1 nm with similar planar array structure. The F,Sn:In_2O_3 NC (10% $Sn(ac)_4$), periodicity is measured as a = 13.4 ± 0.1 nm with scattering peaks consistent with first, second, and third order (Figure 7.3). The interparticle distances and structure of F,Sn:In_2O_3 NC layers on top of PbS QD films are the same as F,Sn:In_2O_3 only monolayer film arrays. For example, a pristine F,Sn:In_2O_3 cube (0% $Sn(ac)_4$) monolayer array is observed to have interparticle distance of a = 17.5 ± 0.1 nm with apparent first, second, and third order scattering peaks, which is near identical to the structure of a NC cube array overlayered on a PbS QD film. Similar results were also observed for other pristine films, with F,Sn:In_2O_3 cube NC (3% $Sn(ac)_4$) interparticle distance at a = 16.8 ± 0.3 nm, and F,Sn:In_2O_3 NC (10% $Sn(ac)_4$) films at a = 13.2 ± 0.4 nm. In a pristine PbS QD film, an interparticle distance of a = 8.1 nm is observed. GISAXS reveals that the F,Sn:In_2O_3 NC cube monolayer films' local architecture observed through SEM is sufficiently uniform over a wide area for further nanocavity spectral characterization.

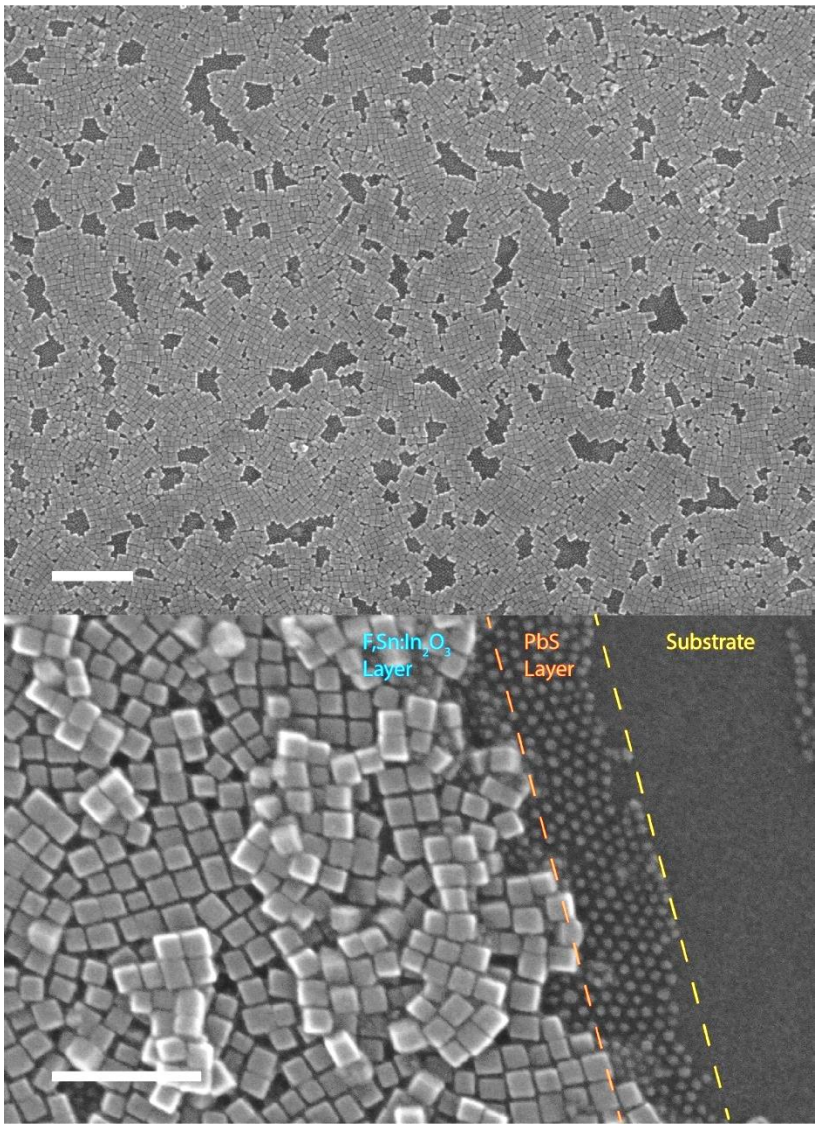

Figure 7.2: NC Cube and PbS QD Monolayer Film SEM

SEM image of PbS QD monolayer underneath F,Sn:In_2O_3 (0% $Sn(ac)_4$) NC cube monolayer on Si substrate. Scale bars are 200 nm (top) and 100 nm (bottom).

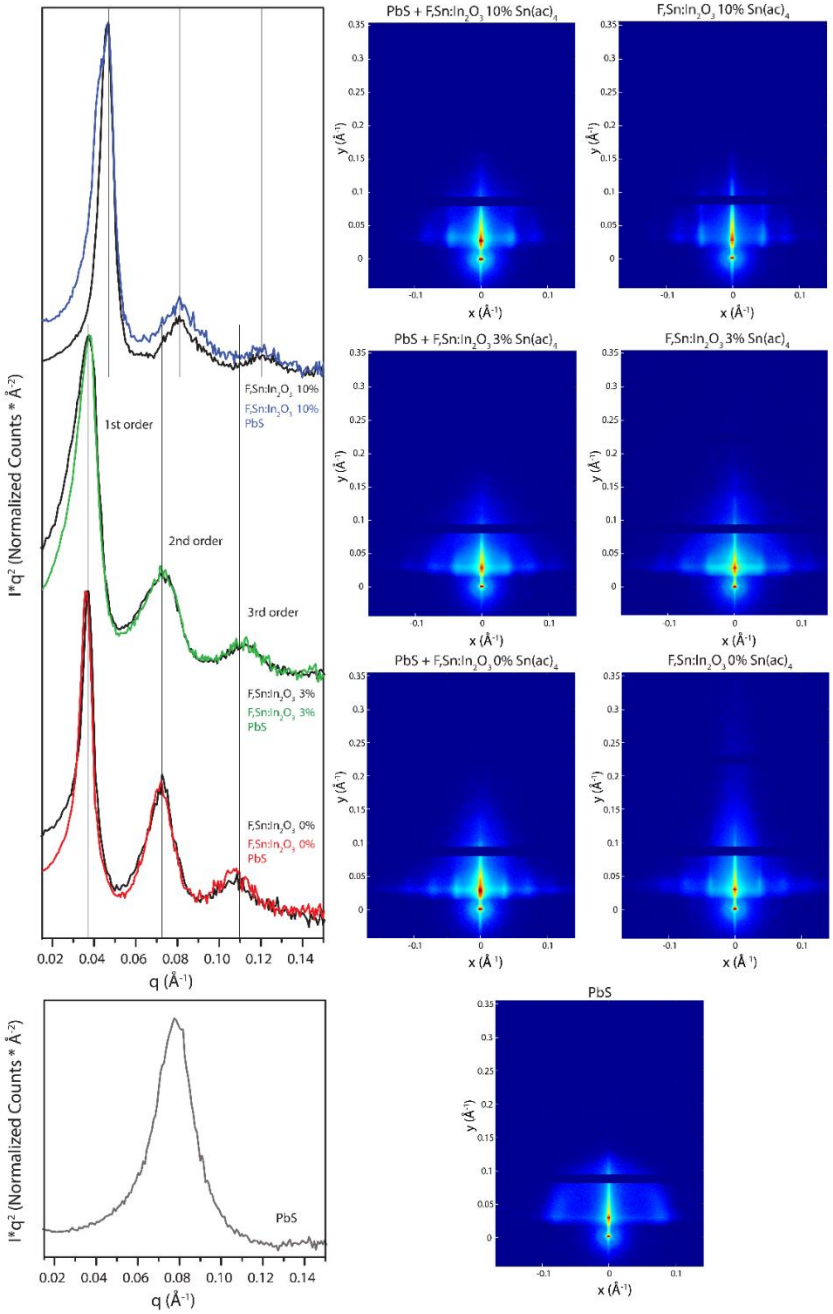

Figure 7.3: Monolayer Film SAXS

SAXS Guinier plot of (a) F,Sn:In_2O_3 (0, 3, 10% $Sn(ac)_4$) NC monolayers over PbS QD monolayers, F,Sn:In_2O_3 NC monolayer, and (b) PbS QD monolayer integrated along x-axis direction.

PLASMON-EXCITON COUPLING AND NANOCAVITY EFFECTS

F,Sn:In_2O_3 cube NCs exhibit IR range LSPR tunability, and simulations predict they will create emergent NFE. These properties can be leveraged to realize dopant induced spectrally tunable IR nanocavities in monolayer film architectures, which has been difficult to access using materials such as Ag or Au noble metal nanoparticles that have high, fixed free carrier concentrations. By placing a PbS QD layer under LSPR active F,Sn:In_2O_3 NC monolayers, QDs can be used to realize exciton-plasmon coupling and to act as a photoluminescent probe to understand tunable IR near-field nanocavities.[275] The photoluminescence decay lifetime (τ_0) is representative of the quantum transition rate from the exciton to the ground state, i.e. hole-electron pair recombination, in PbS QDs. Coupling the LSPR induced enhanced near-field with photoluminescent exciton recombination ($\Gamma_0 = \frac{1}{\tau_0}$) leads to accelerated lifetime decay rate ($\Gamma_{tot} = \frac{1}{\tau_{tot}} = \Gamma_0 + \Gamma_{cav}$).[291,292]

$$\Gamma_{cav} = \left(\frac{4g^2}{\kappa}\right)\frac{1}{1+\left(\frac{2\delta}{\kappa}\right)^2} = \Gamma_{tot} - \Gamma_0 \qquad \text{(Eq. 5)}$$

$$g = \frac{1}{2}\sqrt{(\Gamma_{tot} - \Gamma_0)(1 + \left(\frac{2\delta}{\kappa}\right)^2)\kappa} \qquad \text{(Eq. 6)}$$

The modulation of electromagnetic field in a confined cavity exerts an influence by enhancing the excited state to ground state transition rate (Γ_{cav}) according to Fermi's golden rule, which can be reiterated into the Purcell effect. The coupling strength can be extracted from the experimental photoluminescence lifetime decay rate using Eq. 5. The off-resonance frequency between the plasmonic nanocube monolayer cavity (ω_{cav}) with LSPR cavity linewidth κ, and QD emitter (ω_{emit}) is termed detuning frequency ($\delta = \omega_{cav}$-ω_{emit}).[291] To assess the interaction strength between LSPR and excitons, Eq. 5 can be reorganized to give coupling strength (g) in Eq. 6.[291,293] Controlled dopant

incorporation in NCs is advantageous as LSPR frequency can be tuned in the IR, without relying on size induced tuning as in Ag or Au nanoparticles.

Empirical coupling strength is assessed through IR photoluminescence lifetime measurement with stretched exponential decay curve fitting.[275] A layered assembly of F,Sn:In_2O_3 cube NCs (3% $Sn(ac)_4$) on a PbS QD film was observed to have shortened lifetime of τ_0 = 0.016 ns as compared to a PbS-only film at τ_0 = 0.365 ns (Figure 7.2 a). For reference, a PbS quantum film (ω_{emit} = 6944 cm^{-1}) overlayed by highly off-resonant F,Sn:In_2O_3 (0% $Sn(ac)_4$) NC cubes (ω_{cav} = 3051 cm^{-1}, κ = 28.8 THz) showed little evidence of coupling. The lifetime decay was only weak enhanced, giving g = 0.99 THz (4.09 meV), indicating limited coupling behavior under high detuning frequency (δ = 3893 cm^{-1}). In the case of closer spectral overlap between the LSPR nanocavity and excitonic QD emitters, the F,Sn:In_2O_3 (3% $Sn(ac)_4$) NC cube monolayer (ω_{cav} = 3808 cm^{-1}, κ = 32.7 THz) showed enhanced exciton lifetime decay with a coupling strength of g = 4.08 GHz (16.85 meV) at δ = 3136 cm^{-1}. In a sample wherein PbS QDs are coupled to a film of spherical F,Sn:In_2O_3 (10% $Sn(ac)_4$) NCs (ω_{cav} = 4521 cm^{-1}, κ = 33.3 THz), despite a lower detuning frequency at δ = 2423 cm^{-1} and closer resonant overlap, the coupling strength was observed to be noticeably reduced at g = 1.40 THz (5.78 meV). The narrow cavity linewidth κ at 30 THz range from all monolayer film assemblies (Figure 7.2 c) is representative of the photonic mode decay rate, affirming the IR nanocavity architecture is in the weak coupling regime by comparing the coupling strength to cavity linewidth ($g < \kappa$) .[293–295] The localized photonic mode in the cavity decays faster than the exciton to LSPR coupled Rabi oscillation,[296] leading to enhancement of the accessible pathway in photonic modes of decay, and thus enhanced exciton photoluminescence decay rate induced by F,Sn:In_2O_3 NCs.

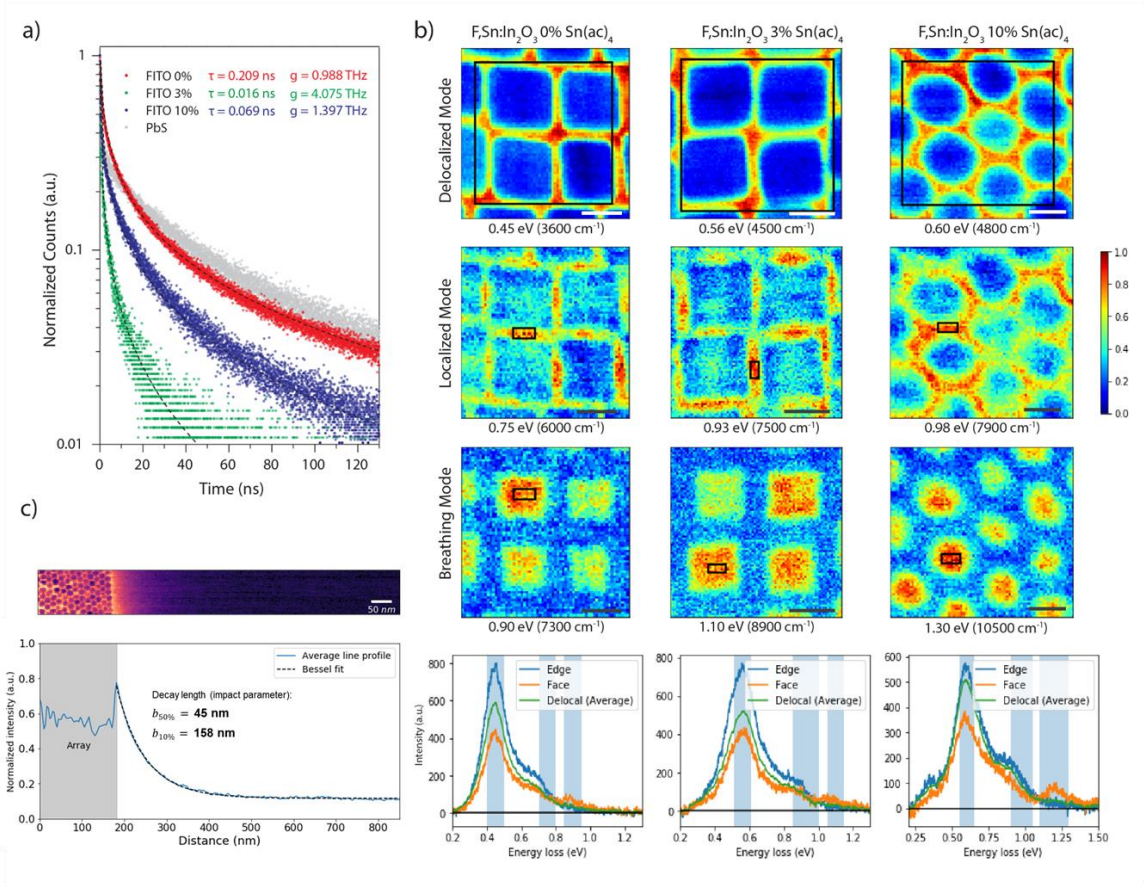
a)
FITO 0% τ = 0.209 ns g = 0.988 THz
FITO 3% τ = 0.016 ns g = 4.075 THz
FITO 10% τ = 0.069 ns g = 1.397 THz
PbS
Normalized Counts (a.u.)
Time (ns)
b)
F,Sn:In2O3 0% Sn(ac)4
F,Sn:In2O3 3% Sn(ac)4
F,Sn:In2O3 10% Sn(ac)4
Delocalized Mode
Localized Mode
Breathing Mode
0.45 eV (3600 cm-1)
0.56 eV (4500 cm-1)
0.60 eV (4800 cm-1)
0.75 eV (6000 cm-1)
0.93 eV (7500 cm-1)
0.98 eV (7900 cm-1)
0.90 eV (7300 cm-1)
1.10 eV (8900 cm-1)
1.30 eV (10500 cm-1)
c)
50 nm
Average line profile
Bessel fit
Decay length (impact parameter):
b50% = 45 nm
b10% = 158 nm
Array
Normalized intensity (a.u.)
Distance (nm)
Edge
Face
Delocal (Average)
Intensity (a.u.)
Energy loss (eV)

Figure 7.4: F,Sn:In_2O_3 NC near-field properties

(a) Photoluminescence lifetime measurement of PbS QD films coupled with F,Sn:In_2O_3 NC monolayer assembly nanocavities. Enhanced decay lifetime is observed when LSPR active F,Sn:In_2O_3 NC cubes are present. (red) PbS QDs coupled to a detuned F,Sn:In_2O_3 (0% $Sn(ac)_4$) NC cube monolayer exhibit weak decay enhancement behavior, while those (green) coupled to a F,Sn:In_2O_3 (3% $Sn(ac)_4$) NC cube monolayer demonstrate high Purcell enhancement. (blue) PbS QDs coupled to spherical F,Sn:In_2O_3 (10% $Sn(ac)_4$) NCs show intermediate decay rate. The laser excitation wavelength was 850 nm, exciting across the PbS band gap, at 25 μW intensity and 5 MHz repetition rate. (b) STEM-EELS maps of F,Sn:In_2O_3 NC arrays. Columns represent (left) F,Sn:In_2O_3 (0% $Sn(ac)_4$) NC cube, (middle) F,Sn:In_2O_3 (3% $Sn(ac)_4$) NC cube, and (right) F,Sn:In_2O_3 (10% $Sn(ac)_4$) NC sphere arrays, with intensity maps normalized to the observed mode. Distinct spatially delocalized, interparticle gap edge localized, and NC localized face breathing modes are observed at respective labeled frequencies. Scale bars are 5 nm. (below) EELS spectra demonstrate near-field tunability, observed in delocalized average mode, localized gap edge, and face breathing mode in demarcated reduced map area for respective F,Sn:In_2O_3 NC arrays. (c) STEM-EELS map of F,Sn:In_2O_3 (0% $Sn(ac)_4$) NC cube assembly array edge. A modified Bessel function of the second kind curve fit of the linear intensity profile shows observation of delocalized LSPR 50% decay length impact parameter of 45 nm and 10% decay length impact parameter of 158 nm. Scale bar is 50 nm.

To further address the nanoscopic localized nature of F,Sn:In_2O_3 NC cube electromagnetic field coupling to PbS QD excitons, the Purcell enhancement[297] in Eq. 7 is

approached with assistance from simulation models and direct STEM-EELS observations. In free space, unperturbed by the local electromagnetic field environment, spontaneous emission can be expressed by Eq. 8.[298] From Fermi's golden rule, the hole-electron pair recombination emission rate in the quantum transition probability can be perturbed by the local electromagnetic field in a photonic cavity environment. This interaction is described in Eq. 9 as a time-independent term expressed by the enhanced local electromagnetic field (E) and exciton transition dipole moment (μ_{12}).[292,299]

$$F_p = \frac{\Gamma_{tot}}{\Gamma_0} \qquad \text{(Eq. 7)}$$

$$\Gamma_0 = \frac{{\omega_0}^3 {\mu_{12}}^2}{3\pi\varepsilon_0\hbar c^3} \qquad \text{(Eq. 8)}$$

$$\Gamma_{tot} = \frac{2\pi}{\hbar^2}|\langle f|\mathrm{d}\cdot\mathrm{E}|i\rangle|^2\rho(\omega_0) = \frac{2\pi}{\hbar^2}|\langle\mu_{12}E\rangle|^2\rho(\omega_0) \qquad \text{(Eq. 9)}$$

The nanocube morphology of infrared LSPR active F,Sn:In_2O_3 NCs allow intense near-field localized resonance due to antenna effects at corners, allowing confinement of light beyond the diffraction limit. In a monolayer assembly array of cubes, the near-field enhancement effect is used to localize a high density of IR range light around the PbS QD array in a nanocavity.[191,275] Whereas photonic modes in free space would be broadly distributed over a wide frequency range, the infrared LSPR active F,Sn:In_2O_3 NCs allow photonic modes to be localized to a controllably tuned resonant frequency. The photonic density of states ($\rho(\omega_0)$) in a nanocavity is confined and centered around an LSPR resonance frequency (ω_{cav}) of quality factor $Q = \omega_{cav}/\kappa$, expressed as a Lorentzian distribution (Eq. 10) corresponding to experimentally observed LSPR cavity extinction spectra. The confined cavity electromagnetic field (E) is expressed and modified into a normalized mode volume (V) in Eq. 11 for a nanocavity architecture.[298,300,301]

$$\rho(\omega_0) = \frac{2}{\pi\kappa}\frac{\left(\frac{\kappa}{2}\right)^2}{\left(\frac{\kappa}{2}\right)^2+(\omega_{cav}-\omega_{emit})^2} \qquad \text{(Eq. 10)}$$

$$|\langle\mu_{12}E\rangle|^2 = \frac{{\mu_{12}}^2\hbar\omega_0}{2\varepsilon_0 n^2 V}\xi^2 \qquad \text{(Eq. 11)}$$

Intraband energy dissipation losses commonly observed in Au and Ag nanocavities can be advantageously avoided in the doped metal oxide nanocavity system. The IR range LSPR is well separated in frequency from band edge loss features, which are located in the near UV spectral range.[300,302] Therefore, emitter to cavity detuning components can be incorporated in Eq. 12 to fully describe the Purcell enhancement factor F_p. To account for the assumed random isotropic orientation between the exciton dipole of spherical QDs in a cavity, a ξ^2 dipole orientation factor of 1/3 is included in the Purcell factor expression. The nanocavity confinement of electromagnetic field modifies the mode volume (V) in Eq. 13, which is a pure electromagnetic property describing the effectiveness of the nanocavity in concentrating the electromagnetic field in confined space.[299,303] The local relative field amplitude of the cavity mode expressed as $\boldsymbol{E}$ is normalized so that norm is unity at the maximum amplitude antinode of the incident electric field (E_0).[299,300]

$$F_p = \frac{3}{4\pi^2}\left(\frac{\lambda_0}{n}\right)^3\left(\frac{Q}{V}\right)\frac{(\frac{K}{2})^2}{(\frac{K}{2})^2+(\omega_{cav}-\omega_{emit})^2}\xi^2 \qquad \text{(Eq. 12)}$$

$$V = \frac{1}{\varepsilon_0 n^2}\int \varepsilon(r)|\boldsymbol{E}(r)|^2 d^3r \qquad \text{(Eq. 13)}$$

NEAR-FIELD SIMULATIONS

STEM-EELS allows direct observation and verification of energy loss signatures associated with spectrally tunable near-field existing in the assembled NC cube arrays (Figure 7.2 b). Near-field intensity was simulated for the interparticle nanocube facet gaps. The emergent delocalized nature of near-field modes was directly observed. Near-field intensity in array assemblies is observed to be stronger compared to a single particle in both simulations and STEM-EELS measurement. In single particle F,Sn:In_2O_3 (10% $Sn(ac)_4$) STEM-EELS, a near-field energy loss peak located at 0.8 eV is weak (Figure

7.6), while a eleven-fold near-field intensity increase was observed in the energy loss peak located at 0.6 eV for assembled NC gaps (Figure 7.6). The interparticle NC array gap near-field shows higher NFE factor ($\log_{10}|E/E_o|^2$) values of 2.35 (Figure 7.7 a), while a single NC shows NFE factor of 1.92 (Figure 6.11). A secondary higher energy mode centered at 0.98 eV emerges from STEM-EELS mapping in NC film arrays that is attributable to a localized gap confined near-field mode (Figure 7.2 b), while map profiles show the main peak mode centered at 0.6 eV is a delocalized near-field ensemble mode. These maps in Figure 7.2 b show elastic scattering contrast due to a relatively significant portion of the electron beam undergoing high angle scattering when positioned on the particles. Hence, while less signal appears to be present when inspecting the map for the delocalized mode, this plasmon is essentially uniform in intensity across the entire ensemble. Figure 7.5 shows this by comparing the zero loss peak map with this delocalized map. The F,Sn:In_2O_3 NC monolayer film series observed by STEM-EELS demonstrates that the near-field is spectrally tunable, noticeable by the blue-shift in the primary energy loss at higher Sn dopant concentration, while the localized secondary mode is also observed in all three F,Sn:In_2O_3 NC assemblies (Figure 7.2 b, Figure 7.5). A high energy breathing mode was observed localized within the NC volume, which is a nonradiative dark mode that evades light scattering due to a symmetrical zero net dipole moment, but is exclusively observed through EELS.[276,304] Through STEM-EELS, long-range plasmonic near-field decay is directly observed at the edge of the nanocube assembly (Figure 7.2 c). Simulated NFE factor values of 2.12 in F,Sn:In_2O_3 (0% $Sn(ac)_4$) NC arrays and 2.09 in F,Sn:In_2O_3 (3% $Sn(ac)_4$) NC arrays were derived at interparticle nanocube gaps (Figure 7.7 a). Secondary localized modes experimentally observed through STEM-EELS were simulated, with NFE factor values of 0.34 between the cube

facet gaps in F,Sn:In_2O_3 (0% Sn(ac)$_4$) NC arrays, 0.36 in F,Sn:In_2O_3 (3% Sn(ac)$_4$) NC arrays, and 0.68 in F,Sn:In_2O_3 (10% Sn(ac)$_4$) NC arrays.

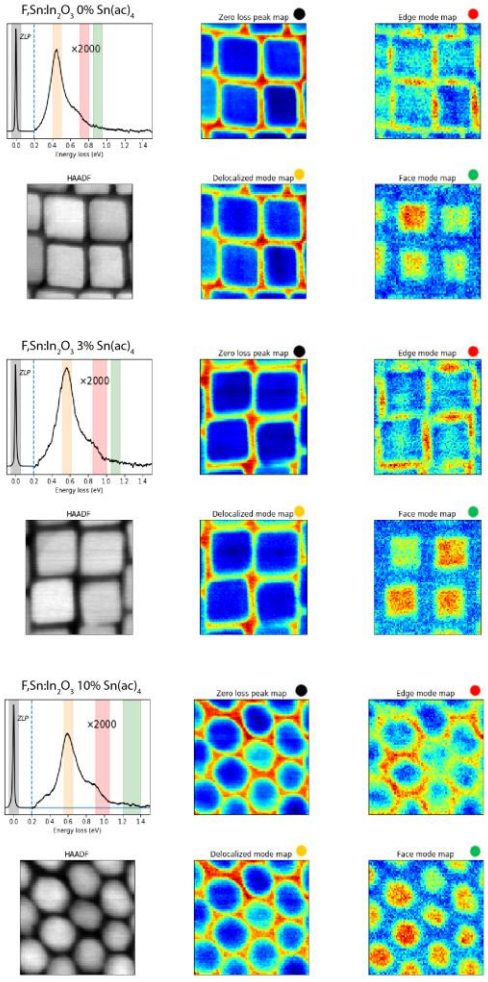

Figure 7.5: STEM-EELS Near-Field Modes

STEM-EELS background subtracted intensity map for F,Sn:In_2O_3 (0, 3, 10% Sn(ac)$_4$, top to bottom, respectively) NC monolayer assembly arrays. STEM-HAADF images in greyscale, zero loss peak prior to background subtraction, delocalized main mode, localized interparticle gap edge mode, and breathing mode at faces of NCs. Note the similarity of the delocalized mode map to the zero loss peak map.

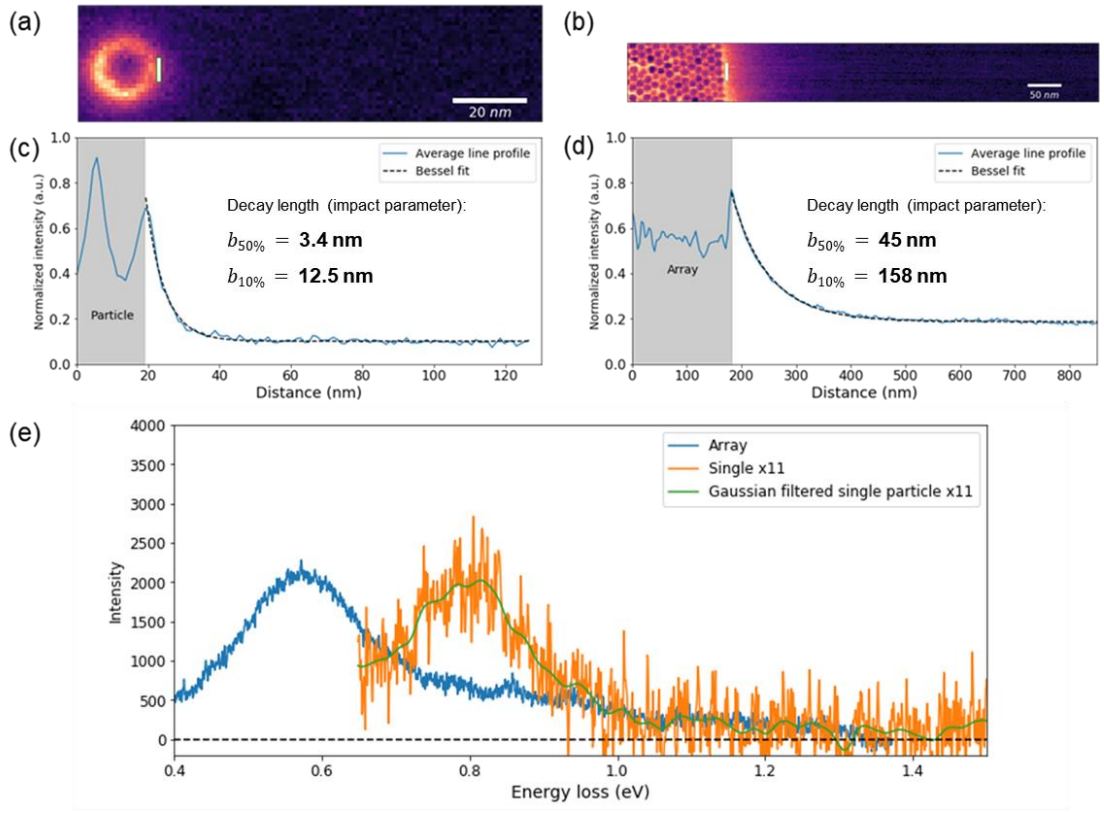

Figure 7.6: Near-Field Comparison

(a) STEM-EELS intensity map of a single F,Sn:In_2O_3 (10% $Sn(ac)_4$) NC and (b) near-field decay fit with modified Bessel function of the second kind, showing a decay length to 50% of max intensity, as well as to 10% of max intensity with lengths of 3.4 nm and 12.5 nm, respectively. (b) STEM-EELS intensity map of NC array edge of same dopant concentration and (d) near-field decay fit with modified Bessel function of the second kind, showing decay lengths of 45 nm and 158 nm, respectively. (e) Intensity comparison of near-field mode located 1 nm from both the particle and edge of the array which shows an eleven-fold increase of the array relative to the single particle.

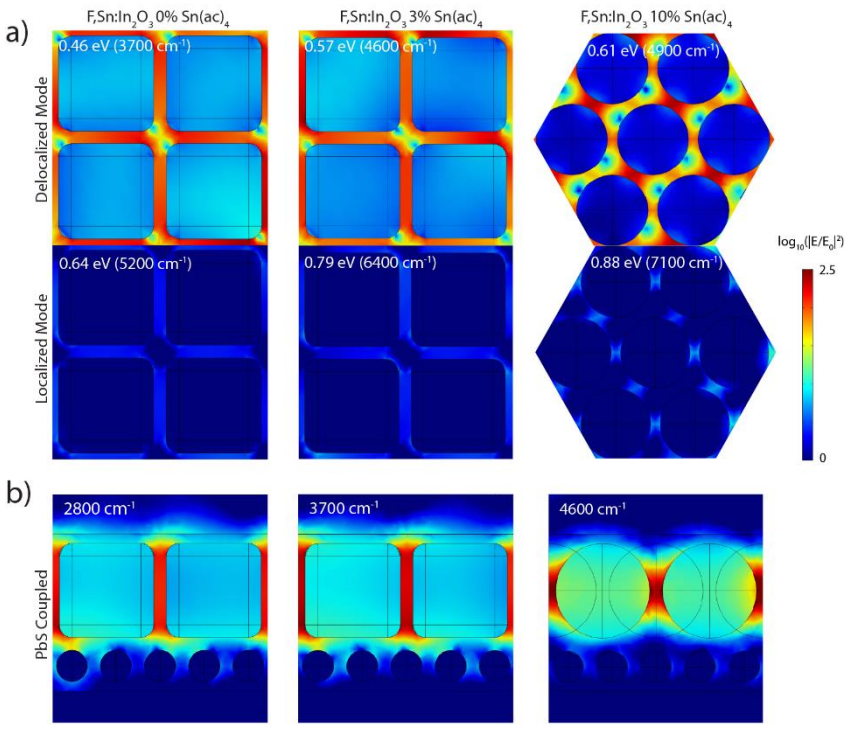

Figure 7.7: F,Sn:In_2O_3 NC near-field simulations

(a) Simulated local NFE maps of F,Sn:In_2O_3 NC assemblies. Top-down view of F,Sn:In_2O_3 NC arrays and interparticle gaps simulating STEM-EELS environmental configuration without coupling to PbS QDs. Delocalized (top) and localized (middle) mode NFE maps at respective frequencies, as observed through STEM-EELS. (b) Cross-section NFE maps of coupled nanocavity assemblies, with PbS QDs coupled between the substrate and F,Sn:In_2O_3 NC array. Columns represent (left) F,Sn:In_2O_3 (0% $Sn(ac)_4$) NC cube, (middle) F,Sn:In_2O_3 (3% $Sn(ac)_4$) NC cube, and (right) F,Sn:In_2O_3 (10% $Sn(ac)_4$) NC sphere arrays.

The collective electromagnetic mode volume in spectrally tuned NC films is correlated and quantified with the above Purcell effect lifetime decay enhancement measurements. The assembled cube array nanocavity local electromagnetic field intensity predicted through FEM simulation (Figure 7.7 b) is used to quantify the near-field enhanced electromagnetic field (E) from incident excitation (E_0).[300–302,305] With the PbS QD emitters (ω_{emit} = 6944 cm^{-1}, λ = 1540 nm), coupled to a F,Sn:In_2O_3 (3% Sn(ac)$_4$) cube NC cavity (Q = 3.49), the components of Eq. 12 can be evaluated. With locally enhanced electromagnetic near-field simulations under E_0 = 0.125 V·m^{-1} incident intensity from the 25 μW excitation source ($I = \frac{cn\varepsilon_0}{2}|E_0|^2$), the delocalized photonic mode volume of the F,Sn:In_2O_3 NC array can be extracted. With the PbS QDs placed in the gap cavity between a cube array and the substrate, excitonic QDs experience an averaged near-field enhancement of E/E_0 = 1.30 (Figure 7.7 b). With the coupled energy exchange between plasmon and exciton, electromagnetic waves may migrate ballistically at a surface plasmon resonance micrometer length scale.[306] The electromagnetic wave can be planarly confined in the nanocavity gap between NC array and substrate, giving arise to a characteristic photonic mode volume.[307,308] The ensemble photonic cavity mode can be estimated (Eq. 13),[309] and the delocalized nanocube mode volume for F,Sn:In_2O_3 (3% Sn(ac)$_4$) NCs correspond to 49 × 49 nm^2 LSPR-exciton coupled real-space delocalization range,[306] while further detuned F,Sn:In_2O_3 (0% Sn(ac)$_4$) NCs with E/E_0 = 1.35 had a 117 × 117 nm^2 delocalization range, when nanocavity thickness of 10 nm is assumed. For the spherical F,Sn:In_2O_3 (10% Sn(ac)$_4$) NC nanocavity (Q = 4.07), a lower NFE enhancement of E/E_0 = 1.03 was simulated and the delocalized NC cavity array is calculated to have 76 × 76 nm^2 real-space delocalization range. This explains the observed differences of the LSPR energy in FTIR extinction spectra between solution dispersed F,Sn:In_2O_3 NCs and the red-shifted spectra

of the monolayer film assemblies. Through the photoluminescence lifetime analysis, the local near-field environment was probed to quantify the delocalized photonic cavity environment in the monolayer film architectures. The existence of near-field delocalization in a NC array was directly observed at the edge of the assembly through STEM-EELS. The intensity of the plasmonic near-field decays exponentially with a decay length of 113 nm (Figure 7.2 c, Figure 7.6) as compared to a single particle characteristic decay length of only 9.1 nm. This dramatic difference further supports that the near-field cavity is not individually confined around each NC, but an ensemble collective behavior is existent in the nano-assembly array leading to a delocalized nanocavity mode volume with an optical effect that is readily apparent through exciton lifetime correlations.

CONCLUSION

Sn co-doping allows LSPR spectral tunability to be achieved in cubic faceted F-doped In_2O_3 NCs. The F dopant plays a role in selectively passivating {100} crystallographic facet surfaces of In_2O_3, while addition of a Sn co-dopant precursor creates a synthetic handle for controlling LSPR tunability. In these colloidally synthesized F,Sn:In_2O_3 NC cubes, shape-dependent LSPR multimodal extinction features arise at the well-defined corners, edges, and faces of the NCs. Near-field enhancement effects arise at these morphological features while retaining spectral tunability. The dopant-induced, size-independent spectral LSPR tunability observed in solution dispersed F,Sn:In_2O_3 NCs can be further exploited in self-assembled films. The tunable near-field effect can be leveraged and enhanced by fabricating dense plasmonic nanocavity arrays

in long-range ordered monolayer architectures, prepared by liquid-air interface assembly. IR range photoluminescent PbS QDs were coupled with the LSPR near-field tunable F,Sn:In_2O_3 NC nanocavity structure, inducing plasmon-exciton coupling. By controlling the detuning frequency between PbS QD emitters and LSPR active F,Sn:In_2O_3 NC nanocavities, variable Purcell enhancement of the exciton decay rate was observed. To further understand the spatial near-field nature of assembled NC arrays, direct observations of LSPR near-field spatial distributions were made by monochromated STEM-EELS mapping. Intense localized near-field was observed between F,Sn:In_2O_3 NCs in the interparticle gap arrays, while ensemble plasmonic behavior was emergent. Extensive LSPR delocalization was apparent within and at the edge of F,Sn:In_2O_3 NC array assemblies, which creates a delocalized collective mode volume as supported by Purcell enhancement analysis.

F,Sn:In_2O_3 NC nanocubes induce strong LSPR near-field response in the IR range, a property that can be further amplified by creating spatially dense and tunable nanocavity arrays, without relying on size dependent tuning as in conventional Ag and Au noble metal nanomaterials. The optical properties observed in F,Sn:In_2O_3 NCs have the potential to be harnessed in photocatalytic applications,[310] ultrafast photonic switching,[275] and plasmonic molecular sensors.[311] Coupling excitonic photoemission and LSPR near-field enhancement, derived from QD and plasmonic material classes of particles respectively, can enable photonic ‘assembly of light’ towards hybrid forms of light-matter interaction.[294] By synthetically tuning LSPR across an extended IR spectral range, faceted NCs with enhanced near-fields may have potential for coupling to low-energy elementary excitations beyond excitons, found only in the IR range. These may include phonons,[312] polarons,[313] polaritons,[314] and molecular vibrations,[315] which were previously hard to approach with conventional noble metal classes of plasmonic

nanostructures. The extended synthetic tunability of LSPR in doped metal oxide NCs, including F,Sn:In_2O_3 nanocubes, may enable this class of materials to unlock previously unrealized LSPR coupled light-matter interactions and phenomena.

Experimental Methods:

Materials:

Indium (III) acetate ($In(ac)_3$, 99.99%), Tin (IV) acetate ($Sn(ac)_4$), Lead (II) chloride ($PbCl_2$, 99.999%), Sulfur (S, 99.99%), Oleic acid (OA, 90%, technical grade), Oleyl alcohol (OlAl, 85%, technical grade), Octane (98%, reagent grade), 1-Butanol (99.9%), Ethylene glycol (99.8%), and Tetrachloroethylene (99%, anhydrous) were purchased from Sigma-Aldrich. Tin (IV) fluoride (SnF_4, 99%) was purchased from Alfa Aesar and Oleylamine (OlAm, 80-90%) was purchased from Acros Organics. Hexane (99.9%), Acetone (99.5%, Certified ACS), Isopropyl alcohol (99.5%, Certified ACS), and Methanol (99.8%, Certified ACS) was purchased from Fisher Chemical. Hellmanex-III cleaning solution was purchased from Hellma Analytics. All chemicals were used as received without any further purification.

Fluorine Doped Indium Tin Oxide (F,Sn:In_2O_3) Cube Synthesis:

All synthesis procedures are undertaken by employing standard Schlenk line techniques using a modification of previously reported methods for continuous slow injection synthesis of indium oxide NCs.[14,316] $In(acac)_3$ 1342.97 mg (4.6 mmol), SnF_4 48.68 mg (5%, 0.25 mmol), $Sn(ac)_4$ 53.23 mg (3%, 0.15 mol), and oleic acid (10 ml) are loaded in a three-neck round-bottom flask in a N_2-filled glove box. The precursors are stirred with a magnetic bar at 600 rpm and degassed under vacuum at 120 °C for 15 min.

The injection solution is added at rate of 0.2 ml/min, into 13 ml of oleyl alcohol maintained at 290 °C vented with a 19-gauge needle under inert N_2 gas flow. The reaction mixture turns blue a few minutes into the injection. Subsequently, growth is terminated by removal of the heating mantle and cooled by blowing air on the three-neck flask vessel. The NCs are dispersed in hexane, then ethanol antisolvent is added and centrifuged at 7500 rpm for 10 min. The washing procedure is repeated 3 times and NCs are re-dispersed in 10 ml of hexane. The resultant NC dispersion is centrifuged at 2000 rpm for 3 min to remove non-dispersible aggregates and the supernatant was collected as the NC stock sample. Larger sized NCs were synthesized by controlling the volume of injection solution (1 to 20 ml) while keeping other reaction parameters identical. Doped F,Sn:In_2O_3 NCs (0 - 15 % $Sn(ac)_4$) concentration series are synthesized by controlling the $Sn(ac)_4$ to $In(ac)_3$ molar precursor ratio, while SnF_4 is maintained at 5% molar ratio, keeping other reaction parameters identical. The Sn doping level of NCs is characterized by ICP-AES on a Varian 720-ES ICP optical emission spectrometer after digesting the NCs with aqua-regia solution (a mixture of 35% concentrated HCl and 70% HNO_3 in 3:1 ratio respectively).

Lead Sulfide (PbS) QD Synthesis:

Synthetic procedures by Weidman et al. with standard Schlenk line techniques are used to synthesize PbS QDs.[268] A sulfur hot injection solution is prepared in a N_2 glovebox with sulfur 20 mg in oleylamine 3.75 ml stirred at 120 °C for 30 min. A lead solution is prepared by combining $PbCl_2$ 2.50 g (9 mmol) with oleylamine 7 ml in a three-neck flask. The solution is degassed at 120 °C for 30 min and pressurized with N_2 until the temperature is stable. 2.25 ml (0.375 mmol) of prepared sulfur solution is swiftly injected into the lead solution and the reaction is allowed to proceed for 5 min. A washing

procedure is repeated 3 times by dispersion in 20 ml of hexane, precipitation with alcohol antisolvents (10 mL butanol, 5 ml methanol), and centrifugation at 4000 rpm for 5 min. Oleic acid 2 ml is added in between wash steps to promote colloidal stability. Excess $PbCl_2$ precipitates are centrifuged out at 4000 rpm for 3 min and PbS QD supernatant in hexane is kept as a stock solution.

Film Fabrication:

Diced (1 x 1 cm^2) undoped silicon (Si) substrates are sonicated in solvents for 30 min in the following order: Hellmanex-III (5% by volume) in deionized (DI) water, DI water rinse prior to next step, acetone, isopropyl alcohol, and hexane. Diluted PbS QD solution (5 mg/ml) in hexane:octane 1:1 by solvent volume is spincoated onto a Si substrate at 1500 rpm for 90 sec, then at 4000 rpm for 2 min for drying, providing monolayer PbS film fabrication. F,Sn:In_2O_3 NC monolayers over PbS films are fabricated by modification of liquid-air interface assembly described earlier by Dong et al.[271,272] A Teflon well (2 × 4 × 4 cm^3) was custom made with a ball valve at trough bottom to minimize liquid-air interface perturbation during liquid drainage. A Si substrate with a PbS QD film is placed on an elevated (1 cm) Teflon platform immersed in an ethylene glycol subphase. 100 µl of dilute F,Sn:In_2O_3 NC dispersion in hexane (1 mg/ml) is dropcast onto the subphase surface with a pipette, and trough is covered with a glass slide. F,Sn:In_2O_3 NC monolayer self-assembly is allowed to proceed while hexane gradually evaporates for a duration of 15 min. The ethylene glycol subphase is allowed to drain out of the trough by opening the ball valve with minimal perturbation to the self-assembled NC film. Residual ethylene glycol on the film substrate is dried in a room temperature vacuum oven for 24 h. The same procedure is used for NC array fabrication over SiN

TEM supports, but with the absence of PbS QDs. Surface organic ligands are removed by plasma cleaning under Ar in excess of 15 min for TEM support samples.

UV-Vis-NIR/FTIR Spectra Measurement:

UV-Vis-NIR spectral measurement are conducted using an Agilent Cary 5000 UV−Vis−NIR spectrophotometer, FTIR spectral measurement are conducted using a Bruker Vertex 70 FTIR at 4 cm^{-1} scan resolution for solution and film samples. Hexane dispersed NCs are vacuum dried, redispersed in tetrachloroethylene (TCE), and loaded into KBr window 0.05 cm pathlength liquid cell for solvent dispersion UV-Vis-NIR and FTIR measurement.

X-ray Diffraction Analysis:

X-ray diffraction (XRD) samples are prepared by drop-casting 20 mg/mL solution of F,Sn:In_2O_3 NCs on Si substrates. The data is collected with a Rigaku MiniFlex 600 X-ray diffractometer using Cu Kα radiation (1.54 Å). High resolution of the (222) diffraction peak is measured in a Rigaku R-Axis Spider diffractometer using Cu Kα radiation at 1.54 Å, with NC powders mounted in a mineral oil loaded Kapton loop. Rietveld refinement is conducted via the GSAS-II software.[209]

Electron Microscopy:

F,Sn:In_2O_3 NCs are characterized by Hitachi S5500 scanning electron microscope (SEM). Particle size analysis is done with ImageJ with a 100 particle count. High resolution transmission electron microscopy (HRTEM) images and selected area electron diffraction (SAED) are acquired with a JEOL 2010F TEM at 200 kV. Elemental spectrum acquisition of F,Sn:In_2O_3 cubes dropcast on silicon substrates is carried out using a

Hitachi S5500 SEM with a Bruker XFlash EDX detector attachment at 5 kV. Elemental deconvolution was performed with Bruker Quantax software reference at zero-tilt angle P/B-ZAF correction.

X-ray Photoelectron Spectroscopy (XPS):

Samples are prepared by drop casting NC dispersions on silicon substrates and the measurements are performed in a Kratos Axis Ultra DLD spectrometer with a monochromatic Al Kα source (1486.6 eV). Wide survey scans are acquired at analyzer pass energy of 80 eV and the high-resolution narrow region scans are performed at a pass energy of 20 eV with steps of 0.1 eV. Spectral acquisitions are performed with photoelectron take-off angle of 0° with respect to the surface normal and pressure in the analysis chamber maintained at around 10^{-9} torr. Data analysis is performed in CasaXPS software using the Kratos relative sensitivity factor library. The binding energy (BE) scale is internally referenced to the C 1s peak (BE for C-C = 284.8 eV).

Grazing Incidence Small-Angle X-ray Scattering (GISAXS):

Grazing incidence small-angle X-ray scattering is performed using a SAXSLAB Ganesha SAXS system. Assembled NC film samples on Si substrates are loaded in the SAXS system vacuum chamber. Monochromatic X-ray radiation of wavelength of 1.54 Å is used. The incident angle of the beam was 0.2°. Small-angle scattered photons are collected with a PILATUS3 R 300K detector with 487 × 619 pixels and a pixel size of 172 μm × 172 μm positioned at appropriate distances from the sample (1084 mm for GISAXS).

Time-resolved Photoluminescence:

The samples are pumped with a Coherent Chameleon Ultra Ti:sapphire laser operating at 850 nm and 5 MHz rep rate, down-converted from 80 MHz using an AOM-based pulse-picker. Excitation and collection are in a reflection geometry using a Mitutoyo NIR 0.42 NA long working distance objective. The collected emission is then sent to a fiber-coupled superconducting nanowire single photon detector (SNSPD) from Single Quantum. Histogram of the SNSPD signal output is done using a PicoQuant HydraHarp 400 Picosecond event timer triggered by the AOM pulse-picker.

Scanning Transmission Electron Microscopy - Electron Energy Loss Spectroscopy (STEM-EELS):

Plasmon near-field mapping is performed in a Nion high energy-resolution monochromated STEM-EELS at Oak Ridge National Laboratory operated at 60 kV and a Nion Iris spectrometer.[256,257] Identical energy resolution of 145 cm^{-1} (18 meV) is set to optimize the resolution between the plasmon peaks and the signal in the monochromated beam.

Appendix

SUPPORTING INFORMATION FOR CHAPTER 2

Size and morphology characterization of Ce:In_2O_3 NCs by STEM and XRD, morphology characterization of thin films by SEM and XRD, discussions on in-filling solution, discussions on the relationship between the concentration of the in-filling solutions and Hall parameters, structural, optical, and electrical properties of Sn:In_2O_3 NC-based films.

Text A2.1. In-filling Solution

The in-filling of combustion solution occurs due to the high capillary pressure, $p_c = 2\gamma\cos\theta/r$, where γ is the surface tension, θ is the contact angle, and r is the effective radius of capillary. The θ between combustion solution and dense tin-doped indium oxide (Sn:In_2O_3) film was very small at 6.4^o (Figure 2.6 a), due to the interaction between the polar metal oxide surface and the polar 2-methoxyethanol solvent (γ = 31.2 mN/m). The r of the NC arrays is only a few nanometers. Assuming that the r of the NC arrays is approximately 10 nm, the capillary pressure between the in-filling solution and the NC pores is calculated as 156 atm, indicating the solution can completely infiltrate into the NC arrays in a short time.

On the other hand, for effective in-filling, the diameter of the solute molecule of the in-filling solution should be smaller than the pore size of NC arrays. Dynamic light scattering (DLS) data of the combustion solution shows that the indium nitrate-urea complex, the solute of in-filling solution, has a hydrodynamic diameter of 0.7 nm, which is small enough to infiltrate into the pores (Figure 2.6 b). The in-filling process is less

practicable by common solution-phase deposition methods such as sol-gel or NC methods because the methods incorporates nanometer-sized particles.

Text A2.2. Relationship Between the Concentration of the In-filling Solution and Hall Parameters

The electrical properties of NC-based composite films are highly dependent on the concentration of the in-filling solution. Undoped indium solutions of various concentrations were in-filled into 21 nm-sized Ce:In_2O_3 NC arrays with a thickness of ~100 nm. The resistivity of the NC array is 1.26 Ω·cm, while that of the nanocomposite films prepared by in-filling the array with the solutions of 0.1, 0.2, 0.3, 0.4, 0.5, 0.75, 1, and 1.5 M are 3.20×10^{-1}, 7.46×10^{-2}, 7.87×10^{-2}, 7.09×10^{-2}, 1.32×10^{-2}, 1.02×10^{-2}, 1.25×10^{-3}, and 1.44×10^{-3} Ω·cm, respectively (Figure 2.7 c). Interestingly, the resistivity decreases stepwise with concentration, dropping sharply between 0.4 and 0.5 M, and between 0.75 and 1 M. The Hall effect measurement of composite films with different in-filling solution was conducted to determine the origin of the stepwise and rapid change of resistivity. As the concentration of in-filling solution increases, mobility increases in a stepwise manner, while carrier concentration increases steadily, indicating that the resistivity decrease is primarily due to the mobility increase (Figure 2.7 c-e).

The stepwise trend can be explained by SEM images and thickness data of the composite films (Figure 2.7 a, b). An SEM image of the NC-only film shows the presence of small voids between NCs, mid-sized gaps of ~10 nm, and large valleys of ~20 nm, which were originated from ligand removal during thermal annealing. Due to these voids, gaps, and valleys, the NC-only film has a poor mobility, 0.197 $cm^2/V{\cdot}s$.

As higher concentrations of in-filling solution fill more pores between the NCs. The mobility and the concentration of the in-filling solution shows a linearly positive

relationship in the range from 0 to 0.2 M. However, the mobility of the 0.2 M in-filled composite film is only 3 $cm^2/V{\cdot}s$ due to the presence of remaining gaps and valleys (Figure 2.7 a). Although the 0.2 M solution allows several NCs to be connected by filling small voids, the concentration is not high enough to fill the large-sized gaps and valleys.

The mobilities of the composite films made of 0.2, 0.3, and 0.4 M of in-filling solution were almost constant. The SEM images of the composite films showed that the small voids between the NCs were completely filled, while the large gaps and valleys were not yet filled. At this concentration range, the thickness of the composite film did not increase compared to the original NC array, indicating that there are gaps in the film that are still not in-filled.

For the $Ce:In_2O_3$ NC-based composite films from 0.5 M and 0.75 M in-filling solution, the mobility increases to ~15 $cm^2/V{\cdot}s$ due to the filling of the medium-sized gaps between NC clusters, but the large-sized valleys are still not in-filled.

The $Ce:In_2O_3$ NC-based composite film in-filled with 1 M solution shows ultra-high mobility of 60.4 $cm^2/V{\cdot}s$. The high mobility indicates that the in-filling process was complete with 1 M solution. The completion of the in-filling process was also confirmed by the fact that the gaps and valleys were not observed in the SEM image of the 1M composite films. When the concentration of in-filling solution exceeded 1 M, the mobility decreased slightly. This reduction seems to be due to the thick indium oxide overlayer (~130 nm). In conclusion, in-filling with the 1 M solution can produce composite transparent conducting oxide (TCO) films with the best electrical properties.

SUPPORTING INFORMATION FOR CHAPTER 4, 5

Details of nanocrystal characterization (SEM, EDX, TOF-SIMS, XPS, EPR, TGA, and XRD), nanocrystal aliquots (time and temperature series SEM, FTIR), solid-state NMR details (quantitative ^{19}F NMR, Knight-Korringa relation, ^{115}In simulated lineshape parameter), DFT simulation (supercell, DFT calculation), and details of monochromated EELS (background subtraction, non-negative matrix factorization, and modal deconvolution).

Text A4.1: DFT Calculation

DFT calculations were performed using the Vienna Ab-initio Simulation Package (VASP)[249,250] with PAW pseudopotentials[251] in the package. The Perdew-Burke-Ernzerhosf (PBE) exchange-correlation functional[252] was used in all the DFT calculations. A 3×3×1 Monkhorst-Pack k point mesh for the Brillouin zone integration and a vacuum layer of 15 Å to prevent interactions between periodic images of the slab were used. A kinetic energy cut-off of 400 eV was used for the plane-wave expansion, and all atomic positions were fully relaxed until the final force on each atom was less than 0.01 eV/Å. For NMR calculations, a higher kinetic energy cut-off (600 eV) was used.

The formation energy of F substitution (F_O) is calculated as following

$$E_f = E(\text{surface w } F_O) - E(\text{surface}) + \mu(O)/2 - \mu(F)/2 \qquad (1)$$

Where E(surface) and E(surface w F_O) are the total energies of surface and surface with one F substituting O. μ(O) and μ(F) are chemical potentials of O and F. Since μ(O) and

μ(F) are independent of different substitution sites, the relative formation energy depends only on the first two terms.

A linear relation was used for converting the DFT calculated NMR isotropic shielding σ_{iso} into the chemical shifts (δ). Five fluorides LiF, NaF, KF, CaF_2, BaF_2 were selected to get the linear relation, an expression agreeing with a previously published result[317]:

$$\delta = -0.83\ \sigma_{iso} + 95 \qquad (2)$$

Coordinates for In_2O_3 (100) and In_2O_3 (111) structures in VASP CONTCAR format are as follows:

In_2O_3 (100)

9.9479999542000002 0.0000000000000000 0.0000000000000000
0.0000000000000000 9.9479999542000002 0.0000000000000000
0.0000000000000000 0.0000000000000000 27.7336997986000000
In O
40 60
Direct
0.7525169732919569 0.0296396430709342 0.1337636414651940
0.7477826996679984 0.4710382993187525 0.3253429990272371
0.2600062118907686 0.4766770192503617 0.1315532765146359
0.7497198736438193 0.7502797525315665 0.2293038077463887
0.4599288701440778 0.0003446014506734 0.2297026591439707
0.0017698430935349 0.7467022479679470 0.1448448708017381
0.4981164739838813 0.2467147270642133 0.1448860548847348
0.4979456256022348 0.7534195680840700 0.3141978917808199
0.0399981163248213 0.5003344941650454 0.2296848808841525
0.2501526969168987 0.7498834438026912 0.2292678509678731
-0.0047885174780774 -0.0574659863919370 0.0333044737218666
-0.0042503524105405 0.0563746103127683 0.4258866439707051
0.5050026671830469 0.4422890021584604 0.0333175862846791
0.5042343817789179 0.5564298911086245 0.4258823802554133
0.0020604979455072 0.2534160184889672 0.3142066020896721
0.2399995638756793 0.0229628782840355 0.3276359426849331
0.7502793484644377 0.2503321228746266 0.2293202744097023
0.2498089396404409 0.2499428868140885 0.2292822632356146
0.2600031523306698 0.5229652579071387 0.3276370324307730
0.2399421985619636 0.9766121746162600 0.1315575232085610
0.7522122471697704 0.9710351801311849 0.3253386906373043
0.2113979140157464 0.2865717132214902 0.0319566721134606

0.2889017461806254 0.2129191576747469 0.4272949439382301
0.9361674038988517 0.4784752040249644 0.0381305867042806
0.9361965410362508 0.5212675300149441 0.4211697661637093
0.4893766215369506 0.2535532304156948 0.3380040311979366
0.0106493262495978 0.7535452227859080 0.3379948479076575
0.0106768218830828 0.2471999959501957 0.1211238803246735
0.5638044778384135 -0.0214700561065124 0.0381399438889196
0.5638111183098856 0.0212089241596164 0.4211659947842135
0.7881682082562118 0.2331509133245561 0.0343569734073174
0.7124090361489703 0.2663289073340482 0.4247625537024564
0.5342590354486102 0.4999851386299261 0.2296377012729126
0.9657379314920804 -0.0000309288883032 0.2296444613560615
0.4893226625256925 0.7472019454628481 0.1211229706882783
0.7474463920191496 0.5296032637316064 0.1337167275970441
0.2886169305173190 0.7865955297889300 0.0319432736595537
0.2110757134266596 0.7130067673589524 0.4273022253393339
0.7119032296535994 0.7334314645938868 0.0343556795763899
0.7875929893143747 0.7663705886083737 0.4247388152022506
0.3884419833857574 0.1550157107652663 0.2799337171893533
0.6158999466758619 0.1040990141292275 0.1888855530569733
0.1174327257975349 0.8944746220722891 0.1904966953261887
0.1593899450025471 0.1300643020536721 0.0815947389622075
0.1439413335934321 0.1307423295655144 0.4723996315788169
0.1095194980830849 0.1591982133171590 0.3704731823972385
0.1176651014425633 0.1054837092421697 0.2685677598023457
0.1436196471068065 0.8685260962938727 -0.0131970692442131
0.1589731051490081 0.8704232590919755 0.3779995890429362
0.6157213737294746 0.8961636070758643 0.2702435831244483
0.3823306114131919 0.6054838144759236 0.2685656391121452
0.8840433842921706 0.6040557964378119 0.1888530593944245
0.9899096914445744 0.2948268570656142 0.0031812175192541
0.8847345251973645 0.3435454787822231 0.3831410200271899
0.1606452499276839 0.3798866868639343 0.2828842385223458
0.6076651832660396 0.3458572628973305 0.2803063222864412
0.8928849152334810 0.1542265218806211 0.1787823480318239
0.6155654116057114 0.1565053197573417 0.0760250474607713
0.5104012442276754 0.2048979430543249 0.4560765295087074
0.8842749174322980 0.3961748433692661 0.2702572042448862
0.3824965950742543 0.3945320848066564 0.1905087078870896
0.1601936534740032 0.6200153854533089 0.1760703434564908
0.1110855839945480 0.3457938588937585 0.1792055539063989
0.3405806582594754 0.6301359601502390 0.0816002010822904
0.3560456960149171 0.6308224271921790 0.4723967381185763
0.3397041259251773 0.1199959517441305 0.1760878600638962
0.3904752958914073 0.3406524284150912 0.0886874885386576
0.3393099877048139 0.8798578667126176 0.2828796309348585
0.3566137102232974 0.3682006466986895 -0.0131657219132079
0.3410017902058393 0.3703825517084519 0.3780000223471583
0.8844048165991567 0.6564758455585699 0.0759982139732335
0.9895988496436332 0.7049728305630563 0.4560736150000165
0.1114879291529695 0.5736888476594835 0.3797314790056293
0.7104029863806860 0.4162037990148684 0.0058613598785576
0.6071858437236053 0.4121832495239300 0.3812010105716666

0.6554473741649393 0.6235661590261274 0.2821723882838827
0.6071101112571776 0.6541979378741175 0.1787569478842874
0.6066778550311418 0.5877520185911750 0.0778786110678378
0.7098807725940578 0.5834208040981355 0.4533579961342082
0.6552492453086789 0.3769323005654893 0.1767905852062364
0.1116992162975002 0.4264715764536274 0.0793364461005822
0.8933594093354014 0.0876858132972737 0.0779475300044535
0.7900965406133152 0.0833190302267801 0.4533557807720184
0.3885298761429513 0.0736288416682970 0.3797292897079259
0.3888978565261295 0.8457797816745890 0.1792112916104437
0.6586335974106767 0.8644753820155902 0.0967791903878677
0.1095073129462155 0.8405984695469069 0.0886576474975356
0.3904803188671857 0.6592119385396182 0.3704650339317172
0.1115343662718217 0.6549808925068831 0.2799213290299286
0.3882922770634633 0.9264646767581304 0.0793451975262456
0.7897248171752193 0.9165078456184568 0.0058729495753927
0.8928312569140008 0.9121841666762877 0.3811787107038878
0.6582929050922557 0.1355779520084339 0.3624536751177566
0.5101836990114385 0.7949738088861631 0.0031551036292739
0.6152789110528384 0.8435395540508912 0.3831040463950261
0.8445591602815878 0.1235777095666033 0.2821818433161787
0.8417248571614886 0.6355753607003869 0.3624464501418229
0.8923208957783165 0.8458318922419762 0.2802988359865186
0.8413566805174200 0.3644189638308232 0.0967646116227202
0.8447284555368183 0.8769202921944323 0.1767924292001187

In_2O_3 (111)

14.0685997009000001 0.0000000000000000 0.0000000000000000
-7.0342998505000001 12.1837647367000006 0.0000000000000000
0.0000000000000000 0.0000000000000000 25.6667995453000017
In O
64 96
Direct
0.4777457936155412 0.5969713902261118 0.1536993152334679
0.1493200916028093 0.9355548285163289 0.3979098777408613
0.0012029428917768 0.1436799571452807 0.1427701379866635
0.6712212496064648 0.4823743805724157 0.3768676110307334
0.5018432345652923 0.1406297859445554 0.1349643778521953
0.1693135063379162 0.4770415458959228 0.3854230337916097
0.7387448616954033 0.8708347538435874 0.1478186141299877
0.3998994965084183 0.1917752829763495 0.3875537108944304
0.7486227798490087 0.6083022325095204 0.1348748213820898
0.4172768202551556 0.9403336557131279 0.3850775117104618
0.5129792652686549 0.8803943758426378 0.1534383447165133
0.1742564396334660 0.2140300687528076 0.3980575112544535
0.5118655536681940 0.3809868867934243 0.1570787533130880
0.1858175427574963 0.7173833059280648 0.3948398037948000
0.9669133300429804 0.8574880305374188 0.1428203200682283
0.6269914798228631 0.1880600806313497 0.3766278947733707
0.7290746865712340 0.1306643654899078 0.1572322505157548

0.3926841923772564	0.4685041825995336	0.3949486325003969
0.9116329394534674	0.6968613546463900	0.0279170728385452
0.5706165982743630	0.0347974972670420	0.2675655728519326
0.2292490336777616	0.6323400317265646	0.1535758890812799
0.8960971200504922	0.9605833342636130	0.3978462496317718
0.2527519244143506	0.1094212898134215	0.1429225534795110
0.9210611063357768	0.4384829527304826	0.3764780066572766
0.9692903412440022	0.3610850861307207	0.1350078343867638
0.6332648563979862	0.6924987397018818	0.3852865072911013
0.9789925209647861	0.5981627888535309	0.1569615337788820
0.6415461945644092	0.9239334868342661	0.3946271492122515
0.8949284603321520	0.1979001376979604	0.0280728663445722
0.5746841459215716	0.5391736215403158	0.2677741665815683
0.7399933749846727	0.3699492941645550	0.1452211880101193
0.4067686130534919	0.7033252010042185	0.3988162976976349
0.1425577211125581	0.9244755784149866	0.0390067064909375
0.8119566903967869	0.2628025397640671	0.2728760753384278
0.6637630291318821	0.4710066224112902	0.0174843670052533
0.3355799429797842	0.8098543432971518	0.2621065341408412
0.1712297704226059	0.4826000108133067	0.0209156302360639
0.8345617861957844	0.8085463348813582	0.2582410953130477
0.4130830730427816	0.2149856968599496	0.0280721871128993
0.0747794901864132	0.5356957016479980	0.2676312584396377
0.4209456810915189	0.9383092908014752	0.0206088579768672
0.0841303221835929	0.2758579104686794	0.2584287785414033
0.1858365472071559	0.2184561360618647	0.0391328662021356
0.8469094718734872	0.5492715336094870	0.2725516512696309
0.1803244421684663	0.7144972439300845	0.0304742391021761
0.8441801016531911	0.0455038014004826	0.2801822793519782
0.6388723543364473	0.1927144295719307	0.0176866434064047
0.3005815280238662	0.5266307086288585	0.2623545022066178
0.3955274671565610	0.4660178078117257	0.0305757823823934
0.0647586479885560	0.7984608926569755	0.2803538564910624
0.2423523525375610	0.3719907151784678	0.1481323107275126
0.9018981056298241	0.7098767782213888	0.3872642542585837
0.8916660638510129	0.9673044968667915	0.0389725450544476
0.5608390830460812	0.2976744734946505	0.2725798182318188
0.9167440508104224	0.4456354405440022	0.0175451920852449
0.5842272349201368	0.7742961600223025	0.2621345403326695
0.6269477664743361	0.6887237505120438	0.0206966541526557
0.3017459540134485	0.0262986641259026	0.2584484685124856
0.6438670463934494	0.9295126194146370	0.0302829922974411
0.3117071730799172	0.2666950899285792	0.2806571454324436
0.2395121832279784	0.8679151825446640	0.1479103479458852
0.9180979742341604	0.2079692937492138	0.3872099367655407
0.4063593660818670	0.7031661313748869	0.0171062892213825
0.0736864666032168	0.0368981005273858	0.2704902976681710
0.8105730588328142	0.5256257770664872	0.1889757521246807
0.4896723863821861	0.8662035868319680	0.4339559038969955
0.6024756295353096	0.5547841039247740	0.1808395136619828
0.2592536027517762	0.8837819349181523	0.4234145278797697
0.8327505655844052	0.5318377638167170	-0.0030912090566694
0.5070034971108772	0.8669136472338678	0.2446160400512731

0.5780302145971647 0.3008328832963026 -0.0030177279436457
0.2426104628183142 0.6400941253778007 0.2446712184288792
0.0623947249433775 0.5076155908988409 0.1806994348985420
0.7345337754020420 0.8507465053307814 0.4234505871128691
0.8953462413300212 0.4557450312124620 0.1020734890211449
0.5577964948859419 0.7794143887611454 0.3456691932444721
0.1315976021689074 0.7026649049023799 0.1201573623599496
0.8028168502203270 0.0410516143070050 0.3647492359148409
0.8005827033576541 0.7632161474776158 0.1735550389448515
0.4731206726617175 0.1024850989477098 0.4157225760944332
0.9687825888473938 0.8737292357674444 0.0397537075334636
0.6419037265550348 0.2099671709644683 0.2903210956391589
0.6808690977142446 0.9783075966313576 0.1200773140445572
0.3483780552230571 0.3072506308815789 0.3651728964814631
0.0727402022496548 0.3097553776239705 0.1737172277544432
0.7396485670403046 0.6365323310144265 0.4157802904777943
0.8247827608392787 0.2992693175586489 0.1891613593330777
0.4867475484969337 0.6204381897534201 0.4341527915584614
0.0149945792051961 0.1411774390297981 0.0399565474214143
0.6780939599120687 0.4674323563247764 0.2904934027129007
0.8089374749002642 0.2767572779374552 -0.0031304136180577
0.4702941762090675 0.6027435493231588 0.2447816337773330
0.4074894384645012 0.4291700894421952 0.1202560991280189
0.0688882268817681 0.7616764586079856 0.3648630796413163
0.8804695154963592 0.1840902386692324 0.1136271607378698
0.5447492227924404 0.5187089535628006 0.3529077387976006
0.5844629123469711 0.2850766534168785 0.1890210829388621
0.2438582722808197 0.6235629464241037 0.4341677332605185
0.5550820915695746 0.0473372114300804 0.1807082462826699
0.2262436577888775 0.3757276436561856 0.4235995445991550
0.6704712728720521 0.2144534701246205 0.1021571488798110
0.3318766778561487 0.5522140594684749 0.3458946074427623
0.3470763242808563 0.0374889220836147 0.1737201433345354
0.0066904574958942 0.3702792987466113 0.4156707716057306
0.6541521012582406 0.4395671679363240 0.1020617690525857
0.3301531236848629 0.7779077137070356 0.3456519709494881
0.4137908552137228 0.2296173497941459 0.1135446197266712
0.0839647011181771 0.5653301705616857 0.3528593408069676
0.9257449958260431 0.6963142522917266 0.1134338790845677
0.5911697615454808 0.0255581740793344 0.3526894284442319
0.2362912817872400 0.0951820298970834 0.0398388304491713
0.8995444133082935 0.4319690486033740 0.2902151602855768
0.4813977058401538 0.8545467788310275 0.0699156877098467
0.1428920724253692 0.1923735521293346 0.3135273407435739
0.2691195533345582 0.8882797021645757 0.0628337650855238
0.9327201004778048 0.2224249120486654 0.3017719072289488
0.1712827419977042 0.1968072342617855 0.1254118541599361
0.8448394221103870 0.5328801468221422 0.3762094591195124
0.9138451514773730 0.9746270124522467 0.1252663911994221
0.5770839354199777 0.3117013887913648 0.3766200962205244
0.7289898380786251 0.8408048674700221 0.0627702697370151
0.3999122518830114 0.1776422625835299 0.3020304916081021
0.5690859128568667 0.7828562405033295 -0.0183709292883462

0.2291700666931274 0.1221337386089679 0.2265906817142750
0.8063494824490809 0.0355883155336140 -0.0004504768417310
0.4666212997151856 0.3697770107329261 0.2418883089776728
0.4648747697541286 0.0996017871464790 0.0503296851127179
0.1325871093564097 0.4283638031824790 0.2954873884315021
0.3064318218764450 0.5398600056093088 0.1712078538215910
0.9804223348062976 0.8746557526867637 0.4185400540835959
0.3394237591967657 0.3038128219005038 -0.0002814327890143
0.0131761544152667 0.6434733322217403 0.2417510372229853
0.7445413479749010 0.6450250551612577 0.0502249313964772
0.4056166722087223 0.9776003580697362 0.2954313734376716
0.4830243849233466 0.6285321850555450 0.0701156928436184
0.1594442719280283 0.9672344104868397 0.3134240576724561
0.3432992889048544 0.8038902684070144 0.1710236240310908
0.0040368397842650 0.1293915488062204 0.4186996469226590
0.1357690126941366 0.9393242634045423 0.1252958384140583
0.7978815548171523 0.2647028912397503 0.3755268517506891
0.0742295237310190 0.7707357384791877 -0.0003552390344887
0.7402118623077822 0.0966924176320952 0.2418992720524071
0.5533906537974991 0.5223347805608070 -0.0078383218272891
0.2112747283049061 0.8523319068776731 0.2347146197363674
0.2553201709396458 0.6269391955948922 0.0700647669345943
0.9180504836491976 0.9507578964681181 0.3133301804032051
0.2216882393845286 0.3810267843777117 0.0630645406873187
0.8876254698989259 0.7102056776135426 0.3017847183746264
0.3233162234095224 0.5403695682707673 -0.0181821622467671
0.0100503639867891 0.3649781678284134 0.0503634708308370
0.6822421946459867 0.7044380315762081 0.2954162586401491
0.3266840861729716 0.7862167216657191 -0.0183666806742366
0.9887840431776279 0.1073438875160558 0.2264312977030123
0.0785156160336196 0.5562071475774245 -0.0076657647706440
0.7510188681050749 0.8989462307584405 0.2346552304728116
0.5873384337670650 0.0310852346889262 -0.0079187535056669
0.2581939340755960 0.3596110505842447 0.2349451871334644
0.5708683372344731 0.7667352761556054 0.1710503533219342
0.2350403633228986 0.1058012615311418 0.4186790243841245
0.0030563442172888 0.8813568764833930 0.2264602812329305

Text A4.2: Solid-State ^{19}F and ^{115}In NMR

The solid-state ^{1}H and ^{19}F magic angle spinning (MAS) nuclear magnetic resonance (NMR) spectra were acquired on a Bruker ASCEND 400 MHz (9.4 T) solid-state DNP NMR spectrometer operating at Larmor frequencies of 400.202 and 376.532 MHz for ^{1}H and ^{19}F nuclei, respectively and equipped with a variable-temperature 2.5 mm triple-resonance HFX MAS NMR probehead. MAS conditions of 25-35 kHz were used to average the strong ^{19}F-^{19}F nuclear dipole-dipole couplings and improve spectral resolution. For the solid-state MAS NMR measurements, the F:In_2O_3 cube NCs (3% InF_3) were mixed with KBr powder in a 1:1 ratio by mass. Rapid magic-angle-spinning of conductive materials within an external magnetic field for solid-state NMR measurements gives rise to substantial heating effects due to electromagnetic eddy currents.[253] The added KBr serves dual purposes: 1] as a diluent to improve penetration of the radiofrequency (rf) pulses throughout the sample and reduce interparticle contacts that exacerbate heating effects, and 2] to provide a highly sensitive internal temperature probe by measurement of the temperature-dependent ^{79}Br T_1 relaxation times.[254] For all of the solid-state NMR measurements, the internal sample temperature was determined to ± 1 K by analysis of the ^{79}Br T_1 relaxation times.

The 1D ^{19}F Hahn echo spectrum in Figure 4.12 a was acquired at 35 kHz MAS, a sample temperature of 395 K, and using a 90°-τ-180°-τ pulse sequence with rotor-synchronized τ delay times of one rotor period and 100 kHz rf pulses. The 2D ^{1}H{^{29}F} NMR correlation spectrum in Figure 4.12 b was acquired at 25 kHz MAS and a sample temperature of 327 K using a 2D dipolar-mediated *H*eteronuclear *M*ultiple *Q*uantum *C*orrelation (HMQC) pulse sequence, where the ^{1}H-^{19}F nuclear dipole-dipole couplings were reintroduced using 24 rotor periods (0.96 ms) $SR26_4^{11}$ recoupling[255] and 50 kHz rf power for recoupling. The ^{19}F excitation frequency was 210 ppm. A recycle delay time of

2.5 s was used with a t_1 increment step size of 20 μs, 20 t_1 increments, and 512 transients for a total acquisition time of 7 h. For the ^{19}F spin-lattice (T_1) relaxation analyses in Figure 5.12, The ^{19}F T_1 relaxation times at different temperatures were measured using a saturation-recovery pulse sequence with Hahn echo detection. An array of 18 saturation recovery delay times were used with 512 transients for each and a recycle delay of 0.2 s. The ^{19}F saturation-recovery curves were fit in MATLAB to a single exponential functional from zero for each isochromat across the ^{19}F NMR spectra to obtain the ^{19}F relaxation times at each temperature as functions of the ^{19}F shift.

The solid-state ^{115}In NMR spectrum of undoped bulk polycrystalline In_2O_3 was acquired at a magnetic field strength of 18.8 T, while the ^{115}In NMR spectrum of F:In_2O_3 was acquired at 19.6 T. As noted in the main text, the bulk undoped In_2O_3 (cubic bixbyite phase by XRD, Figure 5.6) exhibits an isotropic ^{115}In shift of 170 ppm, consistent with diamagnetic ^{115}In environments in the In_2O_3 lattice. By comparison, the ^{115}In spectrum of F:In_2O_3 cube NCs (3% InF_3) exhibits an isotropic ^{115}In shift of 1400 ppm, displaced more than 1200 ppm from the position for diamagnetic In_2O_3. This displacement cannot be accounted for by the slightly different magnetic field strengths used to acquire the two spectra, and instead manifests a substantial Knight shift affecting the ^{115}In nuclei in the F:In_2O_3 NCs.

Parameters for the ^{115}In simulated lineshapes

	η[a]	C_Q (MHz)[b]	δ_{iso} (ppm)[c]	Gaussian Line broadening[d] (ppm)
Bulk undoped In_2O_3	1	128	170	300
F:In_2O_3	1	139	1400	800

[a] Asymmetry parameter

[b] Quadrupolar coupling constant

[c] Isotropic shift (including chemical and Knight shifts)

[d] Gaussian line broadening apodization was applied to account for distributions of chemical shifts, Knight shifts, and/or quadrupolar parameters

Table A4.1: ^{115}In Simulated Lineshape Parameter

Text A4.3: Modal Deconvolution of Monochromated EELS Data

The spectrum images for the electron energy loss spectroscopy (EELS) analysis are all acquired as 60x60 pixels with 200 ms per pixel. We choose 200 ms per acquisition in order to leave the zero-loss peak (ZLP) unsaturated on the EELS detector. In EELS, the most prominent feature of any spectrum is the ZLP, which contains the signal for all electrons which did not interact with the sample or only underwent elastic scattering and hence lost no energy. Thus, the ZLP is important for accurate calibration of the energy offset, since the ZLP is centered on the true $\Delta E=0$ point of the spectrum.

Because the ZLP is so much higher in intensity than the plasmon peaks in the EEL spectra it needs to be removed before applying our deconvolution, as small variations in the ZLP result in much larger (in magnitude) changes to the spectrum and hence dominate the deconvolution. Additionally, to collect the data the NCs must be dispersed on an electron transparent substrate. We chose SiN due to its large band gap so that the surface plasmons in the cubes are as independent of the substrate as possible. However, SiN does have an infrared phonon signature at ~1000 cm^{-1} which can be observed in EELS, we choose a background subtraction region from 1800 cm^{-1}-2400 cm^{-1} to avoid influence from the SiN phonons and the ZLP from the EELS signal.

Lastly, due to the high level of monochromation the total signal in the beam is significantly reduced resulting in a high level of noise in the 200 ms spectra. To combat this we apply a local-low-rank (LLR) denoising algorithm to smooth the spectra and aid in the deconvolution.[257] Here, the ZLP can be observed extending off the top of the figure as we approach lower energies, along with the shoulder corresponding to the SiN phonon. The denoising and background subtraction method removes the influence of noise as well as the ZLP while still accurately representing the as-acquired data.

To deconvolve the different plasmon modes in the signal, we use non-negative matrix factorization (NMF) a technique which deconvolves the spectral imaging (SI) dataset into all-positive spatial and spectral components and has been shown to provide accurate deconvolution in noisy data.[239] In NMF the number of components is chosen as an input parameter, that controls the dimensions of the optimized matrices. Cube structures like those examined in these experiments are known to have dominant corner and edge modes, so we compared the three structures in terms of a 2-component NMF deconvolution.

Here it can be seen that the corner and edge modes are clearly separated by the NMF deconvolution, since the two spatial components are shown to be highly localized to the corners and edges respectively. Additionally, it can be seen (especially in the cases of the cube and concave cube structures) that the edge mode is a combination of multiple peaks. The two dominant peaks are likely the edge and face plasmon modes of the cubes, which are spatially overlapped in the 2D projection when the electron beam passes normal to the edges. This is supported by the fact that in the octapod structure, where the faces of the structure are highly recessed with respect to the edges, there is only one strongly observed peak. The peaks are found by fitting a Lorentzian to a small region around each peak, which are the peak centers reported in Figure 5.12 of the main text. For

the edge modes in the concave cubes and cubes where the there are two distinct peaks, we report the average of the two in the main text.

It is also important to consider deconvolutions with a higher number of output components. We show the NMF deconvolution of the spectrum image for the 3% InF_3-doped nanocube with 2, 3, 4, and 5 output components. The 2-component fit is a duplication of the one observed in Figure A4.22, but overlaid with the FTIR data. Here, the edge peaks closely overlap with the high energy FTIR peak, but the corner mode is observed at a significantly higher energy than the dominant low energy FTIR peak. However, in the 3-component fit it can be seen that now the corner mode has been split into a higher and lower energy component, and the low energy component is now much closer to the expected FTIR peak. The result is not so surprising, since the liquid cell FTIR observes the ensemble behavior of many cubes, while the EELS isolates individual locations on a single nanocube, and more importantly, such plasmon modes are highly sensitive to the dielectric environment. In FTIR, the cubes are surrounded by a fluid with $n>1$, while the EELS measurements are conducted with an ultra-high vacuum surrounding the NC and one side of the NC adjacent to the SiN membrane. It is known that the interaction between LSPR modes and dielectric substrates causes shifts in plasmon peak energies, so likely the presence of the SiN membrane is significantly responsible for the disparities between energies of the modes observed by FTIR and EELS. This is supported by the 4-component deconvolution, where now the edge mode has also been split into a low-energy and high-energy component, indicating that substrate interaction has caused a split into a proximal and distal mode.[244] We also attempted to fit higher numbers of components, but at the 5-component fit the NMF deconvolution begins to return signals spatially localized in the background region with non-physical spectra, so we limited our analysis to four components or fewer.

Text A4.4: Surface Fluorine Estimation

To estimate surface fluorine in F:In_2O_3 cube NC (3% InF_3), ^{19}F NMR fluorine quantification is used in conjunction with total quantified fluorine from EDX. Relative bulk and surface ^{19}F NMR signal is used to define the number of surface fluorine atom in DFT simulations of F:In_2O_3 cube NC. The ideal bulk cubic bixbyite phase In_2O_3 has a unit cell parameter of a = 1.012 nm, containing 32 In atoms, 48 O atoms. Substituting 4 F atoms per unit cell provides a F/In at.% ratio of $\frac{\mathrm{F_{bulk}}}{\mathrm{In}} = \frac{4}{32} = 12.50\ \%$. Fluorine atomic content in F:In_2O_3 cube NCs (3% InF_3) quantified by EDX, sensitive to bulk fluorine due to deep secondary electron profiling depth, is at 11.76% (F/In% ratio), corresponding to approximately 3.70 F atoms per unit cell.

$$F_{bulk} = 3.70\ F\ atom/nm^3$$

The quantification of our ^{19}F NMR results indicates that 82% of the F is in a metallic environment and the relatively weak 1% signal identified as surface fluorine based on $^{1}H\{^{19}F\}$ MAS NMR, allowing an experimental determination of the surface-to-bulk fluorine ratio to be obtained. unit cell.

NMR surface-to-bulk ratio:

$$\frac{F_{NMR\ surface}}{F_{NMR\ bulk}} = \frac{1\ atom}{82\ atom} = 1.22\ \%$$

The total surface fluorine on NC is estimated from the NMR surface-to-bulk ratio, bulk fluorine quantification, volume and surface area from 162.1 nm edge-to-edge sized F:In_2O_3 cube NC (3% InF_3). The estimation provides surface fluorine atom coverage of 1.14 F atom/nm^2. It can be ascertained that one F atom substitution for DFT surface modeling (1 F atom/nm^2) reasonably corresponds to the experimental surface fluorine quantification.

Surface F Estimation: $V \times F_{bulk} \times \frac{F_{NMR\,surface}}{F_{NMR\,bulk}} \div \mathrm{S}$

$$(162.1\ nm)^3 \times 3.70\ F\ atom/nm^3 \times 1.22\ \% \div (6 \times (162.1\ nm)^2)$$

$$= 1.14\ F\ atom/nm^2$$

An ideal uniformly doped F:In_2O_3 cube NC can be assumed have surface-to-bulk fluorine atomic ratio corresponding to the surface-to-volume ratio of cubic shaped NC. Due to the large nature of 162.1 nm edge-to-edge sized NC cube, the surface-to-bulk ratio is low with most of fluorine found internally in the sub-surface NC lattice. The estimated fluorine surface coverage in F:In_2O_3 cube is physically within reasonable bounds.

$$F_{surface}(atom) : F_{bulk}(atom) = Surface\ (nm^3) : Volume\ (nm^3)$$

Ideal surface-to-bulk ratio: $\frac{S}{V} = \frac{6 \times (162.1\ nm)^2}{(162.1\ nm)^3} = \frac{F_{surface}}{F_{bulk}} = 3.70\ \%$

SUPPORTING INFORMATION FOR CHAPTER 6, 7

Supplementary material for additional information regarding NC sample.

Sample (% $Sn(ac)_4$)	ω_{LSPR} (cm^{-1})	ω_p (cm^{-1})	γ_L (cm^{-1})	γ_H (cm^{-1})	γ_X (cm^{-1})	γ_W (cm^{-1})	n_e (cm^{-3})	κ (cm^{-1})
0%	3744	12495	551	1056	3992	2105	0.69×10^{21}	1044
0.5%	3845	12885	517	1056	4112	2850	0.74×10^{21}	950
1%	4438	14495	756	1075	4243	2265	0.94×10^{21}	1152
3%	4789	15995	585	1050	3985	2155	1.15×10^{21}	916
4%	5066	16145	780	1094	4472	2450	1.17×10^{21}	1189
5%	5216	16715	623	1174	4597	1270	1.25×10^{21}	1971
10%	5858	17155	745	1082	5474	142	1.32×10^{21}	1045
12.5%	5737	16750	1588	1291	1811	757	1.26×10^{21}	1325

Table A6.1: Extended Drude Parameters

Text A6.1. COMSOL Finite Element Method

An array of cubic F,Sn:In_2O_3 NCs with 15 nm edge length, and an underlayer of PbS quantum dots of 2.5 nm radius was modeled using the Wave Optics Module in COMSOL. Film substrate was represented by Si (Salzberg), with the quantum dot layer

represented by PbS (Zemel) with the refractive index provided by the built-in Optical Materials Database. Dielectric function for NC in finite element method based COMSOL module was iteratively defined. Extended Drude model initial parameter from MATLAB least square methods was iteratively adjusted to accompany dielectric function of NC to match experimental NC spectra. A surrounding ligand layer around the NCs was represented with oleic acid (ε_m= 2.46) as the medium, while the remaining surrounding volume was set as air (ε_m= 1). For simulation conditions representing the samples for electron microscopy, the ligand medium and quantum dot layer were omitted. The system was then immersed in a perfect index matching layer (PML) that prevents unwanted backscattering from the outside boundary at the port electromagnetic source. Floquet boundary conditions were implemented with periodicity along x and y axis directions to represent NC arrays. The maximum and minimum mesh sizes were set at 0.5 and 0.05 nm, respectively, enabling fine physics-controlled meshing. This yielded 438,350 degrees of freedom and corresponded to 30.2 GB RAM for the biconjugate gradient stabilized method (BiCGStab) solver. The finite element method solutions to the Maxwell equations were then obtained in the full field mode for the near-field field formulation with de-polarized background electric field k-vector propagating perpendicular to the substrate.

References

(1) Comin, A.; Manna, L. New Materials for Tunable Plasmonic Colloidal Nanocrystals. *Chem. Soc. Rev.* **2014**, *43* (11), 3957–3975. https://doi.org/10.1039/C3CS60265F.

(2) LaMer, V. K.; Dinegar, R. H. Theory, Production and Mechanism of Formation of Monodispersed Hydrosols. *J. Am. Chem. Soc.* **1950**, *72* (11), 4847–4854. https://doi.org/10.1021/ja01167a001.

(3) Thanh, N. T. K.; Maclean, N.; Mahiddine, S. Mechanisms of Nucleation and Growth of Nanoparticles in Solution. *Chem. Rev.* **2014**, *114* (15), 7610–7630. https://doi.org/10.1021/cr400544s.

(4) Wang, F.; Richards, V. N.; Shields, S. P.; Buhro, W. E. Kinetics and Mechanisms of Aggregative Nanocrystal Growth. *Chem. Mater.* **2014**, *26* (1), 5–21. https://doi.org/10.1021/cm402139r.

(5) Lee, J.; Yang, J.; Kwon, S. G.; Hyeon, T. Nonclassical Nucleation and Growth of Inorganic Nanoparticles. *Nature Reviews Materials* **2016**, *1* (8), natrevmats201634. https://doi.org/10.1038/natrevmats.2016.34.

(6) Xia, Y.; Xia, X.; Peng, H.-C. Shape-Controlled Synthesis of Colloidal Metal Nanocrystals: Thermodynamic versus Kinetic Products. *J. Am. Chem. Soc.* **2015**, *137* (25), 7947–7966. https://doi.org/10.1021/jacs.5b04641.

(7) Yin, Y.; Alivisatos, A. P. Colloidal Nanocrystal Synthesis and the Organic–Inorganic Interface. *Nature* **2005**, *437* (7059), 664–670. https://doi.org/10.1038/nature04165.

(8) Gilroy, K. D.; Ruditskiy, A.; Peng, H. C.; Qin, D.; Xia, Y. Bimetallic Nanocrystals: Syntheses, Properties, and Applications. *Chem Rev* **2016**, *116*, 10414–10472. https://doi.org/10.1021/acs.chemrev.6b00211.

(9) Xia, X.; Xie, S.; Liu, M.; Peng, H.-C.; Lu, N.; Wang, J.; Kim, M. J.; Xia, Y. On the Role of Surface Diffusion in Determining the Shape or Morphology of Noble-Metal Nanocrystals. *PNAS* **2013**, *110* (17), 6669–6673. https://doi.org/10.1073/pnas.1222109110.

(10) Kwon, S. G.; Piao, Y.; Park, J.; Angappane, S.; Jo, Y.; Hwang, N.-M.; Park, J.-G.; Hyeon, T. Kinetics of Monodisperse Iron Oxide Nanocrystal Formation by "Heating-Up" Process. *J. Am. Chem. Soc.* **2007**, *129* (41), 12571–12584. https://doi.org/10.1021/ja074633q.

(11) Owen, J. S.; Chan, E. M.; Liu, H.; Alivisatos, A. P. Precursor Conversion Kinetics and the Nucleation of Cadmium Selenide Nanocrystals. *J. Am. Chem. Soc.* **2010**, *132* (51), 18206–18213. https://doi.org/10.1021/ja106777j.

(12) Kwon, S. G.; Hyeon, T. Formation Mechanisms of Uniform Nanocrystals via Hot-Injection and Heat-Up Methods. *Small* **2011**, *7* (19), 2685–2702. https://doi.org/10.1002/smll.201002022.

(13) Abe, S.; Čapek, R. K.; De Geyter, B.; Hens, Z. Tuning the Postfocused Size of Colloidal Nanocrystals by the Reaction Rate: From Theory to Application. *ACS Nano* **2012**, *6* (1), 42–53. https://doi.org/10.1021/nn204008q.
(14) Jansons, A. W.; Hutchison, J. E. Continuous Growth of Metal Oxide Nanocrystals: Enhanced Control of Nanocrystal Size and Radial Dopant Distribution. *ACS Nano* **2016**, *10* (7), 6942–6951. https://doi.org/10.1021/acsnano.6b02796.
(15) Franke, D.; Harris, D. K.; Chen, O.; Bruns, O. T.; Carr, J. A.; Wilson, M. W. B.; Bawendi, M. G. Continuous Injection Synthesis of Indium Arsenide Quantum Dots Emissive in the Short-Wavelength Infrared. *Nature Communications* **2016**, *7*, ncomms12749. https://doi.org/10.1038/ncomms12749.
(16) Ito, D.; Yokoyama, S.; Zaikova, T.; Masuko, K.; Hutchison, J. E. Synthesis of Ligand-Stabilized Metal Oxide Nanocrystals and Epitaxial Core/Shell Nanocrystals via a Lower-Temperature Esterification Process. *ACS Nano* **2014**, *8* (1), 64–75. https://doi.org/10.1021/nn401888h.
(17) van Embden, J.; Chesman, A. S. R.; Jasieniak, J. J. The Heat-Up Synthesis of Colloidal Nanocrystals. *Chemistry of Materials* **2015**, *27*, 2246–2285. https://doi.org/10.1021/cm5028964.
(18) Blanchard, J.; In, M.; Schaudel, B.; Sanchez, C. Hydrolysis and Condensation Reactions of Transition Metal Alkoxides: Calorimetric Study and Evaluation of the Extent of Reaction. *European Journal of Inorganic Chemistry* **1998**, *1998*, 1115–1127. https://doi.org/10.1002/(SICI)1099-0682(199808)1998:8<1115::AID-EJIC1115>3.0.CO;2-N.
(19) Darr, J. A.; Zhang, J.; Makwana, N. M.; Weng, X. Continuous Hydrothermal Synthesis of Inorganic Nanoparticles: Applications and Future Directions. *Chem. Rev.* **2017**. https://doi.org/10.1021/acs.chemrev.6b00417.
(20) Rabenau, A. The Role of Hydrothermal Synthesis in Preparative Chemistry. *Angew. Chem. Int. Ed. Engl.* **1985**, *24* (12), 1026–1040. https://doi.org/10.1002/anie.198510261.
(21) Nütz, T.; Felde, U. zum; Haase, M. Wet-Chemical Synthesis of Doped Nanoparticles: Blue-Colored Colloids of n-Doped SnO2:Sb. *The Journal of Chemical Physics* **1999**, *110* (24), 12142–12150. https://doi.org/10.1063/1.479151.
(22) Huang, Q.; Hu, S.; Zhuang, J.; Wang, X. MoO(3-x)-Based Hybrids with Tunable Localized Surface Plasmon Resonances: Chemical Oxidation Driving Transformation from Ultrathin Nanosheets to Nanotubes. *Chemistry* **2012**, *18*, 15283–15287. https://doi.org/10.1002/chem.201202630.
(23) Yoshimura, M.; Byrappa, K. Hydrothermal Processing of Materials: Past, Present and Future. *J Mater Sci* **2008**, *43* (7), 2085–2103. https://doi.org/10.1007/s10853-007-1853-x.
(24) Li, J.; Wu, Q.; Wu, J. Synthesis of Nanoparticles via Solvothermal and Hydrothermal Methods. In *Handbook of Nanoparticles*; Aliofkhazraei, M., Ed.;

Springer International Publishing, 2016; pp 295–328. https://doi.org/10.1007/978-3-319-15338-4_17.
(25) Zhong, X.; Feng, Y.; Zhang, Y.; Lieberwirth, I.; Knoll, W. Nonhydrolytic Alcoholysis Route to Morphology-Controlled ZnO Nanocrystals. *Small* **2007**, *3* (7), 1194–1199. https://doi.org/10.1002/smll.200600684.
(26) Bronstein, L. M.; Huang, X.; Retrum, J.; Schmucker, A.; Pink, M.; Stein, B. D.; Dragnea, B. Influence of Iron Oleate Complex Structure on Iron Oxide Nanoparticle Formation. *Chem. Mater.* **2007**, *19* (15), 3624–3632. https://doi.org/10.1021/cm062948j.
(27) Pham, H. T.; Jeong, H.-D. Non-Monotonic Size Dependence of Electron Mobility in Indium Oxide Nanocrystals Thin Film Transistor. *Bulletin of the Korean Chemical Society* **2014**, *35* (8), 2505–2511. https://doi.org/10.5012/bkcs.2014.35.8.2505.
(28) Zhang, Z.; Zhong, X.; Liu, S.; Li, D.; Han, M. Aminolysis Route to Monodisperse Titania Nanorods with Tunable Aspect Ratio. *Angewandte Chemie International Edition* **2005**, *44* (22), 3466–3470. https://doi.org/10.1002/anie.200500410.
(29) Zhang, Z.; Lu, M.; Xu, H.; Chin, W.-S. Shape-Controlled Synthesis of Zinc Oxide: A Simple Method for the Preparation of Metal Oxide Nanocrystals in Non-Aqueous Medium. *Chem. Eur. J.* **2007**, *13* (2), 632–638. https://doi.org/10.1002/chem.200600293.
(30) Narayanaswamy, A.; Xu, H.; Pradhan, N.; Kim, M.; Peng, X. Formation of Nearly Monodisperse In2O3 Nanodots and Oriented-Attached Nanoflowers: Hydrolysis and Alcoholysis vs Pyrolysis. *J. Am. Chem. Soc.* **2006**, *128* (31), 10310–10319. https://doi.org/10.1021/ja0627601.
(31) Deshmukh, R.; Niederberger, M. Mechanistic Aspects in the Formation, Growth and Surface Functionalization of Metal Oxide Nanoparticles in Organic Solvents. *Chem. Eur. J.* **2017**, *23* (36), 8542–8570. https://doi.org/10.1002/chem.201605957.
(32) Sowers, K. L.; Swartz, B.; Krauss, T. D. Chemical Mechanisms of Semiconductor Nanocrystal Synthesis. *Chemistry of Materials* **2013**, *25*, 1351–1362. https://doi.org/10.1021/cm400005c.
(33) Kriegel, I.; Rodríguez-Fernández, J.; Wisnet, A.; Zhang, H.; Waurisch, C.; Eychmüller, A.; Dubavik, A.; Govorov, A. O.; Feldmann, J. Shedding Light on Vacancy-Doped Copper Chalcogenides: Shape-Controlled Synthesis, Optical Properties, and Modeling of Copper Telluride Nanocrystals with Near-Infrared Plasmon Resonances. *ACS Nano* **2013**, *7* (5), 4367–4377. https://doi.org/10.1021/nn400894d.
(34) Kriegel, I.; Jiang, C.; Rodriguez-Fernandez, J.; Schaller, R. D.; Talapin, D. V.; da Como, E.; Feldmann, J. Tuning the Excitonic and Plasmonic Properties of Copper Chalcogenide Nanocrystals. *J Am Chem Soc* **2012**, *134*, 1583–1590. https://doi.org/10.1021/ja207798q.

(35) Xie, Y.; Riedinger, A.; Prato, M.; Casu, A.; Genovese, A.; Guardia, P.; Sottini, S.; Sangregorio, C.; Miszta, K.; Ghosh, S.; et al. Copper Sulfide Nanocrystals with Tunable Composition by Reduction of Covellite Nanocrystals with Cu+ Ions. *J. Am. Chem. Soc.* **2013**, *135* (46), 17630–17637. https://doi.org/10.1021/ja409754v.

(36) Hessel, C. M.; Pattani, V. P.; Rasch, M.; Panthani, M. G.; Koo, B.; Tunnell, J. W.; Korgel, B. A. Copper Selenide Nanocrystals for Photothermal Therapy. *Nano Lett.* **2011**, *11* (6), 2560–2566. https://doi.org/10.1021/nl201400z.

(37) Hsu, S.-W.; Ngo, C.; Bryks, W.; Tao, A. R. Shape Focusing During the Anisotropic Growth of CuS Triangular Nanoprisms. *Chemistry of Materials* **2015**, *27*, 4957–4963. https://doi.org/10.1021/acs.chemmater.5b01223.

(38) Li, W.; Shavel, A.; Guzman, R.; Rubio-Garcia, J.; Flox, C.; Fan, J.; Cadavid, D.; Ibanez, M.; Arbiol, J.; Morante, J. R.; et al. Morphology Evolution of Cu(2-x)S Nanoparticles: From Spheres to Dodecahedrons. *Chem Commun (Camb)* **2011**, *47*, 10332–10334. https://doi.org/10.1039/c1cc13803k.

(39) Liu, X.; Wang, X.; Zhou, B.; Law, W.-C.; Cartwright, A. N.; Swihart, M. T. Size-Controlled Synthesis of Cu2-XE (E = S, Se) Nanocrystals with Strong Tunable Near-Infrared Localized Surface Plasmon Resonance and High Conductivity in Thin Films. *Adv. Funct. Mater.* **2013**, *23* (10), 1256–1264. https://doi.org/10.1002/adfm.201202061.

(40) Turo, M. J.; Macdonald, J. E. Crystal-Bound vs Surface-Bound Thiols on Nanocrystals. *ACS Nano* **2014**, *8* (10), 10205–10213. https://doi.org/10.1021/nn5032164.

(41) Deka, S.; Genovese, A.; Zhang, Y.; Miszta, K.; Bertoni, G.; Krahne, R.; Giannini, C.; Manna, L. Phosphine-Free Synthesis of p-Type Copper(I) Selenide Nanocrystals in Hot Coordinating Solvents. *J. Am. Chem. Soc.* **2010**, *132* (26), 8912–8914. https://doi.org/10.1021/ja103223x.

(42) Pearson, R. G. Hard and Soft Acids and Bases, HSAB, Part 1: Fundamental Principles. *J. Chem. Educ.* **1968**, *45* (9), 581. https://doi.org/10.1021/ed045p581.

(43) Pearson, R. G. Hard and Soft Acids and Bases, HSAB, Part II: Underlying Theories. *J. Chem. Educ.* **1968**, *45* (10), 643. https://doi.org/10.1021/ed045p643.

(44) Pearson, R. G. Hard and Soft Acids and Bases. *J. Am. Chem. Soc.* **1963**, *85* (22), 3533–3539. https://doi.org/10.1021/ja00905a001.

(45) Pearson, R. G. Acids and Bases. *Science* **1966**, *151* (3707), 172–177. https://doi.org/10.1126/science.151.3707.172.

(46) Luther, J. M.; Jain, P. K.; Ewers, T.; Alivisatos, A. P. Localized Surface Plasmon Resonances Arising from Free Carriers in Doped Quantum Dots. *Nat Mater* **2011**, *10*, 361–366. https://doi.org/10.1038/nmat3004.

(47) Buonsanti, R.; Milliron, D. J. Chemistry of Doped Colloidal Nanocrystals. *Chemistry of Materials* **2013**, *25*, 1305–1317. https://doi.org/10.1021/cm304104m.

(48) Ghosh, S.; Saha, M.; De, S. K. Tunable Surface Plasmon Resonance and Enhanced Electrical Conductivity of In Doped ZnO Colloidal Nanocrystals. *Nanoscale* **2014**, *6* (12), 7039–7051. https://doi.org/10.1039/C3NR05608B.
(49) Dalpian, G. M.; Chelikowsky, J. R. Self-Purification in Semiconductor Nanocrystals. *Phys Rev Lett* **2006**, *96*, 226802. https://doi.org/10.1103/PhysRevLett.96.226802.
(50) Erwin, S. C.; Zu, L.; Haftel, M. I.; Efros, A. L.; Kennedy, T. A.; Norris, D. J. Doping Semiconductor Nanocrystals. *Nature* **2005**, *436* (7047), 91–94. https://doi.org/10.1038/nature03832.
(51) Ho, T.-L. Hard Soft Acids Bases (HSAB) Principle and Organic Chemistry. *Chem. Rev.* **1975**, *75* (1), 1–20. https://doi.org/10.1021/cr60293a001.
(52) Pearson, R. G. Recent Advances in the Concept of Hard and Soft Acids and Bases. *J. Chem. Educ.* **1987**, *64* (7), 561. https://doi.org/10.1021/ed064p561.
(53) Coughlan, C.; Ibanez, M.; Dobrozhan, O.; Singh, A.; Cabot, A.; Ryan, K. M. Compound Copper Chalcogenide Nanocrystals. *Chem Rev* **2017**, *117*, 5865–6109. https://doi.org/10.1021/acs.chemrev.6b00376.
(54) Buonsanti, R.; Llordes, A.; Aloni, S.; Helms, B. A.; Milliron, D. J. Tunable Infrared Absorption and Visible Transparency of Colloidal Aluminum-Doped Zinc Oxide Nanocrystals. *Nano Lett* **2011**, *11*, 4706–4710. https://doi.org/10.1021/nl203030f.
(55) Liang, X.; Ren, Y.; Bai, S.; Zhang, N.; Dai, X.; Wang, X.; He, H.; Jin, C.; Ye, Z.; Chen, Q.; et al. Colloidal Indium-Doped Zinc Oxide Nanocrystals with Tunable Work Function: Rational Synthesis and Optoelectronic Applications. *Chemistry of Materials* **2014**, *26*, 5169–5178. https://doi.org/10.1021/cm502812c.
(56) Tolman, C. A. Steric Effects of Phosphorus Ligands in Organometallic Chemistry and Homogeneous Catalysis. *Chem. Rev.* **1977**, *77* (3), 313–348. https://doi.org/10.1021/cr60307a002.
(57) Lounis, S. D.; Runnerstrom, E. L.; Llordes, A.; Milliron, D. J. Defect Chemistry and Plasmon Physics of Colloidal Metal Oxide Nanocrystals. *J Phys Chem Lett* **2014**, *5*, 1564–1574. https://doi.org/10.1021/jz500440e.
(58) Manthiram, K.; Alivisatos, A. P. Tunable Localized Surface Plasmon Resonances in Tungsten Oxide Nanocrystals. *J Am Chem Soc* **2012**, *134*, 3995–3998. https://doi.org/10.1021/ja211363w.
(59) Zhao, Y.; Pan, H.; Lou, Y.; Qiu, X.; Zhu, J.; Burda, C. Plasmonic Cu2−xS Nanocrystals: Optical and Structural Properties of Copper-Deficient Copper(I) Sulfides. *J. Am. Chem. Soc.* **2009**, *131* (12), 4253–4261. https://doi.org/10.1021/ja805655b.
(60) Dorfs, D.; Härtling, T.; Miszta, K.; Bigall, N. C.; Kim, M. R.; Genovese, A.; Falqui, A.; Povia, M.; Manna, L. Reversible Tunability of the Near-Infrared Valence Band Plasmon Resonance in Cu2–XSe Nanocrystals. *J. Am. Chem. Soc.* **2011**, *133* (29), 11175–11180. https://doi.org/10.1021/ja2016284.

(61) Mattox, T. M.; Bergerud, A.; Agrawal, A.; Milliron, D. J. Influence of Shape on the Surface Plasmon Resonance of Tungsten Bronze Nanocrystals. *Chem. Mater.* **2014**, *26* (5), 1779–1784. https://doi.org/10.1021/cm4030638.
(62) Lesnyak, V.; George, C.; Genovese, A.; Prato, M.; Casu, A.; Ayyappan, S.; Scarpellini, A.; Manna, L. Alloyed Copper Chalcogenide Nanoplatelets via Partial Cation Exchange Reactions. *ACS Nano* **2014**, *8* (8), 8407–8418. https://doi.org/10.1021/nn502906z.
(63) Akkerman, Q. A.; Genovese, A.; George, C.; Prato, M.; Moreels, I.; Casu, A.; Marras, S.; Curcio, A.; Scarpellini, A.; Pellegrino, T.; et al. From Binary Cu2S to Ternary Cu–In–S and Quaternary Cu–In–Zn–S Nanocrystals with Tunable Composition via Partial Cation Exchange. *ACS Nano* **2015**, *9* (1), 521–531. https://doi.org/10.1021/nn505786d.
(64) Ye, X.; Fei, J.; Diroll, B. T.; Paik, T.; Murray, C. B. Expanding the Spectral Tunability of Plasmonic Resonances in Doped Metal-Oxide Nanocrystals through Cooperative Cation–Anion Codoping. *J. Am. Chem. Soc.* **2014**, *136* (33), 11680–11686. https://doi.org/10.1021/ja5039903.
(65) Agrawal, A.; Singh, A.; Yazdi, S.; Singh, A.; Ong, G. K.; Bustillo, K.; Johns, R. W.; Ringe, E.; Milliron, D. J. Resonant Coupling between Molecular Vibrations and Localized Surface Plasmon Resonance of Faceted Metal Oxide Nanocrystals. *Nano Lett.* **2017**, *17* (4), 2611–2620. https://doi.org/10.1021/acs.nanolett.7b00404.
(66) Shanker, G. S.; Tandon, B.; Shibata, T.; Chattopadhyay, S.; Nag, A. Doping Controls Plasmonics, Electrical Conductivity, and Carrier-Mediated Magnetic Coupling in Fe and Sn Codoped In2O3 Nanocrystals: Local Structure Is the Key. *Chem. Mater.* **2015**, *27* (3), 892–900. https://doi.org/10.1021/cm5040936.
(67) Lounis, S. D.; Runnerstrom, E. L.; Bergerud, A.; Nordlund, D.; Milliron, D. J. Influence of Dopant Distribution on the Plasmonic Properties of Indium Tin Oxide Nanocrystals. *J. Am. Chem. Soc.* **2014**, *136* (19), 7110–7116. https://doi.org/10.1021/ja502541z.
(68) Urso, C.; Barawi, M.; Gaspari, R.; Sirigu, G.; Kriegel, I.; Zavelani-Rossi, M.; Scotognella, F.; Manca, M.; Prato, M.; De Trizio, L.; et al. Colloidal Synthesis of Bipolar Off-Stoichiometric Gallium Iron Oxide Spinel-Type Nanocrystals with Near-IR Plasmon Resonance. *J. Am. Chem. Soc.* **2017**, *139* (3), 1198–1206. https://doi.org/10.1021/jacs.6b11063.
(69) Biswas, K.; Rao, C. N. R. Metallic ReO3 Nanoparticles. *J. Phys. Chem. B* **2006**, *110* (2), 842–845. https://doi.org/10.1021/jp055670b.
(70) Ferretti, A.; Rogers, D. B.; Goodenough, J. B. The Relation of the Electrical Conductivity in Single Crystals of Rhenium Trioxide to the Conductivities of Sr2MgReO6 and NaxWO3. *Journal of Physics and Chemistry of Solids* **1965**, *26* (12), 2007–2011. https://doi.org/10.1016/0022-3697(65)90237-4.
(71) Corà, F.; Stachiotti, M. G.; Catlow, C. R. A.; Rodriguez, C. O. Transition Metal Oxide Chemistry: Electronic Structure Study of WO3, ReO3, and NaWO3. *J. Phys. Chem. B* **1997**, *101* (20), 3945–3952. https://doi.org/10.1021/jp963724z.

(72) Ghosh, S.; Biswas, K.; Rao, C. N. R. Core–Shell Nanoparticles Based on an Oxide Metal: ReO3@Au (Ag) and ReO3@SiO2 (TiO2). *J. Mater. Chem.* **2007**, *17* (23), 2412–2417. https://doi.org/10.1039/B701137G.

(73) Mattox, T. M.; Agrawal, A.; Milliron, D. J. Low Temperature Synthesis and Surface Plasmon Resonance of Colloidal Lanthanum Hexaboride (LaB6) Nanocrystals. *Chem. Mater.* **2015**, *27* (19), 6620–6624. https://doi.org/10.1021/acs.chemmater.5b02297.

(74) Xiao, L.; Su, Y.; Zhou, X.; Chen, H.; Tan, J.; Hu, T.; Yan, J.; Peng, P. Origins of High Visible Light Transparency and Solar Heat-Shielding Performance in LaB6. *Appl. Phys. Lett.* **2012**, *101* (4), 041913. https://doi.org/10.1063/1.4733386.

(75) Zhang, M.; Yuan, L.; Wang, X.; Fan, H.; Wang, X.; Wu, X.; Wang, H.; Qian, Y. A Low-Temperature Route for the Synthesis of Nanocrystalline LaB6. *Journal of Solid State Chemistry* **2008**, *181* (2), 294–297. https://doi.org/10.1016/j.jssc.2007.12.011.

(76) Yuan, Y.; Zhang, L.; Liang, L.; He, K.; Liu, R.; Min, G. A Solid-State Reaction Route to Prepare LaB6 Nanocrystals in Vacuum. *Ceramics International* **2011**, *37* (7), 2891–2896. https://doi.org/10.1016/j.ceramint.2011.03.073.

(77) Zhou, J.; Gao, Y.; Zhang, Z.; Luo, H.; Cao, C.; Chen, Z.; Dai, L.; Liu, X. VO_2 Thermochromic Smart Window for Energy Savings and Generation. *Scientific Reports* **2013**, *3*, srep03029. https://doi.org/10.1038/srep03029.

(78) Niklasson, G. A.; Li, S.-Y.; Granqvist, C. G. Thermochromic Vanadium Oxide Thin Films: Electronic and Optical Properties. *J. Phys.: Conf. Ser.* **2014**, *559* (1), 012001. https://doi.org/10.1088/1742-6596/559/1/012001.

(79) Bergerud, A.; Buonsanti, R.; Jordan-Sweet, J. L.; Milliron, D. J. Synthesis and Phase Stability of Metastable Bixbyite V2O3 Colloidal Nanocrystals. *Chem. Mater.* **2013**, *25* (15), 3172–3179. https://doi.org/10.1021/cm401530t.

(80) Dahlman, C. J.; LeBlanc, G.; Bergerud, A.; Staller, C.; Adair, J.; Milliron, D. J. Electrochemically Induced Transformations of Vanadium Dioxide Nanocrystals. *Nano Lett.* **2016**, *16* (10), 6021–6027. https://doi.org/10.1021/acs.nanolett.6b01756.

(81) Paik, T.; Hong, S.-H.; Gaulding, E. A.; Caglayan, H.; Gordon, T. R.; Engheta, N.; Kagan, C. R.; Murray, C. B. Solution-Processed Phase-Change VO2 Metamaterials from Colloidal Vanadium Oxide (VOx) Nanocrystals. *ACS Nano* **2014**, *8* (1), 797–806. https://doi.org/10.1021/nn4054446.

(82) Goodenough, J. B. Anomalous Properties of the Vanadium Oxides. *Annual Review of Materials Science* **1971**, *1* (1), 101–138. https://doi.org/10.1146/annurev.ms.01.080171.000533.

(83) Aetukuri, N. B.; Gray, A. X.; Drouard, M.; Cossale, M.; Gao, L.; Reid, A. H.; Kukreja, R.; Ohldag, H.; Jenkins, C. A.; Arenholz, E.; et al. Control of the Metal-Insulator Transition in Vanadium Dioxide by Modifying Orbital Occupancy. *Nat Phys* **2013**, *9* (10), 661–666. https://doi.org/10.1038/nphys2733.

(84) J. Chakrabarti, D.; Laughlin, D. The Cu-S (Copper-Sulfur) System. *Journal of Phase Equilibria* **1983**, *4*, 254–271. https://doi.org/10.1007/BF02868665.

(85) Grijalva, H.; Inoue, M.; Boggavarapu, S.; Calvert, P. Amorphous and Crystalline Copper Sulfides, CuS. *Journal of Materials Chemistry* **1996**, *6* (7), 1157–1160. https://doi.org/10.1039/JM9960601157.
(86) Nozaki, H.; Shibata, K.; Ohhashi, N. Metallic Hole Conduction in CuS. *Journal of Solid State Chemistry* **1991**, *91* (2), 306–311. https://doi.org/10.1016/0022-4596(91)90085-V.
(87) Liang, W.; Whangbo, M.-H. Conductivity Anisotropy and Structural Phase Transition in Covellite CuS. *Solid State Communications* **1993**, *85* (5), 405–408. https://doi.org/10.1016/0038-1098(93)90689-K.
(88) Mazin, I. I. Structural and Electronic Properties of the Two-Dimensional Superconductor CuS with 1$\frac{1}{3}$-Valent Copper. *Phys. Rev. B* **2012**, *85* (11), 115133. https://doi.org/10.1103/PhysRevB.85.115133.
(89) Yuan, K. D.; Wu, J. J.; Liu, M. L.; Zhang, L. L.; Xu, F. F.; Chen, L. D.; Huang, F. Q. Fabrication and Microstructure of P-Type Transparent Conducting CuS Thin Film and Its Application in Dye-Sensitized Solar Cell. *Appl. Phys. Lett.* **2008**, *93* (13), 132106. https://doi.org/10.1063/1.2991441.
(90) Morales-García, A.; Soares, A. L.; Dos Santos, E. C.; de Abreu, H. A.; Duarte, H. A. First-Principles Calculations and Electron Density Topological Analysis of Covellite (CuS). *J. Phys. Chem. A* **2014**, *118* (31), 5823–5831. https://doi.org/10.1021/jp4114706.
(91) Gotsis, H. J.; Barnes, A. C.; Strange, P. Experimental and Theoretical Investigation of the Crystal Structure of CuS. *J. Phys.: Condens. Matter* **1992**, *4* (50), 10461. https://doi.org/10.1088/0953-8984/4/50/034.
(92) Kumar, P.; Nagarajan, R.; Sarangi, R. Quantitative X-Ray Absorption and Emission Spectroscopies: Electronic Structure Elucidation of Cu 2 S and CuS. *Journal of Materials Chemistry C* **2013**, *1* (13), 2448–2454. https://doi.org/10.1039/C3TC00639E.
(93) Du, W.; Qian, X.; Ma, X.; Gong, Q.; Cao, H.; Yin, J. Shape-Controlled Synthesis and Self-Assembly of Hexagonal Covellite (CuS) Nanoplatelets. *Chem. Eur. J.* **2007**, *13* (11), 3241–3247. https://doi.org/10.1002/chem.200601368.
(94) Zhang, H.; Zhang, Y.; Yu, J.; Yang, D. Phase-Selective Synthesis and Self-Assembly of Monodisperse Copper Sulfide Nanocrystals. *J. Phys. Chem. C* **2008**, *112* (35), 13390–13394. https://doi.org/10.1021/jp801507h.
(95) Ghezelbash, A.; Korgel, B. A. Nickel Sulfide and Copper Sulfide Nanocrystal Synthesis and Polymorphism. *Langmuir* **2005**, *21* (21), 9451–9456. https://doi.org/10.1021/la051196p.
(96) Wu, H.; Chen, W. Synthesis and Reaction Temperature-Tailored Self-Assembly of Copper Sulfide Nanoplates. *Nanoscale* **2011**, *3* (12), 5096–5102. https://doi.org/10.1039/C1NR10829H.
(97) Xie, Y.; Carbone, L.; Nobile, C.; Grillo, V.; D'Agostino, S.; Della Sala, F.; Giannini, C.; Altamura, D.; Oelsner, C.; Kryschi, C.; et al. Metallic-like Stoichiometric Copper Sulfide Nanocrystals: Phase- and Shape-Selective

Synthesis, Near-Infrared Surface Plasmon Resonance Properties, and Their Modeling. *ACS Nano* **2013**, *7* (8), 7352–7369. https://doi.org/10.1021/nn403035s.
(98) Xie, Y.; Chen, W.; Bertoni, G.; Kriegel, I.; Xiong, M.; Li, N.; Prato, M.; Riedinger, A.; Sathya, A.; Manna, L. Tuning and Locking the Localized Surface Plasmon Resonances of CuS (Covellite) Nanocrystals by an Amorphous CuPdxS Shell. *Chem. Mater.* **2017**, *29* (4), 1716–1723. https://doi.org/10.1021/acs.chemmater.6b05184.
(99) Jain, P. K.; Manthiram, K.; Engel, J. H.; White, S. L.; Faucheaux, J. A.; Alivisatos, A. P. Doped Nanocrystals as Plasmonic Probes of Redox Chemistry. *Angew. Chem. Int. Ed.* **2013**, *52* (51), 13671–13675. https://doi.org/10.1002/anie.201303707.
(100) Alam, R.; Labine, M.; Karwacki, C. J.; Kamat, P. V. Modulation of Cu2–XS Nanocrystal Plasmon Resonance through Reversible Photoinduced Electron Transfer. *ACS Nano* **2016**, *10* (2), 2880–2886. https://doi.org/10.1021/acsnano.5b08066.
(101) White, S. L.; Banerjee, P.; Jain, P. K. Liquid-like Cationic Sub-Lattice in Copper Selenide Clusters. *Nature Communications* **2017**, *8*, ncomms14514. https://doi.org/10.1038/ncomms14514.
(102) Li, W.; Zamani, R.; Ibanez, M.; Cadavid, D.; Shavel, A.; Morante, J. R.; Arbiol, J.; Cabot, A. Metal Ions to Control the Morphology of Semiconductor Nanoparticles: Copper Selenide Nanocubes. *J Am Chem Soc* **2013**, *135*, 4664–4667. https://doi.org/10.1021/ja400472m.
(103) Salje, E.; Güttler, B. Anderson Transition and Intermediate Polaron Formation in WO3-XTransport Properties and Optical Absorption. *Philosophical Magazine Part B* **2006**, *50*, 607–620. https://doi.org/10.1080/13642818408238882.
(104) Deb, S. K. Opportunities and Challenges of Electrochromic Phenomena in Transition Metal Oxides. *Solar Energy Materials and Solar Cells* **1992**, *25* (3), 327–338. https://doi.org/10.1016/0927-0248(92)90077-3.
(105) Hwang, J.-H.; Edwards, D. D.; Kammler, D. R.; Mason, T. O. Point Defects and Electrical Properties of Sn-Doped In-Based Transparent Conducting Oxides. *Solid State Ionics* **2000**, *129* (1), 135–144. https://doi.org/10.1016/S0167-2738(99)00321-5.
(106) Heo, S.; Kim, J.; Ong, G. K.; Milliron, D. J. Template-Free Mesoporous Electrochromic Films on Flexible Substrates from Tungsten Oxide Nanorods. *Nano Lett* **2017**. https://doi.org/10.1021/acs.nanolett.7b02730.
(107) Deb, S. K. Opportunities and Challenges in Science and Technology of WO3 for Electrochromic and Related Applications. *Solar Energy Materials and Solar Cells* **2008**, *92* (2), 245–258. https://doi.org/10.1016/j.solmat.2007.01.026.
(108) Lee, K.; Seo, W. S.; Park, J. T. Synthesis and Optical Properties of Colloidal Tungsten Oxide Nanorods. *J. Am. Chem. Soc.* **2003**, *125* (12), 3408–3409. https://doi.org/10.1021/ja034011e.
(109) Greenblatt, M. Molybdenum Oxide Bronzes with Quasi-Low-Dimensional Properties. *Chem. Rev.* **1988**, *88* (1), 31–53. https://doi.org/10.1021/cr00083a002.

(110) Tan, X.; Wang, L.; Cheng, C.; Yan, X.; Shen, B.; Zhang, J. Plasmonic MoO3-X@MoO3 Nanosheets for Highly Sensitive SERS Detection through Nanoshell-Isolated Electromagnetic Enhancement. *Chem Commun (Camb)* **2016**, *52*, 2893–2896. https://doi.org/10.1039/c5cc10020h.
(111) Li, Y.; Cheng, J.; Liu, Y.; Liu, P.; Cao, W.; He, T.; Chen, R.; Tang, Z. Manipulation of Surface Plasmon Resonance in Sub-Stoichiometry Molybdenum Oxide Nanodots through Charge Carrier Control Technique. *J. Phys. Chem. C* **2017**, *121* (9), 5208–5214. https://doi.org/10.1021/acs.jpcc.6b11047.
(112) Kim, J.; Agrawal, A.; Krieg, F.; Bergerud, A.; Milliron, D. J. The Interplay of Shape and Crystalline Anisotropies in Plasmonic Semiconductor Nanocrystals. *Nano Lett* **2016**, *16*, 3879–3884. https://doi.org/10.1021/acs.nanolett.6b01390.
(113) Mehra, S.; Bergerud, A.; Milliron, D. J.; Chan, E. M.; Salleo, A. Core/Shell Approach to Dopant Incorporation and Shape Control in Colloidal Zinc Oxide Nanorods. *Chem. Mater.* **2016**, *28* (10), 3454–3461. https://doi.org/10.1021/acs.chemmater.6b00981.
(114) Della Gaspera, E.; Chesman, A. S. R.; van Embden, J.; Jasieniak, J. J. Non-Injection Synthesis of Doped Zinc Oxide Plasmonic Nanocrystals. *ACS Nano* **2014**, *8* (9), 9154–9163. https://doi.org/10.1021/nn5027593.
(115) Frank, G.; Köstlin, H. Electrical Properties and Defect Model of Tin-Doped Indium Oxide Layers. *Appl. Phys. A* **1982**, *27* (4), 197–206. https://doi.org/10.1007/BF00619080.
(116) Hamza, M. K.; Bluet, J. M.; Masenelli-Varlot, K.; Canut, B.; Boisron, O.; Melinon, P.; Masenelli, B. Tunable Mid IR Plasmon in GZO Nanocrystals. *Nanoscale* **2015**, *7*, 12030–12037. https://doi.org/10.1039/c5nr03378k.
(117) Gaspera, E. D.; Duffy, N. W.; Embden, J. van; Waddington, L.; Bourgeois, L.; Jasieniak, J. J.; Chesman, A. S. R. Plasmonic Ge-Doped ZnO Nanocrystals. *Chem. Commun.* **2015**, *51* (62), 12369–12372. https://doi.org/10.1039/C5CC02429C.
(118) Gordon, T. R.; Paik, T.; Klein, D. R.; Naik, G. V.; Caglayan, H.; Boltasseva, A.; Murray, C. B. Shape-Dependent Plasmonic Response and Directed Self-Assembly in a New Semiconductor Building Block, Indium-Doped Cadmium Oxide (ICO). *Nano Lett.* **2013**, *13* (6), 2857–2863. https://doi.org/10.1021/nl4012003.
(119) Diroll, B. T.; Gordon, T. R.; Gaulding, E. A.; Klein, D. R.; Paik, T.; Yun, H. J.; Goodwin, E. D.; Damodhar, D.; Kagan, C. R.; Murray, C. B. Synthesis of N-Type Plasmonic Oxide Nanocrystals and the Optical and Electrical Characterization of Their Transparent Conducting Films. *Chem. Mater.* **2014**, *26* (15), 4579–4588. https://doi.org/10.1021/cm5018823.
(120) Kanehara, M.; Koike, H.; Yoshinaga, T.; Teranishi, T. Indium Tin Oxide Nanoparticles with Compositionally Tunable Surface Plasmon Resonance Frequencies in the Near-IR Region. *J. Am. Chem. Soc.* **2009**, *131* (49), 17736–17737. https://doi.org/10.1021/ja9064415.

(121) Choi, S.-I.; Nam, K. M.; Park, B. K.; Seo, W. S.; Park, J. T. Preparation and Optical Properties of Colloidal, Monodisperse, and Highly Crystalline ITO Nanoparticles. *Chem. Mater.* **2008**, *20* (8), 2609–2611. https://doi.org/10.1021/cm703706m.
(122) Runnerstrom, E. L.; Bergerud, A.; Agrawal, A.; Johns, R. W.; Dahlman, C. J.; Singh, A.; Selbach, S. M.; Milliron, D. J. Defect Engineering in Plasmonic Metal Oxide Nanocrystals. *Nano Lett.* **2016**, *16* (5), 3390–3398. https://doi.org/10.1021/acs.nanolett.6b01171.
(123) Fang, H.; Hegde, M.; Yin, P.; Radovanovic, P. V. Tuning Plasmon Resonance of In2O3 Nanocrystals throughout the Mid-Infrared Region by Competition between Electron Activation and Trapping. *Chemistry of Materials* **2017**, *29*, 4970–4979. https://doi.org/10.1021/acs.chemmater.7b01349.
(124) De Trizio, L.; Buonsanti, R.; Schimpf, A. M.; Llordes, A.; Gamelin, D. R.; Simonutti, R.; Milliron, D. J. Nb-Doped Colloidal TiO2 Nanocrystals with Tunable Infrared Absorption. *Chem. Mater.* **2013**, *25* (16), 3383–3390. https://doi.org/10.1021/cm402396c.
(125) Kelchtermans, A.; Elen, K.; Schellens, K.; Conings, B.; Damm, H.; Boyen, H.-G.; D'Haen, J.; Adriaensens, P.; Hardy, A.; Bael, M. K. V. Relation between Synthesis Conditions, Dopant Position and Charge Carriers in Aluminium-Doped ZnO Nanoparticles. *RSC Advances* **2013**, *3* (35), 15254–15262. https://doi.org/10.1039/C3RA41847B.
(126) Kemmitt, T.; Ingham, B.; Linklater, R. Optimization of Sol–Gel-Formed ZnO:Al Processing Parameters by Observation of Dopant Ion Location Using Solid-State 27Al NMR Spectrometry. *J. Phys. Chem. C* **2011**, *115* (30), 15031–15039. https://doi.org/10.1021/jp204283k.
(127) Shi, Y.; Ndione, P. F.; Lim, L. Y.; Sokaras, D.; Weng, T.-C.; Nagaraja, A. R.; Karydas, A. G.; Perkins, J. D.; Mason, T. O.; Ginley, D. S.; et al. Self-Doping and Electrical Conductivity in Spinel Oxides: Experimental Validation of Doping Rules. *Chem. Mater.* **2014**, *26* (5), 1867–1873. https://doi.org/10.1021/cm404031k.
(128) Jansons, A. W.; Koskela, K. M.; Crockett, B. M.; Hutchison, J. E. Transition Metal-Doped Metal Oxide Nanocrystals: Efficient Substitutional Doping through a Continuous Growth Process. *Chem. Mater.* **2017**. https://doi.org/10.1021/acs.chemmater.7b02176.
(129) Crockett, B. M.; Jansons, A. W.; Koskela, K. M.; Johnson, D. W.; Hutchison, J. E. Radial Dopant Placement for Tuning Plasmonic Properties in Metal Oxide Nanocrystals. *ACS Nano* **2017**, *11* (8), 7719–7728. https://doi.org/10.1021/acsnano.7b01053.
(130) Shannon, R. D. Revised Effective Ionic Radii and Systematic Studies of Interatomic Distances in Halides and Chalcogenides. *Acta Cryst A, Acta Cryst Sect A, Acta Crystallogr A, Acta Crystallogr Sect A, Acta Crystallogr A Cryst Phys Diffr Theor Gen Crystallogr, Acta Crystallogr Sect A Cryst Phys Diffr*

Theor Gen Crystallogr **1976**, *32* (5), 751–767. https://doi.org/10.1107/S0567739476001551.

(131) Ye, X.; Fei, J.; Diroll, B. T.; Paik, T.; Murray, C. B. Expanding the Spectral Tunability of Plasmonic Resonances in Doped Metal-Oxide Nanocrystals through Cooperative Cation–Anion Codoping. *J. Am. Chem. Soc.* **2014**, *136* (33), 11680–11686. https://doi.org/10.1021/ja5039903.

(132) Ghosh, S.; Saha, M.; Dev Ashok, V.; Dalal, B.; De, S. K. Tunable Surface Plasmon Resonance in Sn-Doped Zn–Cd–O Alloyed Nanocrystals. *The Journal of Physical Chemistry C* **2015**, *119*, 1180–1187. https://doi.org/10.1021/jp5107873.

(133) Tandon, B.; Shanker, G. S.; Nag, A. Multifunctional Sn- and Fe-Codoped In2O3 Colloidal Nanocrystals: Plasmonics and Magnetism. *J Phys Chem Lett* **2014**, *5*, 2306–2311. https://doi.org/10.1021/jz500949g.

(134) Wang, Y.; He, J.; Liu, C.; Chong, W. H.; Chen, H. Thermodynamics versus Kinetics in Nanosynthesis. *Angew. Chem. Int. Ed.* **2015**, *54* (7), 2022–2051. https://doi.org/10.1002/anie.201402986.

(135) Guria, A. K.; Pradhan, N. Doped or Not Doped: Ionic Impurities for Influencing the Phase and Growth of Semiconductor Nanocrystals. *Chem. Mater.* **2016**, *28* (15), 5224–5237. https://doi.org/10.1021/acs.chemmater.6b02009.

(136) Xia, Y.; Xiong, Y.; Lim, B.; Skrabalak, S. E. Shape-Controlled Synthesis of Metal Nanocrystals: Simple Chemistry Meets Complex Physics? *Angew. Chem. Int. Ed. Engl.* **2009**, *48* (1), 60–103. https://doi.org/10.1002/anie.200802248.

(137) Polarz, S. Shape Matters: Anisotropy of the Morphology of Inorganic Colloidal Particles – Synthesis and Function. *Adv. Funct. Mater.* **2011**, *21* (17), 3214–3230. https://doi.org/10.1002/adfm.201101205.

(138) Herring, C. Some Theorems on the Free Energies of Crystal Surfaces. *Phys. Rev.* **1951**, *82* (1), 87–93. https://doi.org/10.1103/PhysRev.82.87.

(139) Vitos, L.; Ruban, A. V.; Skriver, H. L.; Kollár, J. The Surface Energy of Metals. *Surface Science* **1998**, *411* (1), 186–202. https://doi.org/10.1016/S0039-6028(98)00363-X.

(140) Mackenzie, J. K.; Moore, A. J. W.; Nicholas, J. F. Bonds Broken at Atomically Flat Crystal Surfaces—I: Face-Centred and Body-Centred Cubic Crystals. *Journal of Physics and Chemistry of Solids* **1962**, *23* (3), 185–196. https://doi.org/10.1016/0022-3697(62)90001-X.

(141) Mackenzie, J. K.; Nicholas, J. F. Bonds Broken at Atomically Flat Crystal Surfaces—II: Crystals Containing Many Atoms in a Primitive Unit Cell. *Journal of Physics and Chemistry of Solids* **1962**, *23* (3), 197–205. https://doi.org/10.1016/0022-3697(62)90002-1.

(142) Walsh, A.; A. Catlow, C. R. Structure, Stability and Work Functions of the Low Index Surfaces of Pure Indium Oxide and Sn-Doped Indium Oxide (ITO) from Density Functional Theory. *Journal of Materials Chemistry* **2010**, *20* (46), 10438–10444. https://doi.org/10.1039/C0JM01816C.

(143) Manna, L.; Wang; Cingolani, R.; Alivisatos, A. P. First-Principles Modeling of Unpassivated and Surfactant-Passivated Bulk Facets of Wurtzite CdSe: A Model System for Studying the Anisotropic Growth of CdSe Nanocrystals. *J. Phys. Chem. B* **2005**, *109* (13), 6183–6192. https://doi.org/10.1021/jp0445573.
(144) Zhang, J.-M.; Ma, F.; Xu, K.-W. Calculation of the Surface Energy of FCC Metals with Modified Embedded-Atom Method. *Applied Surface Science* **2004**, *229* (1), 34–42. https://doi.org/10.1016/j.apsusc.2003.09.050.
(145) Khurshid, H.; Li, W.; Chandra, S.; Phan, M.-H.; Hadjipanayis, G. C.; Mukherjee, P.; Srikanth, H. Mechanism and Controlled Growth of Shape and Size Variant Core/Shell FeO/Fe3O4 Nanoparticles. *Nanoscale* **2013**, *5* (17), 7942–7952. https://doi.org/10.1039/C3NR02596A.
(146) Ung, D.; Tung, L. D.; Caruntu, G.; Delaportas, D.; Alexandrou, I.; Prior, I. A.; Thanh, N. T. K. Variant Shape Growth of Nanoparticles of Metallic Fe–Pt, Fe–Pd and Fe–Pt–Pd Alloys. *CrystEngComm* **2009**, *11* (7), 1309–1316. https://doi.org/10.1039/B823290N.
(147) Xiong, Y.; McLellan, J. M.; Chen, J.; Yin, Y.; Li, Z.-Y.; Xia, Y. Kinetically Controlled Synthesis of Triangular and Hexagonal Nanoplates of Palladium and Their SPR/SERS Properties. *J. Am. Chem. Soc.* **2005**, *127* (48), 17118–17127. https://doi.org/10.1021/ja056498s.
(148) van der Stam, W.; Gradmann, S.; Altantzis, T.; Ke, X.; Baldus, M.; Bals, S.; de Mello Donega, C. Shape Control of Colloidal Cu2–XS Polyhedral Nanocrystals by Tuning the Nucleation Rates. *Chem. Mater.* **2016**, *28* (18), 6705–6715. https://doi.org/10.1021/acs.chemmater.6b03098.
(149) Choi, D.-H.; Jeong, G.-H.; Kim, S.-W. Fabrication of Size and Shape Controlled Cadmium Oxide Nanocrystals. *Bulletin of the Korean Chemical Society* **2011**, *32*, 3851–3852. https://doi.org/10.5012/bkcs.2011.32.11.3851.
(150) Chen, L.; Sakamoto, M.; Haruta, M.; Nemoto, T.; Sato, R.; Kurata, H.; Teranishi, T. Tin Ion Directed Morphology Evolution of Copper Sulfide Nanoparticles and Tuning of Their Plasmonic Properties via Phase Conversion. *Langmuir* **2016**, *32* (30), 7582–7587. https://doi.org/10.1021/acs.langmuir.6b02035.
(151) Wang, L.-S.; Sheng, T.-L.; Wang, X.; Chen, D.-B.; Hu, S.-M.; Fu, R.-B.; Xiang, S.-C.; Wu, X.-T. Self-Assembly of Luminescent Sn(IV)/Cu/S Clusters Using Metal Thiolates as Metalloligands. *Inorg. Chem.* **2008**, *47* (10), 4054–4059. https://doi.org/10.1021/ic701741m.
(152) Wang, X.; Sheng, T.-L.; Fu, R.-B.; Hu, S.-M.; Xiang, S.-C.; Wang, L.-S.; Wu, X.-T. Assembly of a Heterometallic Polynuclear SnIV−CuI Cluster Based on Sn(Edt)2 (Edt = Ethane-1,2-Dithiolate) as a Metalloligand. *Inorg. Chem.* **2006**, *45* (14), 5236–5238. https://doi.org/10.1021/ic060131m.
(153) van der Stam, W.; Akkerman, Q. A.; Ke, X.; van Huis, M. A.; Bals, S.; de Mello Donega, C. Solution-Processable Ultrathin Size- and Shape-Controlled Colloidal Cu2–XS Nanosheets. *Chem. Mater.* **2015**, *27* (1), 283–291. https://doi.org/10.1021/cm503929q.

(154) Nørby, P.; Johnsen, S.; Iversen, B. B. In Situ X-Ray Diffraction Study of the Formation, Growth, and Phase Transition of Colloidal Cu2–XS Nanocrystals. *ACS Nano* **2014**, *8* (5), 4295–4303. https://doi.org/10.1021/nn5010638.
(155) van der Stam, W.; Rabouw, F. T.; Geuchies, J. J.; Berends, A. C.; Hinterding, S. O. M.; Geitenbeek, R. G.; van der Lit, J.; Prévost, S.; Petukhov, A. V.; de Mello Donega, C. In Situ Probing of Stack-Templated Growth of Ultrathin Cu2–XS Nanosheets. *Chem. Mater.* **2016**, *28* (17), 6381–6389. https://doi.org/10.1021/acs.chemmater.6b02787.
(156) Kovalenko, M. V.; Bodnarchuk, M. I.; Lechner, R. T.; Hesser, G.; Schäffler, F.; Heiss, W. Fatty Acid Salts as Stabilizers in Size- and Shape-Controlled Nanocrystal Synthesis: The Case of Inverse Spinel Iron Oxide. *J. Am. Chem. Soc.* **2007**, *129* (20), 6352–6353. https://doi.org/10.1021/ja0692478.
(157) Peng, X. Mechanisms for the Shape-Control and Shape-Evolution of Colloidal Semiconductor Nanocrystals. *Adv. Mater.* **2003**, *15* (5), 459–463. https://doi.org/10.1002/adma.200390107.
(158) Goniakowski, J.; Finocchi, F.; Noguera, C. Polarity of Oxide Surfaces and Nanostructures. *Rep. Prog. Phys.* **2008**, *71* (1), 016501. https://doi.org/10.1088/0034-4885/71/1/016501.
(159) Noguera, C. Polar Oxide Surfaces. *J. Phys.: Condens. Matter* **2000**, *12* (31), R367. https://doi.org/10.1088/0953-8984/12/31/201.
(160) Rempel, J. Y.; Trout, B. L.; Bawendi, M. G.; Jensen, K. F. Density Functional Theory Study of Ligand Binding on CdSe (0001), (000$\bar{1}$), and (11$\bar{2}$0) Single Crystal Relaxed and Reconstructed Surfaces: Implications for Nanocrystalline Growth. *J. Phys. Chem. B* **2006**, *110* (36), 18007–18016. https://doi.org/10.1021/jp064051f.
(161) Boles, M. A.; Ling, D.; Hyeon, T.; Talapin, D. V. The Surface Science of Nanocrystals. *Nat Mater* **2016**, *15* (2), 141–153. https://doi.org/10.1038/nmat4526.
(162) Gordon, T. R.; Cargnello, M.; Paik, T.; Mangolini, F.; Weber, R. T.; Fornasiero, P.; Murray, C. B. Nonaqueous Synthesis of TiO2 Nanocrystals Using TiF4 to Engineer Morphology, Oxygen Vacancy Concentration, and Photocatalytic Activity. *J. Am. Chem. Soc.* **2012**, *134* (15), 6751–6761. https://doi.org/10.1021/ja300823a.
(163) Liu, G.; Yang, H. G.; Pan, J.; Yang, Y. Q.; Lu, G. Q. (Max); Cheng, H.-M. Titanium Dioxide Crystals with Tailored Facets. *Chem. Rev.* **2014**, *114* (19), 9559–9612. https://doi.org/10.1021/cr400621z.
(164) Yang, H. G.; Sun, C. H.; Qiao, S. Z.; Zou, J.; Liu, G.; Smith, S. C.; Cheng, H. M.; Lu, G. Q. Anatase TiO2 Single Crystals with a Large Percentage of Reactive Facets. *Nature* **2008**, *453* (7195), 638–641. https://doi.org/10.1038/nature06964.
(165) Liu, Y. Q.; Wang, F. X.; Xiao, Y.; Peng, H. D.; Zhong, H. J.; Liu, Z. H.; Pan, G. B. Facile Microwave-Assisted Synthesis of Klockmannite CuSe Nanosheets and Their Exceptional Electrical Properties. *Sci Rep* **2014**, *4*, 5998. https://doi.org/10.1038/srep05998.

(166) Wang, X.; Swihart, M. T. Controlling the Size, Shape, Phase, Band Gap, and Localized Surface Plasmon Resonance of Cu2–XS and CuxInyS Nanocrystals. *Chem. Mater.* **2015**, *27* (5), 1786–1791. https://doi.org/10.1021/cm504626u.
(167) Millstone, J. E.; Wei, W.; Jones, M. R.; Yoo, H.; Mirkin, C. A. Iodide Ions Control Seed-Mediated Growth of Anisotropic Gold Nanoparticles. *Nano Lett.* **2008**, *8* (8), 2526–2529. https://doi.org/10.1021/nl8016253.
(168) Magnussen, O. M. Ordered Anion Adlayers on Metal Electrode Surfaces. *Chem. Rev.* **2002**, *102* (3), 679–726. https://doi.org/10.1021/cr000069p.
(169) Ghosh, S.; Saha, M.; Paul, S.; De, S. K. Shape Controlled Plasmonic Sn Doped CdO Colloidal Nanocrystals: A Synthetic Route to Maximize the Figure of Merit of Transparent Conducting Oxide. *Small* **2017**, *13* (7), n/a-n/a. https://doi.org/10.1002/smll.201602469.
(170) Shieh, F.; Saunders, A. E.; Korgel, B. A. General Shape Control of Colloidal CdS, CdSe, CdTe Quantum Rods and Quantum Rod Heterostructures. *J. Phys. Chem. B* **2005**, *109* (18), 8538–8542. https://doi.org/10.1021/jp0509008.
(171) Yu, W. W.; Wang, Y. A.; Peng, X. Formation and Stability of Size-, Shape-, and Structure-Controlled CdTe Nanocrystals: Ligand Effects on Monomers and Nanocrystals. *Chem. Mater.* **2003**, *15* (22), 4300–4308. https://doi.org/10.1021/cm034729t.
(172) Chang, J.; R. Waclawik, E. Colloidal Semiconductor Nanocrystals: Controlled Synthesis and Surface Chemistry in Organic Media. *RSC Advances* **2014**, *4* (45), 23505–23527. https://doi.org/10.1039/C4RA02684E.
(173) Chang, J.; Waclawik, E. R. Experimental and Theoretical Investigation of Ligand Effects on the Synthesis of ZnO Nanoparticles. *J Nanopart Res* **2012**, *14* (8), 1012. https://doi.org/10.1007/s11051-012-1012-4.
(174) Joo, J.; Chow, B. Y.; Prakash, M.; Boyden, E. S.; Jacobson, J. M. Face-Selective Electrostatic Control of Hydrothermal Zinc Oxide Nanowire Synthesis. *Nat Mater* **2011**, *10* (8), 596–601. https://doi.org/10.1038/nmat3069.
(175) Gao, Y.; Cao, C.; Dai, L.; Luo, H.; Kanehira, M.; Ding, Y.; Wang, Z. L. Phase and Shape Controlled VO2 Nanostructures by Antimony Doping. *Energy Environ. Sci.* **2012**, *5* (9), 8708–8715. https://doi.org/10.1039/C2EE22290F.
(176) Cao, C.; Gao, Y.; Luo, H. Pure Single-Crystal Rutile Vanadium Dioxide Powders: Synthesis, Mechanism and Phase-Transformation Property. *J. Phys. Chem. C* **2008**, *112* (48), 18810–18814. https://doi.org/10.1021/jp8073688.
(177) Mehra, S.; Chan, E. M.; Salleo, A. Modular Synthetic Design Enables Precise Control of Shape and Doping in Colloidal Zinc Oxide Nanorods. *J. Mater. Chem. C* **2015**, *3* (27), 7172–7179. https://doi.org/10.1039/C5TC01216C.
(178) Agrawal, A.; Cho, S. H.; Zandi, O.; Ghosh, S.; Johns, R. W.; Milliron, D. J. Localized Surface Plasmon Resonance in Semiconductor Nanocrystals. *Chem. Rev.* **2018**, *118* (6), 3121–3207. https://doi.org/10.1021/acs.chemrev.7b00613.
(179) Sasaki, T.; Endo, Y.; Nakaya, M.; Kanie, K.; Nagatomi, A.; Tanoue, K.; Nakamura, R.; Muramatsu, A. One-Step Solvothermal Synthesis of Cubic-Shaped ITO Nanoparticles Precisely Controlled in Size and Shape and Their Electrical

Resistivity. *J. Mater. Chem.* **2010**, *20* (37), 8153–8157. https://doi.org/10.1039/C0JM01338B.
(180) Seo, D.; Park, J. C.; Song, H. Polyhedral Gold Nanocrystals with Oh Symmetry: From Octahedra to Cubes. *J. Am. Chem. Soc.* **2006**, *128* (46), 14863–14870. https://doi.org/10.1021/ja062892u.
(181) Zhou, S.; Li, J.; Gilroy, K. D.; Tao, J.; Zhu, C.; Yang, X.; Sun, X.; Xia, Y. Facile Synthesis of Silver Nanocubes with Sharp Corners and Edges in an Aqueous Solution. *ACS Nano* **2016**, *10* (11), 9861–9870. https://doi.org/10.1021/acsnano.6b05776.
(182) DeSantis, C. J.; Skrabalak, S. E. Size-Controlled Synthesis of Au/Pd Octopods with High Refractive Index Sensitivity. *Langmuir* **2012**, *28* (24), 9055–9062. https://doi.org/10.1021/la3002509.
(183) Alvarez, M. M.; Khoury, J. T.; Schaaff, T. G.; Shafigullin, M. N.; Vezmar, I.; Whetten, R. L. Optical Absorption Spectra of Nanocrystal Gold Molecules. *J. Phys. Chem. B* **1997**, *101* (19), 3706–3712. https://doi.org/10.1021/jp962922n.
(184) Naik, G. V.; Shalaev, V. M.; Boltasseva, A. Alternative Plasmonic Materials: Beyond Gold and Silver. *Adv. Mater.* **2013**, *25* (24), 3264–3294. https://doi.org/10.1002/adma.201205076.
(185) Agrawal, A.; Kriegel, I.; Milliron, D. J. Shape-Dependent Field Enhancement and Plasmon Resonance of Oxide Nanocrystals. *J. Phys. Chem. C* **2015**, *119* (11), 6227–6238. https://doi.org/10.1021/acs.jpcc.5b01648.
(186) Ghosh, S.; Manna, L. The Many "Facets" of Halide Ions in the Chemistry of Colloidal Inorganic Nanocrystals. *Chem. Rev.* **2018**, *118* (16), 7804–7864. https://doi.org/10.1021/acs.chemrev.8b00158.
(187) Meyns, M.; Iacono, F.; Palencia, C.; Geweke, J.; Coderch, M. D.; Fittschen, U. E. A.; Gallego, J. M.; Otero, R.; Juárez, B. H.; Klinke, C. Shape Evolution of CdSe Nanoparticles Controlled by Halogen Compounds. *Chem. Mater.* **2014**, *26* (5), 1813–1821. https://doi.org/10.1021/cm4037082.
(188) Ghosh, S.; Gaspari, R.; Bertoni, G.; Spadaro, M. C.; Prato, M.; Turner, S.; Cavalli, A.; Manna, L.; Brescia, R. Pyramid-Shaped Wurtzite CdSe Nanocrystals with Inverted Polarity. *ACS Nano* **2015**, *9* (8), 8537–8546. https://doi.org/10.1021/acsnano.5b03636.
(189) Avadhut, Y. S.; Weber, J.; Hammarberg, E.; Feldmann, C.; Schellenberg, I.; Pöttgen, R.; Schmedt auf der Günne, J. Study on the Defect Structure of SnO2:F Nanoparticles by High-Resolution Solid-State NMR. *Chem. Mater.* **2011**, *23* (6), 1526–1538. https://doi.org/10.1021/cm103286t.
(190) Sherry, L. J.; Chang, S.-H.; Schatz, G. C.; Van Duyne, R. P.; Wiley, B. J.; Xia, Y. Localized Surface Plasmon Resonance Spectroscopy of Single Silver Nanocubes. *Nano Lett.* **2005**, *5* (10), 2034–2038. https://doi.org/10.1021/nl0515753.
(191) Hoang, T. B.; Akselrod, G. M.; Argyropoulos, C.; Huang, J.; Smith, D. R.; Mikkelsen, M. H. Ultrafast Spontaneous Emission Source Using Plasmonic Nanoantennas. *Nature Communications* **2015**, *6*, 7788. https://doi.org/10.1038/ncomms8788.

(192) Hsu, S.-W.; Tao, A. R. Halide-Directed Synthesis of Square Prismatic Ag Nanocrystals by the Polyol Method. *Chem. Mater.* **2018**, *30* (14), 4617–4623. https://doi.org/10.1021/acs.chemmater.8b01166.
(193) Hrelescu, C.; Sau, T. K.; Rogach, A. L.; Jäckel, F.; Feldmann, J. Single Gold Nanostars Enhance Raman Scattering. *Appl. Phys. Lett.* **2009**, *94* (15), 153113. https://doi.org/10.1063/1.3119642.
(194) Stiles, P. L.; Dieringer, J. A.; Shah, N. C.; Duyne, R. P. V. Surface-Enhanced Raman Spectroscopy. *Annual Review of Analytical Chemistry* **2008**, *1* (1), 601–626. https://doi.org/10.1146/annurev.anchem.1.031207.112814.
(195) Coughlan, C.; Ibáñez, M.; Dobrozhan, O.; Singh, A.; Cabot, A.; Ryan, K. M. Compound Copper Chalcogenide Nanocrystals. *Chem. Rev.* **2017**, *117* (9), 5865–6109. https://doi.org/10.1021/acs.chemrev.6b00376.
(196) Hsu, S.-W.; On, K.; Tao, A. R. Localized Surface Plasmon Resonances of Anisotropic Semiconductor Nanocrystals. *J. Am. Chem. Soc.* **2011**, *133* (47), 19072–19075. https://doi.org/10.1021/ja2089876.
(197) Sardar, K.; Deepak, F. L.; Govindaraj, A.; Seikh, M. M.; Rao, C. N. R. InN Nanocrystals, Nanowires, and Nanotubes. *Small* **2005**, *1* (1), 91–94. https://doi.org/10.1002/smll.200400011.
(198) Palomaki, P. K.; Miller, E. M.; Neale, N. R. Control of Plasmonic and Interband Transitions in Colloidal Indium Nitride Nanocrystals. *J Am Chem Soc* **2013**, *135*, 14142–14150. https://doi.org/10.1021/ja404599g.
(199) Kim, J.; Agrawal, A.; Krieg, F.; Bergerud, A.; Milliron, D. J. The Interplay of Shape and Crystalline Anisotropies in Plasmonic Semiconductor Nanocrystals. *Nano Lett.* **2016**, *16* (6), 3879–3884. https://doi.org/10.1021/acs.nanolett.6b01390.
(200) Nakamoto, K. Applications in Coordination Chemistry. In *Infrared and Raman Spectra of Inorganic and Coordination Compounds*; John Wiley & Sons, Inc., 2008; pp 1–273. https://doi.org/10.1002/9780470405888.ch1.
(201) Jin, Y.; Yi, Q.; Ren, Y.; Wang, X.; Ye, Z. Molecular Mechanism of Monodisperse Colloidal Tin-Doped Indium Oxide Nanocrystals by a Hot-Injection Approach. *Nanoscale Res Lett* **2013**, *8* (1), 153. https://doi.org/10.1186/1556-276X-8-153.
(202) Pavia, D. L.; Lampman, G. M.; Kriz, G. S.; Vyvyan, J. A. *Introduction to Spectroscopy*; Cengage Learning, 2014.
(203) Dean, J. A. *Lange's Handbook of Chemistry*; McGraw-Hill, 1992.
(204) Karsi, N.; Lang, P.; Chehimi, M.; Delamar, M.; Horowitz, G. Modification of Indium Tin Oxide Films by Alkanethiol and Fatty Acid Self-Assembled Monolayers: A Comparative Study. *Langmuir* **2006**, *22* (7), 3118–3124. https://doi.org/10.1021/la052677b.
(205) Jansons, A. W.; Plummer, L. K.; Hutchison, J. E. Living Nanocrystals. *Chem. Mater.* **2017**, *29* (13), 5415–5425. https://doi.org/10.1021/acs.chemmater.7b00899.

(206) Sadoc, A.; Biswal, M.; Body, M.; Legein, C.; Boucher, F.; Massiot, D.; Fayon, F. NMR Parameters in Column 13 Metal Fluoride Compounds (AlF3, GaF3, InF3 and TlF) from First Principle Calculations. *Solid State Nuclear Magnetic Resonance* **2014**, *59–60*, 1–7. https://doi.org/10.1016/j.ssnmr.2014.01.001.
(207) Subba Ramaiah, K.; Sundara Raja, V. Structural and Electrical Properties of Fluorine Doped Tin Oxide Films Prepared by Spray-Pyrolysis Technique. *Applied Surface Science* **2006**, *253* (3), 1451–1458. https://doi.org/10.1016/j.apsusc.2006.02.019.
(208) Maruyama, T.; Nakai, T. Fluorine-doped Indium Oxide Thin Films Prepared by Chemical Vapor Deposition. *Journal of Applied Physics* **1992**, *71* (6), 2915–2917. https://doi.org/10.1063/1.351023.
(209) Toby, B. H.; Von Dreele, R. B. GSAS-II: The Genesis of a Modern Open-Source All Purpose Crystallography Software Package. *J Appl Cryst, J Appl Crystallogr* **2013**, *46* (2), 544–549. https://doi.org/10.1107/S0021889813003531.
(210) Zhou, X.-D.; Huebner, W. Size-Induced Lattice Relaxation in CeO2 Nanoparticles. *Appl. Phys. Lett.* **2001**, *79* (21), 3512–3514. https://doi.org/10.1063/1.1419235.
(211) Nadaud, N.; Lequeux, N.; Nanot, M.; Jové, J.; Roisnel, T. Structural Studies of Tin-Doped Indium Oxide (ITO) and In4Sn3O12. *Journal of Solid State Chemistry* **1998**, *135* (1), 140–148. https://doi.org/10.1006/jssc.1997.7613.
(212) Akkad, F. E.; Joseph, S. Physicochemical Characterization of Point Defects in Fluorine Doped Tin Oxide Films. *Journal of Applied Physics* **2012**, *112* (2), 023501. https://doi.org/10.1063/1.4736798.
(213) Costa, B. J.; Soufiane, A.; Messaddeq, Y. New Compositions of Fluoroindate Glasses with Higher Chemical Resistance. *Química Nova* **1998**, *21* (3), 370–371. https://doi.org/10.1590/S0100-40421998000300025.
(214) Li, J.; Liu, C.; Ye, Y.; Zhu, J.; Wang, S.; Guo, J.; Sham, T.-K. Tracking the Local Effect of Fluorine Self-Doping in Anodic TiO2 Nanotubes. *J. Phys. Chem. C* **2016**, *120* (8), 4623–4628. https://doi.org/10.1021/acs.jpcc.5b11445.
(215) Kröger, F. A.; Vink, H. J. Relations between the Concentrations of Imperfections in Crystalline Solids. In *Solid State Physics*; Seitz, F., Turnbull, D., Eds.; Academic Press, 1956; Vol. 3, pp 307–435. https://doi.org/10.1016/S0081-1947(08)60135-6.
(216) Walsh, A. Surface Oxygen Vacancy Origin of Electron Accumulation in Indium Oxide. *Appl. Phys. Lett.* **2011**, *98* (26), 261910. https://doi.org/10.1063/1.3604811.
(217) Runnerstrom, E. L.; Kelley, K. P.; Sachet, E.; Shelton, C. T.; Maria, J.-P. Epsilon-near-Zero Modes and Surface Plasmon Resonance in Fluorine-Doped Cadmium Oxide Thin Films. *ACS Photonics* **2017**, *4* (8), 1885–1892. https://doi.org/10.1021/acsphotonics.7b00429.
(218) Seo, J.-S.; Jeon, J.-H.; Hwang, Y. H.; Park, H.; Ryu, M.; Park, S.-H. K.; Bae, B.-S. Solution-Processed Flexible Fluorine-Doped Indium Zinc Oxide Thin-Film

Transistors Fabricated on Plastic Film at Low Temperature. *Scientific Reports* **2013**, *3*, 2085. https://doi.org/10.1038/srep02085.
(219) Schimpf, A. M.; Ochsenbein, S. T.; Buonsanti, R.; Milliron, D. J.; Gamelin, D. R. Comparison of Extra Electrons in Colloidal N-Type Al3+-Doped and Photochemically Reduced ZnO Nanocrystals. *Chem. Commun.* **2012**, *48* (75), 9352–9354. https://doi.org/10.1039/C2CC34635D.
(220) Schimpf, A. M.; Gunthardt, C. E.; Rinehart, J. D.; Mayer, J. M.; Gamelin, D. R. Controlling Carrier Densities in Photochemically Reduced Colloidal ZnO Nanocrystals: Size Dependence and Role of the Hole Quencher. *J. Am. Chem. Soc.* **2013**, *135* (44), 16569–16577. https://doi.org/10.1021/ja408030u.
(221) Zhang, L.; Yin, L.; Wang, C.; lun, N.; Qi, Y.; Xiang, D. Origin of Visible Photoluminescence of ZnO Quantum Dots: Defect-Dependent and Size-Dependent. *J. Phys. Chem. C* **2010**, *114* (21), 9651–9658. https://doi.org/10.1021/jp101324a.
(222) Whitaker, K. M.; Ochsenbein, S. T.; Polinger, V. Z.; Gamelin, D. R. Electron Confinement Effects in the EPR Spectra of Colloidal N-Type ZnO Quantum Dots. *J. Phys. Chem. C* **2008**, *112* (37), 14331–14335. https://doi.org/10.1021/jp804763y.
(223) Yamakawa, N.; Jiang, M.; Key, B.; Grey, C. P. Identifying the Local Structures Formed during Lithiation of the Conversion Material, Iron Fluoride, in a Li Ion Battery: A Solid-State NMR, X-Ray Diffraction, and Pair Distribution Function Analysis Study. *J. Am. Chem. Soc.* **2009**, *131* (30), 10525–10536. https://doi.org/10.1021/ja902639w.
(224) Kiczenski, T. J.; Stebbins, J. F. Fluorine Sites in Calcium and Barium Oxyfluorides: F-19 NMR on Crystalline Model Compounds and Glasses. *Journal of Non-Crystalline Solids* **2002**, *306* (2), 160–168. https://doi.org/10.1016/S0022-3093(02)01157-2.
(225) Kiczenski, T. J.; Stebbins, J. F. The Effect of Fictive Temperature on the Structural Environment of Fluorine in Silicate and Aluminosilicate Glasses. *Journal of the American Ceramic Society 89* (1), 57–64. https://doi.org/10.1111/j.1551-2916.2005.00677.x.
(226) Yesinowski, J. P. Solid-State NMR of Inorganic Semiconductors. In *Solid State NMR*; Topics in Current Chemistry; Springer, Berlin, Heidelberg, 2011; pp 229–312. https://doi.org/10.1007/128_2011_208.
(227) Yesinowski, J. P.; Berkson, Z. J.; Cadars, S.; Purdy, A. P.; Chmelka, B. F. Spatially Correlated Distributions of Local Metallic Properties in Bulk and Nanocrystalline GaN. *Phys. Rev. B* **2017**, *95* (23), 235201. https://doi.org/10.1103/PhysRevB.95.235201.
(228) Knight, W. D. Nuclear Magnetic Resonance Shift in Metals. *Phys. Rev.* **1949**, *76* (8), 1259–1260. https://doi.org/10.1103/PhysRev.76.1259.2.
(229) Slichter, C. P. *Principles of Magnetic Resonance*, 3rd ed.; Springer Series in Solid-State Sciences; Springer-Verlag: Berlin Heidelberg, 1990.

(230) Korringa, J. Nuclear Magnetic Relaxation and Resonnance Line Shift in Metals. *Physica* **1950**, *16* (7), 601–610. https://doi.org/10.1016/0031-8914(50)90105-4.
(231) Zapart, W.; Zapart, M. B.; Zhukov, A. P.; Popolitov, V. I.; Shuvalov, L. A. Phase Transition in In3Sb5O12 by NQR of 115In Nuclei. *Physics Letters A* **1987**, *121* (5), 248–250. https://doi.org/10.1016/0375-9601(87)90014-4.
(232) Han, O. H.; Timken, H. K. C.; Oldfield, E. Solid-state '"Magic-angle"' Sample-spinning Nuclear Magnetic Resonance Spectroscopic Study of Group III–V (13–15) Semiconductors. *The Journal of Chemical Physics* **1988**, *89* (10), 6046–6052. https://doi.org/10.1063/1.455418.
(233) Jung, W.-S.; Han, O. H.; Chae, S.-A. Characterization of Wurtzite Indium Nitride Synthesized from Indium Oxide by In-115 MAS NMR Spectroscopy. *Materials Letters* **2007**, *61* (16), 3413–3415. https://doi.org/10.1016/j.matlet.2006.11.083.
(234) Schurko, R. W. Ultra-Wideline Solid-State NMR Spectroscopy. *Acc. Chem. Res.* **2013**, *46* (9), 1985–1995. https://doi.org/10.1021/ar400045t.
(235) Pell, A. J.; Pintacuda, G. Broadband Solid-State MAS NMR of Paramagnetic Systems. *Progress in Nuclear Magnetic Resonance Spectroscopy* **2015**, *84–85*, 33–72. https://doi.org/10.1016/j.pnmrs.2014.12.002.
(236) Kim, J.; Ilott, A. J.; Middlemiss, D. S.; Chernova, N. A.; Pinney, N.; Morgan, D.; Grey, C. P. 2H and 27Al Solid-State NMR Study of the Local Environments in Al-Doped 2-Line Ferrihydrite, Goethite, and Lepidocrocite. *Chem. Mater.* **2015**, *27* (11), 3966–3978. https://doi.org/10.1021/acs.chemmater.5b00856.
(237) Hung, I.; Rossini, A. J.; Schurko, R. W. Application of the Carr−Purcell Meiboom−Gill Pulse Sequence for the Acquisition of Solid-State NMR Spectra of Spin-1/2 Nuclei. *J. Phys. Chem. A* **2004**, *108* (34), 7112–7120. https://doi.org/10.1021/jp0401123.
(238) Yin, P.; Hegde, M.; Tan, Y.; Chen, S.; Garnet, N.; Radovanovic, P. V. Controlling the Mechanism of Excitonic Splitting in In2O3 Nanocrystals by Carrier Delocalization. *ACS Nano* **2018**, *12* (11), 11211–11218. https://doi.org/10.1021/acsnano.8b05782.
(239) Nicoletti, O.; Peña, F. de la; Leary, R. K.; Holland, D. J.; Ducati, C.; Midgley, P. A. Three-Dimensional Imaging of Localized Surface Plasmon Resonances of Metal Nanoparticles. *Nature* **2013**, *502* (7469), 80–84. https://doi.org/10.1038/nature12469.
(240) Naumov, I. I.; Li, Z.; Bratkovsky, A. M. Plasmonic Resonances and Hot Spots in Ag Octopods. *Appl. Phys. Lett.* **2010**, *96* (3), 033105. https://doi.org/10.1063/1.3273859.
(241) Mulvihill, M. J.; Ling, X. Y.; Henzie, J.; Yang, P. Anisotropic Etching of Silver Nanoparticles for Plasmonic Structures Capable of Single-Particle SERS. *J. Am. Chem. Soc.* **2010**, *132* (1), 268–274. https://doi.org/10.1021/ja906954f.
(242) García de Abajo, F. J. Optical Excitations in Electron Microscopy. *Rev. Mod. Phys.* **2010**, *82* (1), 209–275. https://doi.org/10.1103/RevModPhys.82.209.

(243) Hachtel, J. A.; Lupini, A. R.; Idrobo, J. C. Exploring the Capabilities of Monochromated Electron Energy Loss Spectroscopy in the Infrared Regime. *Scientific Reports* **2018**, *8* (1), 5637. https://doi.org/10.1038/s41598-018-23805-5.
(244) Li, G.; Cherqui, C.; Bigelow, N. W.; Duscher, G.; Straney, P. J.; Millstone, J. E.; Masiello, D. J.; Camden, J. P. Spatially Mapping Energy Transfer from Single Plasmonic Particles to Semiconductor Substrates via STEM/EELS. *Nano Lett.* **2015**, *15* (5), 3465–3471. https://doi.org/10.1021/acs.nanolett.5b00802.
(245) Ringe, E.; DeSantis, C. J.; Collins, S. M.; Duchamp, M.; Dunin-Borkowski, R. E.; Skrabalak, S. E.; Midgley, P. A. Resonances of Nanoparticles with Poor Plasmonic Metal Tips. *Scientific Reports* **2015**, *5*, 17431. https://doi.org/10.1038/srep17431.
(246) Johns, R. W.; Bechtel, H. A.; Runnerstrom, E. L.; Agrawal, A.; Lounis, S. D.; Milliron, D. J. Direct Observation of Narrow Mid-Infrared Plasmon Linewidths of Single Metal Oxide Nanocrystals. *Nature Communications* **2016**, *7*, 11583. https://doi.org/10.1038/ncomms11583.
(247) Akselrod, G. M.; Weidman, M. C.; Li, Y.; Argyropoulos, C.; Tisdale, W. A.; Mikkelsen, M. H. Efficient Nanosecond Photoluminescence from Infrared PbS Quantum Dots Coupled to Plasmonic Nanoantennas. *ACS Photonics* **2016**, *3* (10), 1741–1746. https://doi.org/10.1021/acsphotonics.6b00357.
(248) Cao, S.; Zhang, S.; Zhang, T.; Lee, J. Y. Fluoride-Assisted Synthesis of Plasmonic Colloidal Ta-Doped TiO2 Nanocrystals for Near-Infrared and Visible-Light Selective Electrochromic Modulation. *Chem. Mater.* **2018**, *30* (14), 4838–4846. https://doi.org/10.1021/acs.chemmater.8b02196.
(249) Kresse, G.; Furthmüller, J. Efficient Iterative Schemes for Ab Initio Total-Energy Calculations Using a Plane-Wave Basis Set. *Phys. Rev. B* **1996**, *54* (16), 11169–11186. https://doi.org/10.1103/PhysRevB.54.11169.
(250) Kresse, G.; Joubert, D. From Ultrasoft Pseudopotentials to the Projector Augmented-Wave Method. *Phys. Rev. B* **1999**, *59* (3), 1758–1775. https://doi.org/10.1103/PhysRevB.59.1758.
(251) Perdew, J. P.; Burke, K.; Ernzerhof, M. Generalized Gradient Approximation Made Simple. *Phys. Rev. Lett.* **1996**, *77* (18), 3865–3868. https://doi.org/10.1103/PhysRevLett.77.3865.
(252) Monkhorst, H. J.; Pack, J. D. Special Points for Brillouin-Zone Integrations. *Phys. Rev. B* **1976**, *13* (12), 5188–5192. https://doi.org/10.1103/PhysRevB.13.5188.
(253) Yesinowski, J. P.; Ladouceur, H. D.; Purdy, A. P.; Miller, J. B. Electrical and Ionic Conductivity Effects on Magic-Angle Spinning Nuclear Magnetic Resonance Parameters of CuI. *The Journal of Chemical Physics* **2010**, *133* (23), 234509. https://doi.org/10.1063/1.3526484.
(254) Thurber, K. R.; Tycko, R. Measurement of Sample Temperatures under Magic-Angle Spinning from the Chemical Shift and Spin-Lattice Relaxation Rate of 79Br in KBr Powder. *Journal of Magnetic Resonance* **2009**, *196* (1), 84–87. https://doi.org/10.1016/j.jmr.2008.09.019.

(255) Brouwer, D. H.; Kristiansen, P. E.; Fyfe, C. A.; Levitt, M. H. Symmetry-Based 29Si Dipolar Recoupling Magic Angle Spinning NMR Spectroscopy: A New Method for Investigating Three-Dimensional Structures of Zeolite Frameworks. *J. Am. Chem. Soc.* **2005**, *127* (2), 542–543. https://doi.org/10.1021/ja043228l.
(256) Krivanek, O. L.; Lovejoy, T. C.; Dellby, N.; Carpenter, R. W. Monochromated STEM with a 30 MeV-Wide, Atom-Sized Electron Probe. *Microscopy (Oxf)* **2013**, *62* (1), 3–21. https://doi.org/10.1093/jmicro/dfs089.
(257) Spiegelberg, J.; Idrobo, J. C.; Herklotz, A.; Ward, T. Z.; Zhou, W.; Rusz, J. Local Low Rank Denoising for Enhanced Atomic Resolution Imaging. *Ultramicroscopy* **2018**, *187*, 34–42. https://doi.org/10.1016/j.ultramic.2018.01.012.
(258) Agrawal, A.; Cho, S. H.; Zandi, O.; Ghosh, S.; Johns, R. W.; Milliron, D. J. Localized Surface Plasmon Resonance in Semiconductor Nanocrystals. *Chem. Rev.* **2018**. https://doi.org/10.1021/acs.chemrev.7b00613.
(259) Cho, S. H.; Ghosh, S.; Berkson, Z. J.; Hachtel, J. A.; Shi, J.; Zhao, X.; Reimnitz, L. C.; Dahlman, C. J.; Ho, Y.; Yang, A.; et al. Syntheses of Colloidal F:In2O3 Cubes: Fluorine-Induced Faceting and Infrared Plasmonic Response. *Chem. Mater.* **2019**, *31* (7), 2661–2676. https://doi.org/10.1021/acs.chemmater.9b00906.
(260) Maier, S. A. *Plasmonics: Fundamentals and Applications*; Springer US, 2007.
(261) Ringe, E.; Langille, M. R.; Sohn, K.; Zhang, J.; Huang, J.; Mirkin, C. A.; Van Duyne, R. P.; Marks, L. D. Plasmon Length: A Universal Parameter to Describe Size Effects in Gold Nanoparticles. *J. Phys. Chem. Lett.* **2012**, *3* (11), 1479–1483. https://doi.org/10.1021/jz300426p.
(262) Link, S.; El-Sayed, M. A. Size and Temperature Dependence of the Plasmon Absorption of Colloidal Gold Nanoparticles. *J. Phys. Chem. B* **1999**, *103* (21), 4212–4217. https://doi.org/10.1021/jp984796o.
(263) Mendelsberg, R. J.; Garcia, G.; Milliron, D. J. Extracting Reliable Electronic Properties from Transmission Spectra of Indium Tin Oxide Thin Films and Nanocrystal Films by Careful Application of the Drude Theory. *Journal of Applied Physics* **2012**, *111* (6), 063515. https://doi.org/10.1063/1.3695996.
(264) Ito, D.; Yokoyama, S.; Zaikova, T.; Masuko, K.; Hutchison, J. E. Synthesis of Ligand-Stabilized Metal Oxide Nanocrystals and Epitaxial Core/Shell Nanocrystals via a Lower-Temperature Esterification Process. *ACS Nano* **2014**, *8* (1), 64–75. https://doi.org/10.1021/nn401888h.
(265) Kovalenko, M. V.; Manna, L.; Cabot, A.; Hens, Z.; Talapin, D. V.; Kagan, C. R.; Klimov, V. I.; Rogach, A. L.; Reiss, P.; Milliron, D. J.; et al. Prospects of Nanoscience with Nanocrystals. *ACS Nano* **2015**, *9* (2), 1012–1057. https://doi.org/10.1021/nn506223h.
(266) Murray, C. B.; Norris, D. J.; Bawendi, M. G. Synthesis and Characterization of Nearly Monodisperse CdE (E = Sulfur, Selenium, Tellurium) Semiconductor Nanocrystallites. *J. Am. Chem. Soc.* **1993**, *115* (19), 8706–8715. https://doi.org/10.1021/ja00072a025.

(267) Allen, P. M.; Walker, B. J.; Bawendi, M. G. Mechanistic Insights into the Formation of InP Quantum Dots. *Angewandte Chemie International Edition* **2010**, *49* (4), 760–762. https://doi.org/10.1002/anie.200905632.
(268) Weidman, M. C.; Beck, M. E.; Hoffman, R. S.; Prins, F.; Tisdale, W. A. Monodisperse, Air-Stable PbS Nanocrystals via Precursor Stoichiometry Control. *ACS Nano* **2014**, *8* (6), 6363–6371. https://doi.org/10.1021/nn5018654.
(269) Shen, G.; Guyot-Sionnest, P. HgS and HgS/CdS Colloidal Quantum Dots with Infrared Intraband Transitions and Emergence of a Surface Plasmon. *J. Phys. Chem. C* **2016**, *120* (21), 11744–11753. https://doi.org/10.1021/acs.jpcc.6b04014.
(270) Willets, K. A.; Van Duyne, R. P. Localized Surface Plasmon Resonance Spectroscopy and Sensing. *Annual Review of Physical Chemistry* **2007**, *58* (1), 267–297. https://doi.org/10.1146/annurev.physchem.58.032806.104607.
(271) Dong, A.; Jiao, Y.; Milliron, D. J. Electronically Coupled Nanocrystal Superlattice Films by in Situ Ligand Exchange at the Liquid–Air Interface. *ACS Nano* **2013**, *7* (12), 10978–10984. https://doi.org/10.1021/nn404566b.
(272) Dong, A.; Chen, J.; Oh, S. J.; Koh, W.; Xiu, F.; Ye, X.; Ko, D.-K.; Wang, K. L.; Kagan, C. R.; Murray, C. B. Multiscale Periodic Assembly of Striped Nanocrystal Superlattice Films on a Liquid Surface. *Nano Lett.* **2011**, *11* (2), 841–846. https://doi.org/10.1021/nl104208x.
(273) Winzer, P. J.; Neilson, D. T.; Chraplyvy, A. R. Fiber-Optic Transmission and Networking: The Previous 20 and the next 20 Years [Invited]. *Opt. Express, OE* **2018**, *26* (18), 24190–24239. https://doi.org/10.1364/OE.26.024190.
(274) Keiser, G. Optical Fiber Communications. In *Wiley Encyclopedia of Telecommunications*; Wiley, 2003. https://doi.org/10.1002/0471219282.eot158.
(275) Akselrod, G. M.; Argyropoulos, C.; Hoang, T. B.; Ciracì, C.; Fang, C.; Huang, J.; Smith, D. R.; Mikkelsen, M. H. Probing the Mechanisms of Large Purcell Enhancement in Plasmonic Nanoantennas. *Nature Photonics* **2014**, *8* (11), 835–840. https://doi.org/10.1038/nphoton.2014.228.
(276) Wu, Y.; Li, G.; Camden, J. P. Probing Nanoparticle Plasmons with Electron Energy Loss Spectroscopy. *Chem. Rev.* **2018**, *118* (6), 2994–3031. https://doi.org/10.1021/acs.chemrev.7b00354.
(277) Hachtel, J. A.; Huang, J.; Popovs, I.; Jansone-Popova, S.; Keum, J. K.; Jakowski, J.; Lovejoy, T. C.; Dellby, N.; Krivanek, O. L.; Idrobo, J. C. Identification of Site-Specific Isotopic Labels by Vibrational Spectroscopy in the Electron Microscope. *Science* **2019**, *363* (6426), 525–528. https://doi.org/10.1126/science.aav5845.
(278) Li, J.; Liu, L.; Sham, T.-K. 2D XANES–XEOL Spectroscopy Studies of Morphology-Dependent Phase Transformation and Corresponding Luminescence from Hierarchical TiO2 Nanostructures. *Chem. Mater.* **2015**, *27* (8), 3021–3029. https://doi.org/10.1021/acs.chemmater.5b00363.
(279) Wang, H.; Dou, K.; Teoh, W. Y.; Zhan, Y.; Hung, T. F.; Zhang, F.; Xu, J.; Zhang, R.; Rogach, A. L. Engineering of Facets, Band Structure, and Gas-Sensing Properties of Hierarchical Sn2+-Doped SnO2 Nanostructures. *Advanced*

Functional Materials **2013**, *23* (38), 4847–4853. https://doi.org/10.1002/adfm.201300303.
(280) Wang, H.; Rogach, A. L. Hierarchical SnO2 Nanostructures: Recent Advances in Design, Synthesis, and Applications. *Chem. Mater.* **2014**, *26* (1), 123–133. https://doi.org/10.1021/cm4018248.
(281) Seo, J.-S.; Jeon, J.-H.; Hwang, Y. H.; Park, H.; Ryu, M.; Park, S.-H. K.; Bae, B.-S. Solution-Processed Flexible Fluorine-Doped Indium Zinc Oxide Thin-Film Transistors Fabricated on Plastic Film at Low Temperature. *Scientific Reports* **2013**, *3*, srep02085. https://doi.org/10.1038/srep02085.
(282) Mergel, D.; Qiao, Z. Dielectric Modelling of Optical Spectra of Thin In 2 O 3 : Sn Films. *J. Phys. D: Appl. Phys.* **2002**, *35* (8), 794. https://doi.org/10.1088/0022-3727/35/8/311.
(283) Hamberg, I.; Granqvist, C. G. Evaporated Sn-doped In2O3 Films: Basic Optical Properties and Applications to Energy-efficient Windows. *Journal of Applied Physics* **1986**, *60* (11), R123–R160. https://doi.org/10.1063/1.337534.
(284) Hamberg, I.; Granqvist, C. G. Optical Properties of Transparent and Heat-reflecting Indium Tin Oxide Films: The Role of Ionized Impurity Scattering. *Appl. Phys. Lett.* **1984**, *44* (8), 721–723. https://doi.org/10.1063/1.94896.
(285) Gerlach, E. Carrier Scattering and Transport in Semiconductors Treated by the Energy-Loss Method. *J. Phys. C: Solid State Phys.* **1986**, *19* (24), 4585–4603. https://doi.org/10.1088/0022-3719/19/24/004.
(286) Bel Hadj Tahar, R.; Ban, T.; Ohya, Y.; Takahashi, Y. Tin Doped Indium Oxide Thin Films: Electrical Properties. *Journal of Applied Physics* **1998**, *83* (5), 2631–2645. https://doi.org/10.1063/1.367025.
(287) Tandon, B.; Ghosh, S.; Milliron, D. J. Dopant Selection Strategy for High-Quality Factor Localized Surface Plasmon Resonance from Doped Metal Oxide Nanocrystals. *Chem. Mater.* **2019**. https://doi.org/10.1021/acs.chemmater.9b02917.
(288) Miszta, K.; Graaf, J. de; Bertoni, G.; Dorfs, D.; Brescia, R.; Marras, S.; Ceseracciu, L.; Cingolani, R.; Roij, R. van; Dijkstra, M.; et al. Hierarchical Self-Assembly of Suspended Branched Colloidal Nanocrystals into Superlattice Structures. *Nature Mater* **2011**, *10* (11), 872–876. https://doi.org/10.1038/nmat3121.
(289) Pietryga, J. M.; Park, Y.-S.; Lim, J.; Fidler, A. F.; Bae, W. K.; Brovelli, S.; Klimov, V. I. Spectroscopic and Device Aspects of Nanocrystal Quantum Dots. *Chem. Rev.* **2016**, *116* (18), 10513–10622. https://doi.org/10.1021/acs.chemrev.6b00169.
(290) Korgel, B. A.; Fullam, S.; Connolly, S.; Fitzmaurice, D. Assembly and Self-Organization of Silver Nanocrystal Superlattices: Ordered "Soft Spheres." *J. Phys. Chem. B* **1998**, *102* (43), 8379–8388. https://doi.org/10.1021/jp981598o.
(291) Hugall, J. T.; Singh, A.; van Hulst, N. F. Plasmonic Cavity Coupling. *ACS Photonics* **2018**, *5* (1), 43–53. https://doi.org/10.1021/acsphotonics.7b01139.

(292) Pelton, M. Modified Spontaneous Emission in Nanophotonic Structures. *Nature Photonics* **2015**, *9* (7), 427–435. https://doi.org/10.1038/nphoton.2015.103.
(293) Singh, A.; de Roque, P. M.; Calbris, G.; Hugall, J. T.; van Hulst, N. F. Nanoscale Mapping and Control of Antenna-Coupling Strength for Bright Single Photon Sources. *Nano Lett.* **2018**, *18* (4), 2538–2544. https://doi.org/10.1021/acs.nanolett.8b00239.
(294) Kockum, A. F.; Miranowicz, A.; Liberato, S. D.; Savasta, S.; Nori, F. Ultrastrong Coupling between Light and Matter. *Nature Reviews Physics* **2019**, *1* (1), 19. https://doi.org/10.1038/s42254-018-0006-2.
(295) Vasa, P.; Lienau, C. Strong Light–Matter Interaction in Quantum Emitter/Metal Hybrid Nanostructures. *ACS Photonics* **2018**, *5* (1), 2–23. https://doi.org/10.1021/acsphotonics.7b00650.
(296) Vasa, P.; Wang, W.; Pomraenke, R.; Lammers, M.; Maiuri, M.; Manzoni, C.; Cerullo, G.; Lienau, C. Real-Time Observation of Ultrafast Rabi Oscillations between Excitons and Plasmons in Metal Nanostructures with J-Aggregates. *Nature Photonics* **2013**, *7* (2), 128–132. https://doi.org/10.1038/nphoton.2012.340.
(297) Purcell, E. M. Spontaneous Emission Probabilities at Radio Frequencies. In *Confined Electrons and Photons: New Physics and Applications*; Burstein, E., Weisbuch, C., Eds.; NATO ASI Series; Springer US: Boston, MA, 1995; pp 839–839. https://doi.org/10.1007/978-1-4615-1963-8_40.
(298) Fox, M. *Quantum Optics: An Introduction*; Oxford University Press USA - OSO: Oxford, UNITED KINGDOM, 2006.
(299) Coccioli, R.; Boroditsky, M.; Kim, K. W.; Rahmat-Samii, Y.; Yablonovitch, E. Smallest Possible Electromagnetic Mode Volume in a Dielectric Cavity. *IEE Proceedings - Optoelectronics* **1998**, *145* (6), 391–397. https://doi.org/10.1049/ip-opt:19982468.
(300) Sauvan, C.; Hugonin, J. P.; Maksymov, I. S.; Lalanne, P. Theory of the Spontaneous Optical Emission of Nanosize Photonic and Plasmon Resonators. *Phys. Rev. Lett.* **2013**, *110* (23), 237401. https://doi.org/10.1103/PhysRevLett.110.237401.
(301) Gérard, J.-M. Solid-State Cavity-Quantum Electrodynamics with Self-Assembled Quantum Dots. In *Single Quantum Dots: Fundamentals, Applications, and New Concepts*; Topics in Applied Physics; Springer Berlin Heidelberg: Berlin, Heidelberg, 2003; pp 269–314. https://doi.org/10.1007/978-3-540-39180-7_7.
(302) Chikkaraddy, R.; de Nijs, B.; Benz, F.; Barrow, S. J.; Scherman, O. A.; Rosta, E.; Demetriadou, A.; Fox, P.; Hess, O.; Baumberg, J. J. Single-Molecule Strong Coupling at Room Temperature in Plasmonic Nanocavities. *Nature* **2016**, *535* (7610), 127–130. https://doi.org/10.1038/nature17974.
(303) Kristensen, P. T.; Hughes, S. Modes and Mode Volumes of Leaky Optical Cavities and Plasmonic Nanoresonators. *ACS Photonics* **2014**, *1* (1), 2–10. https://doi.org/10.1021/ph400114e.

(304) Schmidt, F.-P.; Ditlbacher, H.; Hohenester, U.; Hohenau, A.; Hofer, F.; Krenn, J. R. Dark Plasmonic Breathing Modes in Silver Nanodisks. *Nano Lett.* **2012**, *12* (11), 5780–5783. https://doi.org/10.1021/nl3030938.
(305) Fang, W.; Xu, J. Y.; Yamilov, A.; Cao, H.; Ma, Y.; Ho, S. T.; Solomon, G. S. Large Enhancement of Spontaneous Emission Rates of InAs Quantum Dots in GaAs Microdisks. *Opt. Lett., OL* **2002**, *27* (11), 948–950. https://doi.org/10.1364/OL.27.000948.
(306) Yuen-Zhou, J.; Saikin, S. K.; Zhu, T.; Onbasli, M. C.; Ross, C. A.; Bulovic, V.; Baldo, M. A. Plexciton Dirac Points and Topological Modes. *Nature Communications* **2016**, *7*, 11783. https://doi.org/10.1038/ncomms11783.
(307) Parzefall, M.; Novotny, L. Light at the End of the Tunnel. *ACS Photonics* **2018**, *5* (11), 4195–4202. https://doi.org/10.1021/acsphotonics.8b00726.
(308) Wang, D.; Guan, J.; Hu, J.; Bourgeois, M. R.; Odom, T. W. Manipulating Light–Matter Interactions in Plasmonic Nanoparticle Lattices. *Acc. Chem. Res.* **2019**. https://doi.org/10.1021/acs.accounts.9b00345.
(309) Maier, S. A. Plasmonic Field Enhancement and SERS in the Effective Mode Volume Picture. *Opt. Express, OE* **2006**, *14* (5), 1957–1964. https://doi.org/10.1364/OE.14.001957.
(310) Aslam, U.; Rao, V. G.; Chavez, S.; Linic, S. Catalytic Conversion of Solar to Chemical Energy on Plasmonic Metal Nanostructures. *Nature Catalysis* **2018**, *1* (9), 656. https://doi.org/10.1038/s41929-018-0138-x.
(311) Zhan, C.; Chen, X.-J.; Yi, J.; Li, J.-F.; Wu, D.-Y.; Tian, Z.-Q. From Plasmon-Enhanced Molecular Spectroscopy to Plasmon-Mediated Chemical Reactions. *Nature Reviews Chemistry* **2018**, *2* (9), 216. https://doi.org/10.1038/s41570-018-0031-9.
(312) Caldwell, J. D.; Aharonovich, I.; Cassabois, G.; Edgar, J. H.; Gil, B.; Basov, D. N. Photonics with Hexagonal Boron Nitride. *Nat Rev Mater* **2019**, *4* (8), 552–567. https://doi.org/10.1038/s41578-019-0124-1.
(313) Miyata, K.; Meggiolaro, D.; Trinh, M. T.; Joshi, P. P.; Mosconi, E.; Jones, S. C.; Angelis, F. D.; Zhu, X.-Y. Large Polarons in Lead Halide Perovskites. *Science Advances* **2017**, *3* (8), e1701217. https://doi.org/10.1126/sciadv.1701217.
(314) Sanvitto, D.; Kéna-Cohen, S. The Road towards Polaritonic Devices. *Nat Mater* **2016**, *15* (10), 1061–1073. https://doi.org/10.1038/nmat4668.
(315) Ribeiro, R. F.; Martínez-Martínez, L. A.; Du, M.; Campos-Gonzalez-Angulo, J.; Yuen-Zhou, J. Polariton Chemistry: Controlling Molecular Dynamics with Optical Cavities. *Chem. Sci.* **2018**, *9* (30), 6325–6339. https://doi.org/10.1039/C8SC01043A.
(316) Kim, B. H.; Staller, C. M.; Cho, S. H.; Heo, S.; Garrison, C. E.; Kim, J.; Milliron, D. J. High Mobility in Nanocrystal-Based Transparent Conducting Oxide Thin Films. *ACS Nano* **2018**, *12* (4), 3200–3208. https://doi.org/10.1021/acsnano.7b06783.
(317) Sadoc, A.; Body, M.; Legein, C.; Biswal, M.; Fayon, F.; Rocquefelte, X.; Boucher, F. NMR Parameters in Alkali, Alkaline Earth and Rare Earth Fluorides

from First Principle Calculations. *Phys. Chem. Chem. Phys.* **2011**, *13* (41), 18539–18550. https://doi.org/10.1039/C1CP21253B.